Lyotropic liquid crystalline nanoparticles for multidrug loading involved in neuroprotection and regeneration

Miora Rakotoarisoa

Thèse de doctorat

NNT : 2021UPASQ039

université PARIS-SACLAY

Nanovecteurs lipidiques de molécules neuroprotectrices impliquées dans plusieurs mécanismes de régénération

Lyotropic liquid crystalline nanoparticles for multidrug loading involved in neuroprotection and regeneration

Thèse de doctorat de l'université Paris-Saclay

École doctorale n°569 : Innovation thérapeutique : du fondamental à l'appliqué (ITFA)
Spécialité de doctorat: Pharmacotechnie et Biopharmacie
Unité de recherche : Université Paris-Saclay, CNRS, Institut Galien Paris-Saclay, 92296, Châtenay-Malabry, France.
Référent : Faculté de pharmacie

Thèse présentée et soutenue à Paris-Saclay, le 17 Novembre 2021, par

Miora RAKOTOARISOA

Composition du Jury

Florence AGNELY Professeure, Université Paris-Saclay	Présidente
Pierandrea LO NOSTRO Professeur, University of Florence, Italy	Rapporteur & Examinateur
Yohann CORVIS Maître de Conférences, HDR, Université de Paris	Rapporteur & Examinateur
Chandrashekhar V. KULKARNI Professeur, University of Central Lancashire, United Kingdom	Examinateur

Direction de la thèse

Angelina ANGELOVA Directrice de Recherche, Université Paris-Saclay	Directrice de thèse

Remerciements

Je remercie premièrement ma directrice de thèse, Angelina Angelova pour m'avoir donné l'opportunité de réaliser cette thèse de doctorat, pour les moments partagés et les conseils avisés sur mes travaux, malgré vos nombreuses autres grandes responsabilités. Ce fut pour moi un enseignement précieux.

Je remercie infiniment l'ensemble des membres du jury de thèse : M. Pierandrea Lo Nostro et M. Yohann Corvis pour me faire l'honneur d'évaluer mon travail en tant que rapporteurs ; Mme Florence Agnely et M. Chandrashekhar V. Kulkarni pour avoir accepté de porter un regard critique sur cette thèse en tant qu'examinateurs.

Je remercie également Elias Fattal et Myriam Taverna, pour leurs conseils ainsi que tous les membres de l'équipe 2 « Physico-chimie des systèmes polyphasés » de l'Institut Galien Paris Saclay UMR8612 : Vincent Faivre, Sylviane Lesieur, Gillian Baratt, Claudie Bourgaux, François-Xavier Le Grand, David Chapron et Jean Jacques Vachon pour m'avoir accueillie chaleureusement au sein de l'équipe.

Merci à toutes les personnes avec qui j'ai eu l'opportunité de collaborer pendant ces trois ans : Angelov Borislav, Thomas Bizien, Juliette Vergnaud, Stéphanie Denis, Valérie Nicolas.

Je tiens maintenant à remercier, ceux avec qui j'ai eu la chance de partager l'expérience de la thèse: Islam, Antonio, Matis, Hung, Louis, et dont certains sont maintenant jeunes docteurs.
Un grand merci à Yu Wu, d'une aide précieuse et avec l'aide de qui j'ai pu obtenir ces résultats.

Et merci à ceux qui ont suivi tout ça de très loin, la famille Mennesson, la famille Dodo, mes amies qui m'ont tous soutenu dans la prière. Je pense plus spécifiquement à mon époux, ma fille Myrrhe, mes parents et ma sœur qui me soutiennent continuellement avec amour.

Merci Seigneur pour ta grâce, ton salut et ton aide!

Table of contents

Abbreviations

Aβ:	amyloid βeta
ACh:	acetylcholine
AD:	Alzheimer's disease
ALS:	amyotrophic lateral sclerosis
ApoE:	apolipoprotein E
APP:	amyloid beta precursor protein
ARE:	antioxidant response element
BBB:	blood-brain barrier
BDNF:	brain-derived neurotrophic factor
$Ca^{2+:}$	calcium ion
CAT:	catalase
CHCHD2:	coiled-coil-helix-coiled-coil-helix domain 2
CHOP:	CCAAT-enhancer-binding protein homologous protein
C9ORF72:	chromosome 9 open reading frame 72
COMT:	catechol-O-methyltransferase
CPP:	critical packing parameter
CREB:	cAMP (Cyclic adenosine monophosphate response) element-binding protein
cryoTEM:	cryogenic transmission electron microscopy
CU:	curcumin
CYP:	cytochrome P450
DARPP:	dopamine and adenosine 3t,5t -monophosphate-regulated phosphoprotein
DHA:	docosahexaenoic acid

DL: dilution line

DNA: deoxyribonucleic acid

DNAJC13: DNA J heat shock protein family (Hsp40) member C13

DSPE: distearoyl phosphatidylethanolamine

EIF4G1: eukaryotic translation initiation factor 4 gamma 1

EMA: European Medicines Agency

EPA: eicosapentaenoic acid

ERK: extracellular signal regulated kinase

FDA: Food and Drug Administration

FO: Fish oil

FUS: RNA binding protein Fused in Sarcoma

GBA: glucocerebrosidase

GRAS: generally recognized as safe

GPx: glutathione peroxidase

GR: glutathione reductase

GSH: glutathione

HEWL: hen egg white lysozyme

HD: Huntington disease

H_2O_2: hydrogen peroxide

HTT: huntingtin

IL-6: interleukin 6

iNOS: induced nitric oxide synthase

IV: intravenous

JNK: Jun N-terminal kinase

LCNPs: liquid crystalline nanoparticles

LDL: low density lipoprotein

Lf: lactoferrin

LLC: lyotropic liquid crystalline

LPS: lipopolysaccharide

LRRK1: leucine-rich repeat kinase 1

LUV: large unilamellar vesicles

MAO-B: monoamine oxidase type B

MDA: malondialdehyde

MLV: multilamellar vesicles

MO: monoolein

MPTP: 1-methyl-4-phenyl-1,2,3,6-tetrahydropyridine

MMSE: mini mental state examination

mRNA: messenger ribonucleic acid

NF-kb: nuclear factor kappa beta

NGF: nerve growth factor

NLC: nanostructured lipid carriers

NO: nitric oxide

NPs: nanoparticles

Nrf2: nuclear factor erythroid 2–related factor 2

NSAIDs: non-steroidal anti-inflammatory drugs

OHDA: 6 hydroxydopamine

OPTN: optineurin

PD: Parkinson disease

PEG: polyethylene glycol

PINK1: PTEN-induced putative kinase 1

PLGA: poly (lactic-co-glycolic acid)

PRKN: parkin

PSEN: presenilin

PUFA: polyunsaturated fatty acids

ROS: reactive oxygen species

SAXS: small angle X-ray scattering

SLCP: solid lipid curcumin nanoparticles

SLN: solid lipid nanoparticles

SOD1: superoxide dismutase 1

SNCA: synuclein alpha

SUV: small unilamellar vesicles

TARDBP: TAR DNA binding protein (TDP-43)

TPGS-PEG_{1000}: d-α-tocopheryl poly (ethylene glycol) 1000 succinate.

TREG: T regulatory cell

TRPME: transient receptor potential mucolipin-1 expression

TrkB: tropomyosin receptor kinase B

UBQLN2: ubiquitin 2

UCH: ubiquitin carboxy-terminal hydrolase

VPS35: vascular protein sorting

WGA: wheat-germ agglutinin

ω-3PUFAs: omega-3 poly unsaturated fatty acids

Résumé en français

1) Introduction générale

Les maladies neurodégénératives comme la maladie d'Alzheimer, la maladie de Parkinson sont des maladies multifactorielles aux étiologies complexes. Le système de délivrance de médicaments par les nanoparticules, introduit dans les années 1960, a fait naître l'espoir d'induire de multiples mécanismes de guérison dans des maladies aussi graves, grâce à une approche mieux ciblée. Les nanoparticules lipidiques ou amphiphiles telles que les liposomes, nanoparticules cristallines liquides, sont particulièrement attractives car elles ont la capacité de transporter de nombreux principes actifs pharmaceutiques, à la fois hydrophiles et lipophiles. Les lipides utilisés pour leur formulation sont généralement des molécules naturelles et améliorent la biodisponibilité des médicaments. De plus, les caractéristiques d'autoassemblage des lipides permettent la production de formulations qui peuvent conserver des similitudes et une affinité importante envers les membranes biologiques. Ensuite, ces nanovecteurs sont biocompatibles et biodégradables avec une faible toxicité pour des applications *in vivo*.

Les cristaux liquides lyotropes à base de lipides ou les nanoparticules cristallines liquides (LCNPs) ont suscité un grand intérêt ces dernières années car ils offrent une efficacité d'encapsulation supérieure à celle des liposomes. Nous nous intéressons aux LCNPs car ils peuvent être facilement synthétisés par autoassemblage à partir de l'exposition de lipides amphiphiles à l'eau et former une phase lamellaire, une phase cubique bicontinue, une phase éponge ou une phase hexagonale. Ce sont des nanostructures internes hautement ordonnées et thermodynamiquement stables qui permettent une administration prolongée ou contrôlée de médicaments. Aussi, nous nous inspirons de leur capacité à mimer les membranes biologiques. Par exemple, dans les mitochondries des amibes *Chaos carolinense*, il existe une

structure membranaire crystalline liquide (LC) cubique qui dépend de l'état de leur régime alimentaire. Lorsqu'ils sont affamés avec leur nourriture naturelle, la structure LC cubique mitochondriale pourrait échapper à l'autophagie et maintenir leur fonction normale de production d'ATP. Ainsi, les LCNPs pourraient transporter et délivrer des médicaments en cas de stress comme le stress oxydatif, le stress du réticulum endoplasmique ou le dysfonctionnement mitochondrial qui représentent des facteurs de risque des maladies neurodégénératives.

Dans ce projet, nous visons à obtenir des structures cubiques bicontinues (Fig. 1), avantageuses pour leur grande capacité d'encapsulation des molécules à la fois lipophiles et hydrophiles. La dispersion de phase cubique bicontinue dite cubosome ont une surface par volume beaucoup plus élevée que les structures micellaires et lamellaires, elles améliorent donc la biodisponibilité et la protection des biomolécules instables.

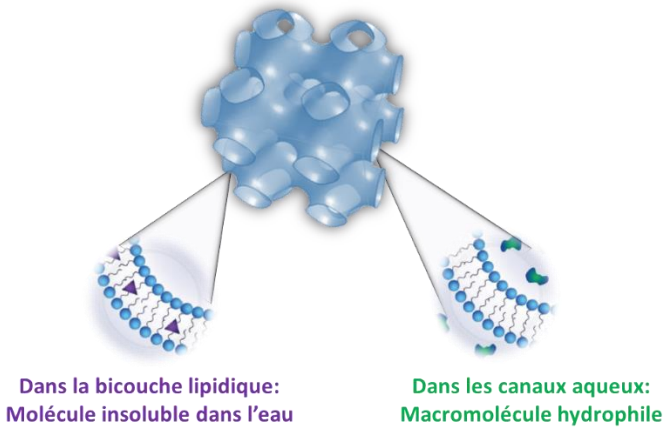

Figure 1. Présentation schématique de l'organisation supramoléculaire des particules de cubosome du groupe d'espace cubique double diamant *Pn3m*, permettant l'encapsulation et la protection de molécules instables d'importance thérapeutique.

La petite molécule insoluble dans l'eau que nous voulons encapsuler est la curcumine qui est un composé naturel sûr avec de nombreux potentiels de neuroprotection. La macromolécule hydrophile pour être transportée dans les canaux aqueux est une protéine instable. Dans un

premier temps, nous étudierons l'encapsulation de la catalase qui est un enzyme antioxydant. Ensuite, le facteur de croissance nerveuse dérivé du cerveau (BDNF), une neurotrophine favorisant la survie neuronale et qui est le principal candidat thérapeutique pour une multitude de troubles neurologiques.

Dans le premier chapitre de ce manuscrit, nous présenterons l'état de l'art sur les facteurs de risque des maladies neurodégénératives, l'effet potentiel de la curcumine et sa délivrance par les nanoparticules lipidiques dans ces maladies.

Ensuite, le second chapitre exposera les travaux expérimentaux sur la préparation et la formulation de nanostructures cristallines liquides (LC) à partir :

- De la monooléine (MO), lipide inclus dans le guide des ingrédients inactifs de la Food and Drug Administration (FDA),
- D'un co-lipide amphiphile naturel et économique : l'huile de poisson (FO), riche source d'acides gras polyinsaturés, bénéfiques pour la santé dans divers troubles humains,
- Et du surfactant d-α-tocophéryl poly(éthylène glycol) 1000 succinate (TPGS-PEG_{1000}) pour la stabilisation stérique.

L'étude des caractéristiques physico-chimiques et structurelles des nanostructures LC obtenues après encapsulation de la curcumine ont été effectuées par différentes techniques analytiques, telles que la diffraction des rayons X aux petits angles (SAXS), la diffusion dynamique de la lumière. Les effets *in vitro* des LCNPs contre le stress oxydatif ont été évalués chez les cellules neuronales humaines SH-SY5Y différenciées.

Le troisième chapitre développera les travaux expérimentaux sur la formulation et caractérisation des nanostructures LC chargées en curcumine, huile de poisson et l'enzyme catalase. Le faible coût de la catalase comme macromolécule hydrophile permet plusieurs expériences structurales et physico-chimiques.

Enfin, le dernier chapitre montrera les travaux expérimentaux sur la formulation et la caractérisation morphologique des nanostructures LC chargées en curcumine, huile de poisson et la protéine BDNF. Un modèle cellulaire de stress du réticulum endoplasmique

induit par la neurotoxine tunicamycine a été étudié pour évaluer la toxicité et les effets *in vitro* des nanoparticules par différentes techniques, telles que la microscopie confocale et différents kits de dosage.

2) LCNPs chargées en curcumine et huile de poisson

Les nanostructures LC ont été préparés par autoassemblage. Les lipides et la curcumine ont été dissous dans du chloroforme qui a été évaporé sous azote pour l'obtention d'un film lipidique mince. Après lyophilisation, les mélanges auto-assemblés ont été obtenus par la méthode d'hydratation suivie d'une agitation physique. Les compositions des systèmes MO/TPGS-PEG_{1000}/FO/CU auto-assemblés ont été choisies à partir du diagramme de phase présenté dans la figure 2A et 3A.

Tout d'abord, le système lipidique à base de MO et de TPGS-PEG_{1000} a été étudié pour déterminer le niveau d'hydratation afin de déterminer les transformations structurelles d'une mésophase lamellaire en mésophases cubiques bicontinues. Les résultats des diagrammes de diffraction des rayons X à température 22°C montrent la formation d'une phase lamellaire de 20 à 40 % de teneur en eau (Fig. 2B). Entre 50 à 80 % de teneur en eau, les diagrammes affichent des pics de Bragg qui indiquent la formation de phases cristallines liquides (LC) périodiques, à savoir des structures cubiques gyroïde *Ia3d* et bicontinues en double diamant *Pn3m* (Fig. 2B). Les mélanges MO/TPGS-PEG_{1000}/eau auto-assemblés montrent la dépendance du type de structure de la mésophase au niveau d'hydratation.

Ensuite, les caractéristiques structurelles des mélanges LC non lamellaires avec incorporation de la curcumine (CU) et l'huile de poisson (FO) ont été étudiées afin de déterminer les assemblages favorisant la formation d'une phase cubique stable dans des systèmes lipidiques chargés de curcumine à partir d'un mélange lipidique binaire composé de MO et de FO. Deux ratios huile de poisson/monooléine (FO:MO) = (20:60) et (60:40) ont été choisis. Les résultats à 22°C montrent que les structures cubiques bicontinues ont été maintenues entre 60 à 80 % de teneur en eau, indépendamment des ratios (FO:MO) (Fig. 3B).

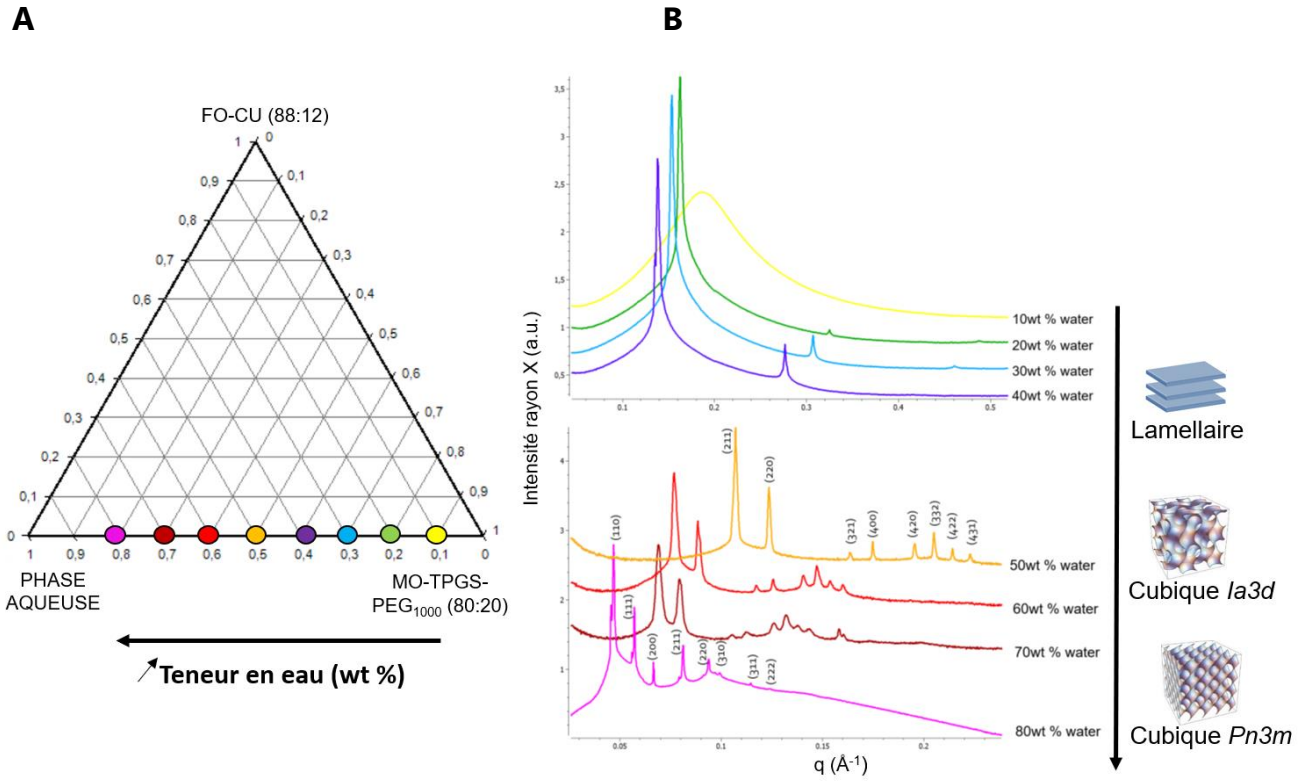

Figure 2. Composition et modèles représentatifs du synchrotron SAXS des mélanges MO/TPGS-PEG$_{1000}$/eau auto-assemblés montrant la dépendance du type de structure mésophase sur le niveau d'hydratation variable à 22°C. **(A)** Diagramme de phase utilisé pour la préparation des nanovecteurs liquides cristallins composés de monooléine (MO), d'amphiphile TPGS-PEG$_{1000}$, et de phase aqueuse contenant du D-(+)-glucose (5%). **(B)** Modèle SAXS révélant la formation d'une phase lamellaire (Lα) à des teneurs en eau de 20 à 40 %, et affichant des pics de Bragg qui indiquent la formation de phases cristallines liquides périodiques, à savoir une structure cubique gyroïde *Ia3d* à 50-70 % de teneur en eau et une structure cubique bicontinue en double diamant *Pn3m* à 80 % de teneur en eau.

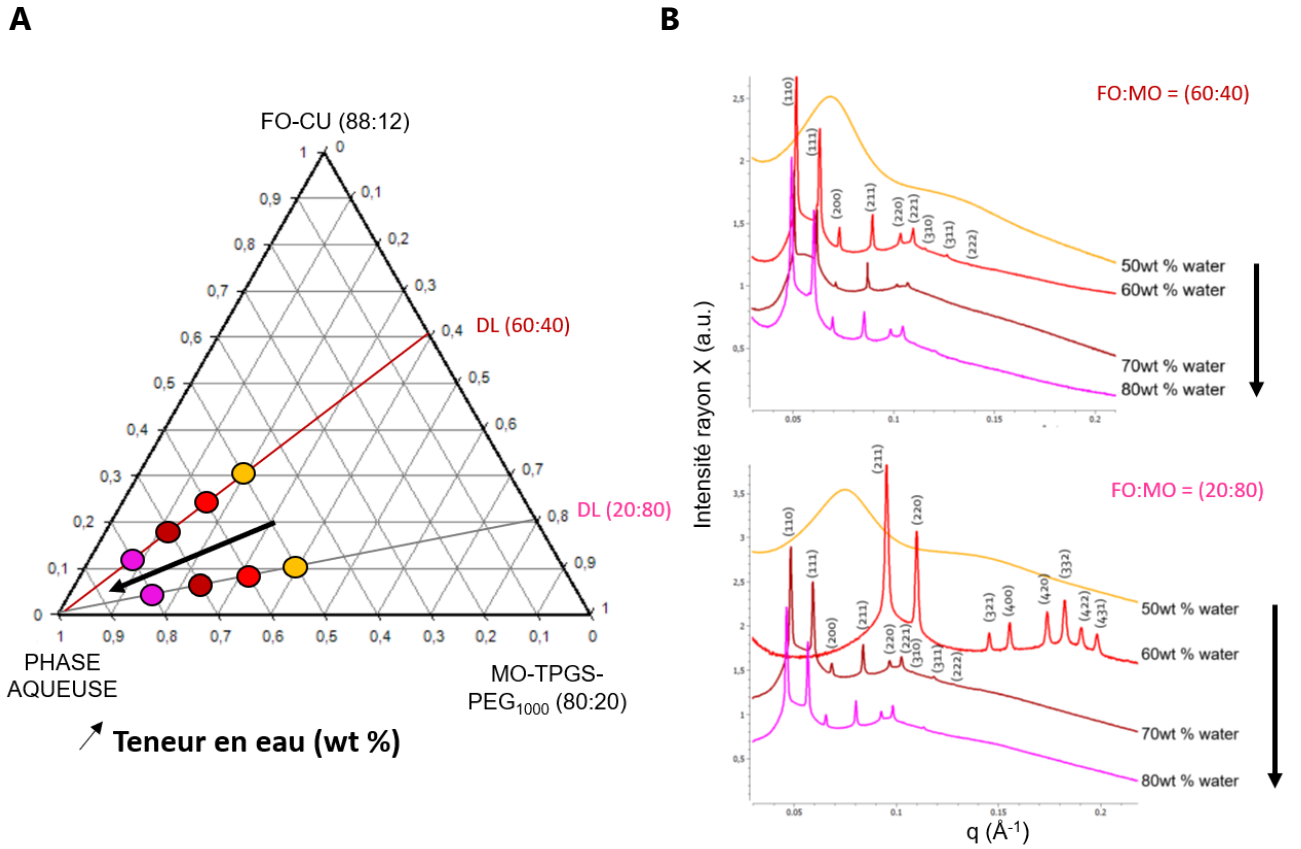

Figure 3. Composition et modèles représentatifs du synchrotron SAXS des mélanges MO/TPGS-PEG$_{1000}$/eau/FO/CU auto-assemblés à 22°C. **(A)** Diagramme de phase utilisé pour la préparation de nanovecteurs liquides cristallins composés de monooléine (MO), d'amphiphile TPGS-PEG$_{1000}$, d'huile de poisson (FO), de curcumine (CU) et de phase aqueuse contenant du D-(+)-glucose (5%). Les rapports pondéraux lipide/colipide [MO:TPGS-PEG$_{1000}$] et ingrédients bioactifs [FO:CU] sont maintenus constants à 80:20 et 88:12 respectivement, avec des rapports pondéraux entre huile de poisson et monooléine [FO:CU]/[MO:TPGS-PEG$_{1000}$] égaux à 20:80 et 60:40 (w/w%). **(B)** Modèle SAXS affichant des pics de Bragg qui indiquent la formation de structures cubiques gyroïdes bicontinues *Ia3d* ou en double diamant *Pn3m* à des teneurs en eau de 60 à 80 %.

Les nanoparticules cristallines liquides (LCNPs) ont été obtenus en dispersant les structures LC en présence d'un excès d'eau (98 wt%). La caractérisation morphologique des LCNPs par cryo-TEM montre la coexistence de vésicules précurseurs uni lamellaires, de

structures à double bicouche membranaire, ainsi que des nanoparticules de spongosomes ou cubosomes. La distribution de taille par DLS a confirmé la présence de deux populations principales : les nanoparticules de cubosomes ou spongosomes avec un diamètre hydrodynamique moyen d'environ 250 à 450 nm, et leurs précurseurs représentés par un diamètre hydrodynamique d'environ 100 nm.

Les évaluations *in vitro* de la toxicité et des effets des LCNPs ont été réalisées sur les cellules de neuroblastome humain SH-SY5Y. Elles ont été différenciées avec 10 µM d'acide rétinoïque pendant 5 jours pour obtenir un phénotype neuronal représenté par l élongation des neurites (Fig. 4). Après l'exposition des cellules différenciées à 500 nM de LCNPs pendant 24h, la viabilité cellulaire a été déterminée par le test MTT (bromure de 3-(4,5-dimethylthiazol-2-yl)-2,5-diphenyl tetrazolium). Les résultats montrent qu'il n'y a pas de diminution significative de la viabilité cellulaire avec les cellules prétraitées par les LCNPs par rapport aux cellules non traitées.

L'effet neuroprotecteur des LCNPs contre l'un des facteurs de risque des maladies neurodégénératives : le stress oxydatif a été effectué en provoquant le stress avec 900 µM de peroxyde d'hydrogène pendant 30 min. La détection des espèces réactives de l'oxygène intracellulaires (ERO ou ROS) a été analysée par cytométrie en flux en utilisant la sonde DCFH-DA (dichloro-dihydro-fluorescéine diacétate) non fluorescent (Fig. 4). Il se transforme dans la cellule en DCF qui est fluorescent en présence de ROS. Son intensité correspond à l'accumulation des ROS intracellulaires. Les résultats montrent une diminution significative de l'accumulation des ROS dans les cellules prétraitées avec les LCNPs par rapport au contrôle.

Pour confirmer l'activité antioxydante des LCNPs, une analyse de l'apoptose a été effectuées en incubant les culots de cellules dans un tampon de liaison avec les sondes : l'Annexin V-PE qui détecte les cellules apoptotiques et le SYTOX qui détecte les cellules nécrosées (Fig. 4). Les résultats montrent la diminution significative du pourcentage de cellules mortes et l'augmentation de la fraction de cellules vivantes dans les cellules prétraitées avec les LCNPs après exposition au H_2O_2.

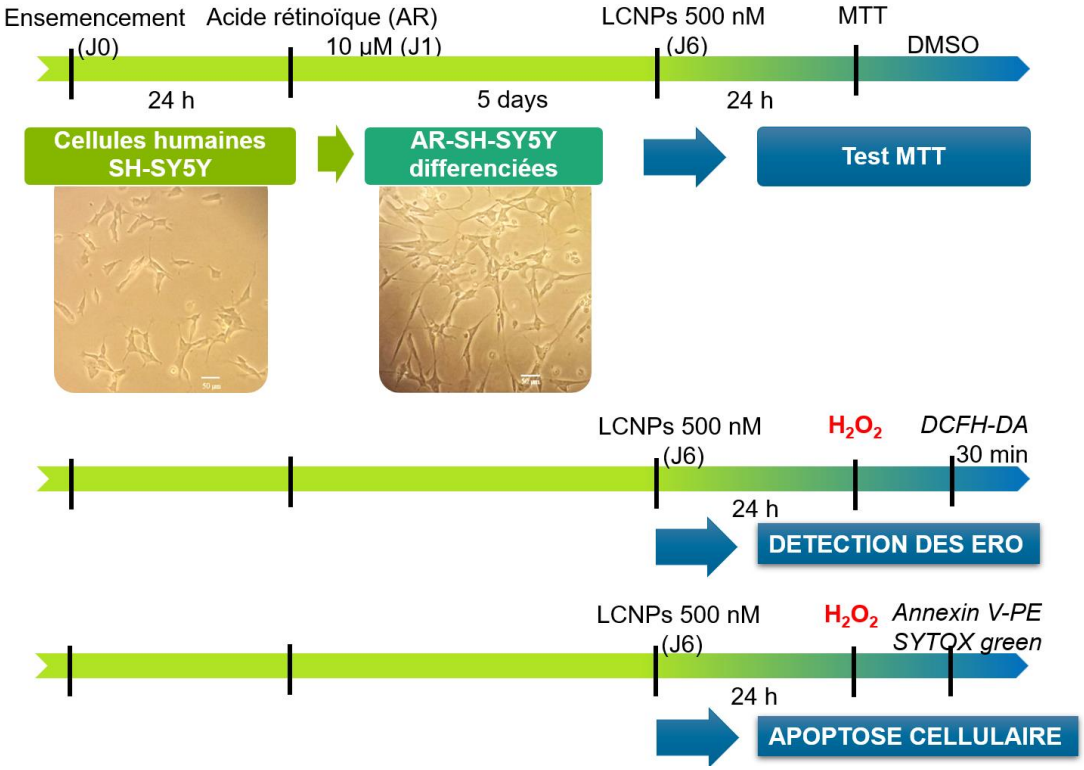

Figure 4. Présentation schématique du protocole de traitement des cellules de neuroblastome humain SH-SY5Y, différenciées pour l'évaluation de la toxicité des LCNPs et de leur effet sur le modèle de stress oxydatif induit par le H_2O_2.

3) LCNPs chargées en curcumine, huile de poisson et catalase

Avec la même préparation des mélanges MO/TPGS-PEG_{1000}/eau/FO/CU auto-assemblés, on ajoute la catalase dans la phase aqueuse. En comparant les LCNPs chargées et non chargées en catalase, le modèle SAXS montre que la structure cubique dans des LCNPs avec ou sans catalase reste intacte. Mais les paramètres de maille dérivés des pics de Bragg sont augmentés avec les LCNPs chargées en catalase. La distribution de taille des LCNPs chargées en catalase est également augmentée de 200 nm à 400 nm. On peut donc associer l'inclusion de la protéine dans les nanoparticules.

L'évaluations *in vitro* de la toxicité des LCNPs chargées en catalase a été vérifiée avec la même concentration à 500 nM et après 3 mois de stockage. Le test MTT a révélé aucune

diminution significative de la viabilité cellulaire par rapport aux cellules non traitées pat les LCNPs.

L' activité enzymatique de la catalase a ensuite été évaluée avec les LCNPs chargées en catalase à l'aide d'un kit de test enzymatique. Les lysats cellulaires ont été soumis à une centrifugation différentielle, pour obtenir des surnageants contenant la catalase cytosolique et avec lesquels les tests ont été réalisées. Cette méthode est basée sur la réaction de la catalase avec le méthanol en présence d'une concentration optimale de H_2O_2, produisant le formaldéhyde. Les mesures colorimétriques a été effectuées après 20 min de réaction. Les résultats montrent l'augmentation de l'activité enzymatique dans les cellules prétraitées avec des LCNPs chargées en catalase. Cette augmentation pourrait être liée à la quantité d'enzyme accrue dans le cytosol et à la préservation de l'enzyme catalase encapsulé par les LCNPs dans son état fonctionnel.

4) LCNPs chargées en curcumine, huile de poisson et BDNF

L'assemblage des nanostructures LCNPs et du facteur neurotrophique dérivé du cerveau (BDNF) a été obtenu à partir de la solution mère de 56 mM de nanoparticules et 500 µg/ml de BDNF humain. Un volume de 4 L de LCNPs et 1 L de solution mère de BDNF a été mélangé pour obtenir une nanoparticule chargée en BDNF qui sera stockée à 4°C.

Les images cryo-TEM des LCNPs ont montrées la topologie des nanoparticules lipidiques de type cubosome et spongosome chargées par des ingrédients bioactifs. L'organisation du domaine montre l'encapsulation de domaines internes riches en huile ou en constituant phytochimique.

L'effet neuroprotecteur des LCNPs chargées en BDNF contre l'un des facteurs de risque des maladies neurodégénératives : le stress du réticulum endoplasmique (ER) a été effectué en provoquant le stress par la tunicamycine. La tunicamycine est un inhibiteur de la N-glycosylation qui est une étape clé au début du repliement de la plupart des protéines ayant

lieu dans le ER. L'inhibition de ce processus provoque l'accumulation de protéines dépliées ou mal repliées dans la lumière du ER provoquant le stress.

La concentration de tunicamycine pour l'induction de stress a été déterminée par MTT (fig. 5). Les résultats montrent une diminution dose-dépendante de la viabilité cellulaire. Une diminution à 50 % de la viabilité cellulaire est atteinte à des concentrations comprises entre 0,5 et 1 µM. Des concentrations plus élevées (10 - 50 µM) ont provoqué une mort cellulaire massive dans les cultures. La concentration de 1 µM de tunicamycine pendant 5 h et une concentration de 2,5 µM de LCNPs chargées en BDNF ont été choisies pour les expériences ultérieures.

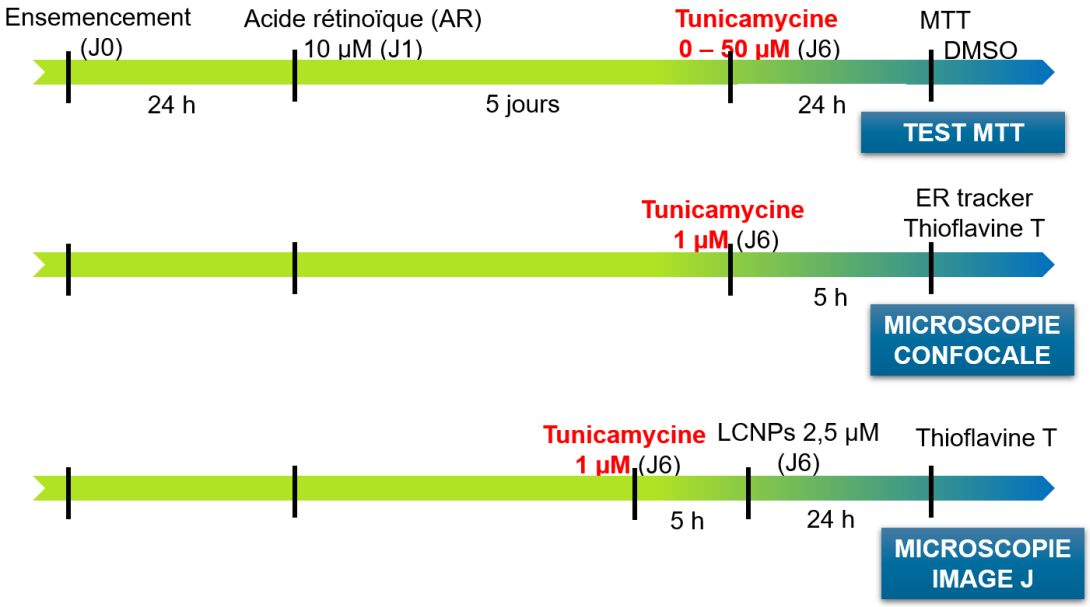

Figure 5. Présentation schématique du protocole de traitement des cellules de neuroblastome humain SH-SY5Y, différenciées pour l'évaluation de l'effet des LCNPs sur le modèle de stress du réticulum endoplasmique induit par la tunicamycine.

Afin de valider notre modèle de stress du ER induit par la tunicamycine, le colorant Thioflavine T (Tht) (5 M) a été ajoutée aux cultures. La Tht interagit directement avec les protéines mal repliées dans le ER. C'est un outil pour détecter les agrégats de protéines en tant que mesure de niveaux de stress du ER dans les cellules vivantes.

La localisation subcellulaire de la coloration par Tht dans les cellules traitées avec 1 M de tunicamycine pendant 5 h a été déterminée en microscopie confocale (fig. 5). La fluorescence du Tht a été visualisée avec celle du ER -tracker dans la région périnucléaire des cellules traitées à la tunicamycine. Les images au microscope et leur traitement par ImageJ (fig. 5) montrent un faible niveau de fluorescence du Tht en l'absence de tunicamycine, une fluorescence renforcée dans les cellules exposées à la tunicamycine et enfin une diminution de celle-ci dans les cellules traitées par les LCNPs chargés en curcumine, huile de poisson et BDNF.

5) Conclusion générale et perspectives

Les troubles neurodégénératifs se caractérisent par des lésions progressives des cellules neuronales dues à de nombreux facteurs de risques : stress oxydatif, déficit en facteurs neurotrophiques, stress du réticulum endoplasmique. Nous avons conçu une nouvelle approche de thérapie combinée par des composés actifs naturels et des biomolécules délivrées par des nanoparticules à base de lipides. Notre étude a apporté de nombreuses découvertes utiles pour de futures recherches, de futures applications thérapeutiques, alimentaires ou environnementales.

Dans un premier temps, nous avons caractérisé en profondeur les propriétés structurales et physico-chimiques des assemblages monooléine-TPGS-PEG_{1000}/huile de poisson/curcumine :

- ✓ Nous avons étudié le taux d'hydratation et le rapport pondéral FO/MO nécessaires à la préparation de nanoparticules stables MO/TPGS-PEG1000/FO/CU par auto-assemblage,
- ✓ Nous avons établi le diagramme de phase des systèmes auto-assemblés amphiphiles à 22°C,
- ✓ Nous avons mis en évidence la formation de nanoparticules de cubosomes et de spongosomes,

- ✓ Nous avons montré l'efficacité d'encapsulation élevée de la curcumine par les nanoparticules LCNPs,
- ✓ Nous avons dévoilé la capacité du type de nano-objet à cristaux liquides à charger, protéger et délivrer des biomolécules comme la catalase, le facteur neurotrophique dérivé du cerveau (BDNF) dans la cellule.

Ensuite, nous avons évalué l'effet *in vitro* des nanoparticules de cubosomes et de spongosomes chargés dans différents modèles cellulaires de neurodégénérescence :

- ✓ Nous avons vérifié la non-toxicité des nanoparticules dans les cellules SH-SY5Y différenciées par l'acide rétinoïque,
- ✓ Nous avons établi des modèles cellulaires de stress induits par la privation de sérum, de stress oxydatif induit par H_2O_2, de stress du réticulum endoplasmique induit par la tunicamycine,
- ✓ Nous avons déterminé la protection contre la mort cellulaire, la promotion de la survie et de la réparation cellulaires par les nanoparticules cristallines liquides chargés par un ou plusieurs molécules actives.

Les systèmes lipidiques auto-assemblés nanodispersés sont très intéressants pour l'administration de molécules et de protéines neuroprotectrices insolubles dans l'eau afin de traiter les dommages neuronaux liés aux troubles neurodégénératifs. Les nanoparticules cristallines liquides [MO-FO-CU-BDNF] ont montré un potentiel de neuroprotection et présentent une application prometteuse dans la réparation cellulaire ou la neurogenèse.
D'autres études sont nécessaires pour déterminer un éventuel effet synergique de la curcumine et du BDNF dans la régénération cellulaire lors de la double administration par les LCNPs. Une compréhension du mécanisme d'action *in vitro* pourrait se faire en déterminant les voies de signalisation impliquées.

Le développement de nanoformulations prenant en compte différentes voies d'administrations sont des perspectives pour de futures applications *in vivo.* Une étude d'une

administration intranasale peut être réalisée en ce qui concerne le confort des futurs patients et éviter la barrière hémato-encéphalique. L'objectif à long terme est d'atteindre la neurogenèse et la neurorégénération grâce à l'action synergique de nanomédicaments innovants.

General introduction

Neurodegenerative disorders like Alzheimer's disease, Parkinson disease are multifactorial diseases with complex and intertwined etiologies. Drug delivery by nanoparticles, introduced in the 1960's has brought hope for inducing multiple mechanisms of recovery in such severe diseases, through better targeted approach. Lipid-based or amphiphilic nanoparticles such as liposomes, liquid crystalline nanoparticles, are particularly attractive for they have the capacity to be loaded by many active pharmaceutical ingredients, both hydrophilic and lipophilic. The lipid used for their formulation are usually naturally occurring molecules and enhance drugs bioavailability. Also, the self-assembly features of lipids allow the production of formulations that may retain important similarities and affinity towards biological membranes. Then, these nanocarriers are biocompatible and biodegradable with low toxicity for *in vivo* applications.

The lipid-based lyotropic liquid crystals (LLC) or liquid crystalline nanoparticles (LCNPs) received wide interests in the recent years because they offer higher encapsulation efficacy compared to liposome. We are interested in LCNPs as they can be easily synthetized by self-assembly from the exposure of amphiphilic lipids to water and form a lamellar, a bicontinuous cubic, sponge or a hexagonal phase. They are highly ordered; they have thermodynamically stable internal nanostructure and allow sustained or controlled drug delivery. Also, we are inspired by their capacity to mimic the biological membranes. For example, in amoeba *Chaos carolinense* mitochondria, there is a cubic LC membrane structure that depends on their diet condition. When they are starved with their natural food, the mitochondrial cubic LC structure could escape autophagy and maintain their normal function of producing ATP. So, LCNPs could transport and deliver drugs in case of stress such as oxidative, endoplasmic reticulum stress or mitochondrial dysfunction which are all risk factors of neurodegenerative diseases.

In this project, we aim to obtain bicontinuous cubic structures (Fig. 1), advantageous for their high encapsulation capacity of both lipophilic and hydrophilic molecules, Dispersions of bicontinuous cubic phase so-called cubosome have much higher surface area per volume than micellar and lamellar structures so they improve the bioavailability and the protection of unstable biomolecules.

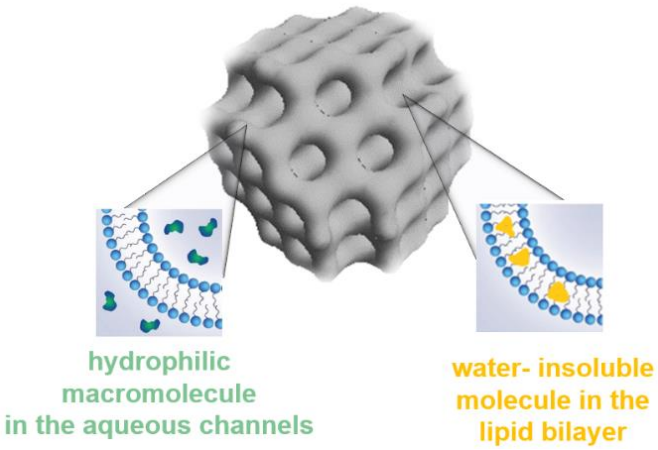

Figure 1. Schematic presentation of the supramolecular organizations of cubosome particles of the double diamond *Pn3m* cubic space group, enabling the encapsulation and protection of unstable molecules of therapeutic significance.

The water insoluble molecule we want to encapsulate is curcumin which is a safe natural compound with many potentials in neuroprotection. The hydrophilic molecule one is the brain-derived nerve growth factor (BDNF), a neurotrophin that promotes neuronal survival and is the prime therapeutic candidate for a host of neurological disorders.

In the first chapter, we will present the risk factors of neurodegenerative disorders, the state of art of the potential effect of our chosen molecules and their delivery by lipid-based nanoparticles in these diseases.

Then, the first experimental work will describe the preparation and formulation of curcumin - loaded LLC nanostructures. The effect of curcumin loading was studied on the structural features of LCNPs from a binary lipid mixture consisting of monoolein and fish oil. The

physico-chemical characterization of the multidrug - loaded LCNPs were checked by different analytical techniques, such as small-angle X-ray, dynamic light scattering. The *in vitro* effects were evaluated in differentiated human SH-SY5Y neuronal cells.

The second experimental work will describe the preparation and formulation of the curcumin, fish oil and catalase - loaded LLC nanostructures. In these structural and physico-chemical experiments, catalase is used as the hydrophilic macromolecule because BDNF is expensive.

The last chapter will present the curcumin, fish oil and BDNF-loaded LCNPs formulation and their interaction with human SH-SY5Y neuronal cells. Disease models of endoplasmic reticulum stress induced by the neurotoxin tunicamycin was studied to evaluate the toxicity and effects of the nanoparticles. Their efficacy was determined by different techniques, such as confocal laser scanning microscopy, and different assay kits.

Overall, this work represents a major step toward the potential use of multidrug delivery by cubic LLC nanoparticles for neurodegenerative disorders by establishing a stable, nontoxic, and reproducible formulation.

Chapter 1: Bibliographic study

Amphiphilic nanocarrier systems for curcumin delivery in neurodegenerative disorders

Miora Rakotoarisoa and Angelina Angelova

Institut Galien Paris-Sud CNRS UMR 8612,

LabEx LERMIT, Univ Paris-Sud, Univ Paris-Saclay, France

Accepted in Medicines (Review)

Accepted in Nanomedicine (Volume 4, Chapter33)

Amphiphilic nanocarrier systems for curcumin delivery in neurodegenerative disorders

Abstract:

Neurodegenerative diseases have become a major challenge for public health because of their incurable status. Soft nanotechnology provides potential for slowing down the progression of neurodegenerative disorders by using innovative formulations of neuroprotective antioxidants like curcumin, resveratrol, vitamin E, rosmarinic acid, 7,8-dihydroxyflavone, coenzyme Q10, and fish oil. Curcumin is a natural, liposoluble compound, which is of considerable interest for nanomedicine development in combination therapies. The neuroprotective effects of combination treatments can involve restorative mechanisms against oxidative stress, mitochondrial dysfunction, inflammation, and protein aggregation. Despite the anti-amyloid and anti-tau potential of curcumin and its neurogenesis-stimulating properties, the utilization of this antioxidant as a drug in neuroregenerative therapies has huge limitations due to its poor water solubility, physico-chemical instability, and low oral bioavailability. We highlight the developments of soft lipid- and polymer-based delivery carriers of curcumin, which help improve the drug solubility and stability. We specifically focus on amphiphilic liquid crystalline nanocarriers (cubosome, hexosome, spongosome, and liposome particles) for the encapsulation of curcumin with the purpose of halting the progressive neuronal loss in Alzheimer's, Parkinson's, and Huntington's diseases and amyotrophic lateral sclerosis (ALS).

1) Introduction

Neurodegenerative diseases (Alzheimer's disease (AD), Parkinson's disease (PD), Huntington disease (HD), and amyotrophic lateral sclerosis (ALS)) are disabling chronic disorders characterized by the progressive loss of neurons in different areas of the central nervous system. Neuronal cell death leads to cognitive, behavioral, sensory, and motor dysfunctions.[1–13] Currently, age-related neuronal diseases have higher incidences because of increasing life expectancies. Neurodegenerative disorders are caused by multiple factors, such as the accumulation of misfolded proteins, the depletion of endogenous antioxidant enzyme activity, mitochondrial dysfunction, and the deficiency of neurotrophin brain-derived neurotrophic factor (BDNF), neuro-inflammation, as well as various genetic mutations.[14–30]

In recent years, several studies have shown that curcumin is a safe natural compound which may prevent the deleterious effects of risk factors causing brain damage as well as slowing down the progressive neuronal loss via different pathways.[26–50] However, clinical studies performed with AD patients with various degrees of progression have reported poor results on the AD symptoms following curcumin treatment.[51–54] This did not allow firm conclusions about the therapeutic or neuroprotective potential of curcumin to be drawn. The obstacles for curcumin utilization as a drug originate from its limited water solubility, poor physicochemical stability, high-grade metabolism, and low plasma concentrations.[36,53–55] The development of nanoparticulate delivery systems for curcumin has attracted scientific interest in order to improve its bioavailability and stability as a drug compound.[56–65] Curcumin administration to neurodegenerative disease models by nanoparticles has been realized using liposomes, solid lipid nanoparticles, and polymeric particles. Delivery by other carriers such as amphiphilic proteins, e.g., casein, is also possible, but has not been examined as a means of transporting curcumin across the BBB towards neuro-regeneration.

In this review, we briefly summarize the *in vitro* and the *in vivo* evaluations of curcumin, which are linked to multiple risk factors and the multi-target mechanisms of neurodegenerative diseases and discuss the reported clinical investigations of varying efficacy in humans. Then, we highlight the variety of amphiphilic curcumin-loaded nanocarriers

including liposomes, liquid crystalline nanoparticles (cubosomes, hexosomes, and spongosomes), solid lipid nanoparticles, micelles, and polymeric nanoparticles as potential nanomedicine formulations in regeneration therapies of the major neurological disorders.

2) Risk factors for neurodegenerative disorders

Alzheimer's disease (AD) is the most common cause of dementia. It currently affects about 10% of the world's population over 60–65 years of age, and about 50% over 85 years of age. More than 30 million people may expect to be affected by AD during the next 20 years due to the increasing lifespan of the world population.[1,2] Major pathological features of AD include the accumulation of extracellular amyloid plaques and fibrils, intracellular neurofibrillary tangles, and disruption of the cholinergic transmission, including reduced acetylcholine levels in the basal forebrain (Table 1). The most common symptom is the short-term memory loss, i.e., difficulty in remembering recent events.[2–5] Other symptoms include disorientation, mood, language, and behavioral issues, and loss of motivation, depending on the progression of the disease. The treatments of AD have employed acetylcholinesterase inhibitors (tacrine, rivastigmine, galantamine, and donepezil) to overcome the decrease of the ACh levels as a result of the death of cholinergic neurons. The NMDA receptor antagonist (memantine) acts by inhibiting the overstimulation by glutamate, which can cause cell death. Atypical antipsychotics have modest efficacy in reducing the aggression and psychosis of AD patients. These medications provide little benefit, and provoke various adverse effects.[6,7]

The second most common disorder, Parkinson's disease (PD), affects more than 1% of the population over 60 years of age and 5% over 85. PD is characterized by progressive impairments in locomotive ability such as tremor, rigidity, and bradykinesia. These symptoms are attributed to the loss of dopaminergic neurons in the substantia nigra and the formation of Lewy bodies in the brain.[8,9] Treatments are symptomatic and aim at boosting the depleted levels of dopamine (Table 1). The most used drug is levodopa. Dopamine agonists are used when the treatment by levodopa becomes less efficient. The inhibitors of MAO-B and COMT

(safinamide, selegiline, rasagiline, and tolcapone) are used to inhibit the activity of the enzymes which degrade dopamine. These medications become less effective as the neurons are continuously lost during disease progression. At the same time, they produce complications marked by the involuntary movements of the patients.[8,9]

Huntington disease (HD) is a rare disease which affects about 1/10,000 people (usually between 30 to 50 years of age) in the United States and 1/18,000 people in Europe. It is a poly-glutamine (PolyQ) autosomal genetic disorder characterized by impairments of cognitive, psychiatric, and motor functions.[10] The hallmark of the HD pathology is the abnormal accumulation of misfolded mutated huntingtin protein (mHTT) as intracellular aggregates. They cause selective neuronal loss, primarily in the cortex and in the medium spiny neurons of striatum. Symptoms develop from a general lack of coordination to apparent uncoordinated, jerky body movements.[11] The physical abilities of the patients gradually worsen until coordinated movement becomes difficult. There is no effective cure available to HD (Table 1). The only approved medication, tetrabenazine, and other tested drugs (neuroleptics and antipsychotics) help to reduce chorea and psychiatric symptoms.

Amyotrophic lateral sclerosis (ALS) is a severe debilitating disease caused by motors neurons degeneration in the brain and the spinal cord. It is generally characterized by progressive paralysis starting at the limbs and ultimately leading to death caused by respiratory failure within 3 to 5 years after the onset of the symptoms. There is no cure for ALS (Table 1). The approved medication, riluzole, may extend life by just a few months.[12,13]

The pathological characteristics, genetic factors, clinical symptoms, and actual medications of these diseases are summarized in Table 1. It should be emphasized that the existing therapeutic approaches do not exert disease-modifying effects on the neurodegeneration. The associated economic and societal challenges lead to a growing public health burden.

Table 1. Pathological characteristics, genetic factors, and clinical symptoms of Alzheimer's disease (AD), Parkinson's disease (PD), Huntington's disease (HD), and amyotrophic lateral sclerosis (ALS).[1–30]

Diseases	Characteristics	Genetics factors	Symptoms	Actual treatments
AD	Senile plaques from extracellular amyloid-Aβ accumulation, Intracellular neurofibrillary tangles, Tau protein aggregation, Irreversible neuronal loss, Brain atrophy	Inherited form (70% of patients): mutations of APP, PSEN1 or PSEN2. Sporadic form (30%): presence of ApoE4 allele in the ApoE gene	Progressive memory loss, Decision judgment loss, Autonomy loss	Anticholinergics (tacrine, rivastigmine, galantamine and donepezil), Memantine, Antipsychotics, NSAIDs
PD	α-Synucleinopathy, Presence of Lewy bodies, Degeneration of dopaminergic neurons in the substance nigra of the brain, Dopamine deficiency	Gene mutations: α-synuclein SNCA, Parkin PRKN, PARK7, PINK1, LRRK2, GBA, DJ-1, VPS35, EIF4G1, DNAJC13 and CHCHD2	Hypokinesia, Bradykinesia, Rigidity, Postural instability, Neuropsychiatric disturbances	Levodopa, Dopamine agonists, MAO-B inhibitors, COMT inhibitors, Anticholinergics
HD	Accumulation of mutant Huntingtin protein in the brain	Expansion of CAG trinucleotide in Huntingtin gene (HTT)	Chorea, Cognitive and neuropsychiatric disorders	Tetrabenazine, Neuroleptics, Antipsychotics
ALS	Progressive degeneration of motor neurons	Sporadic form: 90% of patients. Inherited form: 10% Mutations of SOD1, TARDBP, FUS, UBQLN2, OPTN, and C9ORF72 genes	Spasms, Muscle atrophy, Squelettal muscle paralysis, Cognitive or behavioral dysfunction	Riluzole

Although the etiology and the pathological mechanism of the neurodegenerative diseases are not completely understood, it has been established that the progressive loss of neurons results from the combination of multiple factors (Fig.1).

First, genetic factors are involved in the appearance of misfolded amyloid-Aβ protein and other misfolded mutant forms like hyperphosphorylated Tau (p-Tau) and Huntingtin proteins.[3–5,10,14] All these mutated proteins aggregate and form deposits. The resulting aggregates can be toxic and can affect the intracellular organelles such as mitochondria.[14,21,25,27] The disruption of the mitochondrial membrane causes neuronal cell death.[25,27]

Second, neurotrophic factors deficiency has been reported in the severe neurodegenerative disorders.[33] Neurotrophins regulate the neuronal survival, differentiation, growth, and regeneration, as well as the synaptic plasticity. Studies have shown that the levels of brain derived neurotrophic factor (BDNF) and its tropomyosin kinase B (TrkB) receptor are decreased in the hippocampus and the cerebral cortex at the beginning of the Alzheimer's disease.[11] In addition, the administration of BDNF mimetics into transgenic mouse models of AD has enhanced learning and memory capacities.[31]

Third, oxidative stress is the most common feature of neurodegenerative diseases.[15–20] Reactive Oxygen Species (ROS) such as superoxide anions, hydroxyl radicals, and hydrogen peroxide (H_2O_2) are produced by the mitochondrial transport chain, the endoplasmic reticulum, the Krebs cycle, and the plasma membrane involving the superoxide-generating NADPH oxidase (NOX) macromolecular complex.[17] Oxidative stress occurs under environmental factors and when the generation of ROS exceeds the natural antioxidant defenses of the cell (promoted by superoxide dismutase, catalase, glutathione peroxidase, carotenoids, and vitamins E or C).[15–20] ROS accumulation attacks proteins, nucleic acids, and membrane lipids, and thus, causes impairments of the neuronal cell functions and integrity.[18–20] Mitochondrial lesions are also mediated by ROS. This leads to the alteration of the neuronal cell bioenergetics, the disruption of the calcium (Ca^{2+}) homeostasis, or the activation of the mitochondrial permeability transition pore (mPTP). Thus, a vicious cycle is formed (Fig. 1), which amplifies the cellular dysfunction and triggers neurodegeneration.[17–26]

Fourth, neuro-inflammation is a crucial factor that favors neurodegenerative disease development. Several inflammatory markers (such as chemokines, cytokines, or proteins in the acute phase) are upregulated and cause inflammation. In fact, elevated levels of the inflammatory markers have been found during the progression of the neurodegenerative diseases.[27,28]

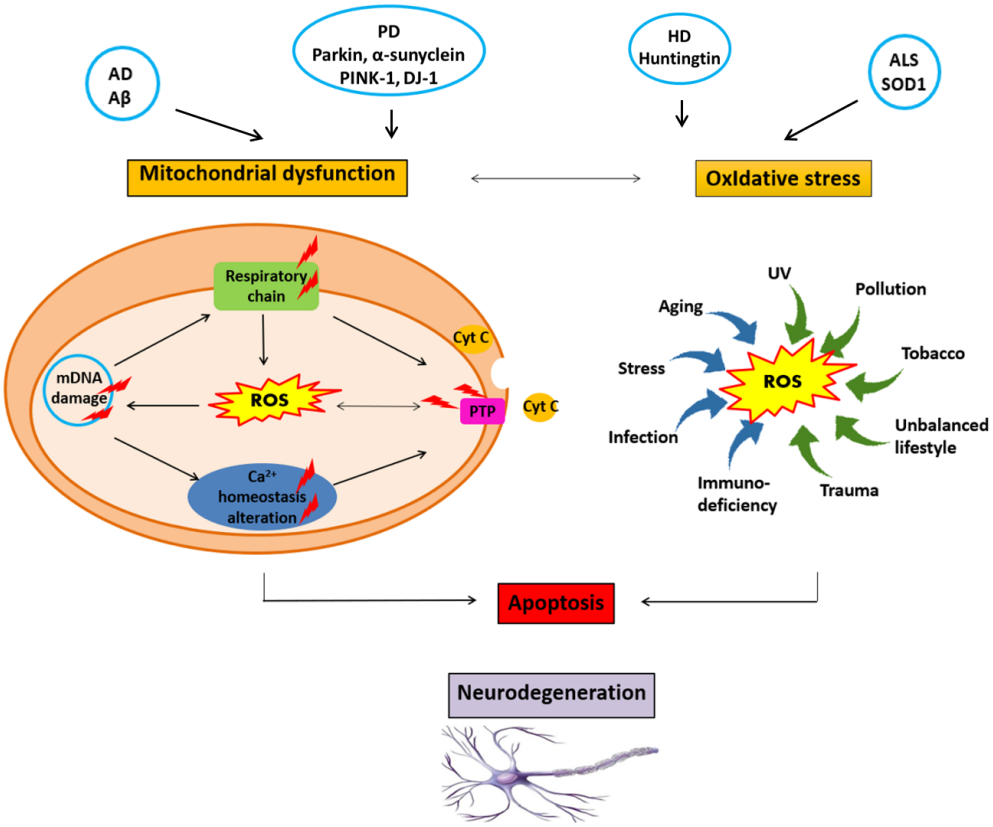

Figure 1. Neurodegeneration is triggered and boosted by a vicious circle involving neurotoxic protein accumulation, oxidative stress, mitochondrial damage, DNA damage, and impairment of the calcium (Ca^{2+}) homeostasis, neurotrophin deficiency, neuroinflammation, genetic, and environmental factors.

3) Curcumin potential for neuroprotection against neurodegenerative diseases

Curcumin is a hydrophobic polyphenolic substance (Fig. 2) produced in the root of the plant *Curcuma Longa L.* This antioxidant compound is extensively marketed worldwide as a nutraceutical in various preparations because it has a very safe nutraceutical profile with low side effects. Curcumin has been reported to be well tolerated at doses up to 8 g per day over short periods in humans.[32] Research on the pharmacological activities of curcumin has attracted strong attention in relation to its multiple actions of therapeutic interest, e.g., the anti-inflammatory, antioxidant, antiviral, antibacterial, antifungal, and antitumor activities [36]. These activities appear to be dose-dependent.[33]

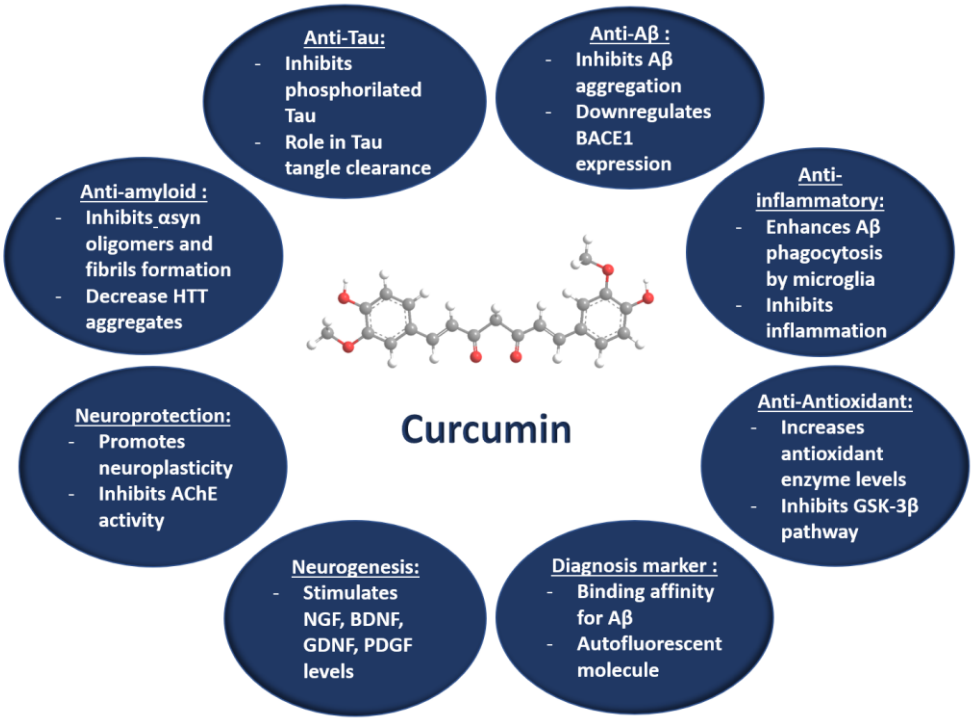

Figure 2. Summary of the curcumin activities and suggested mechanisms of action, which can be exploited for treatment of neurodegenerative diseases.

a. In vitro and in vivo studies of curcumin properties in neurodegenerative disease models

The neuroprotective potential of curcumin (Fig. 2) and its antioxidant, anti-inflammatory, and amyloid Aβ binding properties have been highlighted in *in vitro* and *in vivo* investigations of different neurodegenerative disease models [33–42]. Curcumin has been found to increase the levels of glutathione (GSH) and malondialdehyde (MDA), as well as the antioxidant enzyme [superoxide dismutase (SOD), glutathione peroxidase (GPx), glutathione reductase (GR), and catalase (CAT)] activities in the rat brain, thus preventing the stress-induced oxidative damage of brain.[37,39] The anti-inflammatory properties of curcumin have been characterized by the inhibition of the inflammatory chemokines, by increased levels of the anti-inflammatory cytokines, and by enhanced expression levels of induced nitric oxide synthase (iNOS) and the transcription factor NF-Kb.[39] Curcumin has been shown to prevent

the fibrillation of α-synuclein at the earliest stage of the aggregation process, as well as the fibrillation of the globular protein hen egg-white lysozyme (HEWL).[40] Both proteins are known to form amyloid-like fibrils. These results have suggested that curcumin might be a potential therapeutic agent for preventing protein aggregation in Alzheimer's, and Parkinson's diseases [40]. Recent *in vitro* and *in vivo* investigations of curcumin's activities in neurodegenerative disease models[41–50] are summarized in Table 2.

Table 2 Recently reported curcumin (CU) activities in *in vitro* and *in vivo* models of neurodegenerative diseases.[41–50]

Diseases	Models/administration routes	Mechanisms	Outcomes
AD	*In vitro*: human neuroblastoma SH-SY5Y and IMR-32 cells	Enhancement of the expression of DNA repair enzymes (APE1, pol β, and PARP1[1]) to halt the oxidative DNA base damage via base excision repair (BER) pathway; Activation of the antioxidant response element (ARE) via Nrf2 upregulation	Revitalization of the neuronal cells from Aβ[2]-induced oxidative stress [41]
AD	*In vitro*: mouse hippocampal clone neuronal cell line HT-22 cells treated with Aβ 1-42, *In vivo*: mice with APP/PS1 transgenes	Decrease of the autophagosomes number, Increase of the lysosomal Ca^{2+} regulation of PI(3,5)P2 and Transient Receptor Potential Mucolipin-1 Expression (TRPME)	Neuronal cell growth, Protective role of CU on memory and cognition impairments [42]
AD	*In vivo*: rat, oral supplementation	Increase of GPx,[3] CAT,[4] GSH[5] activities, and Ach[6] levels	Improving memory and cognitive abilities [43]
PD	*In vivo*: Drosophila model of PD with dUCH[7] knockdown	Effects on dUCH[7] knockdown, a homolog of human UCH-L1	Decrease of ROS levels, Improved locomotive abilities, Reduction of dopaminergic neurons degeneration [44]
PD	*In vivo*: male Sprague-Dawley rats injured by 6-OHDA[8] in the left striatum	Activation of the Wnt/β-catenin signaling pathway, Higher Wnt3a and β-catenin mRNA and protein expressions, c-myc and cyclin D1 mRNA expression, enhanced SOD[9] and GPx[3] contents, decreased MDA[10] content and elevated mitochondrial membrane potential	Protective effect of CU against oxidative stress-induced injury, Enhanced viability, survival, and adhesion, attenuated apoptosis of deutocerebrum primary cells [45]

PD	*In vivo*: MPTP[11] mice, intranasal mode of administration of CU (mucoadhesive system)	Increase of dopamine concentration in brain, which improves muscular coordination and gross behavioral activities of the test animal, Significant reduction of the MPTP[11]-mediated dopamine depletion	Improvement in motor performance, Symptomatic neuroprotection against MPTP-induced neurodegeneration in the striatum [46]
HD	*In vivo*: CAG140 mice, a knock-in (KI) mouse model of HD	Decreased huntingtin aggregates, increased striatal DARPP-32 and D1 receptor mRNAs	Partial improvement of transcriptional deficits, partial behavioral improvement [47]
Diazepam - induced cognitive impairment	*In vivo*: diazepam-treated rats, oral supplementation	Downregulation of the extracellular signal-regulated kinase (ERK 1/2)/nuclear transcription factor-(NF-)κB/pNF-κB pathway in the hippocampus and the iNOS[12] expression in the hippocampus and frontal cortex	Improvement of the cognitive performance, Decrease of blood and brain oxidative stress levels [48]
Alcohol - induced neurodegeneration	*In vivo*: rat, oral supplementation	Decrease of the reduced form of GSH,[5] SOD,[9] GPx,[3] GR,[13] change in the Bcl-2 levels, Activation of the CREB-BDNF signaling pathway	Neuroprotection against alcohol-induced oxidative stress, apoptosis and inflammation [49]
Nicotine - induced neurodegeneration	*In vivo*: rat, oral supplementation	Activation of the CREB-BDNF signaling pathway	Neuroprotection against nicotine-induced inflammation, apoptosis and oxidative stress, Reduction of the motor activity disturbances [50]

[1]Poly [ADP-ribose] polymerase 1; [2] Aβ-amyloid; [3] Glutathione Peroxidase; [4] Catalase; [5] Glutathione; [6] Acetylcholine; [7] Ubiquitin carboxy-terminal hydrolase; [8] 6-Hydroxydopamine; [9] Superoxide dismutase; [10] Malondialdehyde; [11] 1-Methyl-4-phenyl-1,2,3,6-tetrahydropyridine; [12] Induced nitric oxide synthase; [13] Glutathione reductase.

b. Clinical trials and curcumin limits

A serious obstacle to the pharmaceutical application of curcumin has arisen from its limited water-solubility and low bioavailability. In addition, this compound is chemically instable, which may cause a loss of biological activities. The failure of free curcumin in clinical trials is likely due to its limited bioavailability. For instance, curcumin has been delivered in doses between 1 and 4 g/per day as capsules or as powder mixed with food in trials for treatment of Alzheimer's disease patients. The performed 6-month treatment study found no differences in the Aβ-amyloid levels between the treatment groups or in the Mini Mental State Examination (MMSE) scores.[51] Similarly, oral curcumin in a 24-week, randomized, double

blind, and placebo-controlled study for AD treatment has shown no detectable differences in the measured biomarkers from the different treatment groups.[52] A clinical study with three single cases of patients receiving curcumin (100 mg/day) reported that only one patient increased his MMSE score from 12/30 to 17/30 after 12 weeks of treatment (improved calculation, concentration, transcription of the figure, and spontaneous writing). Two of the patients were on donepezil treatment before starting the curcumin trial.[53] Based on all performed trials with AD patients, it was, however, difficult to conclude if curcumin has positive effects on the AD symptoms.[54]

In fact, the major fraction (35–89%) of orally administered curcumin can be lost due to its low bioavailability. The intestinal mucosa and mucus form a physical barrier to curcumin adsorption. The drug cannot reach the circulation in a bioactive form as it undergoes reduction and metabolism/conjugation in the liver. Reductases enzymatically reduce curcumin to dihydrocurcumin, tetrahydrocurcumin, and hexahydrocurcumin. Furthermore, curcumin may be conjugated to sulfates and glucuronides.[55–57] Thus, most of the circulating curcumin is in a conjugated form.

The necessity of the development of a delivery system for the protection of curcumin from rapid metabolism and for the improvement of its bioavailability has become evident.[58] A randomized, double-blind, placebo-controlled clinical trial examined the acute administration (effects 1 h and 3 h after a single dose application), chronic (4 weeks) administration, and acute-on-chronic (1 h or 3 h after a single dose followed by a chronic treatment) effects of solid-lipid-nanoparticle (SLNP) loaded by curcumin. The results of the SLNP formulation of curcumin (400 mg in capsules Longvida®) on cognitive function, mood, and blood biomarkers were obtained with 60 healthy adults (aged 60–85). SLNP-loaded curcumin significantly improved the performance in sustained attention and working memory tasks one hour after its administration (as compared to placebo). Working memory and mood (general fatigue and change in the calmness state, contentedness, and fatigue induced by psychological stress) were essentially improved following chronic treatment. A significant acute-on-chronic treatment effect on alertness and contentedness was also observed.[59]

4) Nanocarrier-mediated curcumin delivery

Nanotechnology for nanomedicine development employs functional materials with appropriate nanoscale organization that can interact with biological systems and induce desired physiological responses while minimizing undesirable side effects.[60] Nanotechnology-based delivery systems can influence drug capacity to cross the biological barriers (e.g., the BBB) and reach the targeted brain regions.[58–61] Therefore, nanocarriers are promising for the development of personalized medicines for the treatment of neurological disorders.[62–67]

Lipid-based nanoparticles, including solid lipid nanoparticles (SLNPs), nanostructured lipid carriers (NLC), liposomes and liquid crystalline nanocarriers (LCN), as well as polymer-based nanoparticles (Fig. 3), have been developed to overcome the poor solubility, stability, and bioavailability of curcumin, and to promote its utilization as a drug in disease treatments.[68–124] Lipid-based nanoparticles have the advantage of being the least toxic carriers for *in vivo* applications. The lipids used to prepare biocompatible and biodegradable nanoparticles are usually naturally occurring molecules with low acute and chronic toxicity. In the case of polymeric nanoparticles, the *in vivo* degradation of the polymer matrices might cause toxic effects.[94] The biocompatibility and the physicochemical diversity of lipids and their capacity to enhance the oral bioavailability of drugs have made this kind of nanocarriers very attractive systems for drug delivery. As a matter of fact, lipid-based formulations may positively influence drug absorption in several ways, e.g., by influencing the solubilization properties, preventing the drug precipitation upon intestinal dilution, increasing the membrane permeability, inhibiting the efflux transporters, reducing the CYP enzymes, or enhancing the lymphatic transport.[94,122]

Among the lipid-based nanoparticles, SLNPs have been intensively developed because they combine the advantages of different carrier systems like liposomes and polymeric particles. Similar to liposomes, SLNPs are composed of physiologically biocompatible excipients (lipids and fatty acids). In the same way to polymeric NPs, their solid matrix core

can efficiently protect the loaded active pharmaceutical ingredient against chemical degradation under the harsh conditions of biological milieux. Therefore, SLNPs provide controlled release profiles of the encapsulated drugs.[95]

In addition to the above advantages, liposomes can encapsulate and transport both lipophilic and hydrophilic drugs. They have a high degree of similarity to cell membranes in terms of lipid composition and organization, which facilitates the bioavailability of the pharmaceutical compounds.[102] Liquid crystalline nanocarriers (LCN) such as cubosomes and hexosomes (Fig. 3) involve multiple compartments for encapsulation of either lipophilic or hydrophilic drugs. They display structural advantages which enable high encapsulation efficacy for molecules of various sizes and hydrophilicity.[113,116] LCNs are formed by self-assembly of lyotropic lipids such as unsaturated monoglycerides, phospholipids, glycolipids, and other amphiphilic molecules. For example, monoolein, which is a nontoxic, biodegradable, and biocompatible lipid, is classified as a GRAS (Generally Recognized As Safe), and ω-3 polyunsaturated fatty acids (n-3 PUFA) have been shown to be highly beneficial in various disease models of neurodegeneration.[123,124]

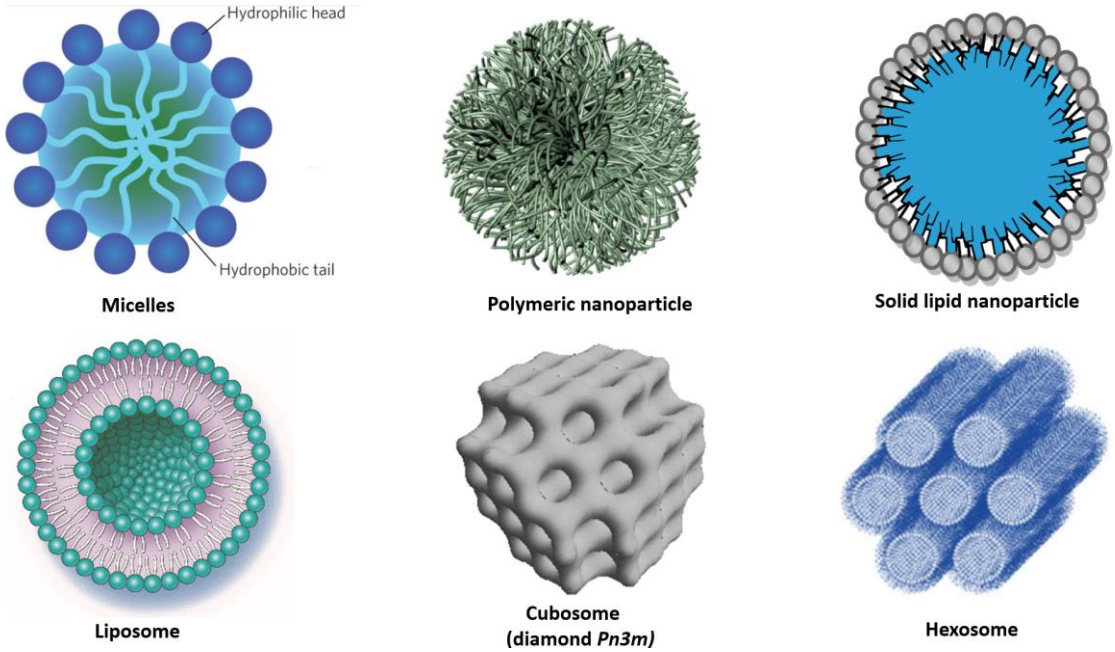

Figure 3 Schematic presentation of amphiphilic nanocarriers enabling the encapsulation and protection of hydrophobic and hydrophilic molecules of therapeutic significance.

In the following section, we summarize recently reported works on curcumin delivery to *in vitro* and *in vivo* models of neurodegenerative diseases.

a. Curcumin delivery by solid lipid nanoparticles

Solid lipid nanoparticles (SLNPs) are submicron colloidal lipid carriers (from 50 nm to 1000 nm in diameter) which maintain a solid, spherical shape at room temperature. They possess a solid lipid core matrix stabilized by emulsifiers that can solubilize lipophilic molecules. The CU-SLNPs are usually small, ranging from 100 to 300 nm in diameter. The total drug content can reach up to 92% when the SLNPs are manufactured using the micro-emulsification technique.[87] In an experimental rat model of cerebral ischemic reperfusion injury, animals fed with CU-loaded SLNPs have had a 90% improvement in their cognitive function along with a 52% inhibition of the acetyl cholinesterase activity.[88] The investigated formula has been shown to increase the levels of superoxide dismutase (SOD), catalase (CAT), glutathione (GSH), and the activities of mitochondrial enzymes, while decreasing the lipid peroxidation and the peroxynitrite levels. Furthermore, this formulation showed a 16.4 to 30-fold improvement in the bioavailability of CU in the brain upon oral and intravenous (IV) administrations, respectively.[88] The product Longvida® (Verdure Sciences Inc.) is a SLNP-formulation of curcumin which can yield from 0.1 to 0.2 μM plasma levels of CU with associated 1–2 μM brain levels of free CU in animals.[89–92] This formula was later optimized as "lipidated Cur," which can yield more than 5 μM CU in mouse brain.[93] Other formulations of CU-loaded SLNPs, tested in Alzheimer's disease models, are outlined in Table 3.

b. Curcumin delivery by nanostructured lipid carriers

Nanostructured lipid carriers (NLC) are referred to as the "second generation" of SLNPs. NLCs are composed of mixtures of sterically different amphiphilic molecules. Often, mixtures of liquid-phase lipids and solid-phase lipids yield matrices with imperfections, which may incorporate increased quantities of drug molecules as compared to the SLNPs. Despite of the presence of the liquid-phase lipid, the NLC matrix appears to be in a solid state at room and

body temperatures. The solid state is controlled by the fraction of the included liquid-phase lipid [94]. Sadegh-Malvajerd et al. have reported an enhanced entrapment efficiency of curcumin in NLCs (94% ± 0.74) as compared to SLNPs (82% ± 0.49). The pharmacokinetic studies, performed after intravenous (IV) administration of 4 mg/kg dose of curcumin in rats, have indicated that the amount of curcumin available in the brain was significantly higher for curcumin-loaded NLCs (AUC0–t = 505.76 ng/g h) as compared to free curcumin (AUC0–t = 0.00 ng/g h) and curcumin-loaded SLNs (AUC0–t = 116.31 ng/g h) ($P < 0.005$).[95] The outcomes of other recent investigations of CU-loaded NLCs in models of neurodegenerative diseases are summarized in Table 3.

c. Curcumin delivery by Liposomes

Liposomes are lipid bilayer-based, self-assembled, closed colloidal structures, typically 25 nm to 5 μm in diameter.[97] They usually have a spherical shape comprising an aqueous core surrounded by a hydrophobic lipid membrane (Fig. 3). The lipid bilayer can be loaded with hydrophobic or amphiphilic molecules, whereas the hydrophilic molecules can be encapsulated in the aqueous reservoir of the liposomes. Often, liposomes are composed of phospholipids (e.g., phosphatidylcholines) or mixtures of phospholipids with co-lipids. Various liposome architectures can form depending on the preparation methods; for instance, multilamellar vesicles (MLV, involving a stack of several lipid bilayers), small unilamellar vesicles (SUV, constituted by a single lipid bilayer), large unilamellar vesicles (LUV), tubular vesicles, and cochleate vesicles.

Curcumin encapsulated in liposomes has been proven to be a safe formulation, which enhances the CU solubility and its cellular uptake.[97–101] Liposomes deliver CU into the cells via membrane fusion or endocytosis process. Liposomal formulations with a PEG surface coating provide a longer circulation time for the encapsulated drug. Biomolecular ligands can be anchored to the liposome surface in order to enhance the receptor targeting capacity, and hence, the permeability across the blood-brain barrier (BBB).[102,103] The outcomes of the investigated CU-loaded liposomes in models of neurodegenerative diseases are summarized

in Table 3.

d. Curcumin delivery by liquid crystalline nanoparticles with internal structure

Liquid crystalline nanoparticles (LCNPs) are self-assembled architectures of lyotropic lipids, co-lipids (surfactants or oils), and water. They are typically formed upon dispersion and fragmentation of bulk lyotropic liquid crystalline phases (e.g., bicontinuous cubic, sponge, or inverted hexagonal phases).[104–106] The amphiphilic molecules spontaneously organize into compartments with hydrophobic and hydrophilic domains (Fig. 3), which can encapsulate lipophilic or hydrosoluble guest compounds. The structures formed by this self-assembly process are thermodynamically stable. The initial liquid crystalline phases are usually viscous and have a short-range order in comparison to solids, but long-range order in comparison to liquids. A typical example of a lyotropic liquid crystalline phase is the inverted bicontinuous cubic phase formed upon mixing of unsaturated monoglyceride lipids with water.[105] Cubosomes are produced upon dispersion of the bicontinuous cubic liquid crystalline phases in excess aqueous medium. Their periodic structures comprise folded bicontinuous lipid bilayer membranes and periodic networks of aqueous channels (Fig. 3). The latter enable high encapsulation capacity for hydrophilic guest macromolecules.[106–111] Lipid nanocarriers of liquid crystalline internal structures have received considerable attention as delivery vehicles through the BBB.[111,112]

Curcumin has been successfully entrapped into monolein-based LCNPs with almost 100% encapsulation efficiency.[113] LCNPs dispersion was very stable in terms of nanocarrier sizes and surface charge upon storage. LCNPs were efficiently taken up by cultures cells following the sustained release of curcumin. In addition, they provided inhibition of the cell proliferation and apoptosis induction in an anticancer study.[113] A recent investigation of an inverse hexagonal (HII) liquid crystalline phase encapsulating curcumin has demonstrated that the release of curcumin was a concentration-diffusion controlled process in the early stages, whereas multiple diffusion mechanisms coexisted in the later stages of drug release. Radical scavenging experiments have shown that curcumin - loaded LCNPs exert the desired

antioxidant activity.[114] Thus, curcumin-loaded LCNPs may be promising for neurodegenerative disease treatments using sustained-release nanoformulations for combination therapies.[115,116] Further results obtained with lipid - based LCNPs in models of neurodegenerative disease are presented in Table 3.

Table 3 Curcumin-loaded lipid nanoparticles studied in *in vitro* and *in vivo* models of neurodegenerative diseases.

Disease	Nanoformulation type	Model/administration route	Outcomes
AD	Solid lipid nanoparticles	*In vitro*: Mouse neuroblastoma cells after Aβ[1] exposure	Decreased ROS production, Prevented apoptotic death, Inhibition of Tau formation [89,90]
AD	Solid lipid curcumin particle (SLCP), Longvida®	*In vitro*: lipopolysaccharide (LPS)-stimulated RAW 264.7 cultured murine macrophages	Improved solubility over unformulated curcumin, Decreased LPS induced pro-inflammatory mediators NO, PGE2, and IL-6 by inhibiting the activation of NF-kB [92]
AD	Solid lipid particles with CU (SLCP)	*In vivo*: one-year-old 5xFAD- and age-matched wild-type mice, intraperitoneal injections of CU/SLCP	Decrease in Aβ plaque loads in dentate gyrus of hippocampus, more anti-amyloid, anti-inflammatory, and neuroprotective [91]
AD	Solid lipid nanoparticles	*In vivo*: Rat, oral	Effective delivery across the BBB[2] [88]
HD	Solid lipid nanoparticles (CU-SLNs)	*In vivo*: (3-NP)-induced HD in rats, oral	Restored glutathione levels and superoxide dismutase activity, Activation of nuclear factor-erythroid 2 antioxidant pathway, Reduction in mitochondrial swelling, lipid peroxidation, protein carbonyls and reactive oxygen species [88]
CNS disorders	Solid lipid nanoparticles (CU-SLNs) and nanostructured lipid carriers (CU-NLCs)	*In vivo*: male Sprague–Dawley rats 6–8 weeks old, oral	Enhanced curcumin brain uptake, Cur-NLCs enhance the absorption of brain curcumin more than 4-folds in comparison with Cur-SLNs [95]
AD	Lipoprotein (LDL)-mimic nanostructured lipid carrier (NLC) modified with lactoferrin (Lf) and loaded with CU	*In vivo*: Rat, oral	Cellular uptake mediated by the Lf receptor, Permeability through the BBB and preferentially accumulation in the brain, Efficacy in controlling the damage associated with AD [96]
AD	Liposomes functionalized with TAT-peptide	*In vitro*	Permeability across the BBB enhanced [98]

AD	Liposomes containing cardiolipin	*In vitro*: SK-N-MC cells	Inhibition of the phosphorylation of p38, JNK, and tau protein, Protection against serious degeneration of Aβ insulted neurons [101]
AD	WGA[3]-conjugated and cardiolipin-incorporated liposomes carrying NGF[4] and CU	*In vitro*: Human astrocytes and to protect SK-N-MC cells Apoptosis induced by β-amyloid 1–42 (A β 1–42) fibrils	Increased entrapment efficiency of NGF and CU, of NGF release and cell viability, Decreased release of CU, Permeability of NGF and CU across the blood–brain barrier [102]
AD	Liposomes	*In vivo*: Mice, stereotaxic injection in the right hippocampus and neocortex	Decrease in Aβ secretion and toxicity [97]
AD	Liposomes decorated with anti-transferrin receptor mAb	*In vivo* injection, hippocampus and neocortex	Decrease in Aβ 1–42 aggregation, Internalization in the BBB model [99]
AD	Liposomes functionalized with a curcumin-alkyne derivative TREG	Human biological fluids from sporadic AD patients and down syndrome subjects	Sequestration of Aβ 1–42 [100,101]
Neuronal loss	Liquid-crystalline lipid nanoparticles carrying curcumin and DHA	*In vitro*: SH-SY5Y cells	Neuronal viability and neurite outgrowth by activation of the TrkB receptor signaling, and promotion of phosphorylated CREB protein expression [118]
AD	Lipopeptide: a short microtubule- stabilizing peptide conjugated to a hydrophobic palmitic acid chain	*In vitro*: Neuro-2a cells, PC-12 differentiated cells	Neurite outgrowth in absence of external growth factors, Neural cells morphology and health amelioration [120,121]

[1] Aβ-amyloid; [2] blood–brain barrier; [3] wheat germ agglutinins; [4] nerve growth factor.

5) Conclusion

The naturally occurring compound curcumin is increasingly studied in neurodegenerative disease models due to its neurogenesis-stimulating properties and its anti-amyloid and anti-tau potential. Nanotechnology-based delivery systems of curcumin have been developed with the purpose of improving its solubility, stability, and bioavailability in potential treatment strategies of neurodegenerative disorders. We summarized recent advances in research on safe liquid crystalline lipid-based nanocarriers (cubosome, spongosome, hexosome, and liposome particles) and solid lipid nanoparticles, as well as on selected biodegradable polymer-based nanocarriers. The emphasis is given on the observed biological outcomes of

the curcumin nanoformulations in *in vitro* and *in vivo* models of the multifactor neurodegenerative diseases (AD, PD, HD and ALS). Despite the difficulty of overcoming biological barriers, promising results on the enhancement of the permeability of the BBB and receptor-mediated delivery across the BBB have been reported with liposome and cubosome nanocarriers. Further investigations will be required in order to understand the involved mechanisms of action of curcumin nanoformulations in the proposed neurodegenerative disease models, and to optimize the delivery systems and strategies towards translation into clinics.

6) References

(1) Brookmeyer, R., Abdalla, N., Kawas, C. H., Corrada, M. M. Forecasting the prevalence of preclinical and clinical Alzheimer's disease in the United States. *Alzheimers Dement.* **2018**, *14*, 121–129.

(2) Jack, C. R., Albert, M. S., Knopman, D. S., McKhann, G. M., Sperling, R. A., Carrillo, M. C., Thies, B., Phelps, C. H. Introduction to the recommendations from the National Institute on Aging-Alzheimer's Association workgroups on diagnostic guidelines for Alzheimer's disease. *Alzheimers Dement.* **2011**, *7*, 257–262.

(3) Haass, C., Selkoe, D. J. Soluble protein oligomers in neurodegeneration: Lessons from the Alzheimer's amyloid beta-peptide. *Nat. Rev. Mol. Cell Biol.* **2007**, *8*, 101–112.

(4) Wakasaya, Y., Kawarabayashi, T., Watanabe, M., Yamamoto-Watanabe, Y., Takamura, A., Kurata, T., Murakami, T., Abe, K., Yamada, K., Wakabayashi, K. Factors responsible for neurofibrillary tangles and neuronal cell losses in tauopathy. *J. Neurosci. Res.* **2011**, *89*, 576–584.

(5) Stoothoff, W. H., Johnson, G. V. Tau phosphorylation: Physiological and pathological consequences. *Biochim. Biophys. Acta* **2005**, *1739*, 280–297.

(6) Wang, J., Wang, Z. M., Li, X. M., Li, F., Wu, J. J., Kong, L. Y., Wang, X. B. Synthesis and evaluation of multi-target-directed ligands for the treatment of Alzheimer's disease

based on the fusion of donepezil and melatonin. *Bioorgan. Med. Chem.* **2016**, *24*, 4324–4338.

(7) Cole, G. M., Morihara, T., Lim, G. P., Yang, F., Begum, A., Frautschy, S. A. NSAID and antioxidant prevention of Alzheimer's disease: Lessons from *in vitro* and animal models. *Ann. N. Y. Acad. Sci.* **2004**, *1035*, 68–84.

(8) Alexander, G. E. Biology of Parkinson's disease: Pathogenesis and pathophysiology of a multisystem neurodegenerative disorder. *Dialogues Clin. Neurosci.* **2004**, *6*, 259–280.

(9) Dauer, W., Przedborski, S. Parkinson's disease: Mechanisms and models. *Neuron* **2003**, *39*, 889–909.

(10) Landles, C., Bates, G. P. Huntingtin and the molecular pathogenesis of Huntington's disease: Fourth in molecular medicine review series. *EMBO Rep.* **2004**, *5*, 958–963.

(11) Zuccato, C., Marullo, M., Vitali, B., Tarditi, A., Mariotti, C., Valenza, M., Lahiri, N., Wild, E. J., Sassone, J., Ciammola, A. Brain-derived neurotrophic factor in patients with Huntington's disease. *PLoS ONE* **2011**, *6*, e22966.

(12) Zhou, S., Zhou, Y., Qian, S., Chang, W., Wang, L., Fan, D. Amyotrophic lateral sclerosis in Beijing: Epidemiologic features and prognosis from 2010 to 2015. *Brain Behav.* **2018**, *19*, e01131.

(13) Glajch, E., Ferraiuolo, L., Mueller, K. A., Stopford, M. J., Prabhkar, V., Gravanis, A., Shaw, P. J., Sadri-Vakili, G. S. Microneurotrophins improve survival in motor neuron-astrocyte co-cultures but co cot improve disease phenotypes in a mutant SOD1 mouse model of amyotrophic lateral sclerosis. *PLoS ONE.* **2016**, *10*, e0164103.

(14) Varinderpal, S. D., Michael, F. Mutations that affect mitochondrial functions and their association with neurodegenerative diseases. *Mutat Res. Rev. Mutat. Res.* **2014**, *759*, 1–13.

(15) Barnham, K. J., Masters, C. L., Bush, A. I. Neurodegenerative diseases and oxidative stress. *Nat. Rev. Drug Discov.* **2004**, *3*, 205–214.

(16) Jiang, T., Suna, Q., Chena, S. B. Oxidative stress: A major pathogenesis and potential therapeutic target of antioxidative agents in Parkinson's disease and Alzheimer's disease. *Progr. Neurobiol.* **2016**, *147*, 1–19.

(17) Gilgun-Sherki, Y., Melamed, E., Offen, D. Oxidative stress induced-neurodegenerative diseases: The need for antioxidants that penetrate the blood brain barrier. *Neuropharmacology* **2001**, *40*, 959–975.

(18) Uttara, B., Singh, A. V., Zamboni, P., Mahajan, R. T. Oxidative stress and neurodegenerative diseases: A review of upstream and downstream antioxidant therapeutic options. *Curr. Neuropharmacol.* **2009**, *7*, 65–74.

(19) Dumont, M., Beal, M. F. Neuroprotective strategies involving ROS in Alzheimer disease. *Free Radic. Biol. Med.* **2011**, *51*, 1014–1026.

(20) Zhong, L., Zhou, J., Chen, X., Lou, Y., Liu, D., Zou, X., Yang, B., Yin, Y., Pan, Y. Quantitative proteomics study of the neuroprotective effects of B12 on hydrogen peroxide-induced apoptosis in SH-SY5Y cells. *Sci. Rep.* **2016**, *6*, 22635.

(21) Onyango, I. G., Khan, S. M., Bennett, J. P. Mitochondria in the pathophysiology of Alzheimer's and Parkinson's diseases. *Front. Biosci.* **2017**, *22*, 854–872.

(22) Ankarcronaa, M., Mangialascheb, F., Winblada, B. Thinking Alzheimer's disease therapy: Are mitochondria the key? *J. Alzheimers Dis.* **2010**, *20* (Suppl. 2), S579–S590.

(23) Federico, A., Cardaioli, E., Da Pozzo, P., Formichi, P., Gallus, G. N. Mitochondria, oxidative stress and neurodegeneration. *J. Neurol. Sci.* **2012**, *322*, 254–262.

(24) Stahon, K. E., Bastian, C., Griffith, S., Kidd, G. J., Brunet, S., Baltan, S. Age-related changes in axonal and mitochondrial ultrastructure and function in white matter. *J. Neurosci.* **2016**, *36*, 9990–10001.

(25) Cho, D. H., Nakamura, T., Lipton, S. A. Mitochondrial dynamics in cell death and neurodegeneration. *Cell Mol. Life Sci* **2010**, *67*, 3435–3447.

(26) Lu, M., Su, C., Qiao, C., Bian, Y., Ding, J., Hu, G. Metformin prevents dopaminergic neuron death in MPTP/P-induced mouse model of Parkinson's disease via autophagy and mitochondrial ROS clearance. *Int. J. Neuropsychopharmacol.* **2016**, *19*, 1–11.

(27) Zádori, D., Klivényi, P., Szalárdy, L., Fülöp, F., Toldi, J., Vécsei, L. Mitochondrial disturbances, excitotoxicity, neuroinflammation and kynurenines: Novel therapeutic strategies for neurodegenerative disorders. *J. Neurol. Sci.* **2012**, *322*, 187–191.

(28) Rahimifard, M., Maqbool, F., Moeini-Nodeh, S., Niaz, K., Abdollahi, M., Braidy, N., Nabavi, S. M., Nabavi, S. F. Targeting the TLR4 signaling pathway by polyphenols: A novel therapeutic strategy for neuroinflammation. *Ageing Res. Rev.* **2017**, *36*, 11–19.

(29) Géral, C., Angelova, A., Lesieur, S. From molecular to nanotechnology strategies for delivery of neurotrophins: Emphasis on brain-derived neurotrophic factor (BDNF). *Pharmaceutics* **2013**, *5*, 127–167.

(30) Angelova, A., Angelov, B., Drechsler, M., Lesieur, S. Neurotrophin delivery using nanotechnology. *Drug Discov. Today* **2013**, *18*, 1263–1271.

(31) Devi, L., Ohno, M. 7,8-Dihydroxyflavone, a small-molecule TrkB agonist, reverses memory deficits and BACE1 elevation in a mouse model of Alzheimer's disease. *Neuropsychopharmacology* **2012**, *37*, 434–444.

(32) Soleimani, V., Sahebkar, A., Hosseinzadeh, H. Turmeric (*Curcuma longa*) and its major constituent (curcumin) as nontoxic and safe substances. *Review. Phytother. Res.* **2018**, *32*, 985–995.

(33) Mahdavi, H., Hadadi, Z., Ahmadi, M. A. Review of the anti-oxidation, anti-inflammatory and anti-tumor properties of curcumin. *Tradit. Integr. Med.* **2017**, *2*, 188–195.

(34) Gupta, S. C., Patchva, S., Aggarwal, B. B. Therapeutic roles of curcumin: Lessons learned from clinical trials. *AAPS J.* **2013**, *15*, 195–218.

(35) Brondino, N., Re, S., Boldrini, A., Cuccomarino, A., Lanati, N., Barale, F., Politi, P. Curcumin as a therapeutic agent in dementia: A mini systematic review of human studies. *Sci. World J.* **2014**, *2014*, 1–6.

(36) Serafini, M. M., Catanzaro, M., Rosini, M., Racchi, M., Lanni, C. Curcumin in Alzheimer's disease: Can we think to new strategies and perspectives for this molecule? *Pharmacol. Res.* **2017**, *124*, 146–155.

(37) Maiti, P., Dunbar, G. Use of curcumin, a natural polyphenol for targeting molecular pathways in treating age-related neurodegenerative diseases. *Int. J. Mol. Sci.* **2018**, *31*, 19.

(38) Haan, J. D., Morrema, T. H. J., Rozemuller, A. J., Bouwman, F. H., Hoozemans, J. J. M. Different curcumin forms selectively bind fibrillar amyloid beta in post mortem Alzheimer's disease brains: Implications for in-vivo diagnostics. *Acta Neuropathol. Commun.* **2018**, *6*, 75.

(39) Samarghandian, S., Azimi-Nezhad, M., Farkhondeh, T., Samini, F. Anti-oxidative effects of curcumin on immobilization-induced oxidative stress in rat brain, liver and kidney. *Biomed. Pharmacother.* **2017**, *87*, 223–229.

(40) Ahmad, B., Borana, M. S., Chaudhary, A. P. Understanding curcumin-induced modulation of protein aggregation. *Int. J. Biol. Macromol.* **2017**, *100*, 89–96.

(41) Sarkar, B., Dhiman, M., Mittal, S., Mantha, A. K. Curcumin revitalizes Amyloid beta (25-35)-induced and organophosphate pesticides pestered neurotoxicity in SH-SY5Y and IMR-32 cells via activation of APE1 and Nrf2. *Metab. Brain Dis.* **2017**, *32*, 2045–2061.

(42) Zhang, L., Fang, Y., Cheng, X., Lian, Y. J., Xu, H. L., Zeng, Z. S., Zhu, H. C. Curcumin exerts effects on the pathophysiology of Alzheimer's disease by regulating PI(3,5)P2 and transient receptor potential mucolipin-1 expression. *Front. Neurol.* **2017**, *8*, 531.

(43) Liaquat, L., Batool, Z., Sadir, S., Rafiq, S., Shahzad, S., Perveen, T., Haider, S. Naringenin-induced enhanced antioxidant defense system meliorates cholinergic neurotransmission and consolidates memory in male rats. *Life Sci.* **2018**, *194*, 213–223.

(44) Nguyen, T. T., Vuu, M. D., Huynh, M. A., Yamaguchi, M., Tran, L. T., Dang, T. P. T. Curcumin effectively rescued Parkinson's disease-like phenotypes in a novel drosophila melanogaster model with dUCH Knockdown. *Oxid. Med. Cell. Longev.* **2018**, *2018*, 1–12.

(45) Wang, Y. L., Ju, B., Zhang, Y. Z., Yin, H. L., Liu, Y. J., Wang, S. S., Zeng, Z. L., Yang, X. P., Wang, H. T., Li, J. F. Protective effect of curcumin against oxidative stress-induced injury in rats with Parkinson's disease through the Wnt/β-catenin signaling pathway. *Cell. Physiol. Biochem.* **2017**, *43*, 2226–2241.

(46) Snigdha, D. M., Surjyanarayan, M., Jayvadan, P. Intranasal mucoadhesive microemulsion for neuroprotective effect of curcumin in mPTP induced Parkinson model. *Braz. J. Pharm. Sci.* **2017**, *53*.

(47) Hickey, M. A., Zhu, C., Medvedeva, V., Lerner, R. P., Patassini, S., Franich, N. R., Maiti, P., Frautschy, S. A., Zeitlin, S., Levine, M. S., et al. Improvement of neuropathology and transcriptional deficits in CAG 140 knock-in mice supports a beneficial effect of dietary curcumin in Huntington's disease. *Mol. Neurodegener.* **2012**, *7*, 12.

(48) Sevastre-Berghian, A. C., Făgărăsan, V., Toma, V. A., Bâldea, I., Olteanu, D., Moldovan, R., Decea, N., Filip, G. A., Clichici, S. V. Curcumin reverses the diazepam-induced cognitive impairment by modulation of oxidative stress and ERK 1/2/NF-κB pathway in brain. *Oxid. Med. Cell. Longev.* **2017**, *2017*, 1–16.

(49) Motaghinejad, M., Motevalian, M., Fatima, S., Hashemi, H., Gholami, M. Curcumin confers neuroprotection against alcohol-induced hippocampal neurodegeneration via CREB-BDNF pathway in rats. *Biomed. Pharmacother.* **2017**, *87*, 721–740.

(50) Motaghinejad, M., Motevalian, M., Fatima, S., Faraji, F., Mozaffari, S. The neuroprotective effect of curcumin against nicotine-induced neurotoxicity is mediated by CREB-BDNF signaling pathway. *Neurochem. Res.* **2017**, *42*, 2921–2932.

(51) Baum, L., Lam, C. W., Cheung, S. K., Kwok, T., Lui, V., Tsoh, J., Lam, L., Leung, V., Hui, E., Ng, C. Six-month randomized, placebo-controlled, double-blind, pilot clinical trial of curcumin in patients with Alzheimer disease. *J. Clin. Psychopharmacol.* **2008**, *28*, 110–113.

(52) Ringman, J. M., Frautschy, S. A., Teng, E., Begum, A. N., Bardens, J., Beigi, M., Gylys, K. H., Badmaev, V., Heath, D. D., Apostolova, L. G. Oral curcumin for Alzheimer's disease: Tolerability and efficacy in a 24-week randomized, double blind, placebo-controlled study. *Alzheimers Res. Ther.* **2012**, *4*, 43.

(53) Hishikawa, N., Takahashi, Y., Amakusa, Y., Tanno, Y., Tuji, Y., Niwa, H., Murakami, N., Krishna, U. K. Effects of turmeric on Alzheimer's disease with behavioral and psychological symptoms of dementia. *AYU* **2012**, *33*, 499–504.

(54) Mazzanti, G., Di Giacomo, S. Curcumin and resveratrol in the management of cognitive disorders: What is the clinical evidence? *Molecules* **2016**, *21*, 1243.

(55) Ireson, C. R., Jones, D. J., Orr, S., Coughtrie, M. W., Boocock, D. J., Williams, M. L., Farmer, P. B., Steward, W. P., Gescher, A. J. Metabolism of the cancer chemopreventive agent curcumin in human and rat intestine. *Cancer Epidemiol. Biomark. Prev.* **2002**, *11*, 105–111.

(56) Marczylo, T. H., Steward, W. P., Gescher, A. J. Rapid analysis of curcumin and curcumin metabolites in rat biomatrices using a novel ultraperformance liquid chromatography (UPLC) method. *J. Agric. Food. Chem.* **2009**, *57*, 797–803.

(57) Marczylo, T. H., Verschoyle, R. D., Cooke, D. N., Morazzoni, P., Steward, W. P., Gescher, A. J. Comparison of systemic availability of curcumin with that of curcumin formulated with phosphatidylcholine. *Cancer Chemother. Pharmacol.* **2007**, *60*, 171–177.

(58) Ghalandarlaki, N., Alizadeh, A. M., Ashkani-Esfahani, S. Nanotechnology-applied curcumin for different diseases therapy. *Biomed. Res. Int.* **2014**, *2014*, 1–23.

(59) Cox, K. H., Pipingas, A., Scholey, A. B. Investigation of the effects of solid lipid curcumin on cognition and mood in a healthy older population. *J. Psychopharmacol.* **2015**, *29*, 642–651.

(60) Modi, G., Pillay, V., Choonara, Y. E. Advances in the treatment of neurodegenerative disorders employing nanotechnology. *Ann. N. Y. Acad. Sci.* **2010**, *1184*, 154–172.

(61) Sahni, J. K., Doggui, S., Ali, J., Baboota, S., Dao, L., Ramassamy, C. Neurotherapeutic applications of nanoparticles in Alzheimer's disease. *J. Control. Release* **2011**, *152*, 208–231.

(62) Craparo, E. F., Bondì, M. L., Pitarresi, G., Cavallaro, G. Nanoparticulate systems for drug delivery and targeting to the central nervous system. *CNS Neurosci. Ther.* **2011**, *17*, 670–677.

(63) Fonseca-Santos, B., Gremiao, D., Palmira, M., Chorilli, M. Nanotechnology-based drug delivery systems for the treatment of Alzheimer's disease. *Int. J. Nanomed.* **2015**, *10*, 4981–5003.

(64) Kanwar, J. R., Sun, X., Punj, V., Sriramoju, B., Mohan, R. R., Zhou, S. F., Chauhan, A., Kanwar, R. K. Nanoparticles in the treatment and diagnosis of neurological disorders: Untamed dragon with fire power to heal. *Nanomedicine* **2012**, *8*, 399–414.

(65) Gao, H. Progress and perspectives on targeting nanoparticles for brain drug delivery. *Acta Pharm. Sin. B* **2016**, *6*, 268–286.

(66) Roney, C., Kulkarni, P., Arora, V., Antich, P., Bonte, F., Wu, A., Mallikarjuana, N. N., Manohar, S., Liang, H. F., Kulkarni, A. R., et al. Targeted nanoparticles for drug delivery through the blood–brain barrier for Alzheimer's disease. *J. Control. Release* **2005**, *108*, 193–214.

(67) Modi, G., Pillay, V., Choonara, Y. E., Ndesendo, V. M. K., Du Toit, L. C., Naidoo, D. Nanotechnological applications for the treatment of neurodegenerative disorders. *Progr. Neurobiol.* **2009**, *4*, 272–285.

(68) Ma, Z., Haddadi, A., Molavi, O., Lavasanifar, A., Lai, R., Samuel, J. Micelles of poly(ethyleneoxide)-b-poly(epsilon-caprolactone) as vehicles for the solubilization, stabilization, and controlled delivery of curcumin. *J. Biomed. Mater. Res. A* **2008**, *86*, 300–310.

(69) Yu, H., Li, J., Shi, K., Huang, Q. Structure of modified epsilon-polylysine micelles and their application in improving cellular antioxidant activity of curcuminoids. *Food Funct.* **2011**, *2*, 373–380.

(70) Podaralla, S., Averineni, R., Alqahtani, M., Perumal, O. Synthesis of novel biodegradable methoxypoly (ethylene glycol)-zein micelles for effective delivery of curcumin. *Mol. Pharm.* **2012**, *9*, 2778–2786.

(71) Song, Z., Feng, R., Sun, M., Guo, C., Gao, Y., Li, L., Zhai, G. Curcumin-loaded PLGA-PEG-PLGA triblock copolymeric micelles: Preparation, pharmacokinetics and distribution *in vivo*. *J. Colloid Interface Sci.* **2011**, *354*, 116–123.

(72) Doggui, S., Sahni, J. K., Arseneault, M., Dao, L., Ramassamy, C. Neuronal uptake and neuroprotective effect of curcumin-loaded PLGA nanoparticles on the human SK-N-SH cell line. *J. Alzheimers Dis.* **2012**, *30*, 377–392.

(73) Tiwari, S. K., Agarwal, S., Seth, B., Yadav, A., Nair, S., Bhatnagar, P., Karmakar, M., Kumari, M., Chauhan, L. K., Patel, D. K., et al. Curcumin-loaded nanoparticles potently induce

adult neurogenesis and reverse cognitive deficits in Alzheimer's disease model via canonical Wnt/β-catenin pathway. *ACS Nano* **2014**, *8*, 76–103.

(74) Mathew, A., Fukuda, T., Nagaoka, Y., Hasumura, T., Morimoto, H., Yoshida, Y., Maekawa, T., Venugopal, K., Kumar, D. S. Curcumin loaded-PLGA nanoparticles conjugated with Tet-1 peptide for potential use in Alzheimer's disease. *PLoS ONE* **2012**, *7*, e32616.

(75) Paka, G. D., Doggui, S., Zaghmi, A., Safar, R., Dao, L., Reisch, A., Klymchenko, A., Roullin, V. G., Joubert, O., Ramassamy, C. Neuronal uptake and neuroprotective properties of curcumin-loaded nanoparticles on SK-N-SH cell line: Role of poly(lactide-coglycolide) polymeric matrix composition. *Mol. Pharm.* **2016**, *13*, 391–403.

(76) Paka, G. D., Ramassamy, C. Optimization of curcumin-loaded PEG-PLGA nanoparticles by GSH functionalization: Investigation of the internalization pathway in neuronal cells. *Mol. Pharm.* **2017**, *14*, 93–106.

(77) Tsai, Y. M., Jan, W. C., Chien, C. F., Lee, W. C., Lin, L. C., Tsai, T. H. Optimised nano-formulation on the bioavailability of hydrophobic polyphenol, curcumin, in freely-moving rats. *Food Chem.* **2011**, *127*, 918–925.

(78) Tsai, Y. M., Chien, C. F., Lin, L. C., Tsai, T. H. Curcumin and its nano-formulation: The kinetics of tissue distribution and blood–brain barrier penetration. *Int. J. Pharm.* **2011**, *416*, 331–338.

(79) Mulik, R. S., Mönkkönen, J., Juvonen, R. O., Mahadik, K. R., Paradkar, A. R. ApoE3mediated poly (butyl) cyanoacrylate nanoparticles containing curcumin: Study of enhanced activity of curcumin against beta amyloid induced cytotoxicity using *in vitro* cell culture model. *Mol. Pharm.* **2010**, *7*, 815–825.

(80) Le Droumaguet, B., Nicolas, J., Brambilla, D., Mura, S., Maksimenko, A., DeKimpe, L., Salvati, E., Zona, C., Airoldi, C., Canovi, M., et al. Versatile and efficient targeting using a single nanoparticulate platform: Application to cancer and Alzheimer's disease. *ACS Nano* **2012**, *6*, 5866–5879.

(81) Ameruoso, A., Palomba, R., Palange, A., Cervadoro, A., Lee, A., Di Mascolo, D., Decuzzi, P. Ameliorating amyloid-β fibrils triggered inflammation via curcumin-loaded polymeric nanoconstructs. *Front. Immunol.* **2017**, *8*, 1411.

(82) Ray, B., Bisht, S., Maitra, A., Maitra, A., Lahiri, D. K. Neuroprotective and neurorescue effects of a novel polymeric nanoparticle formulation of curcumin (NanoCurcTM) in the neuronal cell culture and animal model: Implications for Alzheimer's disease. *J. Alzheimers Dis.* **2011**, *23*, 61–77.

(83) Cheng, K. K., Yeung, C. F., Ho, S. W., Chow, S. F., Chow, A. H., Baum, L. Highly stabilized curcumin nanoparticles tested in an *in vitro* blood–brain barrier model and in Alzheimer's disease Tg2576 mice. *AAPS J.* **2013**, *15*, 324–336.

(84) Sood, S., Jain, K., Gowthamarajan, K. Optimization of curcumin nanoemulsion for intranasal delivery using design of experiment and its toxicity assessment. *Colloids Surf. B Biointerfaces* **2014**, *113*, 330–337.

(85) Hagl, S., Kocher, A., Schiborr, C., Kolesova, N., Frank, J., Eckert, G. P. Curcumin micelles improve mitochondrial function in neuronal PC12 cells and brains of NMRI mice—Impact on bioavailability. *Neurochem. Int.* **2015**, *89*, 234–242.

(86) Siddique, Y. H., Wasi Khan, S. B. R., Naqvi, A. H. Synthesis of alginate-curcumin nanocomposite and its protective role in transgenic drosophila model of Parkinson's disease. *ISRN Pharmacol.* **2013**, *2013*, 1–8.

(87) Kakkar, V., Muppu, S. K., Chopra, K., Kaur, I. P. Curcumin loaded solid lipid nanoparticles: An efficient formulation approach for cerebral ischemic reperfusion injury in rats. *Eur. J. Pharm. Biopharm.* **2013**, *85*, 339–345.

(88) Kakkara, V., Mishrab, A. K., Chuttanib, K., Kaura, I. P. Proof of concept studies to confirm the delivery of curcumin loaded solid lipid nanoparticles (C-SLNs) to brain. *Int. J. Pharm.* **2013**, *448*, 354–359.

(89) Maiti, P., Dunbar, G. L. Comparative neuroprotective effects of dietary curcumin and solid lipid curcumin particles in cultured mouse neuroblastoma cells after exposure to Aβ42. *Int. J. Alzheimers Dis.* **2017**, *2017*, 1–13.

(90) Maiti, P., Hall, T. C., Paladugu, L., Kolli, N., Learman, C., Rossignol, J., Dunbar, G. L. A comparative study of dietary curcumin, nanocurcumin, and other classical amyloid-binding dyes for labeling and imaging of amyloid plaques in brain tissue of 5x-familial Alzheimer's disease mice. *Histochem. Cell Biol.* **2016**, *146*, 609–625.

(91) Maiti, P., Paladugu, L., Dunbar, G. L. Solid lipid curcumin particles provide greater anti-amyloid, anti-inflammatory and neuroprotective effects than curcumin in the 5xFAD mouse model of Alzheimer's disease. *BMC Neurosci.* **2018**, *19*, 7.

(92) Pragati, P., Nahar, A., Slitt, L., Navindra, P. Anti-inflammatory effects of novel standardized solid lipid curcumin formulations. *J. Med. Food* **2015**, *18*, 786–792.

(93) Dadhaniya, P., Patel, C., Muchhara, J., Bhadja, N., Mathuria, N., Vachhani, K., Soni, M. G. Safety assessment of a solid lipid curcumin particle preparation: Acute and subchronic toxicity studies. *Food Chem. Toxicol.* **2011**, *49*, 1834–1842.

(94) Ganesan, P., Narayanasamy, D. Lipid nanoparticles: Different preparation techniques, characterization, hurdles, and strategies for the production of solid lipid nanoparticles and nanostructured lipid carriers for oral drug delivery. *Sustain. Chem. Pharm.* **2017**, *6*, 37–56.

(95) Sadegh-Malvajerd, S., Azadi, A., Izadi, Z., Kurd, M., Dara, T., Dibaei, M., Sharif-Zadeh, M., Akbari-Javar, H., Hamidi, M. Brain delivery of curcumin using solid lipid nanoparticles and nanostructured lipid carriers: Preparation, optimization, and pharmacokinetic evaluation. *ACS Chem. Neurosci.* **2018**.

(96) Meng, F., Asghar, S., Gao, S., Su, Z., Song, J., Huo, M., Meng, W., Ping, Q., Xiao, Y. A novel LDL-mimic nanocarrier for the targeted delivery of curcumin into the brain to treat Alzheimer's disease. *Colloids Surf. B Biointerfaces* **2015**, *134*, 88–97.

(97) Lazar, A. N., Mourtas, S., Youssef, I., Parizot, C., Dauphin, A., Delatour, B., Antimisiaris, S. G., Duyckaerts, C. Curcumin-conjugated nanoliposomes with high affinity for Aβ deposits: Possible applications to Alzheimer disease. *Nanomed. Nanotechnol. Biol. Med.* **2013**, *9*, 712–721.

(98) Sancini, G., Gregori, M., Salvati, E., Cambianica, L., Re, F., Ornaghi, F., Canovi, M., Fracasso, C., Cagnotto, A., Colombo, M., et al. Functionalization with TAT-peptide enhances blood–brain barrier crossing *in vitro* of nanoliposomes carrying a curcumin-derivative to bind amyloid-β peptide. *J. Nanomed. Nanotechnol.* **2013**, *4*, 1–8.

(99) Mourtas, S., Canovi, M., Zona, C., Aurilia, D., Niarakis, A., La Ferla, B., Salmona, M., Nicotra, F., Gobbi, M., Antimisiaris, S. G. Curcumin-decorated nanoliposomes with very high affinity for amyloid beta1–42 peptide. *Biomaterials* **2011**, *32*, 1635–1645.

(100) Airoldi, C., Zona, C., Sironi, E., Colombo, L., Messa, M., Aurilia, D., Gregori, M., Masserini, M., Salmona, M., Nicotra, F., et al. Curcumin derivatives as new ligands of Apeptides. *J. Biotechnol.* **2011**, *156*, 317–324.

(101) Conti, E., Gregori, M., Radice, I., Da Re, F., Grana, D., Re, F., Salvati, E., Masserini, M., Ferrarese, C., Zoia, C. P., et al. Multifunctional liposomes interact with Abeta in human biological fluids: Therapeutic implications for Alzheimer's disease. *Neurochem. Int.* **2017**, *108*, 60–65.

(102) Kuo, Y. C., Lin, C. Y., Li, J. S., Lou, Y. I. Wheat germ agglutinin-conjugated liposomes incorporated with cardiolipin to improve neuronal survival in Alzheimer's disease treatment. *Int. J. Nanomed.* **2017**, *12*, 1757–1774.

(103) Kuo, Y. C., Lin, C. C. Rescuing apoptotic neurons in Alzheimer's disease using wheat germ agglutinin- conjugated and cardiolipin-conjugated liposomes with encapsulated nerve growth factor and curcumin. *Int. J. Nanomed.* **2015**, *10*, 2653–2672.

(104) Valldeperas, M., Wis´niewska, M., Ram-On, M., Kesselman, E., Danino, D., Nylander, T., Barauskas, J. Sponge phases and nanoparticle dispersions in aqueous mixtures of mono- and diglycerides. *Langmuir* **2016**, *32*, 8650–8659.

(105) Milak, S., Zimmer, A. Glycerol monooleate liquid crystalline phases used in drug delivery systems. *Int. J. Pharm.* **2015**, *478*, 569–587.

(106) Angelova, A., Angelov, B., Mutafchieva, R., Lesieur, S., Couvreur, P. Self-assembled multicompartment liquid crystalline lipid carriers for protein, peptide, and nucleic acid drug delivery. *Acc. Chem. Res.* **2011**, *44*, 147–156.

(107) Angelov, B., Angelova, A., Filippov, S. K., Drechsler, M., Šteˇ pánek, P., Lesieur, S. Multi-compartment lipid cubic nanoparticles with high protein upload: Millisecond dynamics of formation. *ACS Nano* **2014**, *8*, 5216–5226.

(108) Zerkoune, L., Lesieur, S., Putaux, J. L., Choisnard, L., Gèze, A., Wouessidjewe, D., Angelov, B., Vebert-Nardin, C., Doutch, J., Angelova, A. Mesoporous self-assembled nanoparticles of biotransesterified cyclodextrins and nonlamellar lipids as carriers of water-insoluble substances. *Soft Matter* **2016**, *12*, 7539–7550.

(109) Han, S., Shen, J. Q., Gan, Y., Geng, H. M., Zhang, X. X., Zhu, C. L., Gan, L. Novel vehicle based on cubosomes for ophthalmic delivery of flurbiprofen with low irritancy and high bioavailability. *Acta Pharmacol. Sin.* **2010**, *31*, 990–998.

(110) Zou, A., Li, Y., Chen, Y., Angelova, A., Garamus, V. M., Li, N., Drechsler, M., Angelov, B., Gong, Y. Self-assembled stable sponge type nanocarriers for *Brucea javanica* oil delivery. *Colloids Surf. B* **2017**, *153*, 310–319.

(111) Azhari, H., Strauss, M., Hook, S., Boyd, B. J., Rizwan, S. B. Stabilising cubosomes with tween 80 as a step towards targeting lipid nanocarriers to the blood–brain barrier. *Eur. J. Pharm. Biopharm.* **2016**, *104*, 148–155.

(112) Wu, H., Li, J., Zhang, Q., Yan, X., Guo, L., Gao, X., Qiu, M., Jiang, X., Lai, R., Chen, H. A novel small odorranalectin-bearing cubosomes: Preparation, brain delivery and pharmacodynamic study on amyloid-b25–35-treated rats following intranasal administration. *Eur. J. Pharm. Biopharm.* **2012**, *80*, 368–378.

(113) Baskaran, R., Madheswaran, T., Sundaramoorthy, P., Kim, H. M., Yoo, B. K. Entrapment of curcumin into monoolein-based liquid crystalline nanoparticle dispersion for enhancement of stability and anticancer activity. *Int. J. Nanomed.* **2014**, *9*, 3119–3130.

(114) Wei, L., Li, X., Guo, F., Liu, X., Wang, Z. Structural properties, *in vitro* release and radical scavenging activity of lecithin based curcumin-encapsulated inverse hexagonal (HII) liquid crystals. *Colloids Surf. A* **2018**, *539*, 124–131.

(115) Angelova, A., Angelov, B. Dual and multi-drug delivery nanoparticles towards neuronal survival and synaptic repair. *Neural. Regen. Res.* **2017**, *12*, 886–889.

(116) Angelova, A., Drechsler, M., Garamus, V. M., Angelov, B. Liquid crystalline nanostructures as pegylated reservoirs of omega-3 polyunsaturated fatty acids: Structural insights toward delivery formulations against neurodegenerative disorders. *ACS Omega* **2018**, *3*, 3235–3247.

(117) Sandhir, R., Yadav, A., Mehrotra, A., Sunkaria, A., Singh, A., Sharma, S. Curcumin nanoparticles attenuate neurochemical and neurobehavioral deficits in experimental model of Huntington's disease. *Neuromol. Med.* **2014**, *16*, 106–118.

(118) Guerzoni, L. P., Nicolas, V., Angelova, A. *In vitro* modulation of TrkB receptor signaling upon sequential delivery of curcumin-DHA loaded carriers towards promoting neuronal survival. *Pharm. Res.* **2017**, *34*, 492–505.

(119) Chen, Y., Angelova, A., Angelov, B., Drechsler, M., Garamus, V. M., Willumeit-Römere, R., Zou, A. Sterically stabilized spongosomes for multi-drug delivery of anticancer nanomedicines. *J. Mater. Chem. B* **2015**, *3*, 7734–7744.

(120) Biswas, A., Kurkute, P., Jana, B., Laskar, A., Ghosh, S. An amyloid inhibitor octapeptide forms amyloid type fibrous aggregates and affects microtubule motility. *Chem. Commun.* **2014**, *50*, 2604–2607.

(121) Adak, A., Das, G., Barman, S., Mohapatra, S., Bhunia, D., Jana, B., Ghosh, S. Biodegradable neuro-compatible peptide hydrogel promotes neurite outgrowth, shows significant neuroprotection, and delivers anti-Alzheimer drug. *ACS Appl. Mater. Interfaces* **2017**, *9*, 5067–5076.

(122) Shrestha, H., Bala, R., Arora, S. Lipid-based drug delivery systems. *J. Pharm.* **2014**, *2014*, 1–10.

(123) Ganem-Quintanar, A., Quintanar-Guerrero, D., Buri, P. Monoolein: A review of the pharmaceutical applications. *Drug Dev. Ind. Pharm.* **2000**, *26*, 809–820.

(124) Bousquet, M., Saint-Pierre, M., Julien, C., Salem, N., Cicchetti, F., Calon, F. Beneficial effects of dietary omega-3 polyunsaturated fatty acid on toxin-induced neuronal degeneration in an animal model of Parkinson's disease. *FASEB J.* **2008**, *22*, 1213–1225.

Chapter 2: Curcumin and fish oil - loaded lyotropic liquid crystalline nanostructures

I. Composition-switchable liquid crystalline nanostructures as green formulations of curcumin and fish-oil

Miora Rakotoarisoa[a], **Borislav Angelov**[b], **Shirly Espinoza**[b], **Krishna Khakurel**[b], **Thomas Bizien**[c], **Markus Drechsler**[d] **and Angelina Angelova**[a].

[a] Université Paris-Saclay, CNRS, Institut Galien Paris-Sud UMR8612, F-92296 Châtenay-Malabry, France; [b] Institute of Physics, ELI Beamlines, Academy of Sciences of the Czech Republic, Na Slovance 2, CZ-18221 Prague, Czech Republic; [c] Synchrotron SOLEIL, l'Orme des Merisiers, Saint-Aubin - BP 48, 91192 Gif-sur-Yvette Cedex, France; [d] Keylab "Electron and Optical Microscopy", Bavarian Polymer Iinstitute (BPI), University of Bayreuth, Universitätsstrasse 30, D-95440 Bayreuth, Germany,

Submitted in ACS Sustainable Chemistry & Engineering

Composition-switchable liquid crystalline nanostructures as green formulations of curcumin and fish-oil

Abstract:

Green compositions and processes for fabrication of dual- and multi-loaded nanocarriers with antioxidant functionality and neuroprotective, cardioprotective, antiviral, and anti-proliferative activities are of broad interest for innovations in pharmaceutics and nutraceutics. Co-encapsulation of curcumin (studied as a key multipurpose phytochemical antioxidant) with ·-3 polyunsaturated fatty acids (PUFAs) (studied as active ingredients of natural fish oil) may increase the oxidative stability of self-assembled formulations aiming at development of "food drugs" and prevention of disease progression in various pathological states. The objective of this work is to prepare self-assembled lyotropic liquid crystalline nanostructures as dual-loaded biodegradable carriers of ω-3 PUFA-fish oil and curcumin. A detailed structural phase diagram of ternary [monoolein (MO) - PEGylated lipid mixture] / [fish oil - curcumin] / water system is created. A composition-mediated switch between nanostructures of different topologies and polymorphic states is achieved through varying the ratios between the amphiphilic monoglyceride ingredient, fish oil and water, which yielded cubic, sponge, and lamellar mesophases of tunable nanoscale repeat spacings. Synchrotron small-angle X-ray scattering (SAXS) studies are performed with the lyotropic liquid crystalline nanostructures along compositional dilution lines. The temperature effect is examined at 22 °C and 5 °C with regard to preparation conditions and mesophase stability on storage. Bulk mesophases are dispersed into lipid nanoparticles at 22 °C, the structures and topologies of which are revealed by SAXS and cryo-transmission electron microscopy (cryo-TEM) imaging. The new knowledge about the controlled multicomponent supramolecular assembly and the achieved stabilization of low-temperature cubic phases (hydrated in 5 wt% D-(+)-glucose) should facilitate the development of cost-effective stable and safe delivery systems of weakly soluble natural antioxidant compounds co-encapsulated with ω-3 PUFA oils.

1) Introduction

Sustainable nanomedicine development relies on active ingredients and processing nanotechnologies that favor environmental protection.[1-3] Fabrication processes based on spontaneous self-assembly avoid high energy consumption and therefore reduce the environmental pollution. Improving drug bioavailability is one of the major current objectives of the green pharma industry. As a matter of fact, increased bioavailability of the active ingredients will essentially diminish the need of drug elimination, and thus will prevent the risk for the environment. Due to their safety, high efficacy for drug nanoencapsulation, and low immunogenicity, lipid-based liquid crystalline carriers are gaining considerable interest in recent years.[4-22] They are thermodynamically stable and permit development of sustained drug delivery systems in nanomedicine.[23-33]

Lipid-based nanoparticles fabricated from biocompatible and biodegradable natural sources provide safety profiles and the possibility for engineering of green nanosystems with controlled surface area-to-volume ratios.[5,10-17,23] Such particles can be formed by dispersion of lipid-based lyotropic liquid crystalline (LLC) phases, which spontaneously self-assemble upon exposure of lyotropic lipids to water.[11,17] The formation of lamellar (Lα/Lc), bicontinuous cubic (V2), inverted hexagonal (HII), sponge (L3), fluid isotropic (L2) or micellar cubic (I2) mesophases[6,10,14-17,25-30] has been rationalized through the packing parameter (PP).[34] It defines the propensity of lipid compounds and amphiphilic lipid mixtures to form lamellar bilayer or curved membrane structures as a function of their molecular shapes.[12,14-16,28,34] Amphiphilic molecules (for which the molecular space is dominated by a large hydrophobic volume relative to the cross-sectional area of the hydrophilic head group) are characterized by a packing parameter (PP) higher than 1 and tend to form inverse phases.[10,30,34] Examples of nonlamellar phases include bicontinuous cubic, inverted hexagonal and sponge structures.[10,15,28-30,35-40] Various additives and environment conditions may induce phase transitions between these supramolecular architectures.[10,23-28,40-43]

Dispersion of nonlamellar LLC assemblies in excess water (via high-energy fragmentation involving ultrasonication, microfluidization, and homogenization methods) yields liquid crystalline nanoparticles (LCNPs).[6,11-14,16-25,27-31] Lipid nanoparticles derived from bicontinuous cubic phases, called cubosomes, have much higher surface area per volume than micellar and lamellar structures.[6,14,16,23] This feature is advantageous for improving the bioavailability of encapsulated hydrophobic, hydrophilic or amphiphilic compounds.[19] Cubosomes are being intensively studied for development of drug delivery carriers with anti-inflammatory, antimicrobial, antiviral, anticancer, neuroprotective and anti-dementia activities through different kinds of administration routes (oral, intranasal, transdermal, ophthalmic, or mucosal) as well as for protection of food ingredients.[13,18-29] The monoglyceride lipid monoolein (MO or glycerol monooleate) (Fig. 1A) is one of the key lyotropic lipids suitable for the sustainable development of liquid crystalline delivery systems.[5,9-13,20] It is a nonlamellar lipid which is nontoxic, biodegradable and biocompatible material, classified as GRAS (generally recognized as safe).[13,30]

The purpose of the present work is to design and prepare, by environmentally friendly green process, mixed amphiphilic assemblies favoring stable cubic phase formation in curcumin-loaded PEGylated MO-based lipid systems for inclusion of high ω-3 polyunsaturated fatty acids (PUFA)-fish oil amounts. The rationale of the study considers that such safe lipid systems can solubilize molecules for various multi-targeted applications in combination therapy. The choice of co-encapsulation of curcumin and PUFA-fish oil in the same carrier is motivated by the purpose to achieve combined bimodal or multiple effects of the nanoformulations. First, curcumin (CU) is a natural plant-based multipurpose compound with antioxidant, antiviral, antibacterial, antifungal, anti-proliferative, anticancer, anti-inflammatory, neuroprotective and cardioprotective activities.[44-60] This phytochemical agent receives growing attention as health-promoting nutraceutical and multipurpose pharmaceutical product because of its safe profile with low side effects.[50-56] The major challenge is that CU has very low water solubility and low bioavailability. Moreover, CU can be chemically unstable depending on the

environment (pH, light, …), which may cause a loss of biological activity and hampering its use as a free compound.[57] Studies have indicated that the CU bioavailability may be increased upon mixing with oils and amphiphilic lipids.[60-63] For this reason, we choose to encapsulate CU in green lipid-based self-assembled systems.

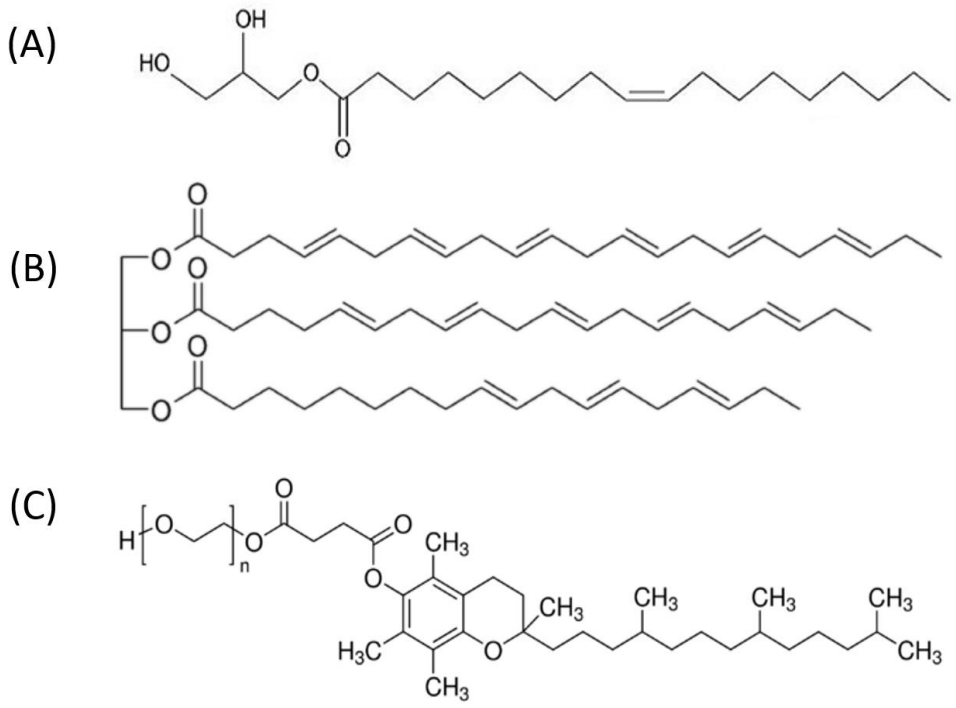

Figure 1. Chemical structures of the lipid components used for fabrication of green liquid crystalline nanocarriers: **(A)** Nonlamellar lipid monoolein (MO); **(B)** General formula of triacylglycerol indicating the presence of ω-3 PUFA chains [e.g. docosahexaenoic acid (DHA; 22:6 n-3) and eicosapentaenoic acid (EPA; 20:5 n-3) chains] in fish oil (FO); and **(C)** PEGylated amphiphilic stabilizer D-α-tocopheryl-poly(ethylene glycol)1000 (TPGS-PEG_{1000}).

Second, fish oil (FO) is chosen as a cost-effective natural source of ω -3 PUFAs. It is attractive for nanomedicine and nutraceutical development owing to its numerous beneficial health effects.[64] FO is rich in eicosapentaenoic (EPA) and docosahexaenoic (DHA) acids, which are ω -3 PUFAs with important preventive health applications against inflammation, infection, hypertension, asthma, cardiovascular disorders, cancer and neurodegenerative diseases.[65-81] It should be noted that humans cannot synthesize PUFAs nor produce precursors of essential

fatty acids (e.g. α-linolenic acid).[64] In the absence of previously published structural phase diagrams of PUFA-encapsulating lyotropic liquid crystalline self-assembled systems, FO, EPA, and DHA have been mostly formulated in nanoemulsions or in oil-in-water emulsions for oral supplementation.[82-88] We consider that these lipophilic substances can be incorporated into synthetic liquid crystalline structures towards enhanced solubility and improved oxidative stability.[89-97] It should be noted that ω-3 PUFAs are mainly present in the form of triacylglycerides in FO (Fig. 1B).[83] The possible use of ω-3 PUFA monoglycerides as major lipid constituents in the development of liquid crystalline nanoparticles (LCNPs) for the delivery of nutraceuticals, therapeutic agents, or their combinations has recently been discussed.[67-71,92,95]

In this work, we conceived and produced lipid-based nanocarriers with dual loading of curcumin and fish oil via a composition-tuning self-assembly methodology.[15] The amphiphilic compositions with dual CU and FO loading were designated by the phase diagram shown in Figure 2. The preparations involve a constant fraction of D-α-tocopheryl poly(ethylene glycol)1000 succinate (TPGS-PEG_{1000}) (Fig. 1C). The role of this vitamin E-derived PEGylated amphiphile is to facilitate the dispersion of stable lipid nanoparticles in diluted aqueous formulations (see the water-rich region marked in yellow color in Figure 2). Our choice of the MO/FO/CU/TPGS-PEG_{1000} mixed systems is further motivated by the fact that these amphiphilic compositions may serve for large scale cost-effective production of lipid nanoparticles and bulk phase LC formulations for supportive treatments and preventive health applications. The aqueous phase contained 5 wt% D(+)-glucose, a concentration that would be suitable for in vivo delivery applications or for cryopreservation of the studied formulations. The structural and morphological features of the generated liquid crystalline mesophases and lipid nanoparticles were investigated by means of synchrotron small-angle X-ray scattering (SAXS), cryogenic transmission electron microscopy (cryo-TEM) and quasi-elastic light scattering (QELS). The SAXS experiments were performed at room temperature and after that the temperature effect on the structural organization was examined under conditioning at temperature 5 °C. Considering that both the natural plant-based compound curcumin and the

marine-derived PUFAs are sensible to degradation in oxidizing media, it can be expected that the phytochemical antioxidant (CU) may exert protective action on the fish oil in the dual-loaded formulations in terms of oxidative stability.[81,84] Owing to its hydrophobic nature, curcumin can be protected from expose to oxidizing environment upon its incorporation in the lipid bilayers of the created multicompartment nanocarriers.

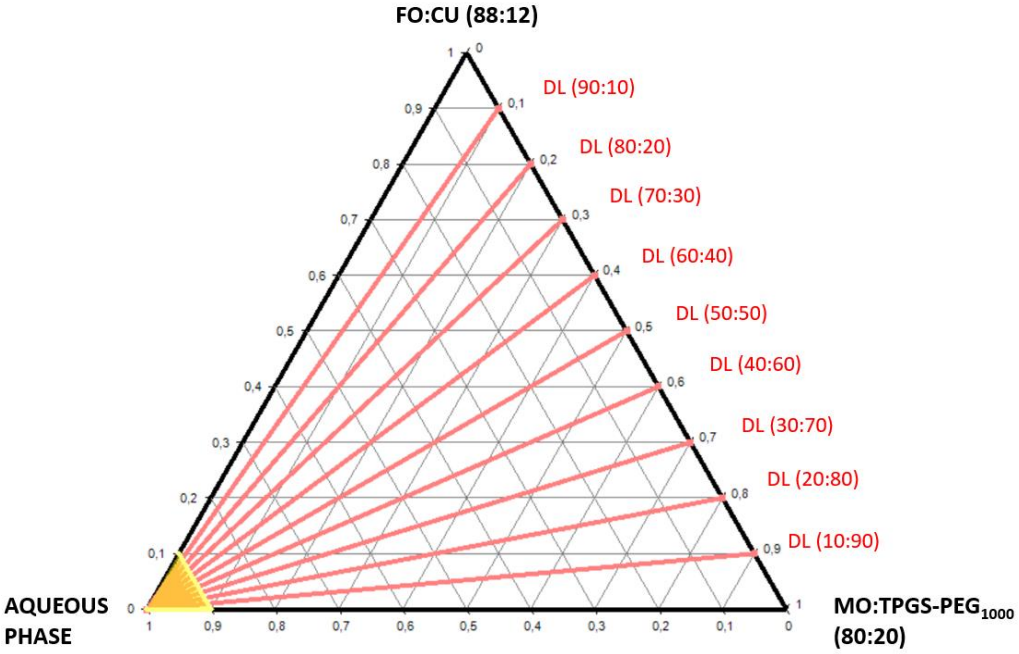

Figure 2. Phase diagram employed for designation of ten dilution lines for preparation of liquid crystalline nanocarriers composed of monoolein (MO), TPGS-PEG_{1000} amphiphile, fish oil (FO), curcumin (CU), and aqueous phase containing D-(+)-glucose (5 wt%). The lipid/co-lipid [MO:TPGS-PEG1000] and bioactive ingredients [FO:CU] weight ratios are kept constant at 80:20 and 88:12 (w/w%) respectively. The water-rich region, serving for lipid nanoparticles dispersion, is represented by a yellow triangle. Experimental synchrotron small-angle X-ray scattering (SAXS) data were acquired for multiple compositions along the dilution lines drawn in red. For every composition studied, five measurements were averaged at two positions of the X-ray beam along the height of the samples sealed in capillaries.

2) Materials and methods

a. Materials

Monoolein (MO) (purity > 99%) was obtained from Hampton Research. Fish oil from menhaden (crude source of ω-3 fatty acids), D-α-tocopheryl poly(ethylene glycol)1000 succinate (TPGS-PEG_{1000}), curcumin (purity > 66% in the curcuminoid mixture), and D-(+)-glucose (dextrose, purity ≥ 99.5%) were purchased from Sigma-Aldrich.

b. Design of self-assembled nanocarriers for loading of fish oil and curcumin

The compositions of the investigated self-assembled MO/TPGS-PEG_{1000}/FO/CU systems are chosen from the phase diagram presented in Figure 2. Ten dilution lines (DL), denoted as DL 10:90, DL 20:80, DL 30:70, DL 40:60, DL 50:50, DL 60:40, DL 70:30, DL 80:20 and DL 90:10 (w/w %), are defined in order to characterize the lyotropic behavior of the multicomponent amphiphilic mixtures of therapeutic significance. The water-rich region corresponds to dispersions of nanocarriers in excess aqueous medium. The lipid-rich region corresponds to bulk liquid crystalline assemblies. About 200 samples were prepared for SAXS measurements. The quantity of MO was minimum 10 mg per sample. Depending on the hydration level, the volume of the aqueous phase varied from 0.01 mL to 1 mL for the different sample preparations.

c. Preparation of bulk and dispersed liquid crystalline systems

The lipid nanoparticles were prepared by the method of hydration of a lyophilized thin lipid film followed by physical agitation in excess aqueous phase.[9,28,34,43,59] The lipid monoolein (MO), the amphiphilic stabilizer TPGS-PEG_{1000}, fish oil (FO), and curcumin (CU) were weighed, dissolved in chloroform, and mixed at desired proportions. The samples were prepared at room temperature at ten different fish oil/monoolein weight ratios of 10:90, 20:80, 30:70, 40:60, 50:50, 60:40, 70:30, 80:20, and 90:10 (w/w %). The solvent was evaporated under a stream of a nitrogen gas for 1 h at room temperature to create a thin film lipid sample.

The samples were lyophilized overnight under cooling to remove the excess solvent. This step was followed by the hydration of the thin film samples by a solution of D(+)-glucose (5 wt %) (prepared using Milli-Q water) for 24 h at room temperature. Finally, the samples were vortexed vigorously at room temperature in cycles during 15 min.

d. Synchrotron small angle X-ray scattering (SAXS)

Characterization of the lyotropic liquid crystalline structures was performed using SAXS experiments at the SWING beamline of synchrotron SOLEIL (Saint Aubin, France).[106] The sample-to-detector distance was 3 m. The patterns were recorded with a two-dimensional EigerX 4-M detector (DECTRIS Ltd.) at 12 keV, allowing measurements in the q-range from 0.00426 to 0.37 Å−1. The q-vector was defined as $q = (4\pi/\lambda) \sin \theta$, where 2θ is the scattering angle. The synchrotron radiation wavelength was $\lambda = 1.033$ Å. The q-range calibration was done using a standard sample of silver behenate ($d = 58.38$ Å). The temperature was 22 °C. The investigated samples were filled in capillaries with a diameter of 1.5 mm and were sealed by paraffin wax. They were oriented in front of the X-ray beam (25 × 375 μm^2) using a designed holder for multiple capillaries positioning (X, Y, Z). Exposure times of 500 ms (for bulk lipid samples) or 1 s (for diluted nanoparticles) were used. No radiation damage was observed at these exposure times. Scattering patterns of an empty capillary and a capillary filled with MilliQ water were recorded for intensity background subtraction. Data processing of the recorded 2D images was performed by the FOXTROT software.[43,102] An average of three spectra per capillary was acquired.

The lattice parameters of the liquid crystalline phases were derived from the Bragg peaks detected in the X-ray diffraction patterns. The lattice parameter a is determined by $a = d\,(h^2 + k^2 + l^2)^{1/2}$ for the cubic phases, where d is defined by Bragg's law $d = 2\pi/q$ and is the repeat distance between the scattering planes. The assigned reflections were fitted through the Miller indexes according to the following relationships:

a/d = 1,2,3, … for structures with a lamellar spacing (1)

$(a/d)^2$ = 2,3, 4, 6, 8, 9, 10, 12, 14, … for the *Pn3m* space group (Diamond cubic, D) (2)

$(a/d)^2$ = 2,4, 6, 8, 10, 12, 14, 16, 18, … for the *Im3m* space group (Primitive cubic, P) (3)

$(a/d)^2$ = 6, 8, 14, 16, 20, 22, 24, 26, … for the *Ia3d* space group (Gyroid cubic, G) (4)

e. Nanoparticles size distribution

The particle size distribution was determined by means of a Nano-ZS90 device (Malvern Instruments) collecting the intensity of the scattered light at an angle of 90° with regards to the incident laser beam. The hydrodynamic diameters were determined by the software using Stoke-Einstein's relation to describe the Brownian motion of the particles. The samples were diluted to 1/10 in Milli-Q water in order to ensure Brownian motion conditions. The refractive index and viscosity of MilliQ water were equal to 1.330 and 0.8872 mPa.s, respectively. Each analysis was a result of three consecutive measurements carried out at 25 °C. The Zetasizer software produces reports about the particle size distribution expressed as QELS intensity, volume, or number size distributions. To get more insight about the studied samples, the mean hydrodynamic diameters were determined from both the intensity and volume distributions. The recorded intensity of the volume distribution indicated that the larger particles (250 – 400 nm) with inner liquid crystalline organization prevail over the population of small precursors (50 – 100 nm), which results from the sonication process.

f. Cryogenic transmission electron microscopy (cryo-TEM)

For cryo-TEM investigation, a sample droplet of 2µL was placed on a lacey carbon film covered copper grid (Science Services, Munich, Germany), which was hydrophilized by glow discharge (Solarus, Gatan, Munich, Germany) for 30 s. Most of the liquid was then removed with blotting paper, leaving a thin film stretched over the lace holes. The specimen was instantly shock frozen by rapid immersion into liquid ethane and cooled to approximately 90 K by liquid nitrogen in a temperature and humidity controlled freezing unit (Leica EMGP, Wetzlar, Germany). The temperature and humidity were monitored and kept constant in the

chamber during all sample preparation steps. The specimen was inserted into a cryo-transfer holder (CT3500, Gatan, Munich, Germany) and transferred to a Zeiss EM922 Omega energy-filtered TEM (EFTEM) instrument (Carl Zeiss Microscopy, Jena, Germany). Examinations were carried out at temperatures around 90 K. The TEM instrument was operated at an acceleration voltage of 200 kV. Zero-loss-filtered images (DE = 0 eV) were taken under reduced dose conditions (100-1000 e/nm^2). The images were recorded digitally by a bottom-mounted charge-coupled device (CCD) camera system (Ultra Scan 1000, Gatan, Munich, Germany) and combined and processed with a digital imaging processing system (Digital Micrograph GMS 1.9, Gatan, Munich, Germany). The sizes of the investigated nanoparticles were in the range or below the film thickness and no deformations were observed. The images were taken very close to focus or slightly under the focus (some nanometers) due to the contrast enhancing capabilities of the in-column filter of the employed Zeiss EM922 Omega. In EFTEMs, the deep underfocused images can be totally avoided.

3) Results and discussion

a. Structural characterization of PEGylated bulk liquid crystalline systems

i. *Dependence of the Self-assembled Liquid Crystalline Structures on the Hydration Level of the PEGylated Lipid Mixtures*

Monoolein and D-α-tocopherol poly(ethylene glycol)1000 succinate were mixed in thin lipid films and assembled in aqueous phase containing D-(+)-glucose (5 wt% solution suitable for development of in vivo delivery formulations or for cryo-protection). The effect of the hydration level on the structural properties of the PEGylated blank lipid carriers was investigated at different lipid/water proportions. Synchrotron SAXS experiments were performed with MO/TPGS-PEG$_{1000}$ 80:20 (w/w%) lipid mixtures at water contents from 10 to 80 wt% at temperature 22°C. In preliminary experiments, the 80:20 weight ratio MO/TPGS-PEG$_{1000}$ was established to yield spontaneous formation of stable lipid nanoparticles upon dispersion of the self-assembled mixtures. Representative SAXS plots revealing the presence

or absence of long-range periodicity in the structure of MO/TPGS-PEG_{1000}/water liquid crystalline assemblies are presented in Figure 3. Figure 3A shows the structural results obtained at low water content (< 50 wt%) at 22°C. At 10 wt%, the SAXS pattern displays a single broad correlation peak centered at q = 0.190 Å-1 typical for lamellar precursors or onion phases.[24,52,55] The self-assembled system forms a lamellar phase with increasing water content from 20 to 40 wt%. The determined repeat spacing of the lamellar phase at 20 wt% water content (d = 3.9 nm) (Table 1) is slightly bigger than that of the lamellar precursor phase (d=3.3 nm) and progressively increases (d = 4.6 nm) at 40 wt% water content.

The structural results obtained at higher water contents (≥ 50 wt%) and temperature of 22°C (Figure 3B) revealed two kinds of cubic structures with long-range three-dimensional (3D) periodicities. They were identified by different sets of observed Bragg peaks, namely

- ✓ A bicontinuous gyroid cubic *Ia3d* phase was identified at 50–70 wt% water content. Figure 3B shows the set of Bragg peaks with q-vector positions spaced in the ratio √6: √8: √14: √16: √20: √22: √24: √26. These Bragg peaks were assigned to the (211), (220), (321), (400), (420), (332), (422), and (431) reflections of a gyroid cubic lattice Q^{IIG} (*Ia3d* space group);
- ✓ A bicontinuous double diamond cubic *Pn3m* phase was identified at 80 wt% water content. Figure 3B shows the set of Bragg peaks with q-vector positions spaced in the ratio √2: √3: √4: √6: √8: √9: √10: √11: √12: √14. The observed Bragg peaks were assigned to the (110), (111), (200), (211), (220), (221), (310), (311), and (222) reflections of a double diamond cubic lattice Q^{IID} (*Pn3m* space group). The (321) reflections were weak at ambient temperature.

The determined internal structures and repeat spacings of the studied MO/TPGS-PEG_{1000} self-assembled architectures are summarized in Table 1. The unit cell lattice parameters of the cubic structures, $a_{(Q)}$, were calculated from the reciprocal slope of the linear plots q *(Å-1)* versus $(h^2 + k^2 + l^2)^{1/2}$, where (*hkl*) are the Miller indices of the detected Bragg peaks (Eq. 5).

$$q = (2\pi/a_{(Q)})\,(h^2 + k^2 + l^2)^{1/2} \qquad (5).$$

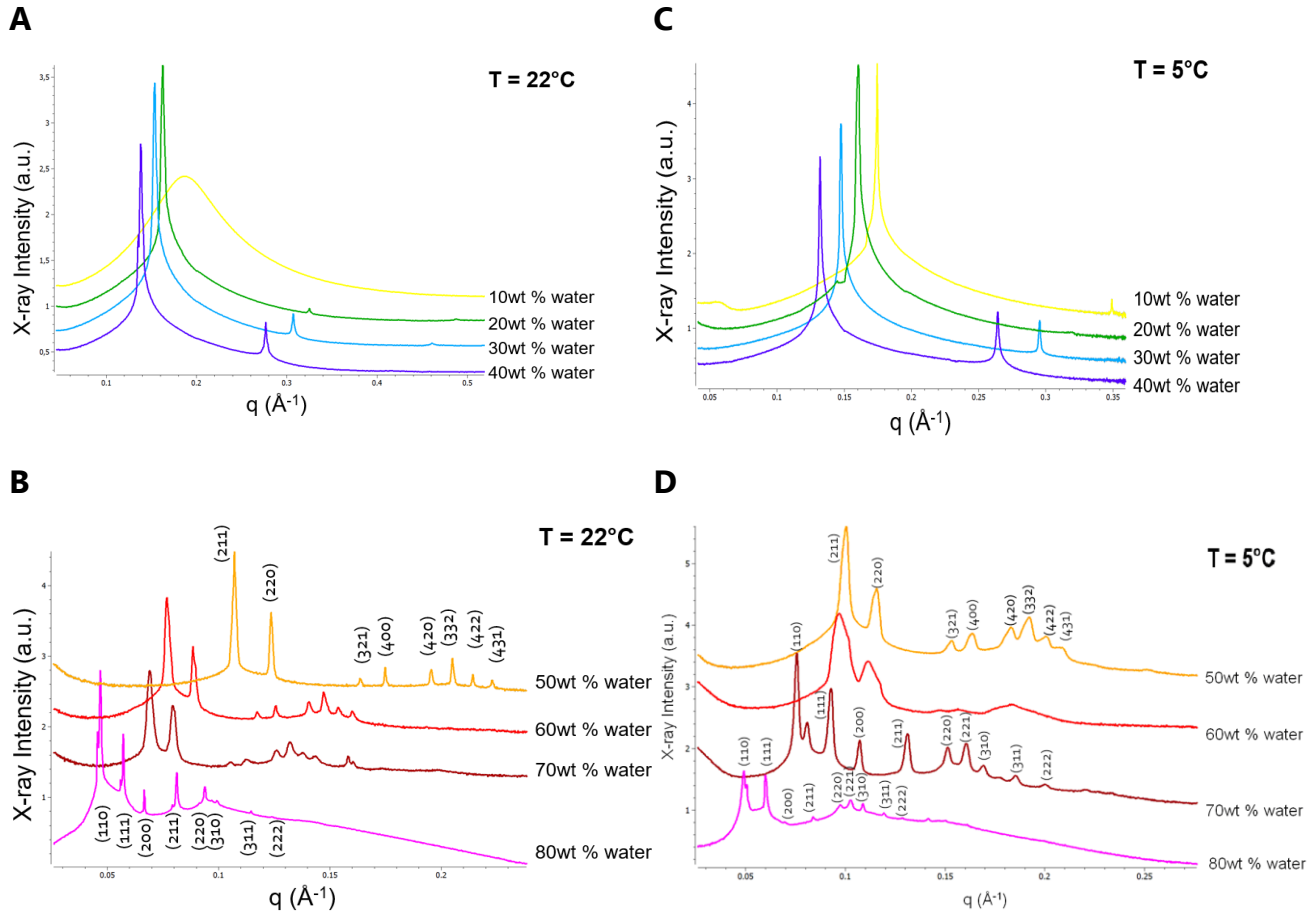

Figure 3. Representative synchrotron SAXS patterns of self-assembled MO/TPGS-PEG_{1000}/water mixtures showing the dependence of the mesophase-structure type on the varying hydration level [D-(+) glucose (5 wt%) solution] at two temperatures: 22°C (ambient condition) and 5°C (storage condition in a refrigerator). **(A)** SAXS pattern revealing the formation of a lamellar precursor phase at 10 wt% water content and a lamellar phase (Lα) at water contents from 20 wt% to 40 wt% at 22°C. **(B)** SAXS patterns displaying Bragg peaks that are indicative of formation of periodic liquid crystalline phases, namely a gyroid Ia3d cubic structure at 50-70 wt% water content and a bicontinuous double diamond *Pn3m* cubic structures at 80 wt % water content at 22°C. The Bragg peak splitting for the sample with 80 wt % water content results from uneven lipid hydration likely due to inhomogeneous mixing. **(C)** SAXS patterns corresponding to lamellar phase formation at 10-40 wt% water content at 5°C. **(D)** SAXS patterns of bicontinuous cubic liquid crystalline phases of the gyroid *Ia3d* and the double diamond *Pn3m* cubic crystallographic space groups observed at 5°C for 50-60

wt% and above 70 wt% water contents, respectively. The Bragg peak splitting for the sample with 80 wt % water content results from uneven lipid hydration likely due to inhomogeneous mixing. The aqueous phase contains D-(+)-glucose (5 wt%).

Table 1. Internal liquid crystalline structure types, repeat spacings (*d*) or cubic unit cell lattice parameters, $a_{(Q)}$, of hydrated MO/TPGS-PEG_{1000} [80:20 (w/w%)] self-assembled architectures determined by SAXS analyses of the structural data presented in Figure 3.

Water content (wt%)	**T = 22°C**		**T = 5°C**	
	LLC structures	**Repeat spacing (*d*) or Lattice $a_{(Q)}$ (nm)**	**LLC structures**	**Repeat spacing (*d*) or Lattice $a_{(Q)}$ (nm)**
10	Lamellar precursor	3.3	Lamellar	3.5
20	Lamellar	3.9	Lamellar	3.9
30	Lamellar	4.1	Lamellar	4.2
40	Lamellar	4.6	Lamellar	4.8
50	*Ia3d* cubic	14.3	*Ia3d* cubic	15.2
60	*Ia3d* cubic	19.9	Cubic intermediate	(15.2 - 16.1)
70	*Ia3d* cubic	22.2	Cubic intermediate / *Pn3m* cubic coexistence	17.9 / 11.7
80	*Pn3m* /*Pn3m* cubic coexistence	19.3 / 18.9	*Pn3m* /*Pn3m* cubic coexistence	18.4 / 18.2

The estimated cubic *Ia3d* and *Pn3m* unit cell lattice parameters are in the range of $a_{Q1(Ia3d)}$ = 14.3 - 22.2 nm and $a_{Q2(Pn3m)}$ = 18.9 - 19.3 nm, respectively. Table 1 indicates that the cubic *Ia3d* unit cell lattice parameter increases with the increase of the water content. The excess water point for the MO/TPGS-PEG_{1000} system was established to be beyond 80 wt% water content. At variance, the excess water point for the pure MO/water system has been determined to be around 60 wt% water content.[30,36,37]

It can be concluded from these SAXS results that that the PEGylation of the self-assembled monoglyceride lipid system (MO/TPGS-PEG_{1000}) requires more hydration water (with regard

to pure MO) in order for a structural transformation of the lamellar mesophase to a fully hydrated bicontinuous cubic mesophase to occur (Figs. 3A,3B). The determined cubic unit cell lattice parameter of the PEGylated lipid double-diamond type cubic phase MO/TPGS-PEG_{1000} ($a_{Q(Pn3m)}$ = 19.3 – 18.9 nm) is bigger than that of the corresponding pure MO/water cubic phase (aQ(Pn3m) = 10.5 nm).[5,15]

ii. *Effect of Low Temperature on the PEGylated Mixed Amphiphilic MO/TPGS-PEG_{1000} Liquid Crystalline Assemblies*

To investigate the effect of low storage temperature on the hydrated MO/TPGS-PEG_{1000} self-assembled mixtures, synchrotron SAXS experiments were also performed at 5°C for the same water concentrations from 10 to 80 wt%. Representative SAXS plots revealing the long-range periodicities of the hydrated MO/TPGS-PEG_{1000} assemblies at 5°C are shown in Figures 3C and 3D. Lowering the temperature down to 5°C caused the formation of lamellar structures within the range from 10 wt% to 40 wt% water contents. The cubic structures were preserved above 50 wt% water content. A cubic (*Ia3d* – *Pn3m*) phase transition was observed above 60 wt% hydration level. The bicontinuous double diamond cubic *Pn3m* phase emerged at 70 wt% hydration, whereas it was stabilized at 80 wt% water content at 22°C (Figure 3D). The SAXS pattern of the sample with 70 wt% water content was ascribed to a cubic intermediate/*Pn3m* cubic phase coexistence at 5°C (Figure 3D). The additional unassigned Bragg peak between the (110) and (111) reflections of the *Pn3m* cubic phase was attributed to a domain of a cubic phase structural intermediate. The estimated structural parameters corresponding to the cubic intermediate/*Pn3m* cubic coexistence are given in Table 1. The bicontinuous double diamond *Pn3m* cubic structure, which formed at 80 wt% water content at 5°C, displays broader Bragg peaks as compared to those recorded at temperature 22°C. This reveals decreased ordering in the mesophase organization. In our opinion, the low-temperature cubic phase should be regarded as a metastable one taking into account that its destabilization and phase transformation upon cooling appear to be retarded by the incorporation of PEGylated chains at the lipid membrane interfaces as well as by the presence

of 5 wt% D-(+)-glucose in the aqueous environment.

Indeed, the performed structural investigation with the MO/TPGS-PEG_{1000}/water system indicated the occurrence of lamellar–cubic and cubic–cubic phase transitions at higher water contents than those for the pure MO/water system. The phase diagram of the latter has been previously studied by Lutton and Caffrey et al.[36-38] The authors have constructed lipid/water phase diagrams spanning the composition region from 0 to 50 wt% aqueous phase content. At low water content (< 10 wt%), the lamellar (Lc) phase melts upon increasing temperature into an isotropic phase.[36] A phase transition to a lamellar liquid crystalline phase (Lα) takes place from 10 to 20 wt% hydration for the pure MO/water system. It melts into a L2 phase at increasing temperature. Whereas the transition to a bicontinuous cubic *Ia3d* phase begins at about 25 wt% hydration in the MO/water system, it takes place at 50 wt% hydration level in the MO/TPGS-PEG_{1000}/water system studied here. This significant structural difference between the MO/water and the MO/TPGS-PEG_{1000}/water assemblies is evidently due to the PEGylation of the lipid mixture by the TPGS-PEG_{1000} agent as the PEGylation is known to influence the mesophase stability.[40,41] In our study, the bicontinuous cubic structures were maintained in the region of 50 – 80 wt% water content. The resulting PEGylated cubic structures are of interest for the preparation of stable lipid mesophase nanoparticles by a green self-assembly process upon dilution.

b. Structural characterization of dual-loaded bulk liquid crystalline systems

i. *Modulation of the Bulk Liquid Crystalline Structures by the Hydration Level at Constant Curcumin and Fish Oil Loading in the Lipid Assemblies*

To investigate the effect of the hydration level on the structural properties of CU- and FO-loaded liquid crystalline phases, generated using the MO/TPGS-PEG_{1000} mixtures, synchrotron SAXS experiments were performed along the dilution lines drawn in Figure 2 (from 10 to 80 wt%) at 22°C. In these measurements, the FO quantity is constant with regard to MO, while the water quantity varies. The most significant changes are shown with

representative SAXS patterns in Figure 4. The associated structural transitions are summarized in Figure 6 below.

SAXS plots revealing the presence or absence of long-range periodicities in the MO/TPGS-PEG_{1000}/FO/CU/water assemblies are shown for two fixed lipid weight ratios 20:80 and 60:40 (w/w%) between fish oil and monoolein in the amphiphilic mixtures [FO:CU]/[MO:TPGS-PEG_{1000}] (Figure 4). The hydration of the two types of MO/TPGS-PEG_{1000}/FO/CU mixtures was found to induce the formation of a sponge (L3) phase at water contents below ≤ 30 wt% (see Figures 4A and 4C for the weight ratios 20:80 and 60:40 w/w%). The observed shape of the scattering curves is similar to that typical for a sponge lipid phase.[15,40] The sponge phase is a bicontinuous phase, which involves a 3D lipid bilayer membrane surrounded by two water channel networks. At variance to the bicontinuous lipid cubic phases,[15,30,39,42] the sponge phase is not periodically ordered, and it is of more fluid nature. Here, the SAXS patterns acquired at low water contents (≤ 30 wt%) were attributed to a sponge phase formation (Figures 4A and 4C).

Increase of hydration above 30 wt% led to structural transitions to precursors of cubic mesophases at 40 wt% and 50 wt % water contents (Figures 4A-4D). The SAXS patterns showed intermediate types of mesophase states and a coexistence of sponge and cubic structures at 40 to 50 wt% water contents. At high water concentrations ≥ 60 wt%, the SAXS patterns were mostly attributed to the formation of bicontinuous diamond cubic phases at both lipid weight ratios 20:80 and 60:40 (w/w). A gyroid *Ia3d* bicontinuous cubic phase was identified in the SAXS plots recorded at 60 wt% water content. This is a relatively weakly hydrated state of a bicontinuous lipid cubic phase involving lower water amount. The higher water contents > 60 wt% yielded the formation of a swollen double diamond type *Pn3m* cubic phase (D_{Large}) with a lattice parameter $a_{Q(Pn3m)}$ = 19.1 nm. The results for the determined unit lattice parameters of the bulk cubic liquid crystalline structures are summarized in Table 2. The estimated cubic *Ia3d* and *Pn3m* unit cell lattice parameters are $a_{Q1(Ia3d)}$ = 16.1 nm and $a_{Q2(Pn3m)}$ = 17.5 - 19.1 nm, respectively. The obtained data indicated that the cubic *Pn3m* unit

lattice parameter increases with the increase of the water content, which corresponds to swelling of the 3D nanochannel networks and the induction of swollen double diamond type *Pn3m* cubic phases (D_{Large}).[39,40,96]

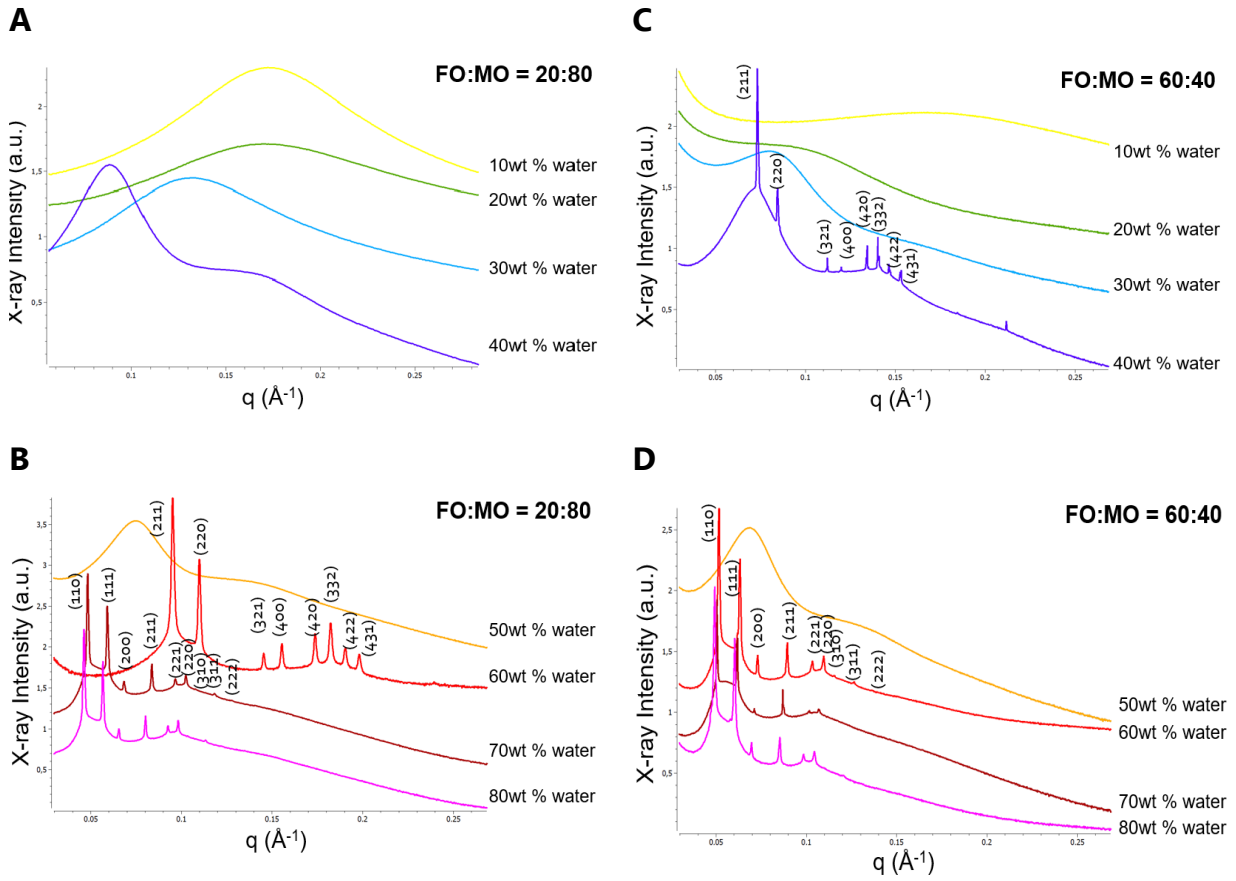

Figure 4. Representative SAXS patterns of self-assembled MO/TPGS-PEG_{1000}/FO/CU/water mixtures with weight ratios between fish oil and monoolein [FO:CU]/[MO:TPGS-PEG_{1000}] equal to 20:80 and 60:40 (w/w%) and hydration performed at 22 °C. **(A-C)** SAXS patterns corresponding to sponge phases and intermediate mesophase states at 10-40 wt% water contents. **(B-D)** The recorded Bragg peaks are indicative of the formation of bicontinuous cubic gyroid *Ia3d* or double diamond *Pn3m* cubic structures at 60-80 wt% water contents. The aqueous phase contains D-(+)-glucose (5 wt%).

Therefore, it can be deduced that the water content has a strong impact on the structural properties of the studied MO/TPGS-PEG_{1000}/FO/CU assemblies. Structural

transitions were established in the order: Sponge phase – Cubic phase precursors – Weakly hydrated gyroid *Ia3d* cubic phase – Swollen double diamond Pn3m cubic phase (D_{Large}) (Figure 4). The sponge phase and the weakly ordered cubic structures, coexisting with sponge-type membranes, were obtained at 10 – 50 wt% water contents (Figure 4). The bicontinuous cubic structures were maintained at 60 – 80 wt% water contents upon the incorporation of both bioactive ingredients fish oil and curcumin. The results in Table 2 reveal that the encapsulated FO acts towards the swelling of the bicontinuous *Pn3m* cubic phase.

Table 2. Internal liquid crystalline structure types and cubic lattice parameters, a(Q), of hydrated MO/TPGS-PEG_{1000}/FO/CU/water (5 wt% D-(+)-glucose) self-assembled systems determined by SAXS analyses of the structural data shown in Figures 4B and 4D. Temperature is 22°C.

Water content (wt%)	**[FO:CU]/[MO:TPGS-PEG_{1000}] ratio 20:80 (w/w%)**		**[FO:CU]/[MO:TPGS-PEG_{1000}] ratio 60:40 (w/w%)**	
	LLC structures	**Lattice $a_{(Q)}$ (nm)**	**LLC structures**	**Lattice $a_{(Q)}$ (nm)**
50	Sponge – cubic intermediate	-	Sponge – cubic intermediate	-
60	*Ia3d* cubic	16.1	*Ia3d* cubic	17.5
70	*Pn3m* cubic	18.5	*Pn3m* cubic	17.5
80	*Pn3m* cubic	19.1	*Pn3m* cubic	18.6

ii. *Impact of the Fish Oil/Monoolein Weight Ratio on the Bulk Liquid Crystalline Self-Assembled Structures*

To gain more insight into the impact of the fish oil content on the inner structural organization of the bulk MO/TPG-PEG_{1000}/FO/CU/water assemblies, a series of synchrotron SAXS experiments was performed with eight lipid weight ratios 10/90, 20/80, 30/70, 40/60, 50/50, 60/40, 70/30 and 80/20 (w/w%) between fish oil and monoolein at 22°C (Figure 5). The [FO:CU]/[MO:TPGS-PEG_{1000}] self-assembled lipid mixtures were hydrated by a solution of D-(+) glucose (5 wt%). Different fixed water contents were examined: (i) 30 wt% aqueous phase

representing the low water content region; (ii) intermediate 60 wt% water content region; (iii) 80 wt% high-water content region, and (iv) 95 wt% aqueous phase corresponding to the large excess water region.

The SAXS plots in Figure 5A were attributed to sponge phase formation upon incorporation of FO in the host MO lipid phase at 30 wt% water content. Previous studies of oil/MO systems yielded similar shapes of the SAXS patterns.[4,94] The SAXS curves in Figure 5A indicated that the correlation length of the sponge-phase membranes, formed at 30 wt% water content and 22°C, depends on the fish oil/monoolein (FO:MO) weight ratio. Interestingly, the SAXS pattern recorded at a lipid ratio 80:20 (w/w) shows peaks, which are characteristic of a coexistence of bicontinuous sponge and cubic *Ia3d* phases.[15,40] This coexistence is observed also at 60 wt% water content at temperature of 22°C (Fig. 5B). The coexistence of sponge and cubic phases, or the formation of a single cubic phase, were strongly dependent on the fish oil/monoolein ratio. The obtained data were used for the construction of the phase diagram of the MO/TPGS-PEG_{1000}/FO/CU/water system (see Figure 6 below).

Figure 5C presents the SAXS patterns of the samples prepared at 80 wt% water content at 22°C, which show Bragg peaks characteristic of the double diamond cubic *Pn3m* space group at all FO:MO weight ratios. The cubic unit cell lattice parameters of the examined eight systems ranged from 15.9 to 19.1 nm (Table 3). A transition state between the cubic *Pn3m* and *Im3m* structures occurred at 95 wt% water content. At 22°C, the phase transition led to the appearance of Bragg peaks with *q*-vector positions spaced in the ratio √2: √4: √6: √8: √10: √12: √14: √16: √18. These peaks were assigned to (110), (200), (211), (220), (310), (222), (321), (400) and (330) reflections of a primitive cubic lattice (Q^{IIP}) of the *Im3m* crystallographic space group. Peaks indicating a coexistence of *Pn3m* and *Im3m* cubic phase domains were observed with FO:MO ratios 10:90 and 20:80 (w/w) as well. The phase coexistences are indicated in Table 3.

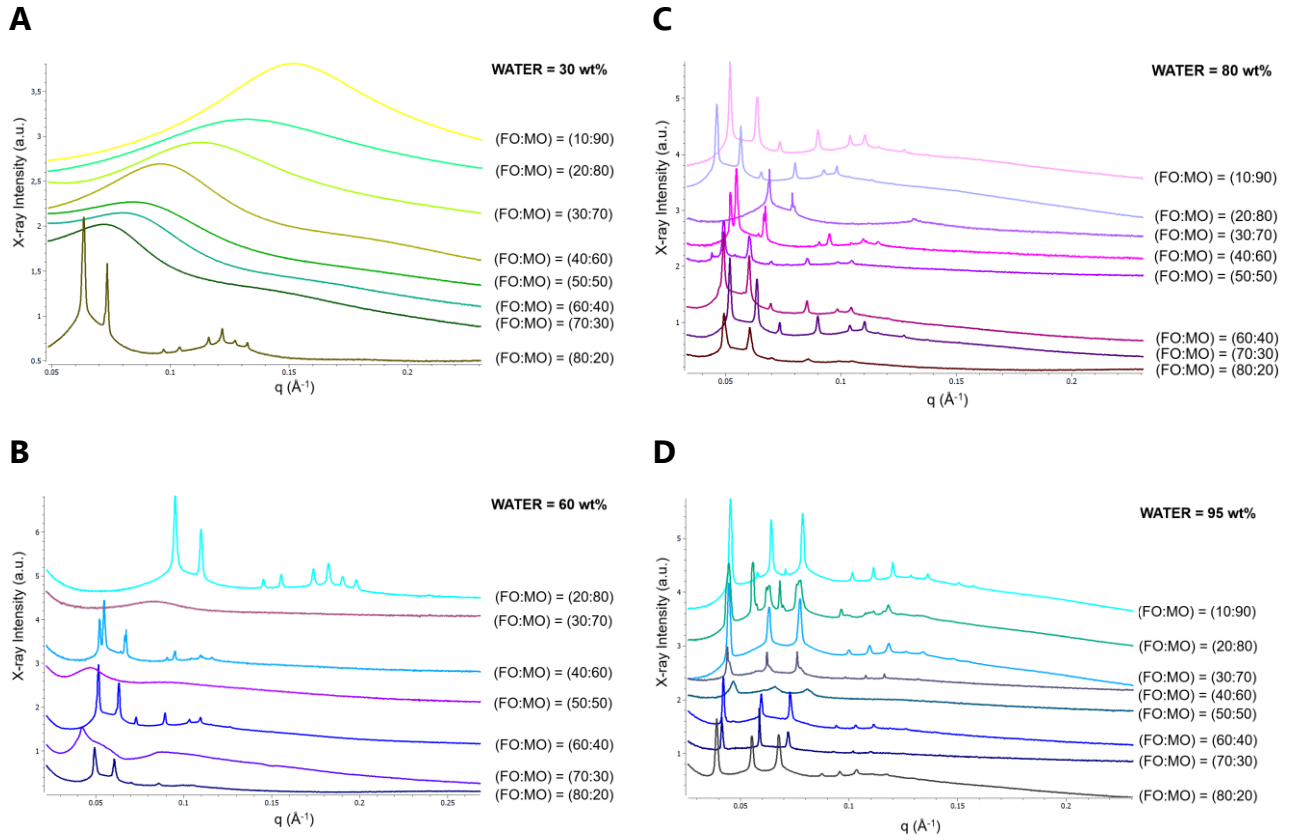

Figure 5. Representative SAXS patterns of MO/TPGS-PEG$_{1000}$/FO/CU/water self-assembled systems hydrated with a D-(+) glucose (5 wt%) solution at eight different weight ratios [FO:CU]/[MO:TPGS-PEG$_{1000}$] between fish oil and monoolein at 22 °C. **(A)** Sponge phase at 30 wt% water content for all [FO:MO] ratios except (80:20); **(B)** Sponge and cubic phases at 60 wt% water content; **(C)** Bicontinuous cubic *Pn3m* phase at 80 wt% water content, and **(D)** Primitive cubic *Im3m* phase at 95 wt% water content. The aqueous phase contains D-(+)-glucose (5 wt%).

The intermediate phase state between the cubic *Pn3m* and *Im3m* structures, and the increase of the lattice parameter determined at 80 to 95 wt% water contents, appear to be affected by the increased fraction of fish oil and curcumin under excess water conditions. Transformations dependent on the oil composition and water contents were also revealed by the shifts in the unit cell lattice parameter of the cubic *Im3m* phase in the range from 18.9 to 23.1 nm (Table 3). As the fish oil content increases, the Bragg peaks shift towards lower *q*-vector values (Fig. 5D), which evidences the increase of the cubic unit cell lattice parameters

(respectively swelling of the cubic structures). The lattice parameter is generally bigger for mixed lipid systems involving longer chain fatty acids.[98]

Table 3. Internal cubic liquid crystalline structure types and cubic unit cell lattice parameters, $a_{(Q)}$, of MO/TPGS-PEG_{1000}/FO/CU/water systems, self-assembled in excess water (5 wt% D-(+)-glucose), which were determined from SAXS analysis of the data shown in Figures 5C and 5D. Temperature is 22°C.

[FO:CU]/[MO:TPGS-PEG_{1000}] ratio (w/w %)	Water content 80 wt%		Water content 95 wt%	
	LLC structures	Lattice $a_{(Q)}$ (nm)	LLC structures	Lattice $a_{(Q)}$ (nm)
10:90	*Pn3m* cubic	17.1	*Pn3m / Im3m* cubic coexistence	*Pn3m* = 16.4, *Im3m* = 19.8
20:80	*Pn3m* cubic	19.1	*Pn3m / Im3m* cubic coexistence	Pn3m = 16.8, Im3m = 20.2
30:70	*Ia3d* cubic	22.9	*Im3m* cubic	20.2
40:60	*Pn3m* cubic	15.9 – 17.1	*Im3m* cubic	20
50:50	*Pn3m* cubic	18.6	*Im3m* cubic	18.9
60:40	*Pn3m* cubic	18.6	*Im3m* cubic	22.2
70:30	*Pn3m* cubic	17.4	*Im3m* cubic	22.8
80:20	*Pn3m* cubic	18.2	*Im3m* cubic	23.1

The results in Figure 5 indicate that at constant water content (30 wt%, 60 wt%, 80 wt%, or 95 wt%) the encapsulated quantity of FO favours the swelling of the self-assembled [FO:CU]/[MO:TPGS-PEG_{1000}] supramolecular organization. The SAXS patterns shown in Figure 5A at 30 wt% water content are similar to those in Figure 4A. The increase of the FO weight fraction at growing FO:MO ratios (from 30:70 to 70:30 (w/w)) causes the swelling of the bicontinuous sponge phase before its transformation into a bicontinuous cubic phase for FO:MO ratio 80:20 (w/w)). Under these conditions, the excess water point was not reached yet below 80 wt% water content.

The universal rationale of the effect of various additives on the mean molecular shape and mean critical packing parameter of ideal amphiphilic mixtures, and the related effects of additives on lowering the curvature of the standard cubic phase of monoglycerides, has been discussed in detail by van't Hag *et al.*[10] The investigated here fish oil (from menhaden source) is not an individual compound, which may form ideal self-assembled lipid mixtures with other lipids. For this reason, eventual CPP calculations based on the molecular shape concept, which might support the observed reduction of curvature of the host lipid cubic phase, would be of speculative character.

c. Compositional phase diagram for dual curcumin- and fish oil-loaded lyotropic liquid crystalline lipid assemblies

Figure 6 shows the phase diagram of the amphiphilic self-assembled systems composed of monoolein, MO-TPGS-PEG_{1000}, fish oil and curcumin, [FO:CU]/[MO:TPGS-PEG_{1000}]/aqueous phase of D-(+) glucose (5 wt% in MilliQ water), which was determined at 22 °C. The phase diagram was constructed using the structural SAXS analyses of the multicomponent samples prepared along the dilution lines (DL) indicated in Figure 2. A very rich phase behavior is deduced considering the various mesophases, which were identified by the SAXS measurements.

The obtained phase diagram is discussed in the series from the DL(0:100) to the DL(90:10) dilution line. At high monoglyceride (MO) lipid and low water contents, a small region of a lamellar precursor phase is observed. With increasing water content up to 40 wt%, a lamellar Lα phase is obtained along the DL(0:100) dilution line (blue area in Figure 6). The formation of sponge phases occurs at compositions belonging to the other dilution lines (green domain in Figure 6) at increasing [FO:CU] content, but at low water contents (ranging from 10 to 40 wt%). At higher water contents from 40 to 60 wt%, the formation of a bicontinuous cubic phase (*Ia3d* space group) occurs along the DL(10:90), DL(20:80), DL(60:40), DL(70:30) and DL(80:20) dilution lines at decreasing [MO:TPGS-PEG*1000*] fractions. In the intermediate regions, the bicontinuous cubic phase (*Ia3d* space group) coexists with a sponge phase

(yellow areas in Fig. 6). The decrease of the fish oil content allows the formation of a bicontinuous cubic *Pn3m* phase in the high-water content region from 70 – 90 wt% (orange domain in Fig. 6). The formation of the primitive cubic *Im3m* phase is observed in large excess of water and low oil content (pink area in Fig. 6).

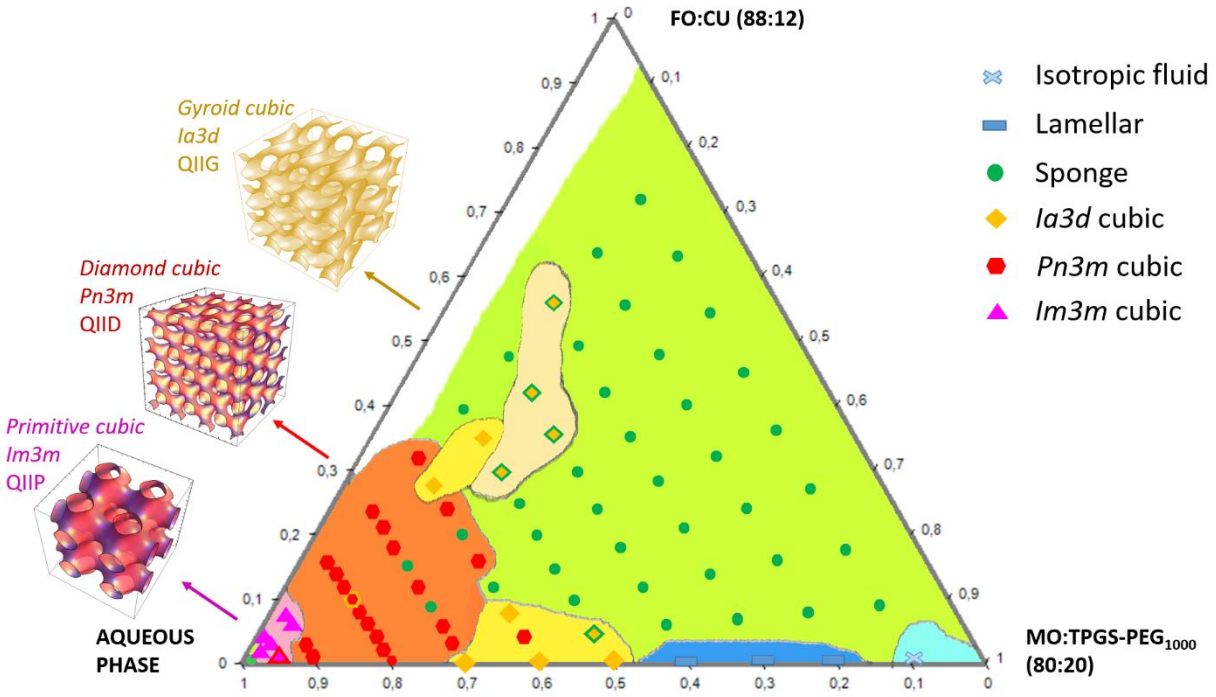

Figure 6: Ternary phase diagram of the MO/TPGS-PEG_{1000}/FO/CU/water system at temperature 22°C displaying the lipid compositional regions that yield cubic liquid crystalline phases of 3D topologies (cubic *Im3m*, cubic *Pn3m*, and cubic *Ia3d* space groups) as well as sponge and lamellar phases. The aqueous medium contains D-(+)-glucose (5 wt%). The shedding indicates the compositions with *Im3m* primitive cubic structure (pink), *Pn3m* double diamond cubic structure (red/orange), *Ia3d* gyroid cubic structure (yellow/beige), sponge (light green), lamellar (blue), and lamellar precursor (light blue) phases. The two-color symbols denote coexistences of mixed liquid crystalline phases.

For the investigated large number of samples below the excess water point, experimental drawbacks related to sample mixing/inhomogeneity, led to the observation of slightly anomalous phase behaviour of isolated samples. Sponge phase architecture (lacking long-

range order of the bicontinuous lipid membranes) was attributed to these samples in the absence of well-defined Bragg diffraction peaks in the SAXS patterns. The isolated samples lacking long-range order, which are noticed in the red/orange and yellow/beige regions in the phase diagram (Figure 6), can be regarded also as cubic phase precursors.

d. Structural and morphological characterization of dispersed liquid crystalline lipid nanoparticles by synchrotron SAXS and cryo-TEM imaging

Dispersing of the bulk lyotropic phases, facilitated by the PEGylated amphiphile TPGS-PEG_{1000} and mechanical agitation, produces liquid crystalline lipid nanoparticles with inner self-assembled structures (called cubosomes, spongosomes, hexosomes or liposomes) in excess aqueous medium.[6,9,11,28,42] We prepared aqueous dispersions of liquid crystalline lipid nanoparticles at eight weight ratios 25/75, 30/70, 40/60, 50/50, 60/40, 70/30, 80/20 and 90/10 (w/w %) between fish oil and monoolein [FO:CU]/[MO:TPGS-PEG_{1000}] at 95-99 wt% water contents. The SAXS patterns of the dispersed MO/TPGS-PEG_{1000}/FO/CU lipid particles, containing low fractions of fish oil, displayed Bragg reflections of an inner primitive cubic lattice structure (*Im3m* space group) (Fig. 7A). The structural parameters determined by the SAXS analysis are presented in Table 4. In agreement with the SAXS data (Fig. 7A), the cryo-TEM images revealed the formation of cubosome type lipid nanoparticles (Fig. 7C). The SAXS patterns of the dispersed MO/TPGS-PEG_{1000}/FO/CU mixtures, which are rich in fish oil, showed scattering curves typical for bicontinuous sponge membranes with no periodic organization (Fig. 7B). The cryo-TEM images revealed the topology of the cubosome and spongosome nanoparticles loaded by high amounts of fish oil and phytochemical antioxidant (Fig. 7C and 7D).

The variety of lipid nanoparticle morphologies, which were present in the studied PEGylated lipid dispersions loaded with fish oil and phytochemical antioxidant are visualized in Fig. 7C-7E. They include monoolein-based cubosome and spongosome nanoparticles, double membrane vesicles, and vesicular precursors of bicontinuous liquid crystalline phases. The size distribution of the fish oil and curcumin-loaded cubosome and spongosome

nanoparticles was studied by quasi-elastic light scattering (QELS) (Table 5). The results show the presence of two main populations, which represent the cubosome and spongosome nanoparticles (with mean hydrodynamic diameters of about 250 nm – 450 nm) and their precursors (with hydrodynamic diameters of about 100 nm) (Table 5).

A cryo-TEM image of liquid crystalline lipid nanoparticles with dual-encapsulated bioactive ingredients is shown in Figure 7F. Lipid-based cubosomes and spongosomes involve multiple internal compartments, which represent a structural advantage enabling the encapsulation efficacy.[5-8,11-13,19-27,33] It has been suggested that encapsulated curcumin may increase the negative curvature of the polar/apolar interfaces of the lipid nano-assemblies and therefore may stabilize the cubic structure formation.[43]

Table 4. Internal cubic liquid crystalline structure type and unit cell lattice parameters of [FO:CU]/[MO:TPGS-PEG$_{1000}$] self-assembled lipid nanoparticles dispersed in 95-99 wt% aqueous environment determined by structural SAXS analysis of the data shown in Figure 7A.

[FO:CU]/[MO:TPGS-PEG$_{1000}$] ratio (w/w%)	**LLC structures**	**Lattice a$_{(Q)}$ (nm)**
50/50	*Im3m* cubic	19.7
30/70	*Im3m* cubic	20.6
25/75	*Im3m cubic*	20.6

A

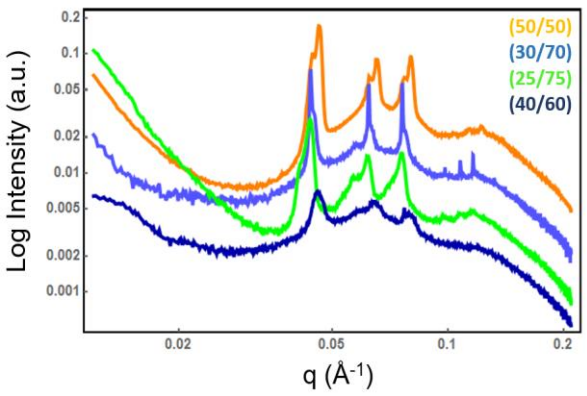

B

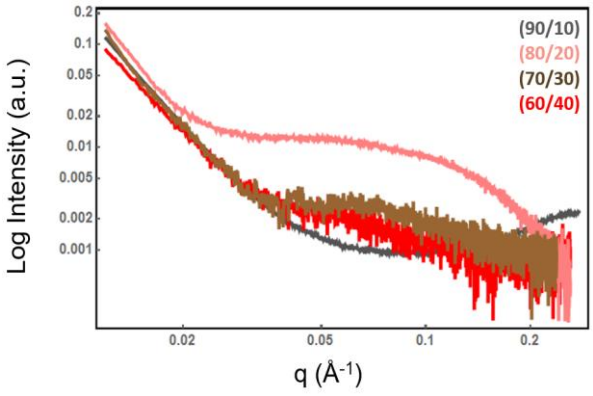

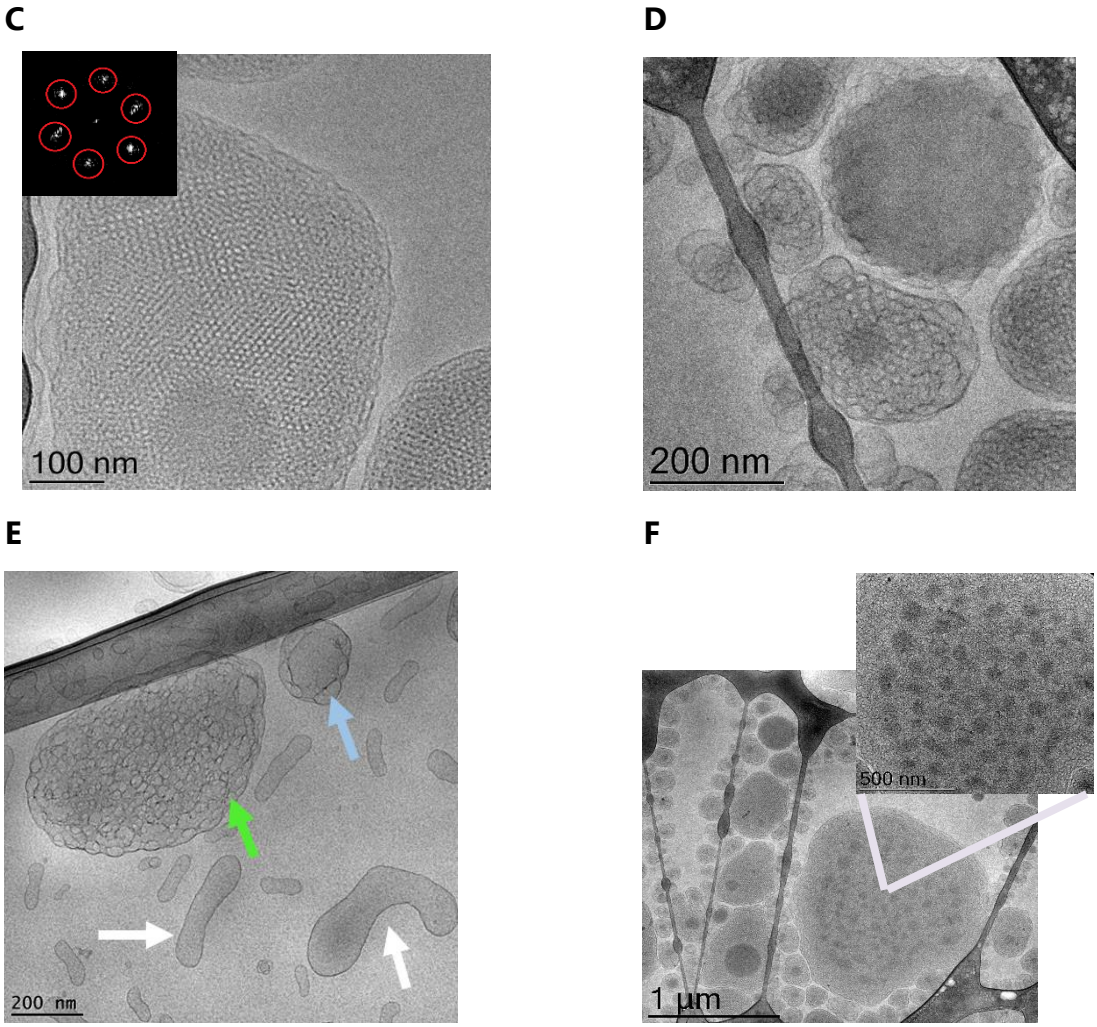

Figure 7: (A-B) SAXS patterns of liquid crystalline lipid nanoparticle dispersions obtained at varying fish oil/monoolein ratios [FO:CU]/[MO:TPGS-PEG$_{1000}$] (w/w%) at 22°C. **(C-F)** Cryo-TEM images of dispersed mixed assemblies showing **(C)** Cubosomal architectures with inner oil-rich domains. The inset shows the fast Fourier transform (FFT) of the image, which confirms the presence of cubic liquid crystalline organization in the inner structure of the lipid-based nanoparticles; **(D)** High oil-loaded sponge nanocarriers; **(E)** Double bilayer membrane containers (white arrows) in a coexistence with unilamellar vesicle precursors (blue arrow) as well as spongosome nanoparticles (green arrow); **(F)** Liquid crystalline lipid nanoparticles with encapsulated phytochemical antioxidant and fish oil. Inset: Magnified area showing the inner nanodomain organization of the dual-loaded lipid nanoparticles.

Table 5. Hydrodynamic size determination of dual fish oil- and curcumin-loaded cubosome liquid crystalline lipid nanoparticles in excess aqueous phase (98 wt%) by quasi-elastic light scattering (QELS).

[FO:CU]/[MO:TPGS-PEG_{1000}] ratio (w/w %)	Mean hydrodynamic particle diameter by intensity distribution (nm)	Mean hydrodynamic particle diameter by volume distribution (nm)
0/100	51 – 255	79 – 295
20/80	106 – 255	106 – 220
40/60	122 – 395	106 – 395
50/50	106 – 396	106 – 460

Controlled delivery of multiple active compounds is required for various pharmaceutical and nutraceutical applications. The overall efficacies of the obtained formulations will be an outcome of the encapsulation and release properties of the nanocarriers. Whereas the multicompartment structure of the lipidic cubosome and spongosome nanoparticles is advantageous for the enhanced encapsulation of bioactive molecules, the retention of the entrapped molecules and the multiple drug release could be hampered by the compartmentalized nanoparticle structure. In addition, drug release may trigger structural changes in the supramolecular organization of the nanocarriers. Therefore, future work should be envisioned to study the modulation of the release profiles through the multicompartment liquid crystalline lipid nanoparticle organization at varying multicomponent compositions.

Regarding the potential applications of the investigated dual-loaded nanoscale liquid crystalline lipid systems, various research directions may be envisioned towards new therapeutics or nutraceutics strategies. First, cubosomal curcumin has been suggested as an emergent opportunity for therapeutic innovation.[43,55,60] As a multipurpose drug, the natural phytochemical curcumin displays antiviral, anti-proliferative, antioxidant, and neuroprotective

activities.[49,51] In addition, it can boost the PUFAs effects in strategies for prevention of disease progression through the use of nutraceutical formulations.[58,62]

Second, the class of polyunsaturated fatty acids (PUFAs) involves antiviral lipid molecules that may inactivate envelope viruses and inhibit coronavirus proliferation. The antiviral properties of naturally occurring fatty acids and their monoglycerides have been recognized since long time.[99,100] However, the fact that monoglycerides may display equal capacity for viral inactivation, at 5 to 10 times lower concentrations than their corresponding fatty acids,[99,100] has scarcely been exploited for clinical applications. Recently, lipid-targeted treatment of virus-infected cells has been suggested as a strategy for human Severe Acute Respiratory Syndrome Coronavirus (SARS-CoV-2) inhibition.[101] Lipid-based nanoparticles are under advanced development as carriers for vaccine production to prevent the SARS-CoV-2 infection.[102-105] The capacity of rapid safety evaluation and regulatory validation of controlled-release delivery carriers of anti-coronavirus drugs and new vaccines makes the lipid-based nanotechnology a universal platform for advancement of the anti-SARS-CoV-2 research among other therapeutic applications.[102,105]

Third, lipid nanoparticles loaded with natural phytochemical antioxidants represent strong interest for development of new treatments of neurodegenerative diseases.[7,9,59,60,91]
Taking into account that the pharmacological and therapeutic potential of marine-derived omega-3 polyunsaturated fatty acids and their clinical relevance are well underlined,[47,73,79,91] ω-3 PUFAs could be used to impart synergistic effect in dual-loaded formulations.

Considering that the recognized antiviral activity of monoglycerides has not been exploited in the clinic yet, the reported here tunable 2D and 3D nanoscale topologies may serve as a platform for rapid development of (i) antiviral drug delivery systems and vaccine excipients, (ii) lipid-based formulations for multitarget therapies, and (iii) natural adjunctive therapeutics for various health applications using phytochemical antioxidants in combination therapies of inflammatory, cardiovascular and neurodegenerative diseases; and (iv) novel

nutraceutical formulations involving natural plant-based antioxidant substances and marine-derived ω-3 PUFAs. Therefore, the obtained here new knowledge about the PEGylated liquid crystalline nanostructured assemblies should contribute to fabrication of more stable and safe multicomponent green delivery systems.

4) Conclusion

Sustainable development of modern multi-targeted nutraceuticals and pharmaceuticals against various severe diseases, including viral infections, inflammation, neurodegenerative and cardio-vascular disorders, requires novel structural knowledge about phase diagrams enabling the preparation of switchable liquid crystalline nanocarriers of advanced properties. Solubility, encapsulation and enhanced loading of bioactive phytochemicals and natural functional lipids are major issues in the design of innovative delivery formulations with increased bioavailability. In the context of preventive and supportive therapies using combinations with nutraceuticals, natural plant-based antioxidant compounds, such as curcumin, and marine-derived (fish-oil) PUFAs can boost the effects of the co-administered active compounds and drugs in various antiviral, cardiovascular or neurodegenerative targeting mechanisms.

We designed PEGylated dual-loaded liquid crystalline (cubosome and spongosome) lipid nanoparticle formulations suitable for large-scale cost-effective production. They contain natural antiviral compounds and can serve for encapsulation of additional hydrophobic or hydrophilic active substances to target various disease mechanisms. Thus, the obtained nanoscale cubosome and spongosome type carrier systems should be of interest for multi-compound loading. The reported structural results revealed that loading with fish oil leads to a composition-mediated switch between different liquid crystalline nanostructures. Interestingly, a metastable low-temperature cubic phase was observed with bulk PEGylated assemblies prepared with 5 wt% D-(+)-glucose aqueous medium. The multicompartment crystalline organization may impact the mechanical and release properties of the delivery carriers.

The constructed phase diagram characterizes various polymorphic states at different hydration levels. Based on the presented SAXS results, PEGylated multi-loaded sustained release formulations can quickly be developed. In fact, deeper understanding of the structure and phase behavior of mixed pharmaceutical compositions is a key to greatly enhancing the success rate of the drug delivery strategies. Evaluating the stability of the hydrated structures is particularly important because changes in the hydration state may cause alterations of the physicochemical properties of the carrier systems. The acquired knowledge about the PEGylated mixed polymorphic liquid crystalline assemblies and structures may contribute for improving the outcome of combination treatments as well as of the development of vaccine carriers.

5) References

(1) Chen, X.; Yi, Z.; Chen, G.; Ma, X.; Su, W.; Deng, Z.; Ma, L.; Tong, Q.; Ran, Y.; Xudong Li, X. Carrier-Enhanced Photodynamic Cancer Therapy of Self-Assembled Green Tea Polyphenol-Based Nanoformulations. *ACS Sustainable Chem. Eng.* **2020***, 8*, 43, 16372–16384.

(2) Clemente, I.; Falsini, S.; Di Cola, E.; Fadda, G.C.; Gonnelli, C.; Spinozzi, F.; Bacia-Verloop, M.; Grillo, I.; Ristori, S. Green Nanovectors for Phytodrug Delivery: In-Depth Structural and Morphological Characterization. *ACS Sustainable Chem. Eng.* **2019**, *7*, 12838-12846.

(3) Elabbadi, A.; Jerri, H.A.; Ouali, L.; Erni, P. Sustainable Delivery Systems: Retention of Model Volatile Oils Trapped on Hybrid Calcium Carbonate Microparticles. *ACS Sustainable Chem. Eng.* **2015**, *3*, 9, 2178-2186.

(4) Glatter, O.; Salentinig, S. Inverting Structures: From Micelles via Emulsions to Internally Self-assembled Water- and Oil-Continuous Nanocarriers. *Curr. Opinion Colloid Interface Sci.* **2020**, 49, 82-93.

(5) Angelova, A.; Angelov, B.; Mutafchieva, R.; Lesieur, S.; Couvreur, P. Self-Assembled Multicompartment Liquid Crystalline Lipid Carriers for Protein, Peptide, and Nucleic Acid Drug Delivery. *Acc Chem Res* **2011**, 44,147–56.

(6) Alfredsson, V.; Lo Nostro, P.; Ninham, B.; Nylander, T. Morphologies and structure of brain lipid membrane dispersions. *Front. Cell Dev. Biol*. **2021**, *9*, 675140.

(7) Angelova, A.; Angelov, B. Dual and multi-drug delivery nanoparticles towards neuronal survival and synaptic repair. *Neural Regeneration Res*. **2017**, 12, 886-889.

(8) Yaghmur, A.; Mu, H. Recent advances in drug delivery applications of cubosomes, hexosomes, and solid lipid nanoparticles. *Acta Pharmaceutica Sinica B* **2021***, 11*, 871-885.

(9) Angelova, A.; Drechsler, M.; Garamus, V.M.; Angelov, B. Pep-lipid cubosomes and vesicles compartmentalized by micelles from self-assembly of multiple neuroprotective building blocks including a large peptide hormone PACAP-DHA. *ChemNanoMat* **2019**, 5, 1381-1389.

(10) van't Hag, L.; Gras, S.L.; Conn, C.E.; Drummond, C.J. Lyotropic liquid crystal engineering moving beyond binary compositional space - ordered nanostructured amphiphile self-assembly materials by design. *Chem. Soc. Rev.* **2017***, 46*, 2705-2731.

(11) Angelova, A.; Garamus, V.M.; Angelov, B.; Tian, Z.; Li, Y.; Zou, A. Advances in structural design of lipid-based nanoparticle carriers for delivery of macromolecular drugs, phytochemicals and anti-tumor agents. *Adv. Colloid Interface Sci.* **2017**, 249, 331–345.

(12) Yaghmur, A.; Tran, B.V.; Moghimi, S.M. Non-Lamellar Liquid Crystalline Nanocarriers for Thymoquinone Encapsulation. *Molecules* **2019**, 25, 16.

(13) Kulkarni, C.V. ; Vishwapathi, V.K.; Quarshie, A.; Moinuddin, Z.; Page, J. ; Kendrekar, P.; Mashele, S.S. Self-assembled lipid cubic phase and cubosomes for the delivery of a model drug (aspirin). *Langmuir*, **2017**, *33*, 9907-9915.

(14) Chang, D.P.; Barauskas, J.; Dabkowska, A.P.; Wadsäter, M.; Tiberg, F.; Nylander, T. Non-lamellar lipid liquid crystalline structures at interfaces. *Adv Colloid Interface Sci.* **2015**, 222, 135-147.

(15) Angelov, B.; Angelova, A.; Mutafchieva, R.; Lesieur, S.; Vainio, U.; Garamus, V.M.; Jensena, G.V.; Pedersena, J.S. SAXS investigation of a cubic to a sponge (L-3) phase transition in self-assembled lipid nanocarriers. *Phys. Chem. Chem. Phys*. **2011**, 13, 3073–3081.

(16) Mertins, O.; Mathews, P.D.; Angelova, A. Advances in the Design of pH-Sensitive Cubosome Liquid Crystalline Nanocarriers for Drug Delivery Applications. *Nanomaterials (Basel).* **2020**, 10, 963.

(17) Pilkington, C.P.; Seddon, J.M.; Elani, Y. Microfluidic technologies for the synthesis and manipulation of biomimetic membranous nano-assemblies. *Physical Chemistry Chemical Physics* **2021***, 23*, 3693-3706.

(18) Tan, A.; Lam, Y.Y.; Sun, X; Boyd, B. Monocytic Cell-Induced Phase Transformation of Circulating Lipid-Based Liquid Crystalline Nanosystems. *Materials (Basel).* **2020,** 13, 1013.

(19) Yaghmur, A. Nanoencapsulation of food ingredients by cubosomes and hexosomes, in *Lipid-Based Nanostructures for Food Encapsulation Purposes*. Ed. S. M. Jafari, Elsevier Book Series, London, **2019**, 483–522.

(20) Boge, L.; Hallstensson, K.; Ringstad, L.; Johansson, J.; Andersson, T.; Davoudi, M.; Larsson, P.T.; Mahlapuu, M.; Håkansson, J.; Andersson, M. Cubosomes for topical delivery of the antimicrobial peptide LL-37. *Eur J Pharm Biopharm.* **2019**,134, 60-67.

(21) Faria, A.R.; Silvestre, O.F.; Maibohm, C.; Adão, R.M.R.; Silva, B.F.B.; Nieder. J.B. Cubosome nanoparticles for enhanced delivery of mitochondria anticancer drug elesclomol and therapeutic monitoring via sub-cellular NAD(P)H multi-photon fluorescence lifetime imaging. *Nano Res.* **2019**, 12, 991–998.

(22) Elnaggar, Y.S.; Etman, S.M.; Abdelmonsif, D.A.; Abdallah, O.Y. Novel piperine-loaded Tween-integrated monoolein cubosomes as brain-targeted oral nanomedicine in Alzheimer's disease: pharmaceutical, biological, and toxicological studies. *Int J Nanomedicine.* **2015**, 10, 5459-5473.

(23) Fong, W.K.; Negrini, R.; Vallooran, J.J.; Mezzenga, R.; Boyd, B.J. Responsive self-assembled nanostructured lipid systems for drug delivery and diagnostics. *J Colloid Interface Sci.* **2016**, 484, 320-339.

(24) Ramalheiro, A.; Paris, J.L.; Silva, B.F.B.; Pires, L.R., Rapidly dissolving microneedles for the delivery of cubosome-like liquid crystalline nanoparticles with sustained release of rapamycin, *Int. J. Pharm.*, **2020**, 591, 119942.

(25) Avachat, A.M.; Parpani, S.S. Formulation and development of bicontinuous nanostructured liquid crystalline particles of efavirenz. *Colloids Surf B Biointerfaces.* **2015**, 126, 87-97.

(26) Zhang, L.; Li, J.; Tian, D. *et al.* Theranostic combinatorial drug-loaded coated cubosomes for enhanced targeting and efficacy against cancer cells. *Cell Death Dis*, **2020**, 11, 1.

(27) Wu, H.; Li, J.; Zhang, Q.; Yan, X.; Guo, L.; Gao, X.; Qiu, M.; Jiang, X.; Lai, R.; Chen, H. A novel small Odorranalectin-bearing cubosomes: preparation, brain delivery and pharmacodynamic study on amyloid-β_{25-35}-treated rats following intranasal administration. *Eur J Pharm Biopharm.* **2012**, 80, 368-378.

(28) Angelova, A.; Angelov, B.; Drechsler, M.; Bizien, T.; Gorshkova, Y.E.; Deng Y. Plasmalogen-based liquid crystalline multiphase structures involving docosapentaenoyl derivatives inspired by biological cubic membranes. *Front. Cell Dev. Biol.* **2021**, 9, 617984.

(29) Younus, M.; Prentice, R.N.; Clarkson, A.N.; Boyd, B.J. Rizwan, S.B . Incorporation of an endogenous neuromodulatory lipid, oleoylethanolamide, into cubosomes: nanostructural characterization. *Langmuir* **2016***, 32*, 8942-8950.

(30) Kulkarni, C.V.; Wachter, W.; Iglesias-Salto, G.; Engelskirchen, S.; Ahualli, S. Monoolein: a magic lipid? *Phys. Chem. Chem. Phys.* **2011**, 13, 3004−3021.

(31) Rosa, A.; Murgia, S.; Putzu, D,; Meli, V., Falchi, A.M. Monoolein-based cubosomes affect lipid profile in HeLa cells. *Chem Phys Lipids.* **2015**, 191, 96-105.

(32) Mierzwa, M.; Cytryniak, A.; Krysiński, P.; Bilewicz, R. Lipidic Liquid Crystalline Cubic Phases and Magnetocubosomes as Methotrexate Carriers. *Nanomaterials (Basel).* **2019**, 9, 636.

(33) Ali, M.A.; Kataoka, N.; Ranneh, A.H.; Iwao, Y.; Noguchi, S.; Oka, T.; Itai, S. Enhancing the Solubility and Oral Bioavailability of Poorly Water-Soluble Drugs Using Monoolein Cubosomes. *Chem Pharm Bull (Tokyo).* **2017**, 65, 42-48.

(34) Israelachvili, J.N.; Mitchell, D.J.; Ninham, B. Theory of self-assembly of hydrocarbon amphiphiles into micelles and bilayers. *J. Chem. Soc. Faraday Trans. 2* **1976**, 72, 1525–1568.

(35) Hyde, S.T.; Andersson, S.; Ericsson, B.; Larsson, K.; Kristallogr, Z. A cubic structure consisting of a lipid bilayer forming an infinite periodic minimum surface of the gyroid type in the glycerol monooleate-water system. *Zeitschrift für Krist* **1984**, 168:213–219.

(36) Briggs, J.; Qiu, H.; Caffrey, M. The temperature-composition phase diagram and mesophase structure characterization of the monoolein/water system. *J. Phys. II* **1996**, 6, 723–751.

(37) Qiu, H.; Caffrey, M. The phase diagram of the monoolein/water system: metastability and equilibrium aspects. *Biomaterials* **2000**, 21, 223–234.

(38) Lutton, E.S. Phase behavior of aqueous systems of monoglycerides. *J Am Oil Chem Soc.* **1965**, 42, 1068-1070.

(39) Angelov, B.; Angelova, A.; Garamus, V.M.; Drechsler, M.; Willumeit, R.; Mutafchieva, R.; Štěpánek, P.; Lesieur, S. Earliest stage of the tetrahedral nanochannel formation in cubosome particles from unilamellar nanovesicles. *Langmuir* **2012**, 28, 16647−16655.

(40) Angelov, B.; Angelova, A.; Vainio, U.; Garamus, V.M.; Lesieur, S.; Willumeit, R.; Couvreur, P. Long-living intermediates during a lamellar to a diamond-cubic lipid phase transition: a small-angle X-ray scattering investigation. *Langmuir* **2009**, 25, 3734-3742.

(41) Nilsson, C.; Ostergaard, J.; Larsen, S.W.; Larsen, C.; Urtti, A.; Yaghmur, A. PEGylation of phytantriol-based lyotropic liquid crystalline particles–the effect of lipid composition, PEG chain length, and temperature on the internal nanostructure. *Langmuir* **2014**, 30, 6398–6407.

(42) Angelov, B.; Angelova, A.; Filippov, S.K.; Drechsler, M.; Stepanek, P.; Lesieur, S. Multicompartment lipid cubic nanoparticles with high protein upload: Millisecond dynamics of formation. *ACS Nano* **2014**, 8, 5216–5226.

(43) Rakotoarisoa, M.; Angelov, B.; Espinoza, S.; Khakurel, K.; Bizien, T.; Angelova, A. Cubic Liquid Crystalline Nanostructures Involving Catalase and Curcumin: BioSAXS Study and

Catalase Peroxidatic Function after Cubosomal Nanoparticle Treatment of Differentiated SH-SY5Y Cells. *Molecules.* **2019**, 24, 3058.

(44) Zahedipour, F.; Hosseini, S.A.; Sathyapalan, T.; Majeed, M.; Jamialahmadi, T.; Al-Rasadi, K.; Banach, M.; Sahebkar, A. Potential effects of curcumin in the treatment of COVID-19 infection. *Phytotherapy Research*, **2020**, 34, 2911-2920.

(45) Liu, Z.; Ying, Y. The inhibitory effect of curcumin on virus-induced cytokine storm and its potential use in the associated severe pneumonia. *Front. Cell Dev. Biol*. **2020**, 8, 479.

(46) Jennings, M.R.; Parks, R.J. Curcumin as an antiviral agent. *Viruses*. **2020**, 12, 1242.

(47) Ahmed, T.; Gilani, A.-H. Therapeutic Potential of Turmeric in Alzheimer's Disease: Curcumin or Curcuminoids? *Phytother Res.* **2013**, 28, 517−525.

(48) Mahdavi, H.; Hadadi, Z.; Ahmadi, M. A review of the antioxidation, anti-inflammatory and anti-tumor properties of curcumin. *Traditional and Integrative Medicine* **2017**, 2, 188−195.

(49) Zielińska, A.; Alves, H.; Marques, V.; Durazzo, A.; Lucarini, M.; Alves, T.F.; Morsink, M.; Willemen, N.; Eder, P.; Chaud, M.V.; Severino, P.; Santini, A.; Souto, E.B. Properties, extraction methods, and delivery systems for curcumin as a natural source of beneficial health effects. *Medicina* **2020**, *56*, 336.

(50) Gupta, S. C.; Patchva, S.; Aggarwal, B. B. Therapeutic roles of curcumin: lessons learned from clinical trials. *AAPS J.* **2013**, 15, 195−218.

(51) Serafini, M. M.; Catanzaro, M.; Rosini, M.; Racchi, M.; Lanni, C. Curcumin in Alzheimer's disease: can we think to new strategies and perspectives for this molecule? *Pharmacol. Res*. **2017**, 124, 146−155.

(52) Brondino, N.; Re, S.; Boldrini, A.; Cuccomarino, A.; Lanati, N.; Barale, F.; Politi, P. Curcumin as a therapeutic agent in dementia: a mini systematic review of human studies. *Sci. World J.* **2014**, 2014, 174282.

(53) Wu, J.; Li, Q.; Wang, X.; Yu, S.; Li, L.; Wu, X.; Chen, Y.; Zhao, J.; Zhao, Y. Neuroprotection by curcumin in ischemic brain injury involves the Akt/Nrf2 pathway. *PLoS One* **2013**, 8, 59843.

(54) Esposito, E.; Ravani, L.; Mariani, P.; Contado, C.; Drechsler, M.; Puglia C.; Cortesi, R. Curcumin containing monoolein aqueous dispersions: A preformulative study. *Mater Sci Eng C* **2013**, 33, 4923–34.

(55) Chang, C.; Meikle, T.G.; Drummond, C.J.; Yang, Y.; Conn, C.E. Comparison of cubosomes and liposomes for the encapsulation and delivery of curcumin. *Soft Matter* **2021**, *17*, 3306-3313.

(56) Soleimani, V.; Sahebkar, A.; Hosseinzadeh, H. Turmeric (Curcuma longa) and its major constituent (curcumin) as nontoxic and safe substances: Review. *Phytother Res.* **2018**, 32, 985−995.

(57) Anand, P.; Kunnumakkara, A. B.; Newman, R. A.; Aggarwal, B. B. Bioavailability of curcumin: problems and promises. *Mol. Pharm*. **2007**, 4, 807−818.

(58) Zou, L.; Zheng, B.; Zhang, R.; Zhang, Z.; Liu, W.; Liu, C.; Zhang, G.; Xiao, H.; McClements, D. J. Influence of lipid phase composition of excipient emulsions on curcumin solubility, stability, and bioaccessibility. *Food Biophys*. **2016**, 11, 213−225.

(59) Rakotoarisoa, M.; Angelov, B.; Garamus, V.M.; Angelova, A. Curcumin- and fish oil-loaded spongosome and cubosome nanoparticles with neuroprotective potential against H2O2-induced oxidative stress in differentiated human SH-SY5Y cells. *ACS Omega* **2019**, 4, 3061–3073.

(60) Rakotoarisoa, M.; Angelova, A. Amphiphilic nanocarrier systems for curcumin delivery in neurodegenerative disorders. *Medicines* **2018**, 5, 126.

(61) Chatzidaki, M. D.; Mitsou, E.; Yaghmur, A.; Xenakis, A.; Papadimitriou, V. Formulation and characterization of food-grade microemulsions as carriers of natural phenolic antioxidants. *Colloids Surf. A* **2015**, 483, 130−136.

(62) Jiang, T.; Liao, W.; Charcosset, C. Recent advances in encapsulation of curcumin in nanoemulsions: A review of encapsulation technologies, bioaccessibility and applications. *Food Res Int.* **2020**, *132*, 109035.

(63) Van Hoogevest, P.; Wendel, A. The use of natural and synthetic phospholipids as pharmaceutical excipients. *Eur. J. Lipid Sci. Tech.* **2014**, 116, 1088–1107.

(64) Richter, C.K.; Skulas-Ray, A.C.; Kris-Etherton, P.M. "Chapter 3: Recommended intake of fish and fish oils worldwide," in *Fish and Fish Oil in Health and Disease Prevention*. Eds. S. K. Raatz and D. M. Bibus (San Diego, CA: Academic Press), **2016**, 27–48.

(65) Cholewski, M.; Tomczykowa, M.; Tomczyk, M. A Comprehensive Review of Chemistry, Sources and Bioavailability of Omega-3 Fatty Acids. *Nutrients.* **2018**, 10, 1662.

(66) Wang, W.; Zhu, J.; Lyu, F.; Panigrahy, D.; Ferrara, K.W.; Hammock, B.; Zhang, G. w-3 Polyunsaturated fatty acids-derived lipid metabolites on angiogenesis, inflammation and cancer. *Prostaglandins Other Lipid Mediators* **2014**, 113–115, 13–20.

(67) Khaddaj-Mallat, R.; Morin, C.; Rousseau, E. Novel n-3 PUFA monoacylglycerides of pharmacological and medicinal interest: Anti-inflammatory and anti-proliferative effects. *Eur. J. Pharmacol.* **2016**, 792, 70–77.3

(68) Morin, C.; Rodriguez, E.; Blier, P.U.; Fortin, S. Potential application of eicosapentaenoic acid monoacylglyceride in the management of colorectal cancer. *Mar. Drugs* **2017**, 15, 283.

(69) Morin, C.; Hiram, R.; Rousseau, E.; Blier, P.U.; Fortin, S. Docosapentaenoic acid monoacylglyceride reduces inflammation and vascular remodeling in experimental pulmonary hypertension. *AJP Hear. Circ. Physiol.* **2014**, 307, H574–H586.

(70) Morin, C.; Rousseau, E.; Blier, P.U.; Fortin, S. Effect of docosahexaenoic acid monoacylglyceride on systemic hypertension and cardiovascular dysfunction, *Am. J. Physiol.: Heart Circ. Physiol.* **2015**, 309, H93–H102.

(71) Morin, C.; Rousseau, E.; Fortin, S. Anti-proliferative effects of a new docosapentaenoic acid monoacylglyceride in colorectal carcinoma cells. *Prostaglandins, Leukotrienes Essent. Fatty Acids* **2013**, 89, 203–213.

(72) Avijit, H.; Tripathi, S.K.; Ghosh, A. Pharmacology and therapeutic potential of the n-3 polyunsaturated fatty acids, eicosapentaenoic acid (EPA) and docosahexaenoic acid (DHA) in fish oils. *Indian Journal of Pharmacology* **1999**, 31, 247-264.

(73) Sakamoto, A.; Saotome, M.; Iguchi, K.; Maekawa, Y. Marine-derived omega-3 polyunsaturated fatty acids and heart failure: Current understanding for basic to clinical relevance. *Int. J. Mol. Sci.* **2019**, *20*, 4025.

(74) Ma, Q.L.; Teter, B.; Ubeda, O.J.; Morihara, T.; Dhoot, D.; Nyby, M.D.; Tuck, M.L.; Frautschy, S.A.; Cole, G.M. Omega-3 fatty acid docosahexaenoic acid increases SorLA/LR11, a sorting protein with reduced expression in sporadic Alzheimer's disease (AD): relevance to AD prevention. *J Neurosci,* **2007**, 27, 14299-14307.

(75) Ulven, S.M.; Holven, K.B. Comparison of bioavailability of krill oil versus fish oil and health effect. *Vasc. Health Risk Manag.* **2015**, 11, 511–524.

(76) Walker, R.; Decker, E.A.; McClements, D.J. Development of food-grade nanoemulsions and emulsions for delivery of omega-3 fatty acids: opportunities and obstacles in the food industry. *Food Funct.* **2015**, *6*, 42-55.

(77) Wang, J.; Luo, T.; Li. S.; Zhao, J. The powerful applications of polyunsaturated fatty acids in improving the therapeutic efficacy of anticancer drugs. *Expert Opinion on Drug Delivery* **2012**, 9, 1-7.

(78) Berquin, I.M.; Edwards, I.J.; Chen, Y.Q. Multi-targeted therapy of cancer by omega-3 fatty acids. *Cancer Lett.* **2008**, 269, 363-377.

(79) Pan, Y.; Khalil, H.; Nicolazzo, J. The impact of docosahexaenoic acid on Alzheimer's disease: Is there a role of the blood-brain barrier? *Curr. Clin. Pharmacol.* **2015**, 10, 222−241.

(80) Bousquet, M.; Saint-Pierre, M.; Julien, C.; Salem, N.; Cicchetti, F.; Calon, F. Beneficial effects of dietary omega-3 polyunsaturated fatty acid on toxin-induced neuronal degeneration in an animal model of Parkinson's disease. *FASEB J.* **2008**, 22, 1213−1225.

(81) Shehzad, Q.; Rehman, A.; Jafari, S.M.; Zuo, M.; Khan, M.A.; Ali, A.; Khan, S.; Karim, A.; Usman, M., Hussain, A. Xia, W. Improving the oxidative stability of fish oil nanoemulsions by co-encapsulation with curcumin and resveratrol. *Colloids Surf B Biointerfaces.* **2021**, 199, 111481.

(82) Gulotta, A.; Saberi, A.H.; Nicoli, M.C.; McClements, D.J. Nanoemulsion-based delivery systems for polyunsaturated (omega-3) oils: formation using a spontaneous emulsification method. *Journal of agricultural and food chemistry* **2014**, 62, 1720-1725.

(83) Dey, K.T.; Ghosh, S.; Ghosh, M.; Koley, H.; Dhar, P. Comparative study of gastrointestinal absorption of EPA & DHA rich fish oil from nano and conventional emulsion formulation in rats. *Food research international* **2012,** 49, 72-79.

(84) Venugopalan, V.K.; Gopakumar, L.R.; Kumaran, A.K.; Chatterjee, N.S.; Soman, V.; Peeralil, S.; Mathew, S.; McClements, D.J.; Nagarajarao RC. Encapsulation and protection of omega-3-rich fish oils using food-grade delivery systems. *Foods.* **2021***, 10*, 1566.

(85) Den Ruijter, H.M.; Berecki, G.; Opthof, T.; Verkerk, A.O.; Zock, P.L.; Coronel, R. Pro- and antiarrhythmic properties of a diet rich in fish oil. *Cardiovasc Res.* **2007**, 73, 316-325.

(86) Jafari, S.M.; Assadpoor, E.; Bhandari, B.; He, Y. Nano-particle encapsulation of fish oil by spray drying. *Food Research International* **2008**, 41, 172-183.

(87) Kalmijn, S.; van Boxtel, M.P.; Ocke, M.; Verschuren, W.M.; Kromhout, D.; Launer, L.J. Dietary intake of fatty acids and fish in relation to cognitive performance at middle age. *Neurology* **2004**, 62, 275-280.

(88) Barbosa, D.S.; Cecchini, R.; El Kadri, M.Z.; Rodríguez, M.A.; Burini, R.C.; Dichi, I. Decreased oxidative stress in patients with ulcerative colitis supplemented with fish oil omega. *Nutrition*. **2003**, 19, 837-42.

(89) Zheng, M.; Wang, Z.; Liu, F.; Mi, Q.; Wu, J. Study on the microstructure and rheological property of fish oil lyotropic liquid crystal. *Colloids and Surfaces A: Physicochemical and Engineering Aspects* **2011**, 385, 47-54.

(90) Nilsson, C.; Edwards, K.; Eriksson, J.; Larsen, S.W.; Østergaard, J.; Larsen, C.; Urtti, A.; Yaghmur, A. Characterization of oil-free and oil-loaded liquid-crystalline particles stabilized by negatively charged stabilizer citrem. *Langmuir* **2012**, 28, 11755-11766.

(91) Angelova, A.; Drechsler, M.; Garamus, V. M.; Angelov, B. Liquid crystalline nanostructures as pegylated reservoirs of omega-3 polyunsaturated fatty acids: structural insights toward delivery formulations against neurodegenerative disorders. *ACS Omega* **2018**, 3, 3235−3247.

(92) Shao, X.; Bor, G.; Al-Hosayni, S.; Salentinig, S.; Yaghmur, A. Structural characterization of self-assemblies of new omega-3 lipids: docosahexaenoic acid and docosapentaenoic acid monoglycerides. *Phys Chem Chem Phys.* **2018**, 20, 23928-23941.

(93) Yaghmur, A.; Al-Hosayni, S.; Amenitsch, H.; Salentinig, S. Structural investigation of bulk and dispersed inverse lyotropic hexagonal liquid crystalline phases of eicosapentaenoic acid monoglyceride. *Langmuir* **2017**, 33, 14045−14057.

(94) Yaghmur, A., de Campo, L., Sagalowicz, L., Leser, M.E., Glatter, O. Emulsified microemulsions and oil-containing liquid crystalline phases. *Langmuir* **2005**, 21, 569–577.

(95) Yaghmur, A., Ghazal, A., Ghazal, R., Dimaki, M., Svendsen, W.E. A hydrodynamic flow focusing microfluidic device for the continuous production of hexosomes based on docosahexaenoic acid monoglyceride. *Phys. Chem. Chem. Phys.* **2019**, 21, 13005–13013.

(96) Angelova, A.; Angelov, B.; Garamus, V. M.; Couvreur, P.; Lesieur, S. Small-angle X-ray scattering investigations of biomolecular confinement, loading, and release from liquid-crystalline nanochannel assemblies. *J. Phys. Chem. Lett.* **2012**, 3, 445−457.

(97) Yaghmur, A.; Lotfi, S.; Ariabod, S.A., Bor, G.; Gontsarik, M.; Salentinig, S. Internal Lamellar and Inverse Hexagonal Liquid Crystalline Phases During the Digestion of Krill and Astaxanthin Oil-in-Water Emulsions. *Front Bioeng Biotechnol*. **2019,** 7, 384.

(98) Fong, C.; Zhai, J.; Drummond, C.J.; Tran, N. Micellar *Fd3m* cubosomes from monoolein - long chain unsaturated fatty acid mixtures: Stability on temperature and pH response. *J Colloid Interface Sci.* **2020**, 566, 98-106.

(99) Thormar, H.; Isaacs, C.E.; Brown, H.R.; Barshatzky, M.R., Pessolano, T. Inactivation of enveloped viruses and killing of cells by fatty acids and monoglycerides. *Antimicrobial Agents and Chemotherapy*. **1987**, 31, 27-31.

(100) Knapp, H.R.; Melly, M.A.; Knapp, H.R. Bactericidal effects of polyunsaturated fatty acids. *The Journal of Infectious Diseases*. **1986**, 154, 84-94.

(101) Deng, Y.; Angelova A. Coronavirus-induced host cubic membranes and lipid-related antiviral therapies: A focus on bioactive plasmalogens. *Front. Cell Dev. Biol*. **2021**, 9, 630242.

(102) Schoenmaker, L.; Witzigmann, D.; Kulkarni, J.A.; Verbeke, R.; Kersten, G.; Jiskoot, W.; Crommelin, D.J.A. mRNA-lipid nanoparticle COVID-19 vaccines: Structure and stability. *Int. J. Pharm.* **2021***, 601*, 120586

(103) Eygeris, Y.; Patel, S.; Jozic, A.; Sahay. G. Deconvoluting lipid nanoparticle structure for messenger RNA delivery. *Nano Letters* **2020**, *20*, 4543-4549.

(104) Kim, J.; Eygeris, Y.; Gupta, M.; Sahay, G. Self-assembled mRNA vaccines. *Adv. Drug Delivery Rev.* **2021,** *170* , 83-112.

(105) Pilkington, E.H.; Suys, E.J.A.; Trevaskis, N.L.; Wheatley, A.K.; Zukancic, D.; Algarni, A.; Al-Wassiti, H.; Davis, T.P.; Pouton, C.W.; Kent, S.J.; Truong, N.P.. From influenza to COVID-19: Lipid nanoparticle mRNA vaccines at the frontiers of infectious diseases. *Acta Biomaterialia* **2021**, *131*, 16-40.

(106) David, G.; Pérez, J. Combined sampler robot and high-performance liquid chromatography: a fully automated system for biological small-angle X-ray scattering experiments at the synchrotron SOLEIL SWING beamline. *J. Applied Crystallography*, **2009**, 42, 892-900.

II. Curcumin and fish oil - loaded spongosome and cubosome nanoparticles with neuroprotective potential against H_2O_2 - induced oxidative stress in differentiated human SH-SY5Y cells

Miora Rakotoarisoa[a], **Borislav Angelov**[b], **Vasil M. Garamus**[c] **and Angelina Angelova**[a].

[a] *Université Paris-Saclay, CNRS, Institut Galien Paris-Sud UMR8612, F-92296 Châtenay-Malabry, France;* [b] *Institute of Physics, ELI Beamlines, Academy of Sciences of the Czech Republic, Na Slovance 2, CZ-18221 Prague, Czech Republic;* [c] *Helmholtz-Zentrum Geesthacht: Centre for Materials and Coastal Research, D-21502 Geesthacht, Germany*

Accepted in ACS Omega

Curcumin and fish oil - loaded spongosome and cubosome nanoparticles with neuroprotective potential against H_2O_2 - induced oxidative stress in differentiated human SH-SY5Y cells

Abstract:

Many phytochemical antioxidant compounds, including curcumin (CU), are water-insoluble and thus require delivery carriers in order to increase their bioavailability for *in vivo* applications. Oxidative stress-related apoptosis is a common cause for the neuronal loss in the progression of neurodegenerative diseases. Lipid nanoparticles (NPs) with internal self-assembled liquid crystalline structures present strong interest as safe drug delivery systems for neuronal regeneration through combination therapies. Here, we report spongosome and cubosome lipid NPs, which co-encapsulate CU and fish oil (FO), rich in ω-3 polyunsaturated fatty acids. The performed structural investigation by synchrotron small-angle X-ray scattering evidenced the liquid crystalline organization of the self-assembled NPs. The encapsulation efficiency for CU in the lipid nanocarriers was found to be higher as compared to that reported for polymer-based carriers. The cytotoxicity of the blank and antioxidant-loaded nanocarriers was negligible at lipid concentrations 300 and 500 nM. Morphological changes were observed for neuronally derived human SH-SY5Y cells subjected to damage by reactive oxygen species (ROS) upon exposure to hydrogen peroxide. Using flow cytometry, we quantified the effects of CU and FO, co-encapsulated in spongosome and cubosome lipid NPs on the response of differentiated SH-SY5Y cells to H_2O_2-induced oxidative stress. Measurements of the intracellular ROS levels (using a 2′,7′ dichlorodihydrofluorescein diacetate probe) and of apoptotic cells (using an Annexin V-PE/SYTOX-green assay) were performed to compare the neuroprotective potential of the liquid crystalline spongosome and cubosome nanocarriers to that of ethanolic solutions or aqueous suspensions of the CU/FO mixtures. The results indicated that dual drug-loaded cubosomes may be suitable for combination treatments against neurodegenerative disorders.

1) Introduction

Neurodegenerative diseases [Alzheimer's disease (AD), Parkinson's disease (PD), Huntington disease, and amyotrophic lateral sclerosis] have become a major challenge for public health because of their high incidence as impacted by the increased life expectancy.[1–4] They are disabling chronic disorders characterized by the progressive loss of neurons in different areas of the central nervous system, which leads to cognitive, behavioral, sensory, and motor dysfunctions.[1–14] Unfortunately, these diseases are still incurable and thus represent a growing public health burden.[1]

A common feature of the neurodegenerative diseases is the oxidative stress risk factor.[2–7] The brain is vulnerable to damage by reactive oxygen species (ROS) because of its increased oxygen consumption with regard to other organs. It has a high content of oxidizable polyunsaturated fatty acid (PUFA)-rich membranes and a relatively low antioxidant defense.[5–8] ROS such as superoxide anions, hydroxyl radicals, and hydrogen peroxide (H_2O_2) are easily generated under conditions of oxidative stress, which lead to neuronal cell death.[6,10] The main sources of ROS production are the mitochondrial transport chain, endoplasmic reticulum, Krebs cycle, and plasma membrane.[4,8] Oxidative stress occurs when the generation of ROS exceeds the natural antioxidant defenses of the cells. The defense system against the adverse effects of ROS includes antioxidant enzymes [superoxide dismutase (SOD), catalase (CAT), and glutathione peroxidase (GPx)] and nonenzymatic components. Nonetheless, the accumulated free radicals attack the electron-rich biomolecules such as proteins, nucleic acids, and lipids. This causes impairment of the neuronal cell functions.[3–10] Among the various ROS, H_2O_2 rapidly induces neurotoxicity because it can disrupt the cellular integrity. ROS mediate the mitochondrial dysfunction through mutations of the mitochondrial DNA, disruption of the calcium (Ca^{2+}) homeostasis, activation of the mitochondrial permeability transition pore, and alteration of the intracellular bioenergetics.[9–14] Thus, a vicious cycle is formed, which amplifies the neuronal cell dysfunction and triggers neurodegeneration.[8,9]

Therapeutic strategies including antioxidants are gaining increasing interest.[6,15] Curcuminoids have received attention as health-promoting nutraceutical and pharmaceutical products because of their anti-inflammatory, antioxidant, antiviral, antibacterial, antifungal, and antitumor activities.[15–21] The curcumin (CU) substance has a safe nutraceutical profile with low side effects. It can be tolerated at doses up to 8 g per day in humans.[16] Recently, the neuroprotective potential of CU and its antioxidant, anti-inflammatory, and amyloid Aβ binding properties have attracted interest in *in vitro* and *in vivo* investigations of neurodegenerative disease models.[17–26] However, a serious obstacle for the therapeutic use of CU arises from its limited water solubility and its low bioavailability.[27–29] This compound is chemically unstable, which often causes a loss of biological activity.[27,28]

Nanotechnology-based delivery systems have been developed in recent years to promote the utilization of unstable and insoluble neuroprotective compounds as drugs.[30–81] Among them, oil-in-water emulsions have shown capacities to improve the solubility and stability of phytochemicals such as CU.[29–33] These excipient formulations consist of oil droplets dispersed in aqueous medium. The influence of the oil type on the ability of the oil-in-water emulsions to enhance the stability and bioavailability of encapsulated drugs has been investigated.[30–32] Among the various kinds of oils [sunflower oil, coconut oil, corn oil, flaxseed oil, or fish oil (FO)], the FO ingredients have led to the highest CU bioavailability.[29] FO provides a rich source of ω-3 PUFAs (ω-3 PUFAs), mostly eicosapentaenoic acid and docosahexaenoic acid (DHA).[33–38] Experimental studies have shown that the FO supplements are highly beneficial in animal models of neurodegeneration.[34,35] Moreover, a protective effect of FO combined with phytochemicals or other antioxidant compounds has been reported for oral supplementations in a rat model of PD.[36] Synthetic monoglyceride derivatives[37,38] with ω-3 PUFA chains can also be expected to be beneficial for such purposes.

Nanoscale delivery systems are promising for the elaboration of personalized medicines for treatment of neurological disorders.[39–81] The ability of CU to penetrate organs and

brain regions has been shown to be influenced by the nanoformulation type.[65–69,71] CU administration to neurodegenerative disease models by nanoparticles (NPs) has primarily been realized using liposomes, solid lipid NPs, and polymeric particles.[43–63] In recent years, lipid nanocarriers of inner liquid crystalline organization (cubosome, spongosome, hexosome, and multicompartment NPs) have receive considerable attention for delivery of various drug types.[55,56,82–113] Generally, lipid-based NPs have more advantages than the synthetic polymer-based carriers for increasing the bioavailability of encapsulated biomolecules.[81,86,93,109] The lipids, used to prepare the nanocarriers, are usually naturally occurring molecules with low acute and chronic toxicities. At variance, not every polymer matrix is biocompatible and biodegradable. The *in vivo* degradation of synthetic polymer matrices might cause toxic effects.[111] Similarly to liposomes, the liquid crystalline lipid NPs (cubosomes, spongosomes and hexosomes) can transport both lipophilic and hydrophilic molecules.[55,56,59,88–92] However, the liquid crystalline nanocarriers display multiple compartments and structural advantages (e.g., nanochannel network organization), which enable a higher encapsulation efficacy for guest molecules. They support the sustained release of encapsulated substances including therapeutic macromolecules.[56,59,96,111] It has been estimated that the lipid cubic phases have very large surface area of the lipid/water interfaces (on the order of 400 m^2/g).[112] Thus, the additional advantages of the cubosomes and spongosomes over the liposome nanocarriers are due to their large specific surface areas.[112,113]

Liquid crystalline nanocarriers are formed by self-assembly of lyotropic lipids such as unsaturated monoglycerides, phospholipids, and other co-lipids upon contact with an aqueous medium.[37,38,40,82–92,96–106] Sponge-type nanocarriers (spongosomes) and cubosomes are produced upon dispersion of bulk bicontinuous sponge and cubic liquid crystalline phases[40,90–93] in an excess aqueous environment (Figure 1). Their structures involve bicontinuous lipid bilayers and networks of aqueous channels allowing for the encapsulation of either hydrophilic or hydrophobic molecules.[82–100]

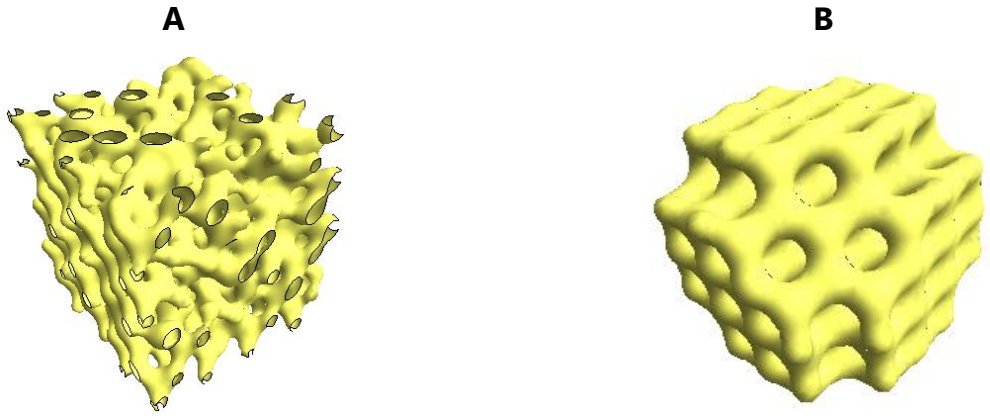

Figure 1. Schematic presentation of the supramolecular organizations of: **(A)** spongosome carriers and **(B)** cubosome particles of the double diamond *Pn3m* cubic space group enabling the encapsulation and protection of unstable molecules of therapeutic significance.

To our knowledge, no studies have been previously performed on the bioactivity of CU-loaded spongosome and cubosome NPs (Figure 1) for treatment or prevention of neurodegenerative disorders by combination therapies. The purpose of our work is first to formulate original monoolein (MO)-based spongosome and cubosome carriers, which coencapsulate CU and FO in their self-assembled nanostructures. Second, we evaluate the neuroprotective effects of the CU- and FO-loaded nanocarriers against H_2O_2-induced neuronal cell damage. The properties of the lipid nanoassemblies are examined in vitro using the human neuroblastoma SH-SY5Y cell line, which is differentiated by retinoic acid (RA).[114,115] It represents a neuronal cell phenotype that has been accepted as an *in vitro* model of the AD and PD pathologies involving oxidative stress.[116–120] We use flow cytometry as a method[121,122] to determine the possible outcomes of the spongosome and cubosome formulations (with a combined loading of CU and FO) in the chosen in vitro neurodegeneration model of differentiated SH-SY5Y human cells.

Thus, the focus of our work is to find out whether the liquid crystalline nanocarriers, which co-encapsulate CU and FO, can have a neuroprotective potential in combination treatments of neurodegenerative disorders.

2) Materials and methods

a. Materials

CU, FO, MO, a PEGylated amphiphile denoted as TPGS-PEG_{1000}, RA, hydrogen peroxide (H_2O_2), D(+)-glucose, and DCFH-DA were purchased from Sigma-Aldrich. For cell culture experiments, DMEM, streptomycin−penicillin, phosphate-buffered saline (PBS), and trypsin−ethylenediaminetetraacetic acid (EDTA) were supplied by Sigma-Aldrich. FBS was provided by Thermo Fisher Scientific. Water was of Milli-Q quality (Millipore Corp.). The Annexin V-PE apoptosis detection kit (Premium) was supplied by Abnova.

b. Lipid NP preparation by self-assembly

The NPs were prepared by the method of hydration of a lyophilized thin lipid film followed by physical agitation in excess aqueous phase.[87,88,92,106] The amphiphilic components were weighed, dissolved in chloroform, and mixed at desired proportions (Table 1). Then, the solvent was evaporated under a stream of nitrogen gas for 1 h at room temperature in order to create a thin-film lipid sample. The excess organic solvent was removed overnight using a lyophilizer. This step was followed by the hydration of the thin-film samples by a solution of D(+)-glucose (5 wt %) (prepared using Milli-Q water) for 24 h at room temperature. Finally, the mixtures were dispersed using an ultrasonic ice bath during 15 min.

c. Size distribution

The particle size distribution was determined by means of a Nano-ZS90 device (Malvern Instruments) by collecting the intensity of the scattered light at an angle of 90° with regard to the incident laser beam. Data collection was carried out at 25 °C. The samples were diluted to 1/100 in D(+)-glucose (5 wt %) prepared with Milli-Q water in order to ensure Brownian motion conditions for the particles. The refractive index and viscosity of the aqueous medium were equal to 1.335 and 1.9 mPa·s, respectively. The hydrodynamic diameter of the particles

in the nanodispersions was determined based on the principle of QELS. Each analysis was a result of three consecutive measurements.

d. Lipid NP structure determination

The determination of the nanostructures generated in the self-assembled lipid based formulations was performed by synchrotron SAXS experiments at the P12 BioSAXS beamline of the European Molecular Biology Laboratory (EMBL)123 at the PETRA III ring of synchrotron DESY (Hamburg, Germany) at 20 °C. A Pilatus 2M detector (1475 × 1679 pixels) (Dectris, Switzerland) was used and synchrotron radiation with a wavelength λ = 1 Å. The sample detector distance was 3 m, allowing measurements in the range of q from 0.005 to 0.44 Å−1. The q-vector was defined as $q = (4\pi/\lambda) \sin \theta$, where 2θ is the scattering angle.

e. Entrapment efficiency and drug loading capacity

The entrapment efficiency (EE) of CU was determined using the information about its spectroscopic properties.[29,66−68] The absorbance of the NP samples was read at 405 nm using a microplate reader. The dosage of the total CU in the |MO−FO−CU] NP dispersions was performed after direct dilution (1/100 ratio) of the NPs in ethanol. The determination of free CU was performed after centrifugation of the aqueous dispersions in AMICON filter devices (10 000 MWCO) at 4000 rpm for 5 min. A calibration curve of the CU solution in ethanol from 5 to 50 μM was obtained with the equation y = 0.0346x + 0.0322 and a R^2 value of 0.9905. The EE and drug loading rate were calculated according to the following equations:

$$\text{Entrapment efficiency EE (\%)} = \text{curcumin}_{(\text{encapsulated})} / \text{curcumin}_{(\text{total})} \times 100$$

$$\text{Drug loading (\%)} = \text{curcumin}_{(\text{encapsulated})} / \text{excipients}_{(\text{total})} \times 100$$

f. Cell culture

The human neuroblastoma SH-SY5Y cells were cultured in DMEM with high glucose supplement, 10% FBS, and 0.5% streptomycin−penicillin. They were incubated at 37 °C in a saturated humidity atmosphere containing 5% CO_2. Before every experiment, the cells were

grown in plastic flasks (75 cm^2) (Nunc Corp.) and were treated for 5 days with 10 µM retinoix acid (RA) toward differentiation into neuronal cells.[114,115] The adherent SH-SY5Y cells were divided twice weekly with the use of 0.05% trypsin and EDTA for up to 5 min, followed by centrifugation (×200g) at 4 °C during 5 min. The cells were counted using a KOVA cell and seeded at densities of 3 × 105 cells/well in six-well plates or 1.7 × 104 cells/well in 96-well plates (depending on the type of the biological analysis to be carried out). After 24 h, the SH-SY5Y cells were incubated with RA (10 µM) for 5 days, changing the medium with RA at least once. The neuronal phenotype was distinguished by the extensive proliferation of neurites.

g. MTT test

The cell viability was determined by the tetrazolium salt test (MTT).[124] The solution of MTT was prepared in PBS and filtered prior to use. This reagent is reduced to formazan by the mitochondrial succinate dehydrogenase enzyme in the living cells. The MTT compound forms a purple precipitate, the quantity of which is proportional to the metabolic activity of the living cells. The cells were seeded at a density of 20 000 cells/well in 96-well plates. After 5 days of treatment with 10 µM RA, the lipid NPs were incubated with the cells at lipid concentrations of 300 and 500 nM at 37 °C for 24 h. Untreated cells maintained in DMEM were used as controls. MTT was incubated at a concentration of 5 mg/mL at 37 °C. After 1 h of incubation of the cells with MTT, the medium was removed and the cells were dissolved in 100% dimethyl sulfoxide in order to solubilize the formazan precipitate. The optical density was then measured at 570 nm by a microplate reader.

h. ROS detection by flow cytometry

Detection of ROS in the differentiated SH-SY5Y cells was performed by flow cytometry. The principle of this method is to count the fluorescently labeled cells in a suspension, which passes in a capillary illuminated by a laser beam. The fluorescence of the specific fluorochrome was detected by the BD Accuri C6 flow cytometer. In the present study, the DCFH-DA dye probe[121,122] was used for the detection of intracellular ROS in cells subjected to H_2O_2-

induced oxidative stress or treated by nanoformulations. The excitation was done at a wavelength of 488 nm. The fluorescence emission of the probe was collected in the FL1 533 nm region. DCFH-DA is a nonpolar permeable dye, which is converted to DCFH by cellular esterases into a nonfluorescent polar derivative. DCFH is then converted to highly fluorescent DCF when oxidized by the intracellular ROS and other peroxides. The DCF accumulation is measured by the increase in the fluorescence at 530 nm when the sample is excited at 488 nm. The measured intensity is proportional to the concentration of ROS inside the cells. The measurements were carried out after 30 min of incubation of the cells with 10 µM of DCFH-DA in DMEM without FBS at 37 °C. The incubation with hydrogen peroxide was done (i) at a concentration of 100 mM H_2O_2 for 5 min after the incubation with the DCFH-DA probe or (ii) at a concentration of 900 µM for 60 min before the incubation with DCFH-DA.

i. Apoptosis analysis by flow cytometry.

The induction of apoptosis by H_2O_2 and the eventual prevention of apoptosis by [MO−FO−CU] NPs were studied by flow cytometry. SH-SY5Y cells were seeded at a density of 106 cells in 25 cm^2 culture flasks containing 5 mL of DMEM. After 24 h, the cell culture medium was replaced by 10 µM RA solution for 5 days of incubation. Then, lipid NPs (500 nM) were introduced in the FBS-free medium. After 24 h of incubation, H_2O_2 (900 µM) was added and the cells were incubated for 60 min. The cells were washed with PBS and collected by trypsinization. The pelleted cells were resuspended in 500 µL binding buffer, 5 µL Annexin V-PE, and 1 µL SYTOX green dye and incubated at room temperature in dark for 10 min. The stained cells were analyzed on the BD C6 Accuri flow cytometer using the FL-1 channel (Ex. 488 nm/Em 530 nm) for detection of SYTOX green fluorescence and the FL-2 channel (Ex. 488 nm/Em 578 nm) for the Annexin V-PE fluorescence.

j. Statistical Analysis

The data are presented as the mean values of standard deviation (SD) of three independent experiments. The results were analyzed by the Tukey test after one-way analysis of

variance. The probability values $p < 0.05$ and $p < 0.01$ were considered statistically significant across the treatment groups.

3) Results and discussion

a. Physicochemical characterization of lipid NPs loaded with CU and FO

We prepared MO-based nanocarriers using the self-assembly method.[87,88,90,92] The nanocarriers with co-encapsulated CU and FO were stabilized by a PEGylated corona (see Table 1 for the investigated compositions).

Table 1. Constituents of the formulated lipid NPs and their mass proportions

NPs	MO (g)	TPGS-PEG$_{1000}$ (g)	FO (g)	CU (g)
MO	0.010	0.0027		
MO−FO	0.010	0.0027	0.00394	
MO−FO$_1$−CU	0.010	0.0027	0.00162	0.00054
MO−FO$_2$−CU	0.010	0.0027	0.00394	0.00054

The small-angle X-ray scattering (SAXS) method was employed to study the liquid crystalline organization of the obtained dispersed NPs. Figure 2A, B shows that the resulting SAXS patterns depend on the amount of FO incorporated in the MO−FO−CU NPs. The MO−FO$_1$−CU formulation with a low FO content (FO$_1$) favored the fabrication of cubosomes, which display Bragg's peaks in the SAXS patterns. The amphiphilic composition involving a higher FO content (MO−FO$_2$−CU) yielded the formation of spongosomes. The latter were evidenced by smooth SAXS curves typical for sponge-type lipid particles.[90,92] The presence of Braggs peaks in figure 2A and 2B characterized the nanocarriers with a periodic inner organization (cubosomes). The determined lattice parameters of the coexisting cubic unit cells in the *Pn3m* cubosome particles are a_1 = 21.1 nm and a_2 = 16.4 nm (Fig. 2B). These unit cell values result from the fragmentation of the drug-loaded lyotropic lipid cubic phase by using

a PEGylated dispersion agent. They are bigger as compared to that typical for the bulk lipid cubic phase (a = 10.5 nm).[40,99]

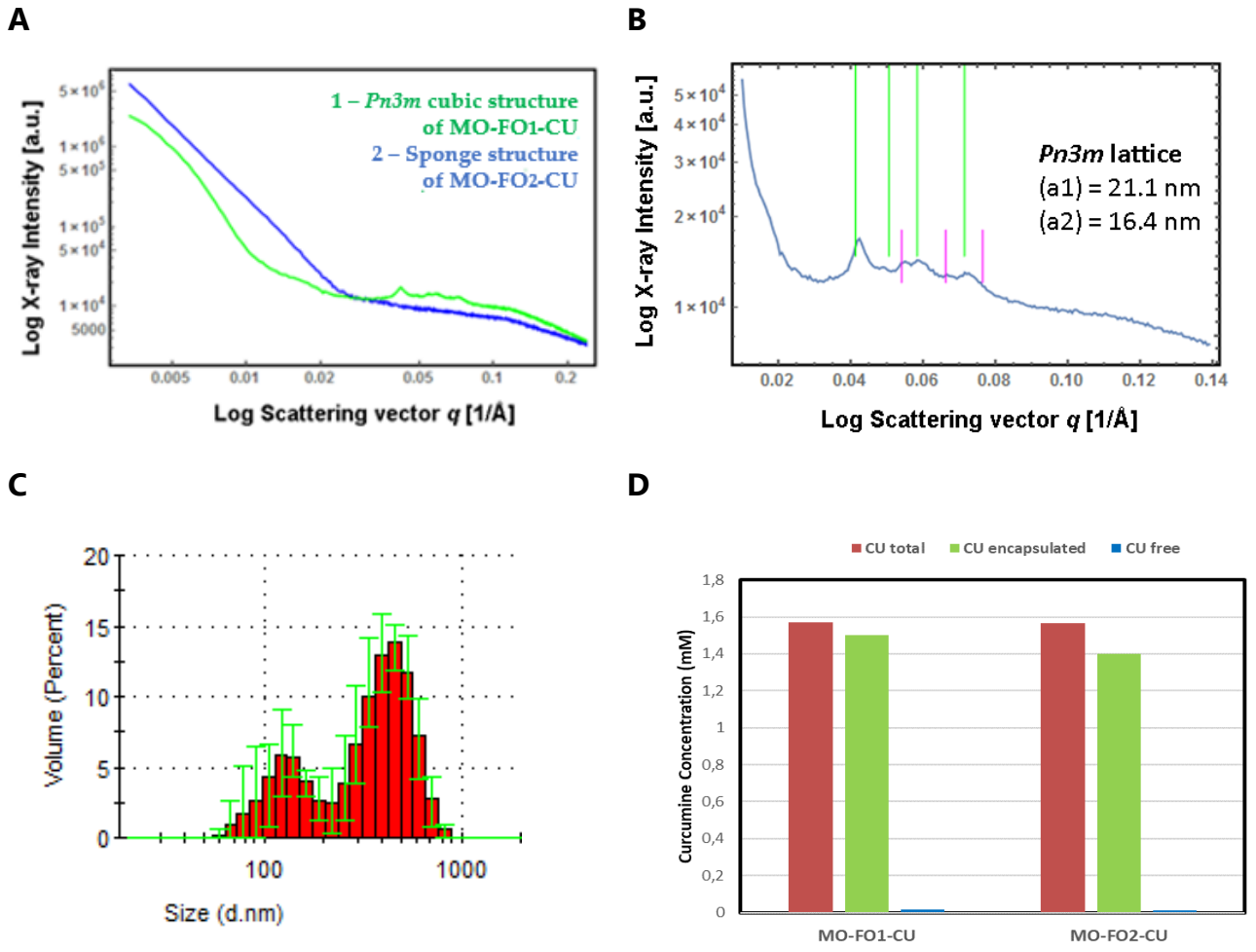

Figure 2. Physicochemical characteristics of [MO−FO−CU] NPs. **(A)** Synchrotron SAXS patterns of lipid carriers co-encapsulating FO and CU and indicating the formation of cubic (1) and sponge (2) inner structures depending on the amount of encapsulated FO (FO_1 or FO_2). **(B)** Indexing of the Bragg peaks detected in the SAXS patterns of cubosome [MO−FO−CU] NPs. The fitting of the plots yielded a coexistence of two cubic lattices with lattice parameters a_1 (green bars) and a_2 (pink bars). **(C)** NP size distributions determined by QELS. The mean hydrodynamic diameters are centered at $d_h \approx 91$ and 531 nm. **(D)** Concentrations of total (red), free (blue), and NP-encapsulated CU (green) determined by UV−visible spectroscopy.

The MO−FO−CU nanocarriers were also characterized by quasi-elastic light-scattering (QELS) measurements. A typical NP size distribution plot is shown in Figure 2C as a volume diagram. It reveals the presence of two main populations of nanocarriers in the dispersed system. They correspond to a coexistence of cubosomes (or spongosomes) and small vesicles or precursors of intermediate-type liquid crystalline structures.[40,87,88] Indeed, the bimodal distribution represents a coexistence of small-size (~100 nm) NPs and larger-size (~400 nm) particles (cubosomes or spongosomes) in the dispersed samples. This corroborates with the obtained SAXS results.

The entrapment efficiency (EE) and the loading capacity of the nanocarriers for CU were estimated using UV−visible spectroscopy measurements (Figures 2D and S2). The absorption band of CU at 405 nm was employed for the quantification. The total concentration of CU in the [MO−FO−CU] NPs was equal to 1.6×10^{-3} M. The concentrations of the encapsulated and free CU were determined after centrifugation and ultrafiltration. The results are shown in Figure 2D. We found that [MO−FO_1−CU] and {MO−FO_2−CU] NPs have the same EE of CU (EE = 99%). They were characterized by 2.7 and 2.3% of drug loading, respectively. This indicates that the studied cubosomes and spongosomes have a higher EE of CU with regard to other types of NPs. For comparison, the polymer-based CU-polylactic-co-glycolic (PLGA) NPs have displayed EE in the range from 77 to 85%.[69,81]

b. SH-SY5Y cell viability after treatment by blank or drug-loaded nanocarriers

3-(4,5-Dimethylthiazol-2-yl)-2,5-diphenyl tetrazolium bromide (MTT) assays were performed in order to establish whether the amphiphilic ingredients, from which the liquid crystalline NPs were derived, may be cytotoxic to the neuronal cell culture. The viability of SH-SY5Y cells, differentiated by RA, was determined by MTT assays at two concentrations of the lipid nanocarriers as well as at the equivalent concentrations of the nonencapsulated drugs. Unexposed cells were used as viability controls.

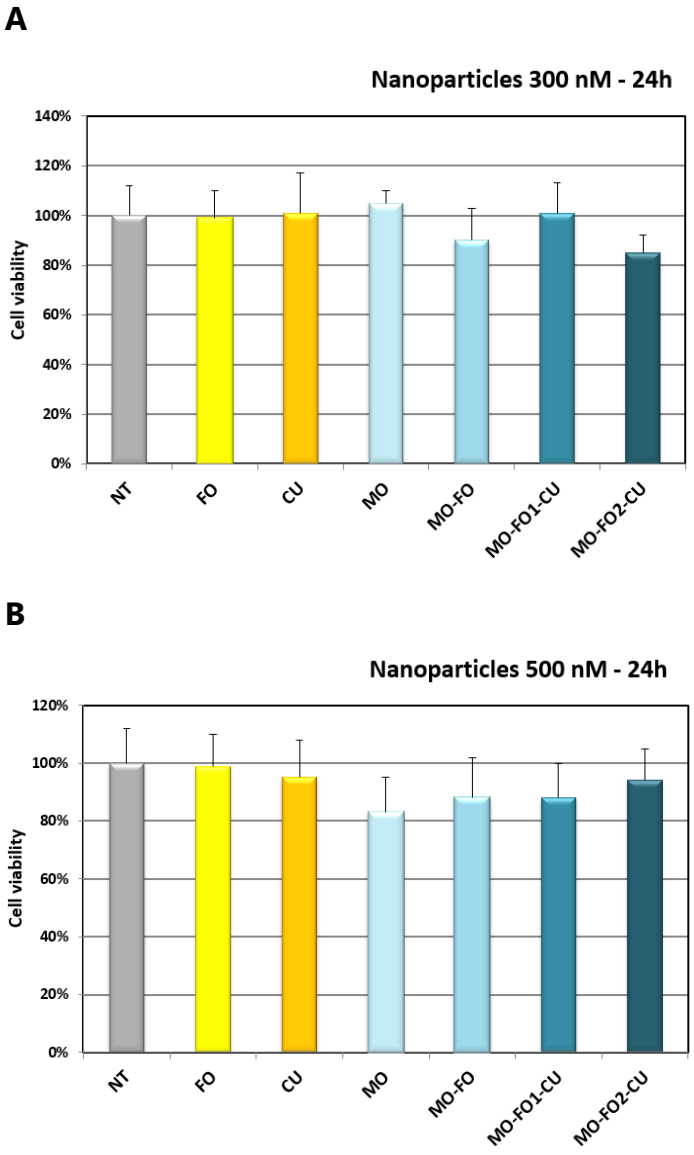

Figure 3. Viability of RA-differentiated SH-SY5Y cells after incubation with nonencapsulated free drugs (CU or FO), blank lipid nanocarriers (MO), and drug-loaded nanocarriers (MO−FO and MO−FO−CU) during 24 h. **(A)** NPs are diluted in a serum-free DMEM cell culture medium to lipid concentrations 300 nM. **(B)** NPs are diluted to 500 nM. The concentrations of free FO and free CU in the DMEM correspond to those in the diluted NPs.

The results in Figure 3 indicate that the cellular viability was in the range between 84 ± 7 and 119 ± 13% and did not show a significant difference upon increase of the lipid NPs concentration from 300 nM (Figure 3A) to 500 nM (Figure 3B). The MTT data at both lipid concentrations indicated that the exposure of RA-differentiated SH-SY5Y to lipid nanocarriers

(300 or 500 nM) does not cause significant cell death. Therefore, these concentrations were considered as the nontoxic doses suitable for the investigation of the neuroprotective effects of the nanocarriers against H_2O_2 - induced cellular damage. Under the studied concentration conditions, the sponge or cubic structures did not influence the cellular viability.

c. SH-SY5Y cellular damage upon exposure to H_2O_2

The human neuroblastoma SH-SY5Y cells were seeded and treated with RA (10 μM) for 5 days in order to obtain the typical neuronal cell phenotype (Fig. 4A). Then, they were exposed to H_2O_2 for the induction of the oxidative stress. Optical micrographs recorded following the exposition of the RA-differentiated SH-SY5Y cells to H_2O_2 are shown in Figure 4. The microscopy examination showed extensive proliferation of neurites and reduced cell body sizes (Fig. 4A-C) prior to H_2O_2 exposure. The exposition to 100 mM H_2O_2 for 5 min, which mimics an acute stress condition, revealed that the elongated cells tend to evolve into more rounded shapes (Fig. 4D). This was indicative of the onset of an apoptotic and/or cell death process.

The toxicity of H_2O_2 to RA-differentiated SH-SY5Y cells was determined by MTT assays at increasing H_2O_2 concentrations from 100 to 1000 μM and at two exposure times (30 and 180 min) (Fig. 4E). The cells were seeded in 96-well plates at a density of 1.7 × 104 cells/well in 100 μL of Dulbecco's modified Eagle's medium (DMEM) supplemented with fetal bovine serum (FBS). The results showed that the cell viability decreased with the increase of the H_2O_2 concentration and also with the exposure time. The concentrations required to elicit 50% cytotoxic effects were ~650 μM at 180 min and 950 μM at 30 min H_2O_2 exposure, respectively.

According to literature, the 180 min exposure of undifferentiated SH-SY5Y cells to H_2O_2 (250 μM) has resulted in about 50% cell death.[119] A concentration of 1000 μM H_2O_2 has induced 100% cell death for cells seeded at a density of 1 × 10^4 cells/well in 100 μL of growth culture medium containing FBS.[118] In addition, Gay *et al.* have reported that the H_2O_2 treatment of SH-SY5Y cells (1 × 10^5 cells/mL in 96-well plates) at concentrations ranging from 200 to 500 μM H_2O_2 (namely 200, 300, 400, and 500 μM) for 24 h has led to cell viability

reduction in a dose-dependent manner. The concentration of 400 μM H_2O_2 has efficiently induced about 34−35% cell death.[119,120] It is speculative to conclude that the RA-differentiated SH-SY5Y cells are more responsive to H_2O_2 treatment as compared to the undifferentiated SHSY5Y cells because the cited experiments have been performed at other cell densities. However, investigations of the responsiveness of RA-differentiated SH-SY5Y cells to neurotoxins (such as 6-hydroxydopamine or Aβ-amyloid) have demonstrated that RA-differentiated SH-SY5Y cells exhibit high sensitivity to the neurotoxins.[116,117] This fact has confirmed the suitability of the chosen in vitro model for studying the molecular and cellular mechanisms, which underlie the pathophysiology of AD and PD.[116,117]

We performed assays on determination of the intracellular ROS in order to characterize the oxidative stress induced by H_2O_2 in the RA-differentiated SH-SY5Y cells. The ROS detection was done by flow cytometry using a 2′,7′-dichlorodihydrofluorescein diacetate (DCFH-DA) dye according to a methodology established in the literature.[121,122] The cells were seeded in six-well plates at a density of 3×10^5 cells/ well. They were incubated with the dye for 30 min at 37 °C after 60 min exposure to 250, 500, and 900 μM H_2O_2, which mimics a moderate or a chronic stress condition. The histograms in Figure 4f show no significant difference of the fluorescence intensity signals for cells exposed to 250 and 500 μM H_2O_2 as compared to the fluorescence detected with unexposed cells (control). At variance, a significant increase of the fluorescence intensity was observed at a concentration of 900 μM H_2O_2 (compared with the control). The shift toward higher fluorescence intensities demonstrated the accumulation of ROS in the neuronal cells exposed to H_2O_2. Therefore, the concentration of 900 μM H_2O_2 was chosen for the subsequent experiments with 60 min exposure.

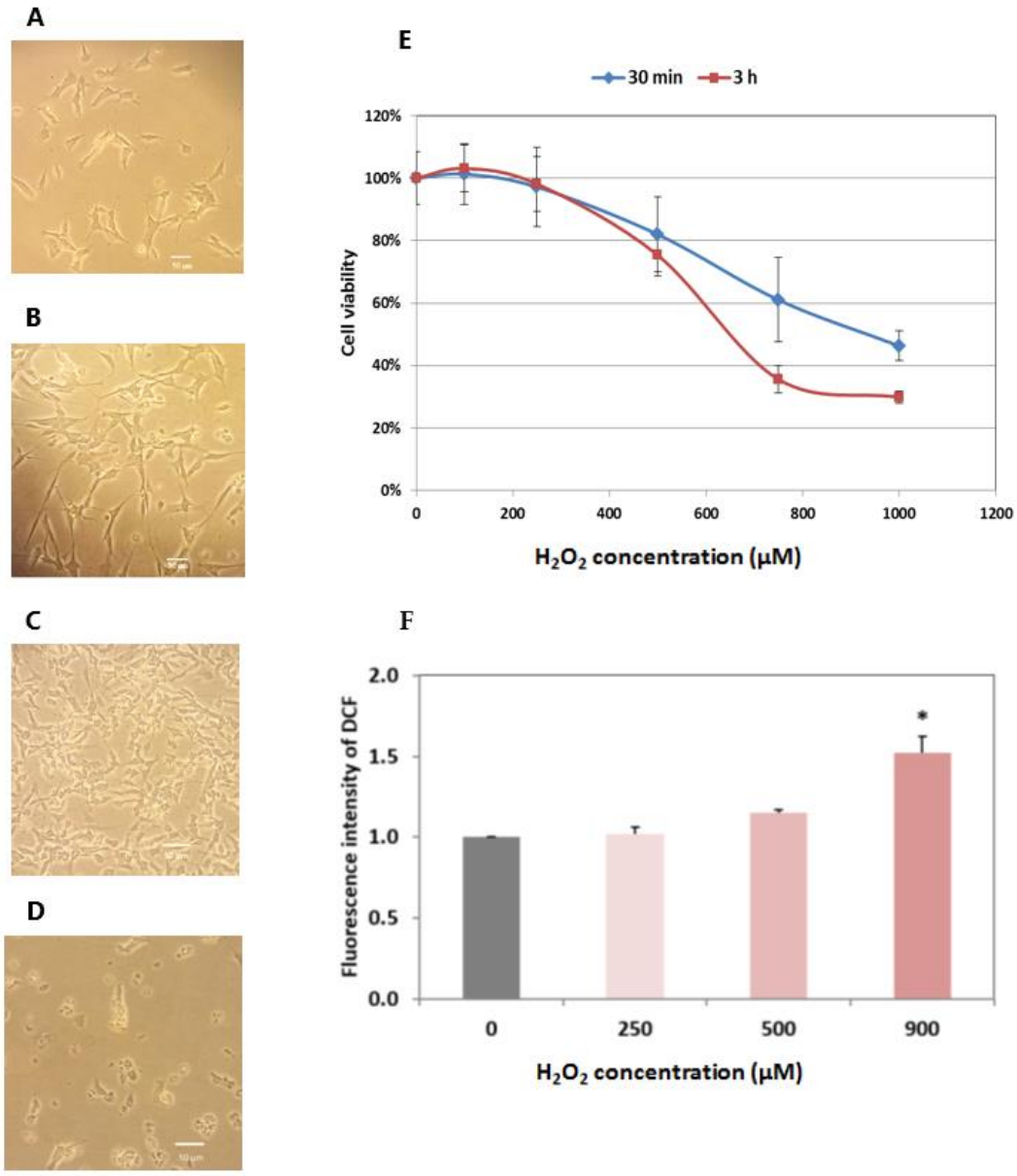

Figure 4. Exposure of RA-differentiated SH-SY5Y cells to H_2O_2 leading to accumulation of ROS. The optical microscopy images show the SH-SY5Y cellular morphology observed **(A)** before treatment with 10 µM RA; **(B)** after 3 days of incubation with 10 µM RA; **(C)** after 5 days of incubation with 10 µM RA; and **(D)** after 5 days of treatment with 10 µM RA followed by incubation with 0.3% (v/v) H_2O_2 (equal to 100 Mm H_2O_2) for 5 min. The magnification of the microscope objective is ×10. **(E)** Viability of the RA-differentiated SH-SY5Y cells after their exposure to increasing concentrations of H_2O_2 for 30 min (blue plot) or for 3 h (red plot). **(F)** Mean fluorescence intensity of the DCF dye determined by flow cytometry with differentiated SH-SY5Y cells exposed for 60 min to H_2O_2 of varying concentrations.

d. Effects of CU- and FO-loaded cubosome and spongosome NPs on H_2O_2-induced oxidative stress in differentiated SH-SY5Y cells

The neuroprotective effects of the MO−FO−CU NPs against oxidative stress were evaluated using H_2O_2 as a stress inducer. Two procedures of exposure to H_2O_2 were applied (Fig. 5). The intracellular ROS levels were measured by the flow cytometry method. For this purpose, the probe DCFH-DA (10−5 M) was incubated for 30 min with the cell culture after 24 h of preincubation of the latter with NPs.

First, H_2O_2 was incubated for 5 min at a concentration of 100 mM H_2O_2 before the flow cytometry measurements in order to mimic an acute stress (Fig. 5A, B). The RA-differentiated SH-SY5Y cells were preincubated (i) with lipid NPs (MO−FO−CU) at a concentration of 500 nM during 24 h in a serum-free DMEM and (ii) with FO or CU dissolved in absolute ethanol at concentrations equal to those in the NPs formulations. The results demonstrated that the fluorescence intensity of the DCF probe in cells exposed directly to 100 mM H_2O_2 was significantly higher than that of the unexposed cells (control) with $p < 0.01$. The augmentation of the intracellular ROS production was nearly threefold upon cell culture exposure to H_2O_2 (Fig. 5B).

The pretreatment with NPs for 24 h prior to the addition of the high-concentration H_2O_2 diminished significantly the intracellular ROS levels as compared to cells exposed directly to H_2O_2 with $p < 0.01$. The MO−FO_2−CU nanocarriers decreased the ROS levels to the values in the control cells or below them (MO−FO_1−CU) (Fig. 5B). The pretreatment by ethanolic solutions of FO or CU for 24 h prior to the addition of H_2O_2 also significantly diminished the intracellular ROS levels as compared to (H_2O_2)-treated cells with $p < 0.01$. CU and FO are weakly soluble in water. Their administration from ethanolic solutions allowed examining the maximal activity, which they can exert under conditions of acute oxidative stress (Figure 5b). The comparison of the pretreatment by MO−FO_2−CU NPs and that by ethanolic solutions of FO or CU revealed a significant difference with $p < 0.01$. At variance, the difference between the pretreatment by MO−FO1−CU NPs and by ethanolic solutions of FO and CU was not significant. Thus, the cubosomes loaded with CU and FO (MO−FO_1−CU) appear to have the

same activity on the attenuation of ROS generation upon acute cell exposure to H_2O_2 as the ethanolic solutions of CU−FO. The spongosomes (MO−FO_2−CU) displayed a lower activity, which indicates that the internal liquid crystalline structure of the nanocarriers plays a role in the delivery mechanism to the target site of action. Despite that ethanol acts as a penetration enhancer for the weakly soluble drugs, it is not recommended as a safe formulation for in vivo delivery of CU and FO. At variance, encapsulation of CU and FO in biocompatible and biodegradable NPs, such as the lipid-based carriers, can protect them against chemical degradation under the harsh conditions of the biological milieu in *in vivo* applications. [26,27,30] On the basis of the established decreased DCF fluorescence intensity (Fig. 5B), it can be concluded that CU encapsulated in liquid crystalline lipid NPs (spongosomes or cubosomes) reduces the intracellular ROS levels in H_2O_2-induced acute oxidative stress neuronal damage. The cubosome organization seems to be more efficient in ROS attenuation as compared to that of the spongosome nanocarriers. This difference might be related to the different kinds of supramolecular architectures and their release mechanisms for bioactive molecules.

Second, H_2O_2 was incubated for 60 min at a concentration of 900 μM (before the dye addition) in order to mimic a moderate stress condition (Figure 5c,d). The effects of the NP formulations (MO−FO_2−CU) were compared with that of the combination of FO and CU suspended in the aqueous phase (FO_2−CU) at an equivalent apparent concentration. The results in Figures 5C and 5D show that the fluorescence intensity of DCF in cells exposed directly to 900 μM H_2O_2 corresponds to a significant 1.5-fold augmentation of the ROS production with regard to the control cells ($p < 0.05$) (Fig. 5D). The pretreatment by (FO−CU)-aqueous suspension for 24 h prior to the addition of H2O2 diminished essentially the intracellular ROS levels with $p < 0.05$. The pretreatment by NPs for 24 h prior to the addition of H_2O_2 resulted in a significant decrease of the ROS levels for both kinds of MO−FO−CU NPs ($p < 0.01$). The decrease of the ROS levels, following the cell pretreatment by NPs, is significantly higher in comparison to the one observed for the (FO−CU)-aqueous suspension. Thus, Figure 5D shows that the cubosome (MO−FO_1−CU) and spongosome (MO−FO_2−CU)

nanocarriers loaded with CU and FO attenuate the ROS generation in H_2O_2 -induced moderate oxidative stress better than the combined aqueous suspension of the drugs (CU−FO). The two procedures of cell incubation with NPs (Fig. 5B,D) yielded similar trends of the results about the ROS level attenuation. This evidenced that the lipid nanocarriers protect the neuronal cells against ROS accumulation induced by H_2O_2 exposure.

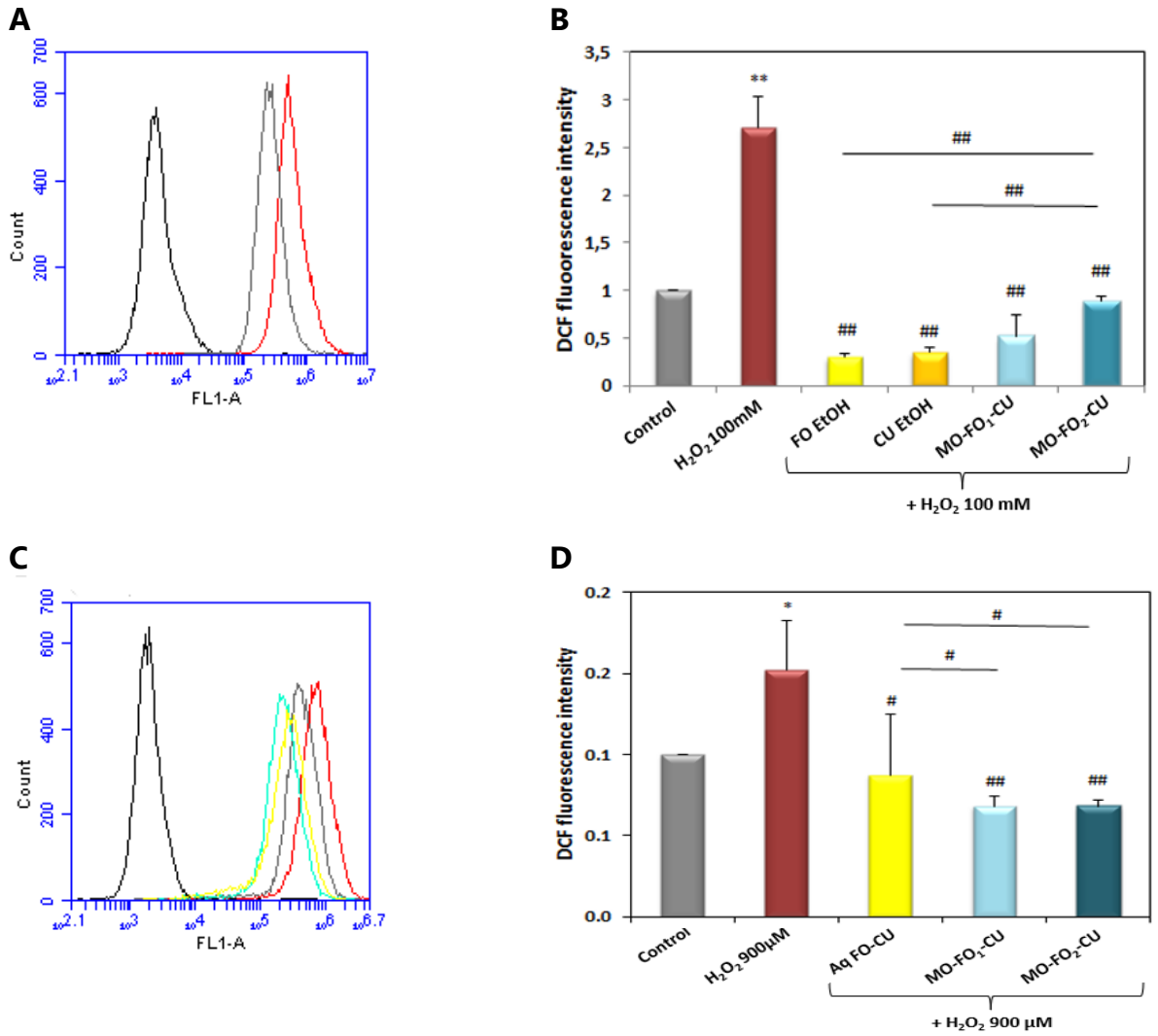

Figure 5. ROS detection in differentiated SH-SY5Y cells by flow cytometry using a DCFH-DA assay. **(A)** Plots of the fluorescence intensities of the DCF dye in cells exposed to H_2O_2 (red color) or untreated cells incubated with the dye (gray color, DC(+)). The black curve corresponds to the background level of untreated cells [DC(−)]. The probe DCFH-DA (10−5M) was incubated with the cell culture for 30 min. (b−d) Pretreatment of differentiated SH-SY5Y human cells by nanocarriers loaded with FO and CU (MO−FO−CU) for 24 h and determination

of the intracellular ROS levels following two procedures of exposure to H_2O_2. **(B)** Cells are incubated with the dye DCFH-DA followed by exposure to 100 mM H_2O_2 during 5 min prior to the flow cytometry measurements. Quantitative histograms of the mean fluorescence intensity of the DCF dye [DC(+)] expressed as the fold change with regard to the background level of untreated cells [DC(−)]. **(C)** Cells are exposed to 900 Mm H_2O_2 during 60 min before their incubation with the DCFH-DA probe for flow cytometry measurements. **(D)** Quantitative histograms are expressed as a fold change of the mean fluorescence intensity of the DCFH-DA probe with regard to the background level of untreated cells. The data are shown as mean ± SD of three independent experiments (*p < 0.05 and **p < 0.01 vs control; #p < 0.05 and ##p < 0.01 vs H_2O_2-treated group).

e. Effects of CU- and FO-loaded cubosome and spongosome NPs on H_2O_2-induced cell death

The neuroprotective effects of the MO−FO−CU NPs against cell death were evaluated by determination of the H_2O_2-induced apoptosis. The flow cytometry analysis of apoptosis was performed using two fluorescent probes (Annexin V-PE and SYTOX green). Cells translocate the phosphatidylserine phospholipid from the inner to the outer membrane leaflet at the early apoptotic stage, which is easily detectable by the Annexin V-PE probe. The SYTOX green dye is impermeable to live cells and apoptotic cells, but it can stain the necrotic cells by binding to their nucleic acids. The flow cytometry results presented in Figures 6A and 6B show a significant decrease of the percentage of live cells and a significant increase of the percentage of dead cells in the H_2O_2-treated sample as compared to the untreated RA-differentiated SHSY5Y cells (positive control). A recent study has indicated that the prolonged incubation with RA under starvation conditions (FBS-free DMEM) leads to SH-SY5Y cellular death as well.[70] The pretreatment by the (FO−CU)-aqueous suspension and by spongosome (MO−FO_2−CU) NPs had no essential effect on the cell death induced by H_2O_2. However, the number of live cells increased significantly, and the dead cells diminished upon pretreatment by cubosome (MO−FO_1−CU) NPs. These results suggest that the dual drug-loaded cubosome

(MO−FO_1−CU) NPs exert neuroprotective effects by attenuation of the H_2O_2-induced cell death. The difference in the quantitative data determined for the cubosome (MO−FO_1−CU) and the spongosome (MO−FO_2−CU) NPs may be due to the kinetics of drug release from the two kinds of self-assembled nanoarchitectures.

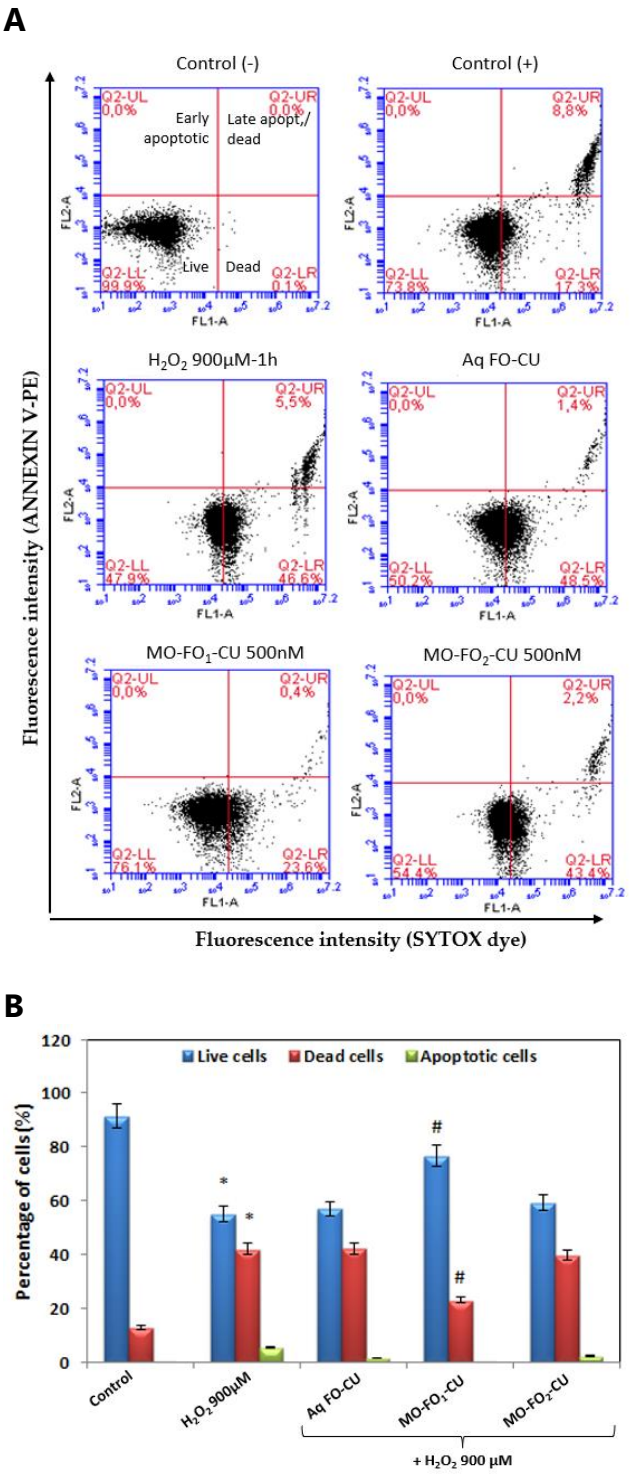

Figure 6. Flow cytometry measurements of live, apoptotic, and dead RA-differentiated SH-

SY5Y cells using Annexin V-PE and SYTOX green staining. **(A)** Four quadrants in every graph correspond to the fractions of healthy, early apoptotic, late apoptotic, and necrotic cells. The experimental conditions are indicated above every graph. The exposure to 900 μM H_2O_2 was done for 60 min. The assays are realized after treatment of the RA-differentiated SH-SY5Y cells by H_2O_2 in the presence or in the absence of drug-loaded NPs (or the corresponding aqueous FO−CU-mixed dispersion). **(B)** Quantitative presentation of the obtained data in histograms showing the percentages of live, total apoptotic, and necrotic cells. The data are shown as mean ± SD of three independent experiments (*$p < 0.05$ vs control; #$p < 0.05$ vs the H_2O_2-treated group).

The exposure of the neuronally derived SH-SY5Y cells to formulations of NPs loaded by CU and FO ameliorated their oxidative status (Figures 5 and 6). In principle, NPs oencapsulating antioxidants and FO, enriched with ω-PUFAs, mediate the neuroprotection through several mechanisms including (i) the activation of the transcription factor Nrf2, a major regulator of the antioxidant responses; (ii) stimulation of the expression of antioxidant enzymes such as SOD, CAT, and GPx; and (iii) upregulation of the antiapoptotic enzyme Bcl-2 and attenuation of apoptosis signal via downregulation of the proapoptotic enzyme Bax.[22,24,47]

In a recent investigation, the neuroprotective and neuroregenerative capacities of CU-PLGA NPs have been demonstrated by targeting of neural stem cells (NSCs).[26] It has been suggested that CU-mediated cell proliferation and neuronal differentiation occur by activating the Wnt/β-catenin signaling pathway. CU NPs have been internalized into the NSCs to enhance their proliferation. This was related to significantly increased expression of the genes involved in the cellular proliferation (reelin, nestin, and Pax6) and the neuronal differentiation (neurogenin, neuroD1, neuregulin, neuroligin, and Stat3). It has been established that CU NPs stimulate the neuronal differentiation by enhancing the nuclear translocation of β-catenin and increase the phosphorylation of GSK-3β. Inhibition of GSK-3β has led to accumulation of cytoplasmic β-catenin and its translocation into the nucleus.

Then, β-catenin interacted with the T-cell factor/lymphoid enhancer factor promoter complex in the nucleus leading to activation of target genes that are involved in the proliferation and differentiation of NSCs. It has been concluded that CU blocks Aβ-mediated inhibitory effects on neurogenesis through induction of the Wnt/β-catenin signaling.[26]

It should be emphasized that CU-encapsulating nanocarriers may provide additional benefits with regard to the abovementioned mechanisms. In a recent study, we have shown that formulations containing CU and DHA exert potentiating effects on the neurotrophin TrkB signaling and the induced brain-derived neurotrophic factor protein biosynthesis.[70] This signaling underlies neuronal survival, differentiation, and proliferation.[47,51] Therefore, future work will be needed to demonstrate the broad therapeutic capacities of CU encapsulating NPs in regenerative medicine, prevention of neurodegenerative disorders, and treatment of neurological diseases.

4) Conclusion

Neurodegeneration is caused by various pathways mediated by ROS. In the present work, we exploit the fact that liquid crystalline nanostructures may successfully co-encapsulate lipophilic molecules with the purpose of neuroprotection in combination therapies. The antioxidant-loaded nanocarriers were characterized by SAXS and QELS. They showed increased encapsulation efficiency for CU as compared to the reported values for PLGA-based NPs. The cellular viability results showed no cytotoxic effects of the nanocarriers at the studied lipid concentrations. Oxidative stress was generated by exposure of differentiated human neuroblastoma SH-SY5Y cells to H_2O_2 and the ROS levels were quantified by flow cytometry. Cubosomes and spongosomes loaded with CU and FO significantly attenuated the ROS accumulation in the neuronally derived cells as compared to the CU−FO-aqueous suspension. The pretreatment of neuronally derived SH-SY5Y cells by cubosomes, co-encapsulating CU and FO, resulted in a decreased percentage of dead cells and an increased number of live cells upon exposure to H_2O_2-induced oxidative stress. The performed study revealed that cubosome lipid particles loaded with CU and FO provide neuroprotective potential against

ROS accumulation and H_2O_2-induced cell death. Therefore, lipid-based cubosomes may be suitable as safe nanocarriers of phytopharmaceuticals in neuroregenerative strategies.

5) References

(1) Brookmeyer, R.; Abdalla, N.; Kawas, C.H.; Corrada, M.M. Forecasting the prevalence of preclinical and clinical Alzheimer's disease in the United States. *Alzheimers Dement*. **2018**, 14, 121-129.

(2) Barnham, K.J.; Masters, C.L.; Bush A.I. Neurodegenerative diseases and oxidative stress. *Nat Rev Drug Discov.* **2004**, *3*, 205-214.

(3) Gilgun-Sherki, Y.; Melamed, E.; Offen, D. Oxidative stress induced-neurodegenerative diseases: the need for antioxidants that penetrate the blood brain barrier. *Neuropharmacology.* **2001,** 40, 959-975.

(4) Jiang, T.; Suna, Q.; Chena, S.B. Oxidative stress: a major pathogenesis and potential therapeutic target of antioxidative agents in Parkinson's disease and Alzheimer's disease. *Progress in Neurobiology* **2016,** 147, 1-19.

(5) Uttara, B.; Singh, A.V.; Zamboni, P.; Mahajan, R.T. Oxidative stress and neurodegenerative diseases: a review of upstream and downstream antioxidant therapeutic options. *Curr Neuropharmacol*. **2009**, 7, 65-74.

(6) Dumont, M.; Beal M.F. Neuroprotective strategies involving ROS in Alzheimer disease. *Free Radic. Biol. Med*. **2011**, 51, 1014-1026.

(7) Zhong, L.; Zhou, J.; Chen, X.; Lou, Y.; Liu, D.; Zou, X.; Yang, B.; Yin, Y.; Pan, Y. Quantitative proteomics study of the neuroprotective effects of B12 on hydrogen peroxide-induced apoptosis in SH-SY5Y cells. *Scientific Rep.* **2016,** 6, 22635.

(8) Onyango, I.G.; Khan, S.M.; Bennett, J.P. Mitochondria in the pathophysiology of Alzheimer's and Parkinson's diseases. *Frontiers in Bioscience* **2017**, *22*, 854-872.

(9) Ankarcrona, M.; Mangialasche, F.; Winblad, B. Thinking Alzheimer's disease therapy: Are mitochondria the key? *Journal of Alzheimer's disease* **2010**, *20*, S579-S590.

(10) Federico, A.; Cardaioli, E.; Da Pozzo, P.; Formichi P.; Gallus, G.N. Mitochondria, oxidative stress and neurodegeneration. *Journal of the Neurological Sci.* **2012,** 322, 254-262.

(11) Stahon, K.E.; Bastian, C.; Griffith, S.; Kidd, G.J.; Brunet, S.; Baltan, S. Age-related changes in axonal and mitochondrial ultrastructure and function in white matter. *The Journal of Neuroscience* **2016**, 36, 9990-10001.

(12) Cho, D.H.; Nakamura, T.; Lipton, S.A. Mitochondrial dynamics in cell death and neurodegeneration. *Cell Mol. Life Sci*. **2010**; 67, 3435-3447.

(13) Lu, M.; Su, C.; Qiao, C.; Bian ,Y.; Ding, J.; Hu, G. Metformin prevents dopaminergic neuron death in MPTP/P-induced mouse model of Parkinson's disease via autophagy and mitochondrial ROS clearance. *International Journal of Neuropsychopharmacology* **2016**, 19, 1-11.

(14) Zádori, D.; Klivényi, P.; Szalárdy, L.; Fülöp, F.; Toldi, J.; Vécsei, L. Mitochondrial disturbances, excitotoxicity, neuroinflammation and kynurenines: novel therapeutic strategies for neurodegenerative disorders. *J. Neurol. Sci.* **2012**, 322, 187-191.

(15) Ahmed, T.; Gilani, A.H. Therapeutic potential of turmeric in Alzheimer's disease: curcumin or curcuminoids? *Phytother. Res.* **2014**, 28, 517-525.

(16) Soleimani, V.; Sahebkar, A.; Hosseinzadeh, H. Turmeric (*Curcuma longa*) and its major constituent (curcumin) as nontoxic and safe substances. *Review Phytother Res.* **2018,** 32, 985-995.

(17) Mahdavi, H.; Hadadi, Z.; Ahmadi, M. A review of the anti-oxidation, anti-inflammatory and anti-tumor properties of curcumin. *Traditional and Integrative Medicine* **2017**, 2, 188-195.

(18) Wilken, R.; Veena, M,S, ; Wang, M.B. ; Srivatsan, E.S. Curcumin: A review of anti-cancer properties and therapeutic activity in head and neck squamous cell carcinoma. *Mol. Cancer* **2011**, 7, 10-12.

(19) Gupta, S.C.; Patchva, S.; Aggarwal, B.B. Therapeutic roles of curcumin: lessons learned from clinical trials. *AAPS J.* **2013**, 15, 195-218.

(20) Serafini, M.M.; Catanzaro, M.; Rosini, M.; Racchi, M.; Lanni, C. Curcumin in Alzheimer's disease: can we think to new strategies and perspectives for this molecule? *Pharmacol. Res*. **2017**, 124, 146-155.

(21) Brondino, N.; Re, S.; Boldrini, A.; Cuccomarino, A.; Lanati, N.; Barale, F. ; Politi, P. Curcumin as a therapeutic agent in dementia: a mini systematic review of human studies. *Scientific World Journal* **2014**, 174282.

(22) Wu, J.; Li, Q.; Wang, X.; Yu, S.; Li, L.; Wu, X.; Chen, Y.; Zhao, J.; Zhao, Y. Neuroprotection by curcumin in ischemic brain injury involves the Akt/Nrf2 pathway. *PloS One* **2013**, 8, 59843.

(23) Lim, G.P.; Chu, T.; Yang, F.; Beech, W.; Frautschy, S.A.; Cole, G.M. The curry spice curcumin reduces oxidative damage and amyloid pathology in an Alzheimer transgenic mouse. *J. Neurosci.* **2001**, 21, 8370-8377.

(24) Hoppe, J.B., Coradini K., Frozza R.L., Oliveira C.M., Meneghetti A.B., Bernardi A., Pires E.S., Beck R.C., Salbego, C.G. Free and nanoencapsulated curcumin suppress beta-amyloid-induced cognitive impairments in rats: involvement of BDNF and Akt/GSK-3beta signaling pathway. *Neurobiol. Learn. Mem.* **2013**, 106, 134-144.

(25) Yang, F.; Lim, G.P.; Begum, A.N.; Ubeda, O.J.; Simmons, M.R.; Ambegaokar, S.S.; Chen, P.P.; Kayed, R.; Glabe, C.G.; Frautschy, S.A.; Cole, G.M. Curcumin inhibits formation of amyloid beta oligomers and fibrils, binds plaques, and reduces amyloid in vivo. *J. Biol. Chem.* **2005**, 280, 5892-5903.

(26) Tiwari, S.K.; Agarwal, S.; Seth, B.; Yadav, A.; Nair, S.; Bhatnagar, P.; Karmakar.; Kumari M.M.; Chauhan, L.K.; Patel, D.K.; Srivastava, V.; Singh, D.; Gupta, S.K.; Tripathi, A.; Chaturvedi, R.K.; Gupta, K.C. Curcumin-loaded nanoparticles potently induce adult neurogenesis and reverse cognitive deficits in Alzheimer's disease model via canonical Wnt/β-catenin pathway. *ACS Nano*. **2014**, 8, 76-103.

(27) Anand, P.; Kunnumakkara, A.B.; Newman, R.A.; Aggarwal, B.B. Bioavailability of curcumin: problems and promises. *Mol. Pharm*. **2007**, 4, 807-18.

(28) Fu, S.; Shen, Z.; Ajlouni, S.; Ng, K.; Sanguansri, L.; Augustin, M.A. Interactions of buttermilk with curcuminoids. *Food Chem.* **2014**, 149, 47-53.

(29) Zou, L.; Zheng, B.; Zhang, R.; Zhang, Z.; Liu, W.; Liu, C.; Zhang, C.; Xiao, H.; McClements, D.J. Influence of lipid phase composition of excipient emulsions on curcumin solubility, stability, and bioaccessibility. *Food Biophysics* **2016**, 11, 213–225.

(30) Chatzidaki, M.D.; Mitsou, E.; Yaghmur, A.; Xenakis, A.; Papadimitriou, V. Formulation and characterization of food-grade microemulsions as carriers of natural phenolic antioxidants. *Colloids Surfaces A. Physicochem. Eng. Asp.* **2015,** 483, 130-136.

(31) Gudipati, V.; Sandra, S.; McClements, D.J.; Decker, E.A. Oxidative stability and in vitro digestibility of fish oil-in-water emulsions containing multilayered membranes. *J. Agric. Food Chem.* **2010**, 58, 8093–8099.

(32) Pangeni, R.; Sharma, S.; Mustafa, G.; Ali, J.; Baboota, S. Vitamin E loaded resveratrol nanoemulsion for brain targeting for the treatment of Parkinson's disease by reducing oxidative stress. *Nanotech*. **2014**, 25, 485102.

(33) Belhaj, N.; Dupuis, F.; Arab-Tehrany, E.; Denis, F.; Paris, C.; Lartaud, I.; Linder, M. Formulation, characterization and pharmacokinetic studies of coenzyme Q10 PUFA's nanoemulsions. *Eur. J. Pharm. Sci.* 2012, 47, 305-312.

(34) Pan, Y.; Khalil, H.; Nicolazzo, J.A. The impact of docosahexaenoic acid on Alzheimer's disease: Is there a role of the blood-brain barrier? *Curr. Clin. Pharmacol*. **2015**, *10*, 222-241.

(35) Bousquet, M.; Saint-Pierre, M.; Julien, C.; Salem, N.; Cicchetti, F.; Calon, F. Beneficial effects of dietary omega-3 polyunsaturated fatty acid on toxin-induced neuronal degeneration in an animal model of Parkinson's disease. *FASEB J.,* **2008**, 22, 1213-1225.

(36) Denny-Joseph, K.M.; Muralidhara, K. Combined oral supplementation of fish oil and quercetin enhances neuroprotection in a chronic rotenone rat model: relevance to Parkinson's disease. *Neurochem. Res.* **2015**, 40, 894-905.

(37) Yaghmur, A.; Al-Hosayni, S.; Amenitsch, H.; Salentinig, S. Structural investigation of bulk and dispersed inverse lyotropic hexagonal liquid crystalline phases of eicosapentaenoic acid monoglyceride. *Langmuir* **2017***, 33*, 14045-14057.

(38) Shao, X.; Bor, G.; Al-Hosayni, S.; Salentinig, S.; Yaghmur, A. Structural characterization of self-assemblies of new omega-3 lipids: docosahexaenoic acid and docosapentaenoic acid monoglycerides. *Phys. Chem. Chem. Phys.,* **2018***, 20*, 23928-23941.

(39) Modi, G.; Pillay, V.; Choonara, Y.E. Advances in the treatment of neurodegenerative disorders employing nanotechnology. *Ann. N.Y. Acad. Sci.* **2010**, 1184, 154-172.

(40) Angelova, A.; Drechsler, M.; Garamus, V.M.; Angelov, B. Liquid crystalline nanostructures as pegylated reservoirs of omega-3 polyunsaturated fatty acids: structural insights toward delivery formulations against neurodegenerative disorders. *ACS Omega* **2018**, 3, 3235−3247.

(41) Sahni, J.K.; Doggui, S.; Ali, J.; Baboota, S.; Dao, L.; Ramassamy, C. Neurotherapeutic applications of nanoparticles in Alzheimer's disease. *J. Controlled Release* **2011**, 152, 208-231.

(42) Craparo, E.F.; Bondì, M.L.; Pitarresi, G.; Cavallaro, G. Nanoparticulate systems for drug delivery and targeting to the central nervous system. *CNS Neurosci. Med.* **2011**, 9, 1-14.

(43) Azhari, H.; Strauss, M.; Hook, S.; Boyd, B.J.; Rizwan, S.B. Stabilising cubosomes with tween 80 as a step towards targeting lipid nanocarriers to the blood–brain barrier. *Eur. J. Pharmaceutics Biopharmaceutics* **2016**, 104, 148-155.

(44) Fonseca-Santos, B.; Gremiao, D.; Palmira, M.; Chorilli, M. Nanotechnology-based drug delivery systems for the treatment of Alzheimer's disease. *International Journal of Nanomedicine* **2015**, 10, 4981-5003.

(45) Liu, Y.; An, S.; Li, J.; Kuang, Y.; He, X.; Guo, Y.; Ma, H.; Zhang, Y.; Ji, B.; Jiang, C. Brain-targeted co-delivery of therapeutic gene and peptide by multifunctional nanoparticles in Alzheimer's disease mice. *Biomaterials* **2016**, 80, 33-45.

(46) Kanwar, J.R.; Sun, X.; Punj, V.; Sriramoju, B.; Mohan, R.R.; Zhou, S.F.; Chauhan, A.; Kanwar, R.K. Nanoparticles in the treatment and diagnosis of neurological disorders: untamed dragon with fire power to heal. *Nanomedicine* **2012**, 8, 399-414.

(47) Angelova, A.; Angelov, B. Dual and multi-drug delivery nanoparticles towards neuronal survival and synaptic repair. *Neural Regen. Res.* **2017**, *12*, 886-889.

(48) Gao, H. Progress and perspectives on targeting nanoparticles for brain drug delivery. *Acta Pharmaceutica Sinica B.* **2016**, 6, 268-286.

(49) Roney, C.; Kulkarni, P.; Arora, V.; Antich, P.; Bonte, F.; Wu, A.; Mallikarjuana, N.N.; Manohar, S.; Liang, H.F.; Kulkarni, A.R.; Sung, H.W.; Sairam, M.; Aminabhavi, T.M. Targeted nanoparticles for drug delivery through the blood–brain barrier for Alzheimer's disease. *J. Control Release* **2005**, 108, 193-214.

(50) Modi, G.; Pillay, V.; Choonara, Y.E.; Ndesendo, V.M.K.; Du Toit, L.C.; Naidoo, D. Nanotechnological applications for the treatment of neurodegenerative disorders. *Progress in Neurobiology* **2009**, 88, 4: 272-285.

(51) Géral, C.; Angelova, A.; Lesieur, S. From molecular to nanotechnology strategies for delivery of neurotrophins: emphasis on brain-derived neurotrophic factor (BDNF). *Pharmaceutics*, **2013**, *5*, 127-167.

(52) Perez-Martınez, F.C.; Carrionc, B.; Cenaa, V. The use of nanoparticles for gene therapy in the nervous system. *Journal of Alzheimer's Disease* **2012**, 31, 697-710.

(53) Pyykkö, I.; Zou, J.; Zhang, W.; Zhang, Y. Nanoparticle-based delivery for the treatment of inner ear disorders. *Curr. Opin. Otolaryngol. Head Neck Surg.* **2011**, 19, 388-396.

(54) Wong, H.L.; Wu, X.Y.; Bendayan, R. Nanotechnological advances for the delivery of CNS therapeutics. *Adv. Drug Deliv. Rev.* **2012**, 16, 311-324.

(55) Angelov, B.; Angelova, A.; Filippov, S.K.; Drechsler, M.; Štěpánek, P.; Lesieur, S. Multicompartment lipid cubic nanoparticles with high protein upload: millisecond dynamics of formation. *ACS Nano* **2014**, 8, 5216–5226.

(56) Angelova, A.; Angelov, B.; Drechsler, M.; Lesieur, S. Neurotrophin delivery using nanotechnology. *Drug Discovery Today* **2013**, 18, 1263-1271.

(57) Lauzon, M.A.; Daviau, A.; Marcos, B.; Faucheux, N. Nanoparticle-mediated growth factor delivery systems: a new way to treat Alzheimer's disease. *J. Control Release* **2015**, 206, 187-205.

(58) Angelov, B.; Angelova, A. Nanoscale clustering of the neurotrophin receptor trkB revealed by super-resolution STED microscopy. *Nanoscale* **2017**, *9*, 9797-9804.

(59) Angelov, B.; Garamus, V.M.; Drechsler, M.; Angelova, A. Structural analysis of nanoparticulate carriers for encapsulation of macromolecular drugs. *J. Mol. Liquids* **2017**, 235, 83-89.

(60) Nazaruk, E.; Miszta, P.; Filipek, S.; Górecka, E.; Landau, E.M.; Bilewicz, R. Lyotropic cubic phases for drug delivery: Diffusion and sustained release from the mesophase evaluated by electrochemical methods. *Langmuir* **2015**, 31, 12753-12761.

(61) Conti, E.; Gregori, M.; Radice, I.; Da Re, F.; Grana, D.; Re, F.; Salvati, E.; Masserini, M.; Ferrarese, C.; Zoia, C.P.; Tremolizzo, L. Multifunctional liposomes interact with Abeta in human biological fluids: therapeutic implications for Alzheimer's disease. *Neurochem. Int.* **2017,** 108, 60-65.

(62) Biswas, A.; Kurkute, P.; Jana, B.; Laskar, A.; Ghosh, S. An amyloid inhibitor octapeptide forms amyloid type fibrous aggregates and affects microtubule motility. *Chem. Commun.* **2014**, 50, 2604–2607.

(63) Adak, A.; Das, G.; Barman, S.; Mohapatra, S.; Bhunia, D.; Jana, B.; Ghosh, S. Biodegradable neuro-compatible peptide hydrogel promotes neurite outgrowth, shows significant neuroprotection, and delivers anti-Alzheimer drug. *ACS Appl. Mater. Interfaces* **2017**, 9, 5067–5076.

(64) Airoldi, C.; Zona, C.; Sironi, E.; Colombo, L.; Messa, M.; Aurilia, D.; Gregori, M.; Masserini, M.; Salmona, M.; Nicotra, F.; La Ferla, B. Curcumin derivatives as newligands of Apeptides. *J. Biotechnol*. **2011**, 156, 317–324.

(65) Siddique, Y.H.; WasiKhan, S.B.R.; Naqvi, A.H. Synthesis of alginate-curcumin nanocomposite and its protective role in transgenic drosophila model of Parkinson's disease. *ISRN Pharmacology* **2013**, ID794582, 8.

(66) Sood, S.; Jain, K.; Gowthamarajan, K. Optimization of curcumin nanoemulsion for intranasal delivery using design of experiment and its toxicity assessment. *Colloids and Surfaces B: Biointerfaces* **2014**, 113, 330-337.

(67) Kakkara, V.; Mishrab, A.K.; Chuttanib, K.; Kaura, I.P. Proof of concept studies to confirm the delivery of curcumin loaded solid lipid nanoparticles (C-SLNs) to brain. *International Journal of Pharmaceutics* **2013**, 448, 354– 359.

(68) Maiti, P.; Dunbar1, G.L. Comparative neuroprotective effects of dietary curcumin and solid lipid curcumin particles in cultured mouse neuroblastoma cells after exposure to Aβ42. International Journal of Alzheimer's Disease **2017**, 4164872.

(69) Tsai, Y.M.; Jan, W.C.; Chien, C.F.; Lee, W.C.; Lin, L.C.; Tsai, T.H. Optimised nano-formulation on the bioavailability of hydrophobic polyphenol, curcumin, in freely-moving rats. *Food Chemistry* **2011**, 127, 918-925.

(70) Guerzoni, L.P.; Nicolas, V.; Angelova, A. in vitro modulation of TrkB receptor signaling upon sequential delivery of curcumin-DHA loaded carriers towards promoting neuronal survival. *Pharm. Res.* **2017,** 34, 492-505.

(71) Tsai, Y.M.; Chien, C.F.; Lin, L.C.; Tsai, T.H. Curcumin and its nano-formulation: the kinetics of tissue distribution and blood–brain barrier penetration. *International Journal of Pharmaceutics* **2011**, 416, 331-338.

(72) Doggui, S.; Sahni, J.K. ; Arseneault, M.; Dao, L.; Ramassamy, C. Neuronal uptake and neuroprotective effect of curcumin-loaded PLGA nanoparticles on the human SK-N-SH cell line. *J. Alzheimers Dis.* **2012**, 30, 377–392.

(73) Paka, G.D.; Doggui, S.; Zaghmi, A.; Safar, R.; Dao, L., Reisch, A.; Klymchenko, A.; Roullin, V.G.; Joubert, O.; Ramassamy, C. Neuronal uptake and neuroprotective properties of curcumin-loaded nanoparticles on SK-N-SH cell line: role of poly(lactide-coglycolide) polymeric matrix composition. *Mol. Pharmaceutics* **2016**, 13, 391-403.

(74) Paka, G.D.; Ramassamy, C. Optimization of curcumin-loaded PEG-PLGA nanoparticles by GSH functionalization: investigation of the internalization pathway in neuronal cells. *Mol. Pharmaceutics* **2017**, 14, 93-106.

(75) Ray, B.; Bisht, S.; Maitra, A., Maitra, A.; Lahiri, D.K. Neuroprotective and neurorescue effects of a novel polymeric nanoparticle formulation of curcumin (NanoCurcTM) in the neuronal cell culture and animal model: implications for Alzheimer's disease. *J. Alzheimers Dis.* **2011***,* 23, 61–77.

(76) Mathew, A.; Fukuda, T.; Nagaoka, Y.; Hasumura, T.; Morimoto, H.; Yoshida, Y.; Maekawa, T.; Venugopal, K.; Kumar, D.S. Curcumin loaded-PLGA nanoparticles conjugated with Tet-1 peptide for potential use in Alzheimer's disease. *PLoSOne* **2012**, 7.

(77) Mulik, R.S.; Mönkkönen, J.; Juvonen, R.O.; Mahadik, K.R.; Paradkar, A.R. ApoE3 mediated poly(butyl) cyanoacrylate nanoparticles containing curcumin: study of enhanced activity of curcumin against beta amyloid induced cytotoxicity using in vitro cell culture model. *Mol. Pharm.* **2010**, 7, 815–825.

(78) Lazar, A.N.; Mourtas, S.; Youssef, I.; Parizot, C.; Dauphin, A.; Delatour; B.; Antimisiaris, S.G., Duyckaerts, C. Curcumin-conjugated nanoliposomes with high affinity for Aβ deposits: possible applications to Alzheimer disease. *Nanomedicine: Nanotechnology, Biology, and Medicine* **2013**, 9, 712-721.

(79) Sancini, G.; Gregori, M.; Salvati, E.; Cambianica, L.; Re, F.; Ornaghi, F.; Canovi, M.; Fracasso, C.; Cagnotto, A.; Colombo, M.; Zona, C.; Gobbi, M.; Salmona, M.; La Ferla, B.; Nicotra, F.; Masserini, M. Functionalization with TAT-peptide enhances blood–brain barrier crossing in vitro of nanoliposomes carrying a curcumin-derivative to bind amyloid-β peptide. *J. Nanomed. Nanotechnol.* **2013,** 4, 3.

(80) Mourtas, S.; Canovi, M.; Zona, C.; Aurilia, D.; Niarakis, A.; La Ferla, B.; Salmona, M.; Nicotra, F.; Gobbi, M.; Antimisiaris, S.G. Curcumin-decorated nanoliposomes with very high affinity for amyloid beta1–42 peptide. *Biomaterials* **2011**, 32, 1635-1645.

(81) Shaikh, J.; Ankola, D.D.; Beniwal, V.; Singh, D.; Kumar, M.N. Nanoparticle encapsulation improves oral bioavailability of curcumin by at least 9-fold when compared to curcumin administered with piperine as absorption enhancer. *Eur. J. Pharm. Sci.* **2009,** 37, 223-30.

(82) Fong, W.K.; Negrini, R.; Vallooran, J.J.; Mezzenga, R.; Boyd, B.J. Responsive self-assembled nanostructured lipid systems for drug delivery and diagnostics. *J. Colloid Interface Sci.* **2016**, 484, 320-339.

(83) Angelova, A.; Angelov, B.; Mutafchieva, R.; Lesieur, S. Biocompatible mesoporous and soft nanoarchitectures. *J. Inorg. Organomet Polym. Mater.* **2015**, 25, 214-232.

(84) Mulet, X.; Boyd, B.J.; Drummond, C.J. Advances in drug delivery and medical imaging using colloidal lyotropic liquid crystalline dispersions. *J. Colloid Interface Sci.* **2013**, 393, 1-20.

(85) Yaghmur, A.; Glatter, O. Characterization and potential applications of nanostructured aqueous dispersions. *Adv. Colloid Interface Sci.* **2009**, 147-148, 333-342.

(86) Wu, H.; Li, J.; Zhang, Q.; Yan, X.; Guo, L.; Gao, X.; Qiu, M.; Jiang, X.; Lai, R.; Chen, H. A novel small odorranalectin-bearing cubosomes: preparation, brain delivery and pharmacodynamic study on amyloid-b25–35-treated rats following intranasal administration. *Eur. J. Pharm. Biopharm.* **2012**, 80, 368-378.

(87) Angelov, B.; Angelova, A.; Garamus, V.M.; Drechsler, M.; Willumeit, R.; Mutafchieva, R.; Štěpánek P., Lesieur, S. Earliest stage of the tetrahedral nanochannel formation in cubosome particles from unilamellar nanovesicles. *Langmuir* **2012**, 28, 16647-16655.

(88) Zerkoune, L.; Lesieur, S.; Putaux, J.L.; Choisnard, L.; Gèze, A.; Wouessidjewe, D.; Angelov, B.; Vebert-Nardin, C.; Doutch, J.; Angelova, A. Mesoporous self-assembled nanoparticles of biotransesterified cyclodextrins and nonlamellar lipids as carriers of water-insoluble substances. *Soft Matter* **2016**, 12, 7539-7550.

(89) Esposito, E.; Drechsler, M.; Mariani, P.; Panico, A. M.; Cardile,V.; Crascì, L.; Carducci, F.; Graziano, A. C. E.; Cortesi, R.; Puglia, C. Nanostructured lipid dispersions for topical administration of crocin, apotent antioxidant from saffron (Crocus sativus L.). *Mater. Sci. Eng. C* **2017**, 71, 669–677.

(90) Valldeperas, M.; Wiśniewska, M.; Ram-On, M.; Kesselman, E.; Danino, D.; Nylander, T.; Barauskas, J. Sponge phases and nanoparticle dispersions in aqueous mixtures of mono- and diglycerides. *Langmuir* **2016**, 32, 8650-8659.

(91) Barauskas, J.; Misiunas, A.; Gunnarsson, T.; Tiberg, F.; Johnsson, M. "Sponge" nanoparticle dispersions in aqueous mixtures of diglycerol monooleate, glycerol dioleate, and polysorbate 80. *Langmuir* **2006**, 22, 6328-6334.

(92) Zou, A.; Li, Y.; Chen, Y.; Angelova, A.; Garamus, V. M.; Li, N.; Drechsler, M.; Angelov, B.; Gong, Y. Self-assembled stable sponge type nanocarries for *Brucea javanica* oil delivery. *Colloids Surf., B* **2017**, 153, 310−319.

(93) Jang, Y.; Chung, H. J.; Hong, J. W.; Yun, C. W.; Chung, H. Absorption mechanism of DHP107, an oral paclitaxel formulation that forms a hydrated lipidic sponge phase. *Acta Pharmacol. Sin.* **2017**, 38, 133−145.

(94) Hazzah, H. A.; Farid, R. M.; Nasra, M. M. A.; El-Massik, M. A.; Abdallah, O. Y. Lyophilized sponges loaded with curcumin solid lipid nanoparticles for buccal delivery: development and characterization. *Int. J. Pharm*. 2015, 492, 248−257.

(95) Han, S.; Shen, J. Q.; Gan, Y.; Geng, H. M.; Zhang, X. X.; Zhu, C.L.; Gan, L. Novel vehicle based on cubosomes for ophthalmic delivery of flurbiprofen with low irritancy and high bioavailability. *Acta Pharmacol. Sin.* **2010**, 31, 990−998.

(96) Angelova, A.; Angelov, B.; Mutafchieva, R.; Lesieur, S.; Couvreur, P. Self-assembled multicompartment liquid crystalline lipid carriers for protein, peptide, and nucleic acid drug delivery. *Acc. Chem. Res*. **2011**, *44*, 147-156.

(97) Rodrigues, L.; Kyriakos, K.; Schneider, F.; Dietz, H.; Winter, G.; Papadakis, C. M.; Hubert, M. Characterization of lipid-based hexosomes as versatile vaccine carriers. *Mol. Pharmaceutics* **2016**, 13, 3945−3954.

(98) Kulkarni, C.V.; Wachter, W.; Iglesias-Salto, G.; Engelskirchen, S.; Ahualli, S. Monoolein: a magic lipid? *Phys. Chem. Chem. Phys.* **2011,** 13, 3004-21.

(99) Angelov, B.; Angelova, A.; Garamus, V.M.; Le Bas, G.; Lesieur, S.; Ollivon, M.; Funari, S.S.; Willumeit, R.; Couvreur P. Small-angle neutron and X-ray scattering from amphiphilic stimuli-responsive diamond type bicontinuous cubic phase, *J. Am. Chem. Soc.,* **2007**, *129,* 13474-13479.

(100) Milak, S.; Zimmer, A. Glycerol monooleate liquid crystalline phases used in drug delivery systems. *Int J.Pharm.* **2015**; 478, 569-587.

(101) Angelova, A.; Fajolles, C.; Hocquelet, C,; Djedaïni-Pilard, F,; Lesieur, S.; Bonnet, V.; Perly, B.; Lebas, G.; Mauclaire, L.; Physico-chemical investigation of asymmetrical peptidolipidyl-cyclodextrins*, J. Coll. Interface Sci.* **2008**, 322, 304-314.

(102) Siekmann, B.; Bunjes, H.; Koch, M.H.J.; Westesen, K. Preparation and structural investigations of colloidal dispersions prepared from cubic monoglyceride-water phases. *Int. J. Pharm.* **2002,** 244, 33-43.

(103) Yaghmur, A.; Sartori, B.; Rappolt, M. Self-assembled nanostructures of fully hydrated monoelaidin–elaidic acid and monoelaidin–oleic acid systems. *Langmuir* **2012,** 28, 10105-10119.

(104) Angelova, A.; Angelov, B.; Garamus, V. M.; Couvreur, P.; Lesieur, S. Small-angle X-ray scattering investigations of biomolecular confinement, loading, and release from liquid-crystalline nanochannel assemblies. *J. Phys. Chem. Lett.* **2012**, 3, 445−457.

(105) Zhai, J.; Tran, N.; Sarkar, S.; Fong, C.; Mulet, X.; Drummond, C.J. Self-assembled lyotropic liquid crystalline phase behavior of monoolein–capric acid–phospholipid nanoparticulate systems. *Langmuir* **2017**, 33, 2571-2580.

(106) Angelova, A.; Angelov, B.; Papahadjopoulos-Sternberg, B.; Bourgaux, C.; Couvreur P. Protein driven patterning of self-assembled cubosomic nanostructures: long oriented nanoridges. *J. Phys. Chem. B* **2005**,109, 3089-3093.

(107) Shen, H.H.; Crowston, J.G.; Huber, F.; Saubern, S.; McLean, K.M.; Hartley, P.G. The influence of dipalmitoyl phosphatidylserine on phase behaviour of and cellular response to lyotropic liquid crystalline dispersions. *Biomaterials* **2010,** 31, 9473-9481.

(108) Zabara, A.; Negrini, R.; Onaca-Fischer, O.; Mezzenga, R. Perforated bicontinuous cubic phases with pH-responsive topological channel interconnectivity. *Small* **2013**, 9, 3602-3609.

(109) Ganem-Quintanar, A.; Quintanar-Guerrero, D.; Buri, P. Monoolein: a review of the pharmaceutical applications. *Drug Dev. Ind. Pharm.* **2000,** 26, 809-20.

(110) Epand, R.M.; Epand, R.F.; Ahmed, N.; Chen, R. Promotion of hexagonal phase formation and lipid mixing by fatty acids with varying degrees of unsaturation. *Chem. Phys. Lipids* **1991**, 57, 75−80.

(111) Rakotoarisoa, M.; Angelova, A. Amphiphilic nanocarrier systems for curcumin delivery in neurodegenerative disorders. *Medicines* **2018**, *5*, 126.

(112) Lawrence, M. J., Surfactant systems: their use in drug delivery, *Chem. Soc. Rev.*, **1994**, *23*, 417-424.

(113) Barriga, H.M.G.; Holme, M.N.; Stevens, M.M. Cubosomes: The next generation of smart lipid nanoparticles? *Angew Chem. Int. Ed. Engl.* **2018**, doi: 10.1002/anie.201804067.

(114) Encinas, M.; Iglesias, M.; Liu, Y.H.; Wang, H.Y.; Muhaisen, A.; Cena, V.; Gallego, C.; Comella, J.X. Sequential treatment of SH-SY5Y cells with retinoic acid and brain-derived neurotrophic factor gives rise to fully differentiated, neurotrophic factor-dependent, human neuron-like cells. *J. Neurochem.* **2000**, 75, 991-1003.

(115) Kaplan, D.R.; Matsumoto, K.; Lucarelli, E.; Thiele, C.J. Induction of trkB by retinoic acid mediates biologic responsiveness to BDNF and differentiation of human neuroblastoma cells. *Neuron* **1993**, 11, 321-331.

(116) Lopes, F.M.; Schröder, R.; da Frota, M.L. Jr.; Zanotto-Filho, A.; Müller, C.B.; Pires, A.S.; Meurer, R.T.; Colpo, G.D.; Gelain, D.P.; Kapczinski, F.; Moreira, J.C.; Fernandes M.d.C.; Klamt F. Comparison between proliferative and neuron-like SH-SY5Y cells as an *in vitro* model for Parkinson disease studies. *Brain Res*. **2010**, *1337*, 85-94.

(117) Zhang, L.; Yu, H.; Zhao, X.; Lin, X.; Tan, C.; Cao, G.; Wang, Z. Neuroprotective effects of salidroside against beta-amyloid-induced oxidative stress in SH-SY5Y human neuroblastoma cells. *Neurochem Int*. **2010**, *57*, 547-55.

(118) Yang, R.; Wei, L.; Fu, Q.Q.; Wang, H.; You, H.; Yu, H.R. SOD3 ameliorates H_2O_2-induced oxidative damage in SH-SY5Y cells by inhibiting the mitochondrial pathway. *Neurochem. Res.* **2016,** 41, 1818-1830.

(119) Gay, N.H.; Phopin, K.; Suwanjang, W.; Songtawee, N.; Ruankham, W.; Wongchitrat, P.; Prachayasittikul, S.; Prachayasittikul, V. Neuroprotective effects of phenolic and carboxylic acids on oxidative stress-induced toxicity in human neuroblastoma SH-SY5Y cells. *Neurochemical Research* **2018**, *43*, 619–636.

(120) Gay, N.H.; Phopin, K.; Suwanjang, W.; Ruankham, W.; Wongchitrat, P.; Prachayasittikul, S.; Prachayasittikul, V. Attenuation of oxidative stress-induced neuronal cell death by *Hydnophytum formicarum Jack*. *Asian Pacific Journal of Tropical Medicine* **2018**, *11*, 415-422.

(121) Eruslanov, E.; Kusmartsev, S. Identification of ROS using oxidized DCFDA and flow-cytometry. *Methods Mol. Biol*. **2010**, 594: 57-72.

(122) Rastogi, R.P.; Shailendra, P.S.; Donat, P.H.; Rajeshwar, P.S. Detection of reactive oxygen species (ROS) by the oxidant-sensing probe 2′,7′-dichlorodihydrofluorescein diacetate in the cyanobacterium *Anabaena variabilis* PCC 7937. *Biochem. Biophys. Res. Commun.* **2010,** 397, 603-607.

(123) Blanchet, C.E.; Spilotros, A.; Schwemmer, F.; Graewert, M.A.; Kikhney, A.G.; Jeffries, C.M.; Franke, D.; Mark, D.; Zengerle, R.; Cipriani, F.; Fiedler, S.; Roessle, M.; Svergun, D.I. Versatile sample environments and automation for biological solution X-ray scattering experiments at the P12 beamline (PETRA III, DESY). *J. Appl. Cryst.* **2015**, *48*, 431–443.

(124) Datki, Z.; Juhász, A.; Gálfi, M.; Soós, K.; Papp, R.; Zádori, D.; Penke, B. Method for measuring neurotoxicity of aggregating polypeptides with the MTT assay on differentiated neuroblastoma cells. *Brain Research Bulletin* **2003**, *62*, 223-229.

Chapter 3: Curcumin, fish oil and catalase - loaded lyotropic liquid crystalline nanostructures

Cubic liquid crystalline nanostructures involving catalase and curcumin: BioSAXS study and catalase peroxidatic function after cubosomal nanoparticle treatment of differentiated SH-SY5Y Cells

Miora Rakotoarisoa[a], Borislav Angelov[b], Shirly Espinoza[b], Krishna Khakurel[b], Thomas Bizien[c] and Angelina Angelova[a].

[a] Université Paris-Saclay, CNRS, Institut Galien Paris-Sud UMR8612, F-92296 Châtenay-Malabry, France; [b] Institute of Physics, ELI Beamlines, Academy of Sciences of the Czech Republic, Na Slovance 2, CZ-18221 Prague, Czech Republic; [c] Synchrotron SOLEIL, l'Orme des Merisiers, Saint-Aubin - BP 48, 91192 Gif-sur-Yvette Cedex, France.

Accepted in Molecules

Cubic liquid crystalline nanostructures involving catalase and curcumin: BioSAXS study and catalase peroxidatic function after cubosomal nanoparticle treatment of differentiated SH-SY5Y Cells

Abstract:

The development of nanomedicines for the treatment of neurodegenerative disorders demands innovative nanoarchitectures for combined loading of multiple neuroprotective compounds. We report dual-drug loaded monoolein-based liquid crystalline architectures designed for the encapsulation of a therapeutic protein and a small molecule antioxidant. Catalase (CAT) is chosen as a metalloprotein, which provides enzymatic defense against oxidative stress caused by reactive oxygen species (ROS) such as hydrogen peroxide (H_2O_2). Curcumin (CU), solubilized in fish oil, is co-encapsulated as a chosen drug with multiple therapeutic activities, which may favor neuro-regeneration. The prepared self-assembled biomolecular nanoarchitectures are characterized by biological synchrotron small-angle X-ray scattering (BioSAXS) at multiple compositions of the lipid/co-lipid/water phase diagram. Constant fractions of curcumin (an antioxidant) and a PEGylated agent (TPGS-PEG_{1000}) are included with regard to the lipid fraction. Stable cubosome architectures are obtained for several ratios of the lipid ingredients monoolein (MO) and fish oil (FO). The impact of catalase on the structural organization of the cubosome nanocarriers is revealed by the variations of the cubic lattice parameters deduced by BioSAXS. The outcome of the cellular uptake of the dual drug-loaded nanocarriers is assessed by performing a bioassay of catalase peroxidatic activity in lysates of nanoparticle-treated differentiated SH-SY5Y human cells. The obtained results reveal the neuroprotective potential of the in vitro studied cubosomes in terms of enhanced peroxidatic activity of the catalase enzyme, which enables the inhibition of H_2O_2 accumulation in degenerating neuronal cells.

1) Introduction

Self-assembled lipid cubic phase (LCP) architectures comprise bilayer lipid membranes with a three-dimensional (3D) crystalline packing order and periodic networks of aqueous channels (Figure 1).[1–6] The amphiphilic nature of the lyotropic liquid crystalline phases and nanoparticles (LCNPs) makes them suitable for the embedding of either lipophilic or hydrophilic guest compounds.[7–19] It has been estimated that LCPs have a large surface area of lipid/water interfaces, which is of the order of 400 m^2/g.[7] Compared to liposome carriers, lipid-based cubosomes, hexosomes and spongosomes involve multiple internal compartments, which represent a structural advantage enabling an enhanced encapsulation efficacy.[9–11,14–19] The entrapment of biomolecules of various dimensions and hydrophilicities is achievable in such nanocarriers as well as their sustained release.[10,12] For example, LCPs have been used to encapsulate proteins of different concentrations and sizes from Cyt C (12 kDa) to fibrinogen (340 kDa).[8,11,20–27] High encapsulation efficacy has been reported for hydrophilic guest macromolecules such as brain-derived neurotrophic factor (BDNF), ovalbulmin and protein vaccines.[11,20–24] Soluble, peripheral, and integral membrane proteins have been studied in LCPs in relation to in meso protein crystallization, biosensor development involving encapsulated enzymes, and drug-delivery systems.[21–28] LCP-derived nanocarriers are increasingly used in a range of applications employing lipophilic drugs and theranostic agents.[14–19] The bioavailability of anti-inflammatory (flurbiprofen)[14], antiretroviral (efavirenz)[15], and anticancer (paclitaxel)[16] agents, as well as of antioxidants such as curcumin[17,19], has been considerably improved thanks to their protection and transport by the host cubic liquid crystalline phases.[18]

Regarding the lipid polymorphism, liquid crystalline phases have been formed by the self-assembly of hydrated mixtures of lyotropic lipids, co-lipids (oils or surfactants), and an aqueous phase, which may contain dissolved biomolecules (e.g., proteins, peptides or nucleic acids).[1–7,18–27,29–36] Hydrated non-lamellar lipids such as monoolein (MO) can self-assemble into inverted bicontinuous cubic phases, bicontinuous sponge or inverted hexagonal phases

depending on the experimental conditions and the applied stimuli.[4,5,18,25,29–32] Different types of bicontinuous cubic phases have been observed in lipid membranous systems.[3–7,25,29] Primitive (also referred to as *Im3m*/Q^{IIP}), double diamond (*Pn3m*/Q^{IID}), and gyroid (*Ia3d*/Q^{IIG}) cubic phases (Figure 1) are the most common ones for lyotropic monoglycerides. Cubosome nanoparticles are fabricated upon dispersion of the bulk cubic liquid crystalline phases in excess aqueous medium.[8,9,13,16–20,24] The cubosome structure is sensitive to the incorporation of additives such as therapeutic molecules and diagnostic probes required for monitoring of the biomedical response to active targeting.[9,16,18,21,35]

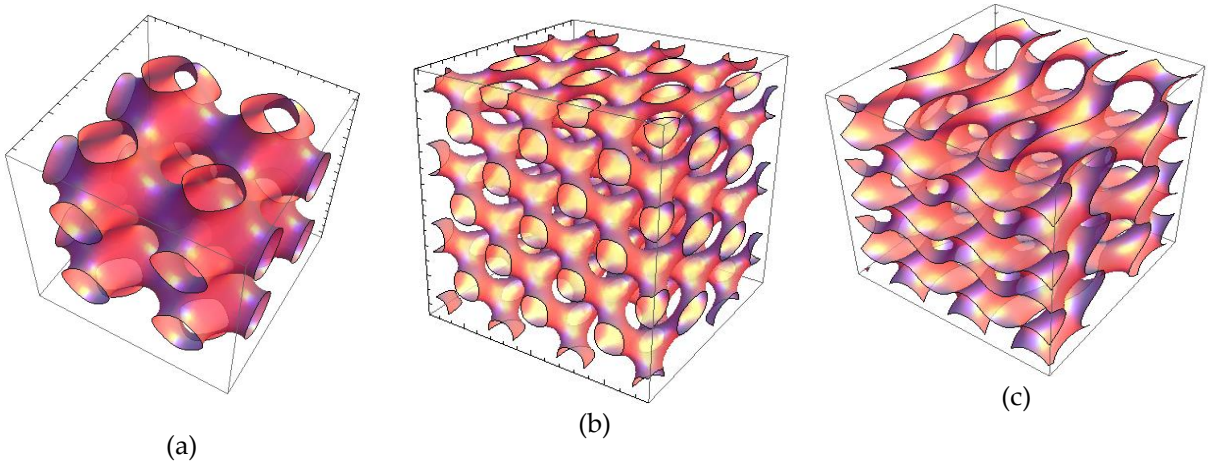

Figure 1. Three-dimensional organizations of cubic liquid crystalline phases: (a) Primitive cubic (also referred to as *Im3m*/Q^{IIP}), (b) bicontinuous double diamond cubic (*Pn3m*/Q^{IID}), and (c) bicontinuous gyroid cubic (*Ia3d*/Q^{IIG}) types.

It is believed that cubosomal nanostructures co-loaded with a therapeutic protein and a natural antioxidant are safe and provide neuroprotection against oxidative stress and neuronal damage.[37] Currently, nanoscale materials are attracting increasing interest for therapeutic applications in the field of neurological disorders.[37–41] In our recent study, we showed that cubosome lipid nanoparticles loaded with curcumin (CU) and fish oil (FO) have neuroprotective potential against the accumulation of reactive oxygen species (ROS) and H_2O_2-induced cell death.[19] Here, we combine curcumin and a therapeutic antioxidant enzyme in such advanced nanostructured lipid carriers.

Catalase (a tetrameric protein formed by 60-kDa monomer units) is a metalloenzyme that catalyzes the dismutation of H_2O_2 (a harmful oxidizing agent) to oxygen and water.[42–46] Catalase (CAT) is expressed in all major bodily organs (especially in the liver and kidneys) and in erythrocytes, where it plays an essential role in cell defense against oxidative stress.[47–50] Polymorphism of the catalase gene is associated with a number of diseases such as diabetes, Alzheimer's disease, cancer, hypertension, vitiligo, and acatalasemia.[51–54] It should be emphasized that catalase undergoes rapid elimination from the bloodstream and is characterized by poor intracellular delivery. Thus, catalase exhibits a short half-life and poor operational stability and reusability as an enzyme, which limits its potential therapeutic applications.[55–60] The unstable biomacromolecule can be immobilized in order to increase its stability and improve its enzymatic performance, solubility and specificity.[61–67] Catalase has been immobilized on solid supports from natural polymers (chitosan, gelatin, etc.), synthetic polymers (styrene, methyl methacrylate, acrylamide, etc.), and inorganic particles (calcium carbonate, silica, gold, etc.).[61–67] This helped to overcome the enzyme's degradation or deactivation. Liposomes have been used for intravenous catalase delivery.[63]

The present work focuses on the design and characterization of advanced self-assembled liquid crystalline nanostructures of catalase and curcumin in view of a prospective combination therapy for neurodegenerative disorders. Self-assembly properties are investigated by biological synchrotron small-angle X-ray scattering (BioSAXS), which is a high-throughput technique providing valuable structural data from weakly scattering biological solutions in real time.[6,35,68,69] BioSAXS can detect and determine the internal nanostructure, the shape and the structural evolution of various kinds of protein, peptide and lipid-protein assemblies.[11,22,32,68–70] We study mixed lipid (MO)/protein (catalase) self-assembly into nanostructures in the presence of a small molecule antioxidant (curcumin).
Our first aim is to determine via BioSAXS the structural effect of the catalase enzyme's inclusion into cubic liquid crystalline assemblies, i.e., catalase-associated cubosomal nanostructures. The second aim of the work is to evaluate the catalase activity after the

treatment of neuronally derived SH-SY5Y cells with catalase-associated cubosome nanoparticles.

2) Materials and methods

a. Materials

Monoolein (MO) with purity > 99% was obtained from Hampton research. The pegylated amphihile, D-α-tocopherol polyethylene glycol-1000 succinate (denoted as TPGS-PEG_{1000}) was purchased from Sigma Aldrich. Fish oil (FO) and curcumin (CU) with purity > 66% were purchased from Sigma Aldrich. The water used was of MilliQ quality (Millipore Corp., Molsheim, France). Catalase (CAT) was purchased from Sigma Aldrich (Lyon, France). For cell culture experiments, Dulbecco's modified Eagle's Medium (DMEM), streptomycin-penicillin, phosphate buffered saline (PBS), trypsin, ethylenediaminetetraacetic acid EDTA, retinoic acid (RA) and 3-(4,5-Dimethylthiazol-2-yl)-2,5-diphenyl tetrazolium bromide (MTT) were supplied by Sigma-Aldrich. Foetal bovine serum (FBS) was provided by Thermo Fischer Scientific (Illkirch, France).

b. Design and production of self-assembled nanocarriers for the loading of catalase and curcumin

The compositions of the investigated self-assembled MO/$TPEG_{1000}$/FO/CU/CAT systems are chosen from the phase diagram presented in Figure 2. Five dilution lines (DL), denoted as DL 10:90, DL 20:80, DL 30:70, DL 40:60, and DL 60:40 (wt%/wt%), are defined in order to characterize the lyotropic behavior of the multicomponent amphiphilic mixtures of therapeutic significance. The water-rich region corresponds to dispersions of nanocarriers in excess aqueous medium. The lipid-rich region corresponds to bulk liquid crystalline assemblies (Figure 2).

c. Preparation of bulk liquid crystalline systems

The lipid monoolein (MO), the surfactant TPGS-PEG_{1000}, fish oil (FO), and curcumin (CU) were weighed and dissolved in chloroform. The samples were prepared at room temperature at four different fish oil/monoolein weight ratios of 10:90, 20:80, 30:70 and 40:60 (wt%/wt%) (Table 1). The solvent was evaporated under a stream of a nitrogen gas for 1 h at room temperature to create a thin film lipid sample. The samples were lyophilized overnight under cooling to remove the excess solvent. This step was followed by the hydration of the thin film samples by a solution of catalase (0.5 wt%) protein (a buffer solution with pH 7 prepared using Milli-Q water). The concentrations were varied from 50 wt% to 90 wt% in aqueous phase with regard to the lipid phase. Finally, the samples were vortexed vigorously at room temperature in cycles during 15 min.

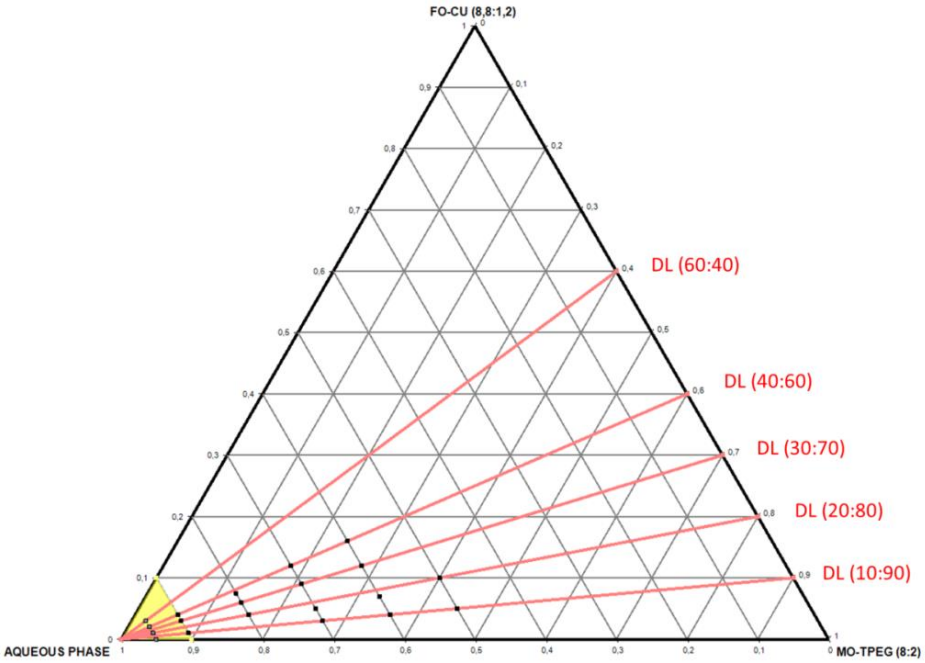

Figure 2. Phase diagram showing the dilution lines for the preparation of nanocarriers composed of monoolein (MO), TPGS-PEG_{1000} amphiphile, fish oil (FO), curcumin (CU), and water. The TPGS-$PEG_{1000}$and FO/MO weight ratios are constant (80:20 and 88:12, respectively). The water-rich region is represented by a yellow triangle. The aqueous phase contains catalase (CAT) in the CAT-loaded formulations. The black points indicate the compositions for which experimental biological synchrotron small-angle X-ray scattering (BioSAXS) data

are shown in Table 1 in the sequence from more concentrated to more diluted assemblies: samples C195, C196, C197 and C199 on the dilution line DL 10:90; samples C285, C286, C287 and C288 on the dilution line DL 20:80; samples C376, C377, C378 and C379 on the dilution line DL 30:70; and samples C466, C467, C468 and C469 on the dilution line DL 40:60.

Table 1. Compositions of bulk liquid crystalline phases presented as mass proportions of MO, TPGS-PEG_{1000}, FO, CU and catalase.

Sample Code	Catalase (0.5 wt%) in aqueous buffer (pH 7) (g)	MO (g)	TPGS-PEG_{1000} (g)	FO (g)	CU (g)
Dilution Line (FO:MO) = DL (10:90)					
C195	0.013	0.0090	0.0020	0.0010	0.00013
C196	0.015	0.0072	0.0018	0.0009	0.00010
C197	0.018	0.0054	0.0013	0.0007	0.00008
C199	0.023	0.0018	0.0004	0.0002	0.00003
Dilution Line (FO:MO) = DL (20:80)					
C285	0.013	0.0080	0.0020	0.0022	0.00025
C286	0.015	0.0066	0.0016	0.0016	0.00018
C287	0.018	0.0050	0.0012	0.0011	0.00013
C288	0.020	0.0032	0.0008	0.0009	0.00010
Dilution Line (FO:MO) = DL (30:70)					
C376	0.015	0.0056	0.0014	0.0027	0.00030
C377	0.018	0.0042	0.0010	0.0020	0.00023
C378	0.020	0.0028	0.0007	0.0013	0.00015
C379	0.023	0.0014	0.0003	0.0007	0.00008
Dilution Line (FO:MO) = DL (40:60)					
C466	0.015	0.0048	0.0012	0.0036	0.00040
C467	0.018	0.0036	0.0009	0.0027	0.00030
C468	0.020	0.0025	0.0006	0.0017	0.00019
C469	0.023	0.0012	0.0003	0.0009	0.00010

d. Preparation of aqueous dispersions of nanoparticles

The lipid nanoparticles were prepared by the method of hydration of a lyophilized thin lipid film followed by physical agitation in excess aqueous phase.[19,22,34,39] The lipids and the

hydrophobic constituents were dissolved in chloroform and mixed at desired proportions (Table 2). The solvent in the vials was evaporated under a stream of nitrogen gas for 1 h at room temperature to create a thin film lipid sample. The excess organic solvent was removed overnight using a lyophilizer. The thin film samples were hydrated for 24 h at room temperature in a buffer solution for blank (catalase-free) lipid nanoparticles and in a solution of catalase (0.5 wt%) for catalase - loaded lipid nanoparticles. The self-assembled mixtures were dispersed using a vortex until milky solutions were obtained.

Table 2. Lipid nanoparticle constituents and their mass proportions.

95 wt% Aqueous Phases		MO (g)	TPGS-PEG$_{1000}$ (g)	FO (g)	CU (g)
CU-Loaded NPs	CU and CAT-Loaded NPs				
MO	MO-CAT	0.02	0.005		
MO_1-FO_1		0.016	0.004	0.0045	
$(MO\text{-}FO\text{-}CU)_1$	$(MO\text{-}FO\text{-}CU\text{-}CAT)_1$	0.016	0.004	0.0045	0.0005
$(MO\text{-}FO\text{-}CU)_2$	$(MO\text{-}FO\text{-}CU\text{-}CAT)_2$	0.012	0.003	0.0090	0.0010
$(MO\text{-}FO\text{-}CU)_3$	$(MO\text{-}FO\text{-}CU\text{-}CAT)_3$	0.008	0.002	0.0135	0.0015

e. Synchrotron small angle x-ray scattering (BioSAXS)

For nanostructure determination with lipid/protein assemblies, BioSAXS experiments were performed at the SWING beamline [70] of synchrotron SOLEIL (Saint Aubin, France). The sample-to-detector distance was 3 m. The patterns were recorded with a two-dimensional EigerX 4-M detector (Dectris) at 12 keV, allowing measurements in the q-range from 0.00426 to 0.37 Å^{-1}. The q-vector was defined as $q = (4\pi/\lambda) \sin\theta$, where 2θ is the scattering angle. The synchrotron radiation wavelength was $\lambda = 1.033$ Å. The q-range calibration was done using a standard sample of silver behenate ($d = 58.38$ Å). The temperature was 22 °C.

The investigated samples were filled in capillaries with a diameter of 1.5 mm and were sealed by paraffin wax. They were oriented in front of the X-ray beam (25 × 375 μm^2) using a de-signed holder for multiple capillaries positioning (X, Y, Z). Exposure times of 500 ms (for bulk lipid samples) or 1 s (for diluted nanoparticles) were used. No radiation damage was observed at these exposure times. Scattering patterns of an empty capillary and a capillary filled with

MilliQ water were recorded for intensity background subtraction. Data processing of the recorded 2D images was performed by the FOXTROT software.[73] An average of three spectra per capillary was acquired. The lattice parameters of the liquid crystalline phases were derived from the Bragg peaks detected in the X-ray diffraction patterns.

f. Nanoparticle size determination

The hydrodynamic diameters of the particles in the nanodispersions were determined based on the principle of quasi-elastic light scattering (QELS). The particle size distribution was determined by means of a Nano-ZS90 device (Malvern Instruments) collecting the intensity of the scattered light at an angle of 90° with regards to the incident laser beam. Data collection was carried out at 25 °C. The samples were diluted to 1/10 in a buffer in order to ensure Brownian motion conditions for the particles. The refractive index and viscosity of the MilliQ water wree equal to 1.330 and 0.8872 mPa.s, respectively. Each analysis was a result of three consecutive measurements.

g. Cell culture

The human neuroblastoma SH-SY5Y cells were cultured in DMEM medium with high glucose supplement, 10% FBS, and 0.5% streptomycin-penicillin. They were incubated at 37 °C in a saturated humidity atmosphere containing 5% CO_2. Before every experiment, the cells were grown in plastic flasks (75 cm^2) (Thermo Scientific, Illkirch, France) and were treated with 10 µM retinoic acid (RA) for 5 days towards differentiation into neuronal cells.[19,40,71,72] The adherent SH-SY5Y cells were divided twice weekly with the use of 0.05% trypsin-EDTA for up to 5 min, followed by centrifugation (200× *g*) at 4 °C for 5 min. The cells were counted using a KOVA®cell counting chamber (VWR, Fontenay-sous-Bois, France), and seeded at densities of 2 × 10^4 cells/well in 96-well plates or 10^6 cells/flask (25 cm^2) (depending on the type of biological analysis to be carried out). After 24 h, the SH-SY5Y cells were incubated with RA (10 µM) for 5 days, changing the medium with RA at least once. The neuronal phenotype was distinguished by the extensive proliferation of neurites.[71,72]

h. Cell viability

The cell viability was determined by the tetrazolium salt test (3-(4,5-dimethylthiazol-2-yl) -2,5-diphenyl tetrazolium bromide, MTT).[19,40] The solution of MTT was prepared in PBS and was filtered prior to use. This reagent is reduced to formazan by the mitochondrial succinate dehydrogenase enzyme in living cells. The MTT compound forms a purple precipitate, the quantity of which is proportional to the metabolic activity of the living cells. The cells were seeded at a density of 20 × 10^4 cells/well in 96-well plates. After 5 days of treatment with 10 µM retinoic acid, cubosome nanoparticles were incubated with the cells at lipid concentrations of 0.5 µM at 37 °C for 24 h. Untreated cells maintained in DMEM medium were used as controls. MTT was added at a concentration of 5 mg/mL at 37 °C. After 1 h of incubation of the cells with MTT, the medium was removed, and the cells were dissolved in 100% DMSO to solubilize the formazan precipitate. The optical density was then measured at 570 nm by a microplate reader. The quantification was done using measurements of a minimum of six wells.

i. Catalase enzymatic activity (peroxidatic function) in supernatants of cell lysates

Catalase (CAT) activity was measured in SH-SY5Y cell lysates in order to evaluate the effect of the liquid crystalline cubosomal nanoparticle treatment on the enzymatic function. CAT catalyzes the dismutation of two molecules of hydrogen peroxide into molecular oxygen and two molecules of water, according to relationship (1). This enzyme acts at higher concentrations of hydrogen peroxide than the enzyme peroxidase. CAT also exhibits peroxidatic activity, presented by relationships (2) and (3) below.

Here, SH-SY5Y cells were seeded at a density of 10^6 cells in 25 cm^2 culture flasks containing 5 ml of DMEM medium. After 24 h, the cell culture medium was replaced by 10 µM of RA solution for 5 days of incubation. Then, aqueous dispersions of fish oil, curcumin, catalase, or lipid nanoparticles (0.5 µM) were introduced in the FBS-free medium. After 24 h incubation, the cells were collected by centrifugation at 1500× *g* for 10 min at 4 °C (fig. 3). The cell pellet was homogenized on ice in 1 ml of cold buffer of potassium phosphate. Then, the samples

were centrifuged at 10000× *g* for 15 min at 4 °C (fig. 3). The assay was performed with the supernatants according to the instructions of the Cayman's Catalase Assay Kit (catalogue No. 707002) (Cayman Chemical, Ann Arbor, MI, USA), which utilizes the peroxidatic function of CAT for determination of the enzyme activity (fig. 3).

$$\text{CAT catalytic activity:} \quad 2\,H_2O_2 \xrightarrow{\text{catalase}} 2\,H_2O + O_2 \tag{1}$$

$$\text{CAT peroxidatic activity:} \quad H_2O_2 + AH_2 \xrightarrow{\text{catalase}} 2\,H_2O + A \tag{2}$$

where AH_2 and A represent the substrate, i.e., low molecular weight aliphatic alcohols serving as electron donors. In the present methodology,

$$\text{CAT peroxidatic activity:} \quad H_2O_2 + CH_3OH \xrightarrow{\text{catalase}} 2\,H_2O + CH_2O \tag{3}$$

This method is based on the reaction of the enzyme CAT with methanol in the presence of an optimal concentration of H_2O_2 according to equation (3). The produced formaldehyde was measured colorimetrically with Purpald as the chromogen. The absorbance was monitored at 540 nm using a plate reader.

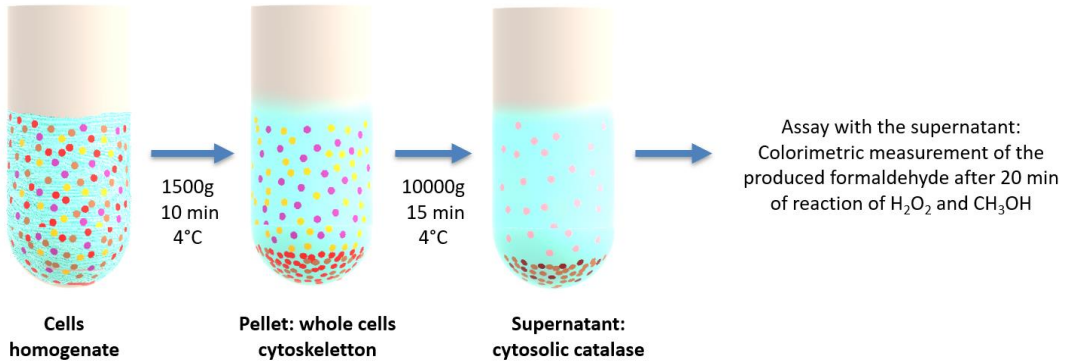

Figure 3. Schematic protocol employed in the catalase enzymatic activity assay. The assay is performed with supernatants of cell lysates, which contain the cytosolic catalase. The cell lysates are first subjected to differential centrifugation, and the colorimetric measurements of the CAT peroxidatic activity are taken with the resulting supernatants.

j. Statistical Analyses

The data are presented as the mean values of standard deviation (SD) of three independent experiments. The results were analyzed by the Tukey test after one-way analysis of variance (ANOVA). The probability values $p < 0.05$ were considered statistically significant across the treatment groups.

3) Results and discussion

a. Liquid crystalline nanostructure identification in MO/TPEG-PEG$_{1000}$/FO/CU/CAT systems by bioSAXS

BioSAXS patterns were recorded at room temperature (22 °C) for all amphiphilic compositions indicated in the diagram in Figure 2. Representative bioSAXS plots revealing the presence or absence of long-range periodicities in the MO/TPGS-PEG$_{1000}$/FO/CU/CAT three-dimensional (3D) assemblies are shown in Figure 4.

The performed structural investigation established that the blank MO/TPGS-PEG$_{1000}$ nanocarriers display a long-range 3D periodicity (Figure 4a). The latter was identified by a set of Bragg peaks with q-vector positions spaced in the ratio √2: √3: √4: √6: √8: √9: √10: √12: √14. These Bragg peaks are assigned to the (110), (111), (200), (211), (220), (221), (310), (222), and (321) reflections of a double diamond cubic lattice QIID (*Pn3m* space group).

The self-assembled MO/TPGS-PEG$_{1000}$/FO/CU/CAT mixtures (see Table 1 in Methods) displayed two kinds of mesophase structures with long-range 3D periodicities depending on the amount of the included oil (FO) and water. Bicontinuous double diamond cubic *Pn3m* (Figure 4b) and primitive cubic *Im3m* phases (Figure 3c) were identified as well as a cubic intermediate from the structural transition to a sponge phase at 22 °C (Figure 4d).

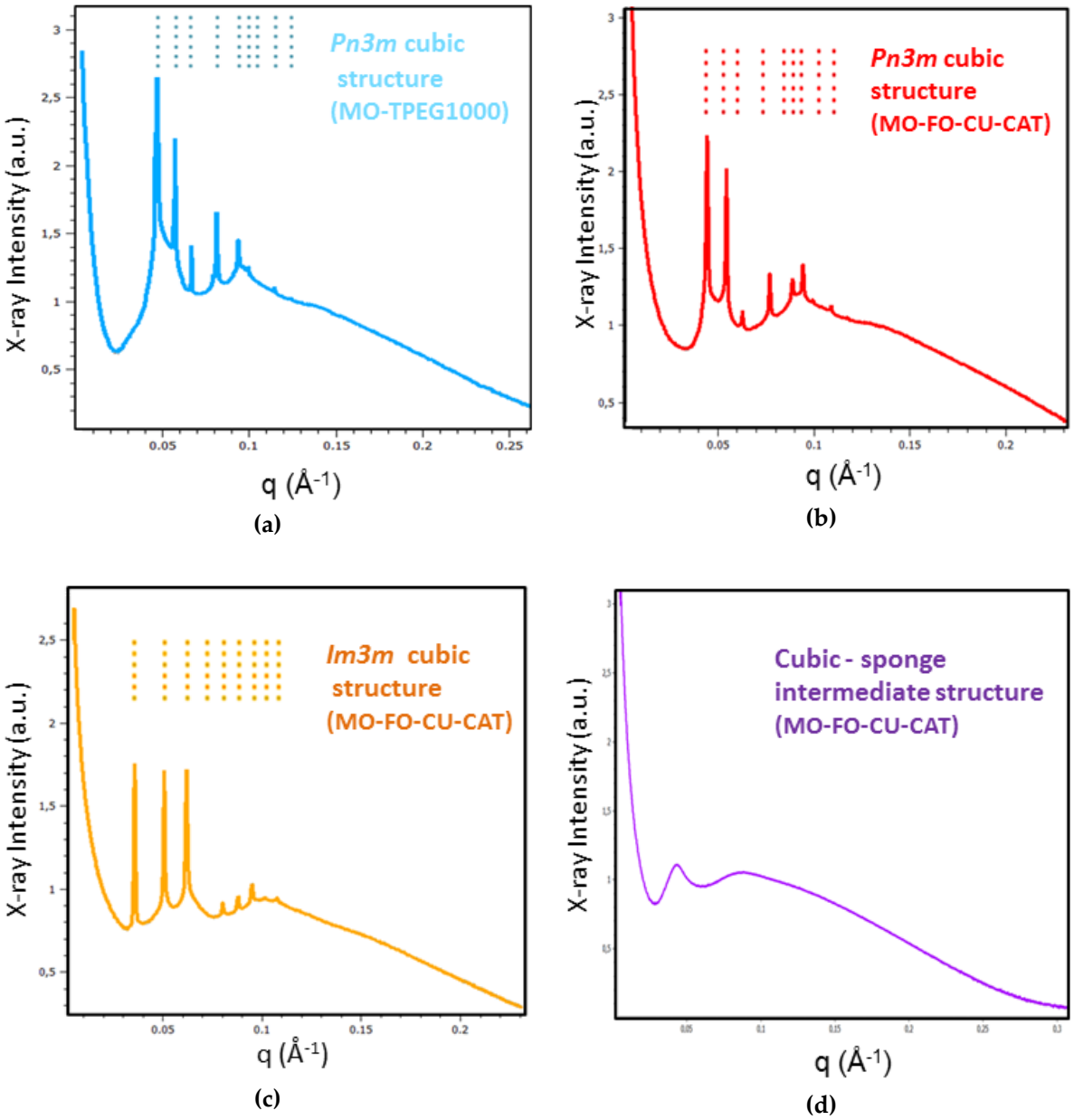

Figure 4. Representative bioSAXS patterns of MO/TPGS-PEG$_{1000}$ and MO/TPGS-PEG$_{1000}$/FO/CU self-assembled mixtures hydrated in a phosphate buffer or in catalase (CAT) solutions at 22 °C. The recorded Bragg peaks are indicative of the formation of periodic liquid crystalline phases (a–c): (a) MO/TPGS-PEG$_{1000}$ lipid mixture hydrated in 0.01 M of phosphate buffer (pH 7.0): the sequence of dashed lines indexes from left to right the (110), (111), (200), (211), (220), (221), (310), (222) and (321) reflections of a diamond cubic lattice (*Pn3m* space group); (b) MO/TPGS-PEG$_{1000}$/FO/CU/CAT mixture: the dashed lines consecutively denote the (110), (111), (200), (211), (220), (221), (310), (222) and (321) reflections of a *Pn3m* cubic

structure, which is preserved in the presence of encapsulated curcumin and catalase protein molecules; (c) Pattern of a MO/TPGS-PEG_{1000}/FO/CU/CAT mixture with indexed (110), (200), (211), (220), (310), (222), (321), (400) and (330) reflections of a primitive cubic lattice (*Im3m* space group); and (d) Pattern lacking well-defined Bragg reflections and corresponding to a cubic intermediate formed by the MO/TPGS-PEG_{1000}/FO/CU/CAT mixture. The sample list is given in Table 1.

Figure 4c shows the set of Bragg peaks with q-vector positions spaced in the ratio √2: √4: √6: √8: √10: √12: √14: √16: √18. These peaks are assigned to (110), (200), (211), (220), (310), (222), (321), (400) and (330) reflections of a primitive cubic lattice QIIP (*Im3m* space group). The increase in the incorporated oil amount in the lipid membrane led to a weakly ordered cubic structure, which coexisted with sponge-type membranes. The resulting pattern is attributed to an intermediate mesophase state owing to the composition-triggered structural transition (Figure 4d).[2,39]

b. Structural characterization of liquid crystalline bulk structures by bioSAXS

Liquid crystalline MO/TPGS-PEG_{1000}/FO/CU assemblies were prepared using four different ratios, 10:90, 20:80, 30:70 and 40:60 (wt%/wt%), for the fish oil/monoolein mixtures hydrated by a catalase solution (5 mg/mL) (see the compositions indicated in Figure 2 and Table 1). The performed BioSAXS experiments were aimed at determining the lipid ratio corresponding to the highest fish oil content, which conserves the cubic mesophase formation at room temperature (22 °C).

Figure 5 presents the BioSAXS patterns characterizing the phase behavior at varying water contents along the dilution lines defined in Figure 2. Three major cases were distinguished: (i) well-ordered lipid/protein assemblies of inner cubic lattice symmetries, (ii) cubic mesophases displaying a coexistence of distinct nanodomains, and (iii) cubic intermediates as precursors of a sponge-membrane phase, which is favored by the increase in the fish oil (FO) content.

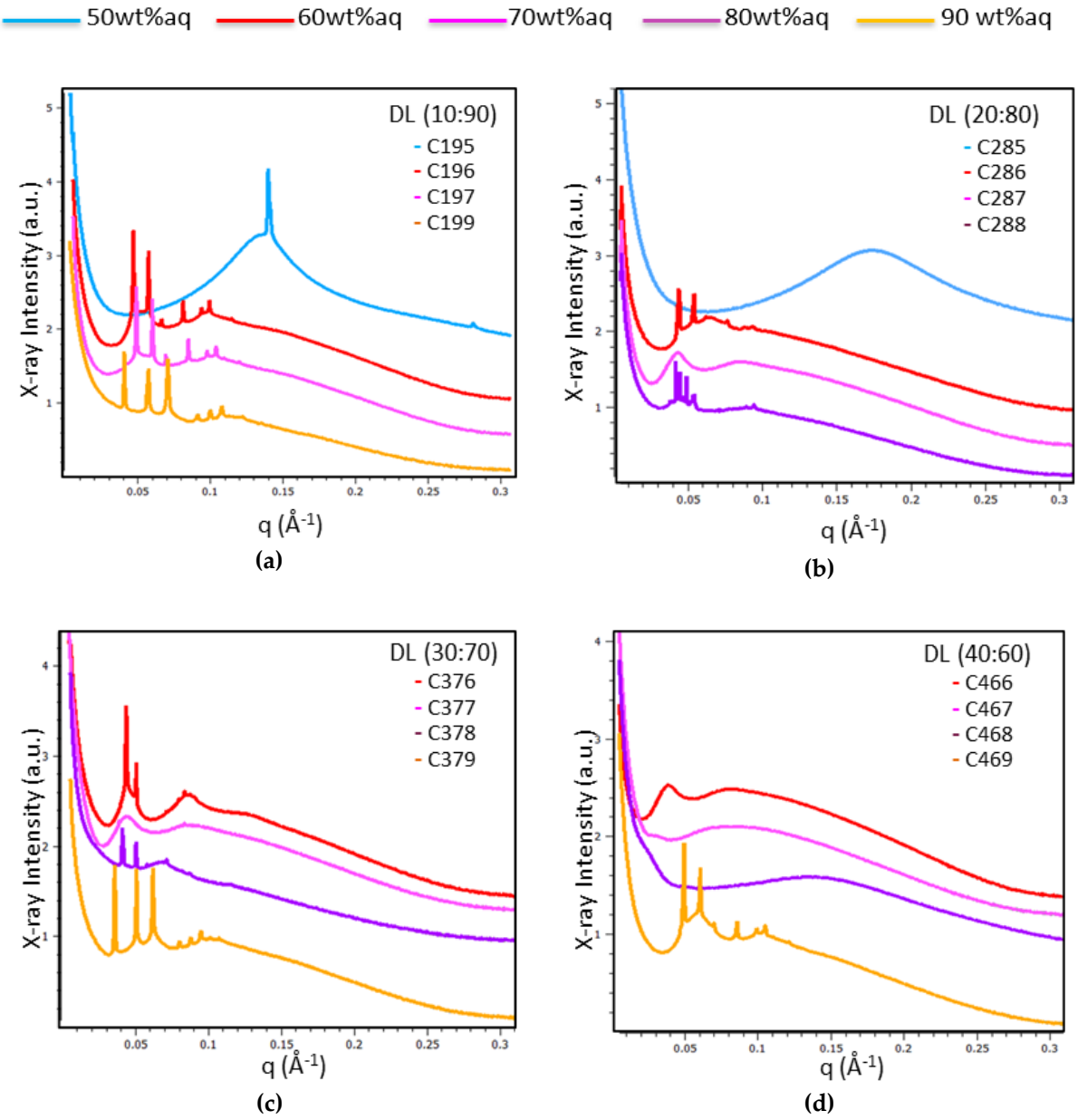

Figure 5. BioSAXS patterns of MO/TPGS-PEG$_{1000}$/FO/CU/CAT assemblies acquired at 22 °C along the dilution lines (DL): (a) DL = 10:90; (b) DL = 20:80; (c) DL = 30:70; and (d) DL = 40:60 from Figure 2 (for the precise compositions see the points drawn in Figure 2). The structural phase behavior is examined with samples prepared using a 5-mg/mL catalase solution.

Figure 5 shows that large domains of ordered cubic phase organization are formed by the self-assembled mixtures C196, C197, and C199 along the dilution line DL = 10:90 (Figure 5a); C286 and C288 along the dilution line DL = 20:80 (Figure 5b); C376, C378, and C379 along

the dilution line DL = 30:70 (Figure 5c), and C469 at DL = 60:40 (Figure 5d). At variance, samples C287 at DL = 20:80 (Figure 5b), C377 at DL = 30:70 (Figure 5c), and C466 at DL = 40:60 (Figure 5d) displayed bioSAXS patterns of weakly ordered cubic phases and the onset of the formation of a sponge membrane phase. The mixtures C467 and C468 (obtained along the dilution line DL = 40:60) formed cubic intermediates of the structural transition to a dominant sponge phase (Figure 5d, pattern C468).

The effect of the variation of the hydration level in the MO/TPGS-PEG_{1000}/FO/CU/CAT systems pointed out that the structural phase behavior is dominated by a bicontinuous cubic phase formation at fish oil/monoolein ratios of 10:90, 20:80, and 30:70 (wt%/wt%) for water contents between 60 wt% and 80 wt% (Table 1). At 90 wt% water content, stable bicontinuous cubic phases were formed at fish oil/monoolein weight ratios from 10:90 to 30:70, and up to 40:60 (wt%/wt%). The MO/TPGS-PEG_{1000}/FO/CU/CAT system formed a primitive cubic Im3m phase at 90 wt% water content, whereas the bicontinuous cubic *Pn3m* phase was most stable at 60 wt% to 80 wt% water contents.

In addition, the hydration of the lipid mixtures by the CAT protein solution at 50 wt% water content (C195, C285) resulted in the formation of lamellar and sponge phases depending on the FO/MO weight ratio (Figure 4a and 4b, respectively). An intermediate cubic phase domain preceded the induction of a dominant sponge phase at a fish oil/monoolein ratio of 40:60 wt%/wt%. The determined internal structures and lattice constants of the studied MO/TPGS-PEG_{1000}/FO/CU/CAT self-assembled architectures are shown in Table 3.

The unit lattice parameters of the cubic structures, $a_{(Q)}$, were calculated from the reciprocal slope of the linear plots q versus $(h^2 + k^2 + l^2)^{1/2}$, where (hkl) are the Miller indices of the recorded Bragg peaks (equation (1)).

$$q = (2\pi/a_{(Q)}) (h^2 + k^2 + l^2)^{1/2} \qquad (1)$$

The results for the structural parameters of the bulk cubic liquid crystalline structures are presented in Table 3.

Table 3. Internal liquid crystalline structure types and lattice parameters of MO/TPGS-PEG_{1000}/FO/CU/CAT self-assembled architectures determined from BioSAXS analysis of the data shown in Figure 5.

Samples	Liquid Crystalline Structures	Lattice $a_{(Q)}$ (nm)
C196	*Pn3m* cubic	18.5
C197	*Pn3m* cubic	18.9
C199	*Im3m* cubic	21.7
C286	*Pn3m* cubic	20.0
C287	Cubic intermediate	-
C288	Coexisting *Pn3m* cubic domains	20.0/22.7 [a]
C376	Cubic intermediate	-
C377	Cubic intermediate	-
C378	*Pn3m* cubic	20.7
C379	*Im3m* cubic	22.2
C466	Cubic intermediate	-
C467	Cubic intermediate	-
C468	Cubic intermediate-sponge	-
C469	*Pn3m* cubic	17.5

[a] Coexistence of two cubic structures.

c. BioSAXS characterization of nanocarrier dispersions

Aqueous dispersions of liquid crystalline nanocarriers were prepared at fish oil/monoolein weight ratios of 0:100, 20:80, 40:60 and 60:40 (wt%/wt%) and a constant water content (95 wt%). Catalase-free (i.e., blank) and catalase (CAT)-loaded nanocarriers were investigated by BioSAXS at the same compositional proportions of the lipid ingredients (see Table 2 in Methods for the amphiphilic compositions). This permitted the evaluation of the structural effect of the catalase association to the lipid nanocarriers by small-angle X-ray scattering.

A synchrotron BioSAXS plot of a catalase solution is shown in Figure 6a for a protein concentration of 5 mg/mL, which was employed for CAT entrapment in nanocarriers. The

experimental curve shifts with regard to that determined for non-interacting catalase tetramers (green plot). The estimated radius of gyration (Rg = 36.6 nm) appears to be nearly ten times larger than that of an isolated catalase tetramer (Rg = 3.86 nm). This result suggests that the protein CAT forms oligomeric structures above a certain solution concentration. Several proteins have a tendency to aggregate in aqueous medium. This is an important problem in biotechnology and the pharmaceutical industry. Proteins in an aggregated state generally do not have the same biological activity as proteins in a native state. The immobilization of catalase is of significant interest for the enhancement of its stability and improving its enzymatic performance. We interpreted the bioSAXS data about CAT aggregation as oligomers because the formed aggregates do not have microscopic sizes. The results also suggest that CAT may show a preference for interaction with the nanostructured lipid phase as the latter can provide interfaces of different polarities and less hydrophilic compartments for embedding the protein.

Figure 6b–d shows the BioSAXS patterns of catalase-free and catalase-loaded nanoparticles samples at three selected (MO-FO-CU) ratios (Table 2). Well-defined Bragg peaks of cubic liquid crystalline structures are detected at 22 °C both in the absence and in the presence of catalase protein. Figure 6b demonstrates that the initial bicontinuous *Pn3m* cubic organization of the blank nanocarriers $(MO\text{-}FO\text{-}CU)_1$ is transformed into a primitive cubic Im3m structure upon addition of CAT at a FO/MO ratio of 20:80 wt%/wt% in the formulation. In the absence of CAT loading, the $(MO\text{-}FO\text{-}CU)_1$ cubosome nanoparticles involved coexisting domains of the *Pn3m* space group with two distinct cubic unit cells dimensions. The Pn3m unit lattice parameters estimated for these cubosome particles are $a_{1(Q)}$ = 16.4 nm and $a_{2(Q)}$ = 20.0 nm, respectively (Table 4). The CAT-loaded cubosome particles $(MO\text{-}FO\text{-}CU\text{-}CAT)_1$ (Figure 6b) were characterized by the *Im3m* space group and displayed a bigger cubic lattice parameter, $a_{(Q)}$ = 23.2 nm. At 95 wt% water content, the increase in the FO/MO weight ratio to 40:60 and 60:40 (wt%/wt%) yielded predominantly primitive cubic *Im3m* inner structures (Figure 6c,d).

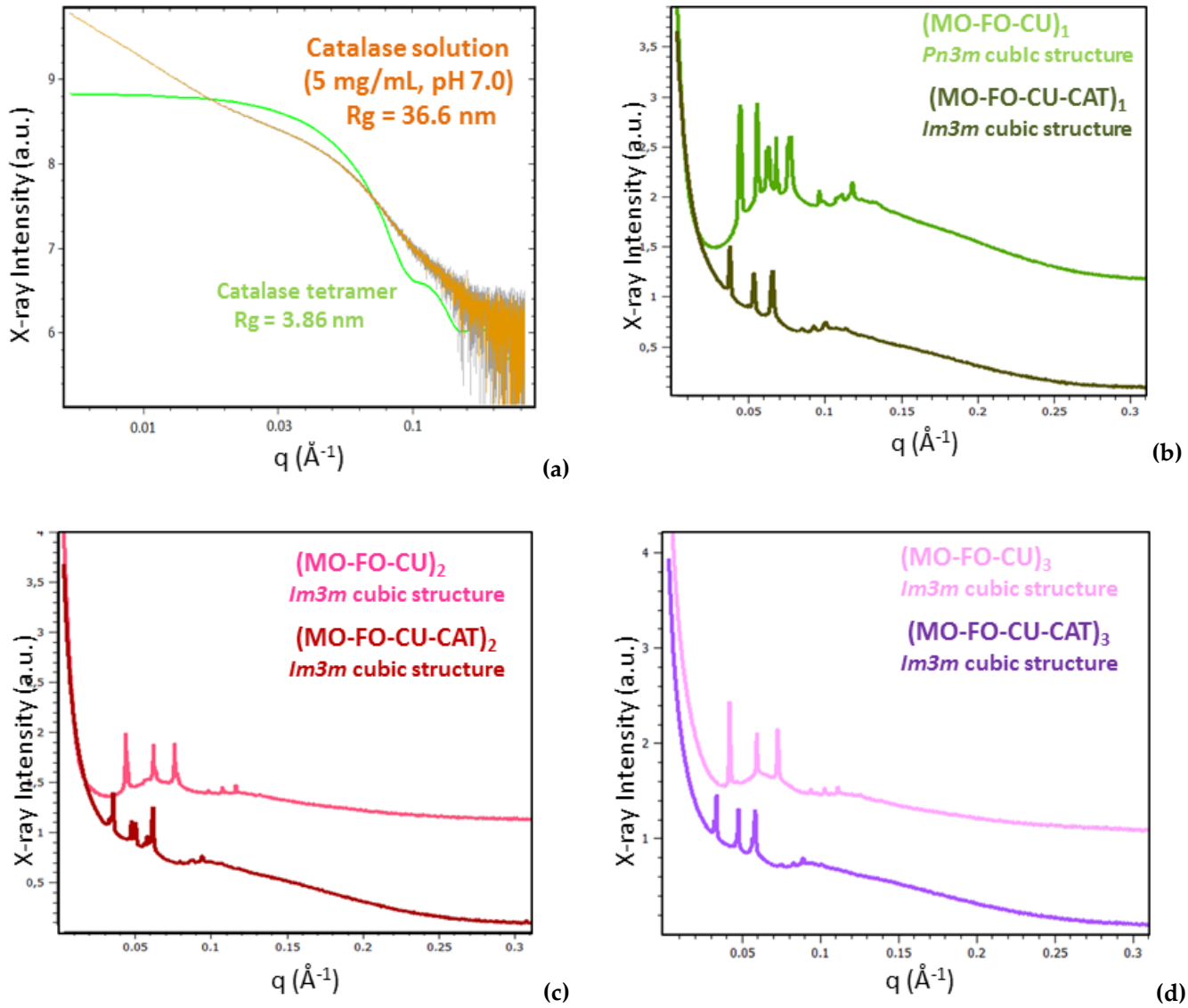

Figure 6. BioSAXS patterns of (a) catalase solution (5 mg/mL) in 0.01 M of phosphate buffer, and (b–d) liquid crystalline nanoparticle dispersions obtained in the presence or absence of catalase (CAT) at varying fish oil (FO)/monoolein (MO) ratios (wt%/wt%): (b) 20:80 (MO-FO-CU)1 vs. (MO-FO-CU-CAT)$_1$; (c) 40:60 (MO-FO-CU)$_2$ vs. (MO-FO-CU-CAT)$_2$; and (d) 60:40 (MO-FO-CU)$_3$ vs. (MO-FO-CU-CAT)$_3$. The percentages of curcumin (CU) and TPGS-PEG$_{1000}$ are constant with regards to MO and FO (see the compositions in Table 2). Temperature is 22 °C.

The cubic unit cell dimensions of the liquid crystalline nanoparticles were estimated from the bioSAXS results using equation (1). Table 4 shows that the cubic lattice parameters in the catalase-free nanocarriers increase with the increase in the fish oil and curcumin

amounts. The values range from $a_{(Q)}$ = 16.4 nm (*Pn3m* inner cubic structure) to $a_{(Q)}$ = 21.3 nm (*Im3m* inner cubic structure). These unit cell magnitudes result from the fragmentation of the drug-loaded lyotropic lipid cubic phase by the PEGylated dispersion agent in excess aqueous medium. They differ from that typical for the pure MO bulk lipid cubic phase ($a_{(Q)}$ = 10.5 nm).[39] The increased cubic lattice parameter of the catalase-loaded nanoparticles ($a_{(Q)}$ = 26.3 nm) as compared to nanoparticles without catalase ($a_{(Q)}$ = 21.3 nm) can be explained by the entrapment of the protein macromolecules, which may cause swelling of the monoolein liquid crystalline structures.[2,8]

Table 4. Unit cell lattice parameters and size distributions of catalase-free and catalase-loaded MO/FO/CU cubosome nanoparticles (NPs) stabilized by TPGS-PEG_{1000}. The cubic space group type is indicated in Figure 6 for every sample.

Nanoparticles	Lattice $a_{(Q)}$ (nm) [a]	NPs' Size (nm) [b]
Curcumin-Loaded NPs		
MO-TPGS-PEG_{1000}	-	106
$(MO\text{-}FO\text{-}CU)_1$	16.4/20.0[c]	106/220[d]
$(MO\text{-}FO\text{-}CU)_2$	20.0	220
$(MO\text{-}FO\text{-}CU)_3$	21.3	255
Curcumin and Catalase-Loaded NPs		
MO-CAT	-	484
$(MO\text{-}FO\text{-}CU\text{-}CAT)_1$	23.2	164/550[b]
$(MO\text{-}FO\text{-}CU\text{-}CAT)_2$	25.0/26.3[a]	150/459[b]
$(MO\text{-}FO\text{-}CU\text{-}CAT)_3$	26.3	164/531[b]

[a] Determined by BioSAXS; [b] determined by QELS; [c] coexistence of two structures; [d] coexistence of two populations of NPs.

The investigated nanodispersions were also characterized by quasi-elastic light scattering (QELS) measurements. The sizes of the particles determined from their volume distributions in the samples are shown in Table 4. The mean hydrodynamic size of the catalase-free nanoparticles increases with the increase in the fish oil and curcumin proportions (see Table

2 in Methods). The values vary between 106 nm and 255 nm. The association of catalase to the lipid nanoparticles increases their sizes as compared to the initial nanoparticle dimensions measured in the absence of catalase. The largest particle sizes (between 484 nm and 530 nm) were reached upon augmentation of the fish oil and curcumin contents. Moreover, a presence of two populations of nanocarriers is established in the dispersed systems (Table 4). The two populations represent a coexistence of large-size (~500 nm) particles and smaller-size (~160 nm) particles. For cubosomal formulations of lipids, it has been suggested that they correspond to coexisting cubosomes and small vesicles or precursors of intermediate-type liquid crystalline structures.[34,39] The inclusion of CAT protein appears to favor the cubosome nanoparticle population.

d. Discussion on the structural effect of catalase entrapped in curcumin-loaded self-assembled liquid crystalline nanocarriers

We determined by bioSAXS the different kinds of mesophase structures obtained in MO/TPGS-PEG_{1000}/FO/CU/CAT self-assembled systems of therapeutic interest (Figures 4-6). Whereas diamond *Pn3m* cubic structures were present in the MO/TPGS-PEG_{1000} assemblies, the cubic liquid crystalline architectures identified in the MO/TPGS-PEG_{1000}/FO/CU/CAT systems were of either *Pn3m* or *Im3m* space group symmetries. Thus, the inclusion of catalase did not disrupt the overall cubic liquid crystalline organization of the curcumin-loaded nanocarriers. However, intermediates of the cubic-to-sponge mesophase transition were observed with increasing fish oil content at a temperature of 22 °C.

At a low co-lipid content (fish oil/monoolein ratio 10:90 wt%/wt%), the bulk MO/TPGS-PEG_{1000}/FO/CU/CAT systems displayed *Pn3m* and *Im3m* cubic phases (Figure 5a). Intermediates of the cubic-to-sponge mesophase transition appeared at FO/MO ratios of 20:80 and 30:70 (wt%/wt%) (Figure 5b,c). A predominant sponge phase was obtained at a high content of fish oil (FO/MO ratio 40:60 wt%/wt%) (Figure 4d). However, the cubic structure was retained at 90 wt% water content despite the elevated percentage of fish oil at

DL 40:60 (Figure 5d). Therefore, the hydration level was crucial for the resulting mesoscale organization of the mixed assemblies.

The observed coexistence of two cubic domains in the nanocarriers with intermediate fish oil content (e.g., FO/MO ratio 20:80, Table 1) may be due to the insufficient amount of co-lipid necessary to trigger a phase transition to a new mesophase type. Thus, the overall *Pn3m* cubic structure will contain coexisting domains, which are more rich or less rich in a co-lipid ingredient or in a PEGylated amphiphile. In a previous study, we showed that the in homogeneous distribution of the PEGylated surfactant along the monoolein membrane can result in the coexistence of cubic phase nanodomains with different lattice parameters, but the same space group (*Pn3m*) symmetry.[39] The domains with the smaller cubic unit cell dimension corresponded to the hydrated pure monoolein lipid, and the larger cubic unit cell corresponded to the mixed lipid assembly. Similar effects of inhomogeneous distribution of lipid components or nanodomain formation are observed in some of the samples studied in the present work. This yields two different magnitudes of the cubic lattice parameters, which characterize the coexisting Pn3m cubic phase domains (e.g., $a_{1(Q)}$ = 16.4 nm and $a_{2(Q)}$ = 20.0 nm).

Nano-dispersions of liquid crystalline particles were obtained with the MO/TPGS-PEG_{1000}/FO/CU/CAT mixtures in the excess water (95 wt%) phase. Their internal organization involved *Pn3m* and *Im3m* cubic structures in the absence of catalase (Figure 6) and the induction of primitive *Im3m* cubic structures in the catalase-loaded nanoparticles. The cubic unit cell dimensions increased in the presence of an associated catalase enzyme, while retaining the overall cubic phase organization. The structural influence of protein incorporation into liquid crystalline lipid assemblies has been discussed in several publications.[8,9,11,20–28] For instance, neurotrophin BDNF confinement resulted in the formation of multiphase and multicompartment liquid crystalline lipid nanoparticles.[11] The transmembrane β-barrel BamA protein caused an increase in the lattice parameter of the host lipid cubic phase upon encapsulation.[26] By contrast, the lipo-protein BamB–E caused the cubic

lattice parameter to decrease.[26] The effect of amphiphilic and soluble proteins on the nanochannel diameters in bicontinuous cubic Pn3m phases of monoolein has received considerable attention as well.[8,11,23,25] Long-living swollen states, corresponding to a diamond cubic phase with large water channels, have been stabilized in some cases.[2,30] Cryo-TEM and freeze-fracture electronic microscopy imaging has indicated the inclusion of proteins into nanopockets of the supramolecular cubosomic assemblies and the induction of nanodomains.[8,11,25] In the present study, catalase was incorporated in the cubosome carriers under excess water conditions. The lattice parameters of the curcumin-loaded cubosomes were between 16.4 nm (*Pn3m* space group) and 21.3 nm (*Im3m* space group), depending on the amount of fish oil and curcumin in the mixtures. The $a_{(Q)}$ values increased to 23.2–26.3 nm (*Im3m* space group) upon the addition of catalase. This implies that the hydrated enzyme catalase causes swelling of the cubosomal network architectures, rather than their dehydration.

e. Viability of cubosome nanoparticle-treated differentiated SH-SY5Y Cells

The human neuroblastoma SH-SY5Y cells were differentiated by 10 µM of retinoic acid (RA) for 5 days in order to obtain extensive proliferation of neurites and reduced cell body sizes, which are typical for a neuronal cell phenotype.[19,71,72] Then, the cells were exposed to 0.5 µM of catalase-loaded cubosome nanocarriers for 24 hours. Freshly prepared nanoparticles (one day after NP preparation) and 90 days-stored NPs were investigated for their impact on the cellular viability. Unexposed cells were used as viability controls. The obtained 3-(4,5-Dimethylthiazol-2-yl)-2,5-diphenyl tetrazolium bromide (MTT) data (Figure 7) demonstrate that the cellular viability decreases from 100 ± 2.2% to 84.5 ± 6.7% for catalase-loaded cubosome particles, which contain increasing amounts of incorporated fish oil and curcumin. This decrease in cellular viability was not significant ($p < 0.05$) compared to the control. The MTT test indicated the safety of the dual drug-loaded nanoparticles. In addition, the data obtained

with the 90-days-stored nanoparticles did not show a significant viability difference as compared to the newly prepared nanoparticles. This result evidenced the stability of the studied cubosome nanoparticles with 90 days of storage.

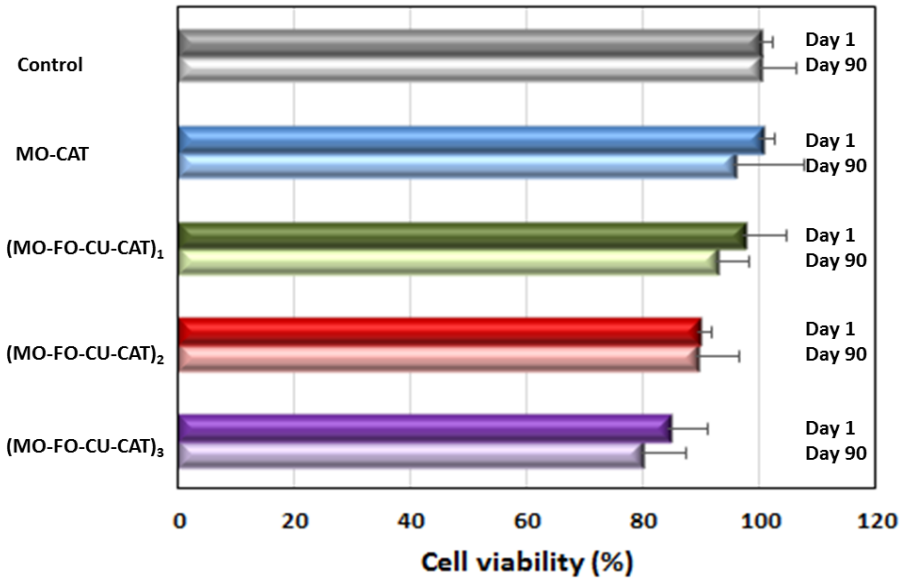

Figure 7. Cellular viability of retinoic acid-differentiated SH-SY5Y cells after 24 hours exposure to 0.5 μM of catalase-loaded liquid crystalline nanoparticles. The histograms at Day 1 and Day 90 correspond to the time elapsed (one day or 90 days) after the nanoparticles' preparation before cell exposure. The MO-FO-CU-CAT compositions are presented in Methods (Table 2).

f. Catalase peroxidatic activity in cell lysates of differentiated SH-SY5Y cells obtained after treatment with cubosome nanoparticles

The successful delivery and uptake of blank and catalase-loaded cubosome nanoparticles in RA-differentiated SH-SY5Y cells was evaluated by determining catalase peroxidatic activity[48,49] in supernatants of cell lysates generated after cubosomal treatment. Catalase is a ubiquitous antioxidant enzyme involved in the detoxification of H_2O_2 (a toxic product of the normal aerobic metabolism or of pathogenic ROS production). One unit of enzymatic reaction activity is defined as the amount of enzyme that will cause the formation of 1 nmol of formaldehyde per minute at 25 °C. It serves for the quantification of the cytosolic catalase. The

determined catalase peroxidatic activity in lysates of non-treated RA-SH-SY5Y cells, used as a control, was 15.37 ± 0.14 nmol/min/mL.

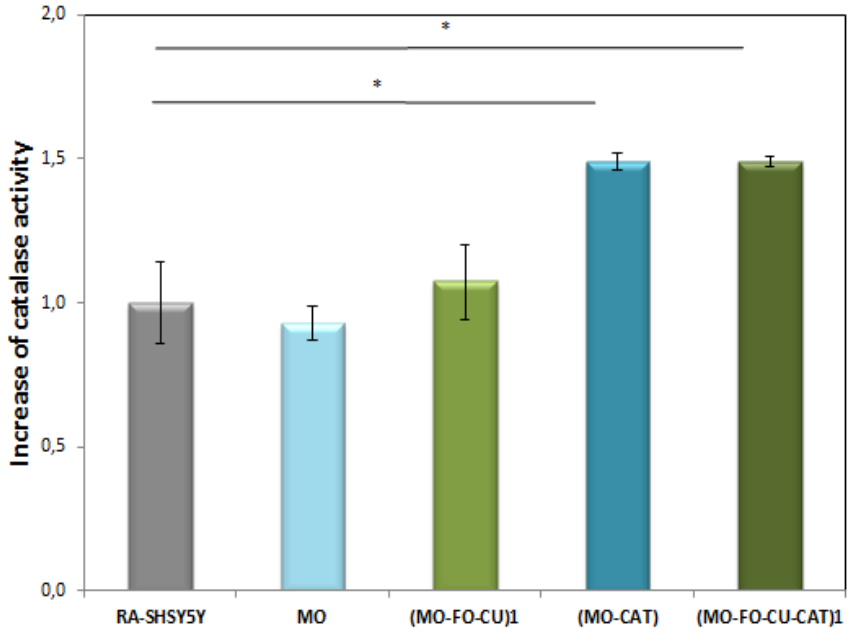

Figure 8. Fold increase in catalase enzymatic activity (peroxidatic function) determined in supernatants of cell lysates of differentiated SH-SY5Y cells (RA-SH-SY5Y) after exposure to blank nanoparticles (MO), catalase-loaded (MO-CAT) cubosome nanoparticles, dual drug-loaded (MO-FO-CU) or enzyme-loaded (MO-FO-CU-CAT) cubosome nanoparticles.

Figure 8 shows that there was no significant difference in the catalase activity between the control and the cells exposed to blank nanoparticles (MO). The measured value of 14.47 ± 0.06 nmol/min/ml was close. A tendency for the catalase activity to increase was observed for RA-SH-SY5Y cells exposed to FO- and CU-loaded nanoparticles $(MO\text{-}FO\text{-}CU)_1$. The peroxidatic activity value raised to 16.51 ± 0.13 nmol/min/mL. The results with cells exposed to catalase-loaded nanoparticles (MO-CAT) demonstrated a significant increase in the catalase peroxidatic activity (activity value equal to 27.09 ± 0.02 nmol/min/mL, $p < 0.05$). An increase in the peroxidatic activity was observed also with catalase- and curcumin-loaded nanoparticles $(MO\text{-}FO\text{-}CU\text{-}CAT)_1$ (Figure 8). This implies that catalase is delivered by the liquid crystalline nanocarriers inside the neuronally derived cells. Noticeably, the cellular uptake of CAT-

loaded nanoparticles results in an overall increase in the measured enzymatic activity (peroxidatic function).

g. Discussion on the catalase peroxidatic function following cellular treatment with dual drug-loaded cubosomes

Catalase plays a crucial role in the adaptive response to hydrogen peroxide as ROS.[44,55] Human catalase belongs to the family of catalases, which catalyze the dismutation of H_2O_2 into water and molecular oxygen (Figure 9). In addition to its dominant catalytic function (decomposition of H_2O_2), catalase can also decompose peroxynitrite and oxidize nitric oxide to nitrogen dioxide. It exhibits marginal peroxidase activity (i.e., oxidation of organic substrates with concomitant reduction of peroxide) and low oxidase activity (O_2-dependent oxidation of organic substrates).[44,47] At a high concentration of H_2O_2, the catalytic pathway starts. At a low concentration of H_2O_2, the peroxidatic pathway is initiated[48,49], in which various hydrogen donors such as alcohols, phenols, hormones, heavy metals and nitrite (serving as the second molecule that assures the role of H_2O_2) are oxidized.[44]

Low levels of catalase expression correlate with a high production of H_2O_2.[53,54] As a consequence, this effect causes the activation of signaling pathways associated with different diseases including Alzheimer 's disease.[51–54] Our work provides experimental evidence that catalase-loaded cubosome nanoparticles are promising candidates for the intracellular delivery of the unstable protein towards treatment or prevention of neurodegenerative disorders. Catalase, like many enzymes, is unstable in aqueous phase and shows a propensity to aggregate. This may lead to a loss of activity.[61] In our strategy, the catalase-loaded cubosome nanoparticles would protect the enzyme and ensure its intracellular uptake.

We analyzed the peroxidatic function of catalase for the quantification of its activity in lysates from RA-differentiated SH-SY5Y cells exposed to blank nanoparticles (NPs), curcumin (CU)-loaded NPs, catalase (CAT)-loaded NPs, and dual (CAT-CU)-loaded NPs. The enzymatic activity was determined by colorimetrical measurements of formaldehyde (Figure 9) formed

thanks to the peroxidatic function of catalase.[48,49] The results shown in Figure 7 indicate an increased catalase activity in supernatants of cells exposed to catalase-loaded nanoparticles (i) without curcumin (MO-CAT) or (ii) with dual loading of CAT and curcumin (MO-FO-CU-CAT). The enhanced enzymatic activity can be explained by an increase in the amount of cytosolic catalase in the cells treated with CAT-loaded nanoparticles. This confirms that the cubosome nanoparticles provide an efficient delivery and uptake of the catalase enzyme into the cells.

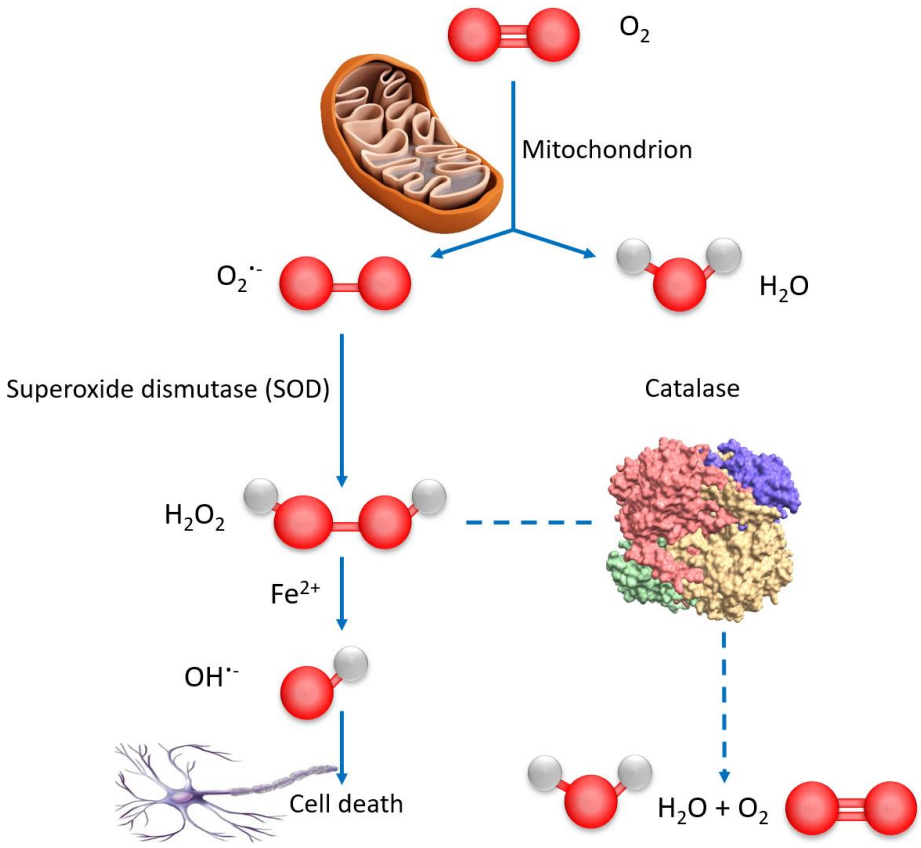

Figure 9. Scheme of reactive oxygen species (ROS) generation and organism self-defense by natural enzymes. The generated ROS levels are principally linked to mitochondria. The superoxide radicals O_2^- are converted to less toxic H_2O_2 by the enzyme superoxide dismutase (SOD). In the presence of Fe^{2+}, some of the H_2O_2 molecules can be reduced to highly reactive OH^- ROS, which attacks various biomolecules (proteins, DNA, and lipids) and causes cell death. Catalase blocks that pathway and saves the organisms by decomposing H_2O_2 into harmless water and oxygen.[44]

We established that the curcumin-containing dual-drug loaded nanoparticles (MO-FO-CU-CAT) maintain the CAT activity (Figure 8), unlike other antioxidants, which can inhibit the catalase enzymatic function.[56,57] Molecular dynamic simulations have demonstrated that curcumin can significantly increase the activity of bovine liver catalase (BLC) as it favors the access of the substrate to the active site of the enzyme.[59] The enzymatic activity has been suggested to increase through a curcumin-triggered re-arrangement of the amino acid residues in the structural pocket of catalase. The increased distances between the residues of the formed channel enable a larger amount of substrate to reach the active site. The entrance space increased, which essentially facilitated the substrate's access to the enzyme active pocket. Curcumin may also increase the amount of α-helical content in BLC, leading to the stabilization of the protein's secondary structure.[59,60]

In conclusion, dual drug-loaded nanocarriers of the cubosome type were obtained and were characterized by stable mesophase organization during three months of storage. The catalase- and curcumin loaded (MO-FO-CU-CAT) cubosome nanoparticles efficiently delivered the therapeutic molecules inside the neuronally derived SH-SY5Y cells as evidenced by the increased activity of the antioxidant enzyme. The cubosomal nanoarchitectures preserved the encapsulated enzyme (CAT) in a functional state, ensuring the cell's defense against reactive oxygen species (catalytic and peroxidatic functions). Moreover, the dual-loaded cubosomes provided an enhanced activity of catalase in differentiated SH-SY5Y cells. Further studies are needed in order to determine an eventual synergistic antioxidant effect of catalase and curcumin upon dual delivery by liquid crystalline nanocarriers.

4) References

(1) Sarkar, S.; Tran, N.; Rashid, M.H.; Le, T.C.; Yarovsky, I.; Conn, C.E.; Drummond, C.J. Toward cell membrane biomimetic lipidic cubic phases: A high-throughput exploration of lipid compositional space. *ACS Appl. Bio Mater.* **2019**, *2*, 182–195.

(2) Angelova, A.; Angelov, B.; Mutafchieva, R.; Lesieur, S. Biocompatible mesoporous and soft nanoarchitectures. *J. Inorg. Organomet. Polym*. **2015**, *25*, 214–232; doi:10.1007/s10904-014-0143-8.

(3) Larsson, K. Cubic lipid-water phases: Structures and biomembrane aspects. *J. Phys. Chem*. **1989**, *93*, 7304–7314; doi:10.1021/j100358a010 .

(4) Seddon, J.M.; Templer, R.H. Polymorphism of Lipid—Water Systems. In *Handbook of Biological Physics*; Lipowsky, R., Sackmann, E., Eds.; Elsevier Science B.V.: North Holland, The Netherlands, 1995; Volume 1, pp. 99–149.

(5) Kulkarni, C.V. Lipid crystallization: From self-assembly to hierarchical and biological ordering. *Nanoscale* **2012**, *4*, 5779–5791.

(6) Kulkarni, C.V.; Yaghmur, A.; Steinhart, M.; Kriechbaum, M.; Michael Rappolt, M. Effects of high pressure on internally self-assembled lipid nanoparticles: A synchrotron small-angle X-ray scattering (SAXS) study. *Langmuir* **2016**, *32*, 11907; doi:10.1021/acs.langmuir.6b03300 .

(7) Lawrence, M.J. Surfactant systems: Their use in drug delivery. *Chem. Soc. Rev.* **1994**, *23*, 417−424.

(8) Angelova, A.; Angelov, B.; Mutafchieva, R.; Lesieur, S.; Couvreur, P. Self-assembled multicompartment liquid crystalline lipid carriers for protein, peptide, and nucleic acid drug delivery. *Acc. Chem. Res.* **2011**, *44*, 147–156.

(9) Angelova, A.; Garamus, V.M.; Angelov, B.; Tian, Z.; Li, Y.; Zou, A. Advances in structural design of lipid-based nanoparticle carriers for delivery of macromolecular drugs, phytochemicals and anti-tumor agents. *Adv. Colloid Interface Sci.* **2017**, *249*, 331–345; doi:10.1016/j.cis.2017.04.006.

(10) Milak, S.; Zimmer, A. Glycerol monooleate liquid crystalline phases used in drug delivery systems. *Int. J. Pharm.* **2015**, *478*, 569–587.

(11) Angelov, B.; Angelova, A.; Filippov, S.K.; Drechsler, M.; Stepanek, P.; Lesieur, S. Multicompartment lipid cubic nanoparticles with high protein upload: Millisecond dynamics of formation. *ACS Nano* **2014**, *8*, 5216–5226.

(12) Garti, N.; Libster, D.; Aserin, A. Lipid polymorphism in lyotropic liquid crystals for triggered release of bioactives. *Food Funct*. **2012**, 3, 700–713; doi:10.1039/c2fo00005a.

(13) Barriga, H.M.G.; Holme, M.N.; Stevens, M.M. Cubosomes: The next generation of smart lipid nanoparticles? *Angew. Chem. Int. Ed.* **2018**, *57*, 2−23.

(14) Han, S.; Shen, J.Q.; Gan, Y.; Geng, H.M.; Zhang, X.X.; Zhu, C.L.; Gan, L. Novel vehicle based on cubosomes for ophthalmic delivery of flurbiprofen with low irritancy and high bioavailability. *Acta Pharmacol. Sin.* **2010**, *31*, 990–998.

(15) Avachat, A.M.; Parpani, S.S. Formulation and development of bicontinuous nanostructured liquid crystalline particles of efavirenz. *Colloids Surf. B: Biointerfaces* **2015**, *126*, 87–97; doi:10.1016/j.colsurfb.2014.12.014.

(16) Aleandri, S.; Bandera, D.; Mezzenga, R.; Landau, E.M. Biotinylated cubosomes: A versatile tool for active targeting and codelivery of paclitaxel and a fluorescein-based lipid dye. *Langmuir* **2015**, *31*, 12770–12776.

(17) Baskaran, R.; Madheswaran, T.; Sundaramoorthy, P.; Kim, H.M.; Yoo, B.K. Entrapment of curcumin into monoolein-based liquid crystalline nanoparticle dispersion for enhancement of stability and anticancer activity. *Int. J. Nanomed*. **2014**, *9*, 3119–3130.

(18) Fong, W.K.; Negrini, R.; Vallooran, J.J.; Mezzenga, R.; Boyd, B.J. Responsive self-assembled nanostructured lipid systems for drug delivery and diagnostics. *J. Colloid Interface Sci*. **2016**, *484*, 320–339; doi:10.1016/j.jcis.2016.08.077.

(19) Rakotoarisoa,M.; Angelov, B.; Garamus, V.M.; Angelova, A. Curcumin- and fish oil-loaded spongosome and cubosome nanoparticles with neuroprotective potential against H_2O_2-induced oxidative stress in differentiated human SH-SY5Y cells. *ACS Omega* **2019**, *4*, 3061−3073.

(20) Nielsen, L.H.; Rades, T.; Boyd, B.; Boisen, A. Microcontainers as an oral delivery system for spray dried cubosomes containing ovalbumin. *Eur. J. Pharm. Biopharm*. **2017**, *118*, 13–20; doi:10.1016/j.ejpb.2016.12.008.

(21) Rizwan, S.B.; Assmus, D.; Boehnke, A.; Hanley, T.; Boyd, B.J.; Rades, T.; Hook, S. Preparation of phytantriol cubosomes by solvent precursor dilution for the delivery of protein vaccines. *Eur. J. Pharm. Biopharm*. **2011**, *79*, 15–22.

(22) Angelov, B.; Garamus, V.M.; Drechsler, M.; Angelova, A. Structural analysis of nanoparticulate carriers for encapsulation of macromolecular drugs. *J. Mol. Liq*. **2017**, *235*, 83–89.

(23) Conn, C.E.; Drummond, C.J. Nanostructured bicontinuous cubic lipid self-assembly materials as matrices for protein encapsulation. *Soft Matter* **2013**, *9*, 3449.

(24) Rizwan, S.B.; Hanley, T.; Boyd, B.J.; Rades, T.; Hook, S. Liquid crystalline systems of phytantriol and glyceryl monooleate containing a hydrophilic protein: Characterisation, swelling and release kinetics. *J. Pharm. Sci.* **2009**, *98*, 4191–4204; doi 10.1002/jps.21724.

(25) Angelova, A.; Ollivon, M.; Campitelli, A.; Bourgaux, C. Lipid cubic phases as stable nanochannel network structures for protein biochip development: X-ray diffraction study. *Langmuir* **2003**, *19*, 6928–6935.

(26) Van't Hag, L.; Shen, H.H.; Lin, T.W.; Gras, S.L.; Drummond, C.J.; Conn, C.E. Effect of lipid-based nanostructure on protein encapsulation within the membrane bilayer mimetic lipidic cubic phase using transmembrane and lipo-proteins from the beta-barrel assembly machinery. *Langmuir* **2016**, *32*, 12442–12452; doi:10.1021/acs.langmuir.6b01800.

(27) Van't Hag, L.; De Campo, L.; Garvey, C.J.; Feast, G.C.; Leung, A.E.; Yepuri, N.R.; Knott, R.; Greaves, T.L.; Tran, N.; Gras, S.L.; et al. Using SANS with contrast-matched lipid bicontinuous cubic phases to determine the location of encapsulated peptides, proteins, and other biomolecules. *J. Phys. Chem. Lett.* **2016**, *7*, 2862–2866; doi:10.1021/acs.jpclett.6b01173.

(28) Darmanin, C.; Sarkar, S.; Castelli, L.; Conn, C.E. Effect of lipidic cubic phase structure on functionality of the dopamine 2l receptor: Implications for *in meso* crystallization. *Cryst. Growth Des.* **2016**, *16*, 5014–5022.

(29) Kulkarni, C.V.; Wachter, W.; Iglesias-Salto, G.; Engelskirchen, S.; Ahualli, S. Monoolein: A magic lipid? *Phys. Chem. Chem. Phys.* **2011**, *13*, 3004–3021.

(30) Angelov, B.; Angelova, A.; Garamus, V.M.; Lebas, G.; Lesieur, S.; Ollivon, M.; Funari, S.S.; Willumeit, R.; Couvreur, P. Small-angle neutron and X-ray scattering from amphiphilic stimuli-responsive diamond-type bicontinuous cubic phase. *J. Am. Chem. Soc.* **2007**, *129*, 13474–13479.

(31) Valldeperas, M.; Wisniewska, M.; Ram-On, M.; Kesselman, E.; Danino, D.; Nylander, T.; Barauskas, J. Sponge phases and nanoparticle dispersions in aqueous mixtures of mono- and diglycerides. *Langmuir* **2016**, *32*, 8650–8659.

(32) Angelova, A.; Angelov, B.; Garamus, V.M.; Drechsler, M. A vesicle-to-sponge transition via the proliferation of membrane-linking pores in w-3 polyunsaturated fatty acid-containing lipid assemblies. *J. Mol. Liq.* **2019**, *279*, 518–523.

(33) Yaghmur, A.; Ghazal, A.; Ghazal, R.; Dimaki, M.; Svendsen, W.E. A hydrodynamic flow focusing microfluidic device for the continuous production of hexosomes based on docosahexaenoic acid monoglyceride. *Phys. Chem. Chem. Phys*. **2019**, *21*, 13005–13013; doi:10.1039/C9CP02393C.

(34) Angelov, B.; Angelova, A.; Garamus, V.M.; Drechsler, M.; Willumeit, R.; Mutafchieva, R.; Štěpánek, P.; Lesieur, S. Earliest stage of the tetrahedral nanochannel formation in cubosome particles from unilamellar nanovesicles. *Langmuir* **2012**, *28*, 16647–16655.

(35) Gontsarik, M.; Mohammadtaheri, M.; Yaghmur, A.; Salentinig, S. pH-Triggered nanostructural transformations in antimicrobial peptide/oleic acid self-assemblies. *Biomater. Sci*. **2018**, *6*, 803–812; doi:10.1039/c7bm00929a.

(36) Yepuri, N.R.; Clulow, A.J.; Prentice RN.; Gilbert EP.; Hawley, A.; Rizwan, S.B.; Boyd, B.J.; Darwish, T.A. Deuterated phytantriol—A versatile compound for probing material distribution in liquid crystalline lipid phases using neutron scattering. *J. Colloid Interface Sci.* **2019**, *534*, 399–407; doi:10.1016/j.jcis.2018.09.022.

(37) Angelova, A.; Angelov, B. Dual and multi-drug delivery nanoparticles towards neuronal survival and synaptic repair. *Neural Regen. Res.* **2017**, *12*, 886–9.

(38) Huang, L.; Hu, J.; Huang, S.; Wang, B.; Siaw-Debrah, F.; Nyanzu, M.; Zhang, Y.; Zhuge, Q. Nanomaterial applications for neurological diseases and central nervous system injury. *Prog. Neurobiol.* **2017**, *157*, 29–48; doi:10.1016/j.pneurobio.2017.07.003.

(39) Angelova, A.; Drechsler, M.; Garamus, V.M.; Angelov, B. Liquid crystalline nanostructures as pegylated reservoirs of omega-3 polyunsaturated fatty acids: Structural insights toward delivery formulations against neurodegenerative disorders. *ACS Omega* **2018**, *3*, 3235–3247.

(40) Guerzoni, L.P.B.; Nicolas, V.; Angelova, A. *In vitro* modulation of TrkB receptor signaling upon sequential delivery of curcumin-DHA loaded carriers towards promoting neuronal survival. *Pharm. Res.* **2017**, *34*, 492–505.

(41) Rakotoarisoa, M.; Angelova, A. Amphiphilic nanocarrier systems for curcumin delivery in neurodegenerative disorders. *Medicines* **2018**, *5*, 126.

(42) Mueller, S.; Riedel, H.D.; Stremmel, W. Direct evidence for catalase as the predominant H_2O_2-removing enzyme in human erythrocytes. *Blood* **1997**, *90*, 4973–4978.

(43) Glorieux, C.; Calderon, P.B. Catalase, a remarkable enzyme: Targeting the oldest antioxidant enzyme to find a new cancer treatment approach. *Biol. Chem.* **2017**, *26*, 1095–1108.

(44) Tehrani, H.S.; Moosavi-Movahedi, A.A. Catalase and its mysteries. *Prog. Biophys. Mol. Biol.* **2018**, *140*, 5–12.

(45) Giordano, C.R.; Roberts, R.; Krentz, K.A.; Bissig, D.; Talreja, D.; Kumar, A.; Terlecky, S.R.; Berkowitz, B.A. Catalase therapy corrects oxidative stress-induced pathophysiology in incipient diabetic retinopathy. *Invest. Ophthalmol. Vis. Sci.* **2015**, *56*, 3095–3102.

(46) Nishikawa, M.; Hashida, M.; Takakura, Y. Catalase delivery for inhibiting ROS- mediated tissue injury and tumor metastasis. *Adv. Drug Deliv. Rev.* **2009**, *61*, 319–326.

(47) Vetrano, A.M.; Heck, D.E.; Mariano, T.M.; Mishin, V.; Laskin, D.L.; Laskin, J.D. Characterization of the oxidase activity in mammalian catalase. *J. Biol. Chem.* **2005**, *280*, 35372–35381.

(48) Kremer, M.L. Peroxidatic activity of catalase. *Biochim. Biophys. Acta* **1970**, *198*, 199–209; doi:10.1016/0005-2744(70)90052-5.

(49) Laser, H. Peroxidatic activity of catalase. *Biochem. J.* **1955**, *61*, 122–127.

(50) Schriner, S.E.; Linford, N.J.; Martin, G.M.; Treuting, P.; Ogburn, C.E.; Emond, M.; Coskun, P.;E.; Ladiges, W.; Wolf, N.; Van Remmen, H.; et al. Extension of murine life span by overexpression of catalase targeted to mitochondria. *Science* **2005**, *308*, 1909–11.

(51) Goth, L.; Rass, P.; Pay, A. Catalase enzyme mutations and their association with diseases. *Mol. Diagn*. **2004**, *8*, 141–149.

(52) Glorieux, C.; Zamocky, M.; Sandoval, J.M.; Verrax, J.; Calderon, P.B. Regulation of catalase expression in healthy and cancerous cells. *Free Radic. Biol. Med.* **2015**, *87*, 84–97.

(53) Kodydkova, J.; Vavrova, L.; Kocik, M.; Zak, A. Human catalase, its polymorphisms, regulation and changes of its activity in different diseases. *Folia Biol.* **2014**, *60*, 153–167.

(54) Winternitz, M.C.; Meloy, C.R. On the occurrence of catalase in human tissues and its variations in diseases. *J. Exp. Med.* **1908**, *10*, 759–781.

(55) Izawa, S.; Inoue, Y.; Kimura, A. Importance of catalase in the adaptive response to hydrogen peroxide: Analysis of acatalasaemic Saccharomyces cerevisiae. *Biochem. J.* **1996**, *320*, 61–67.

(56) Rashtbari, S.; Dehghan, G.; Yekta, R.; Jouyban, A.; Iranshahi, M. Effects of resveratrol on the structure and catalytic function of bovine liver catalase (BLC): Spectroscopic and theoretical studies. *Adv. Pharm. Bull*. **2017**, *7*, 349–357; doi:10.15171/apb.2017.042.

(57) Krych, J.; Gebicka, L. Catalase is inhibited by flavonoids. *Int. J. Biol. Macromol*. **2013**, *58*, 148–53; doi:10.1016/j.ijbiomac.2013.03.070.

(58) Koohshekan, B.; Divsalar, A.; Saiedifar, M.; Saboury, A.A.; Ghalandari, B.; Gholamian, A.; Seyedarabi, A. Protective effects of aspirin on the function of bovine liver catalase: A spectroscopy and molecular docking study. *J. Mol. Liq.* **2016**, *218*, 8–15; doi:10.1016/j.molliq.2016.02.022.

(59) Najjar, M.F.; Ghadari, R.; Yousefi, R.; Safari, N.; Sheikhhasani, V.; Sheibani, N.; Moosavi-Movahedi, A.A. Studies to reveal the nature of interactions between catalase and curcumin using computational methods and optical techniques. *Int. J. Biol. Macromol.* **2017**, *95*, 550–556; doi:10.1016/j.ijbiomac.2016.11.050.

(60) Najjar, M.F.; Taghavi, F.; Ghadari, R.; Sheibani, N.; Moosavi-Movahedi, A.A. Destructive effect of non-enzymatic glycation on catalase and remediation via curcumin. *Arch. Biochem. Biophys.* **2017**, *630*, 81–90; doi:10.1016/j.abb.2017.06.018.

(61) Grigoras, A.G. Catalase immobilization—A review. *Biochem. Eng. J.***2017**, *117*, 1–20.

(62) Kozower, B.D.; Christopher-Solomidou, M.; Sweitzer, T.D.; Muro, S.; Buerk, D.G.; Solomides, C.C.; Albelda, S.M.; Patterson, G.A.; Muzykantov, V.R. Immunotargeting of catalase to the pulmonary endothelium alleviates oxidative stress and reduce acute lung transplantation injury. *Nat. Biotechnol.* **2003**, *21*, 392–398.

(63) Turrens, J.F.; Crapo, J.D.; Freeman, B.A. Protection against oxygen toxicity by intravenous injection of liposome-entrapped catalase and superoxide dismutase. *J. Clin. Invest.* **1984**, *73*, 87–95.

(64) Singhal, A.; Morris, V.B.; Labhasetwar, V.; Ghorpade, A. Nanoparticle-mediated catalase delivery protects human neurons from oxidative stress. *Cell Death Dis.* **2013**, *4*, e903; doi:10.1038/cddis.2013.362.

(65) Czechowska, E.; Ranoszek-Soliwoda, K.; Tomaszewska, E.; Pudlarz, A.; Celichowski, G.; Gralak-Zwolenik, D.; Szemraj, J.; Grobelny, J. Comparison of the antioxidant activity of catalase immobilized on gold nanoparticles via specific and non-specific adsorption. *Colloids Surf. B: Biointerfaces* **2018**, *171*, 707–714.

(66) Abdel-Mageed, H.M.; Fahmy, A.S.; Shaker, D.S.; Mohamed, S.A. Development of novel delivery system for nanoencapsulation of catalase: Formulation, characterization, and in

vivo evaluation using oxidative skin injury model. *Artif. Cells Nanomed. Biotechnol.* **2018**, *46*, 362-371; doi:10.1080/21691401.2018.142521.

(67) Wang, Y.; Zhang, H. Comprehensive studies on the nature of interaction between catalase and SiO_2 nanoparticle. *Mater. Res. Bull.* **2014**, *60*, 51–56.

(68) Bizien, T.; Durand, D.; Roblina, P.; Thureau, A.; Vachette, P.; Pérez, J. A brief survey of state-of-the-art BioSAXS. *Protein Pept. Lett.* **2016**, *23*, 217–231.

(69) Tuukkanen, A.T.; Spilotros, A.; Svergun, D.I. Progress in small-angle scattering from biological solutions at high-brilliance synchrotrons. *IUCrJ* **2017**, *4*, 518–528; doi:10.1107/S2052252517008740.

(70) Liu, D.; Angelova, A.; Liu, J.; Garamus, V.M.; Angelov, B.; Zhang, X.; Li, Y.; Feger, G.; Li, N.; Zou, A. Self-assembly of mitochondria-specific peptide amphiphiles amplifying lung cancer cell death through targeting the VDAC1-hexokinase-II complex. *J. Mater. Chem. B*. **2019**, *7*, 4706–4716; doi:10.1039/c9tb00629j.

(71) Kaplan, D.R.; Matsumoto, K.; Lucarelli, E.; Thiele, C.J. Induction of Trkb by retinoic acid mediates biologic responsiveness to Bdnf and differentiation of human neuroblastoma cells. *Neuron* **1993**, *11*, 321–31.

(72) Encinas, M.; Iglesias, M.; Liu, Y.H.; Wang, H.Y.; Muhaisen, A.; Cena, V.; Gallego, C.; Comella, J.X. Sequential treatment of SH-SY5Y cells with retinoic acid and brain-derived neurotrophic factor gives rise to fully differentiated, neurotrophic factor-dependent, human neuron-like cells*. J. Neurochem*. **2000**, *75*, 991–1003.

(73) David, G.; Pérez, J. Combined sampler robot and high-performance liquid chromatography: A fully automated system for biological small-angle X-ray scattering experiments at the synchrotron SOLEIL SWING beamline. *J. Appl. Crystallogr.* **2009**, *42*, 892–900; doi:10.1107/S0021889809029288.

Chapter 4: Curcumin, fish oil and BDNF - loaded lyotropic liquid crystalline nanostructures and their neuroprotective potential in tunicamycin - induced ER stress cellular model

1) Introduction

Alzheimer's disease (AD) and Parkinson disease (PD) are the most common incurable neurodegenerative diseases whose incidence and prevalence are increasing. They will be expected to surpass cancer as the second highest mortality rate by 2040.[1,2] Current neurodegenerative disease symptomatic treatments do not halt the progressive degeneration that is responsible for many of the debilitating symptoms and impairments in daily life's patient.[3] Most are oral formulations requiring high doses with subsequent high incidence of side effects.[4]

As mentioned in the bibliographic part in the first chapter, it has been established that the progressive loss of neurons results from the combination of multiple factors. The neurotrophic factors (NTFs) deficiency has been reported as a risk factor of neurodegenerative disorders.[5,6] They are a family of biomolecules, which are peptides or small proteins, that support the growth, survival, differentiation, and regeneration as well as the synaptic plasticity of developing and mature neurons and protect them from injury and toxins.[5-12] Many NTFs has been discovered over the years, and are categorized today into three main families: (i) the neurotrophins: nerve growth factor (NGF),[7] brain-derived neurotrophic factor (BDNF), neurotrophin-3 (NT-3), and neurotrophin-4 (NT-4); (ii) the glial cell line-derived neurotrophic factor (GNDF)-family ligands: GDNF, neurturin (NRTN), artemin (ARTN), persephin (PSPN), the neuropoietic cytokines, (iii) and other biomolecules including insulin-like growth factor 1 (IGF-1), pituitary adenylate cyclase-activating peptide (PACAP), macrophage colony-stimulating factor (M-CSF), granulocyte-macrophage colony-stimulating factor (GM-CSF).[8-12]

Studies have shown that the levels of BDNF and its tropomyosin kinase B (TrkB) receptor are decreased in the hippocampus and the cerebral cortex at the beginning of the Alzheimer's disease.[10] BDNF protein promotes the survival of nerve cells (neurons) by playing a role in the growth, maturation (differentiation), and maintenance of these cells. In the brain, the BDNF protein is active at the connections between nerve cells (synapses), where cell-to-cell

communication occurs. The synapses can change and adapt over time in response to experience, a characteristic called synaptic plasticity which is important for learning and memory.[13] The impact of exogenous BDNF on neurogenesis was studied by infusion into the lateral ventricles of the adult rat. BDNF substantially increased the number of newborn cells in many regions, the preponderance of which differentiate into neurons.[14,15] BDNF administration in the hippocampus of the normal adult rat was also associated with an increased neurogenesis of granule cells in the dentate gyrus which is one of the few areas of the brain that demonstrates neurogenesis throughout life.[16,17] BDNF promotes neuronal survival, modulates long-term potentiation of synaptic transmission and regenerative processes after damage which implicates this neurotrophin as a prime therapeutic candidate for a host of neurological disorders.[18,19]

Neuronal regeneration strategy is almost the hope to repair the neural damage. Regeneration of neurons can be induced by enhancing endogenous neurogenesis upon the administration of growth factors, or the transcription of genes. However, the structure of the brain, which is protected by the blood-brain barrier (BBB), through which only very specialized small-molecule drugs can cross cause the difficulty in clinical trials. The therapeutic potential of BDNF is restricted due to its short half-life (< 10 minutes) and inability to cross the blood-brain barrier (BBB) because of its large size (27 kDa).[20]

Nanoscale materials have been developed recently and shown promising safety and efficacy profiles in BDNF protein, BDNF-derived peptide or BDNF gene delivery in the brain or the peripheric nervous system.[21-27] Polymeric-based nanoparticles nano-BDNF: poly(ethylene glycol) -b-poly(l-glutamic acid) by intranasal administration, stabilizes and protects BDNF from nonspecific binding with common proteins in the body fluid, allowing it to associate with its receptors. They improve BDNF delivery throughout the brain and displays a more preferable regional distribution pattern than the native protein.[26] The tail-vein injection of liposomes conjugated to transferrin (Tf) and polyethylene glycol (PEG), carrying BDNF modified were able to traverse the blood-brain barrier, and BDNF was mainly expressed in

the cerebral cortex.[24] Géral *et al.*[27] have shown the potentiation effect of multicompartment lipid carriers cubosome-type containing omega-3 polyunsaturated fatty acid, the eicosapentaenoic acid (EPA), on the BDNF activity in *in vitro* neuroprotective experiments with a SH-SY5Y cell line. Cubosome nanoparticle with a dense core of periodically ordered bilayer lipid membranes may provide high encapsulation rate for both hydrophilic proteins or peptides and poor water-soluble antioxidant substances.[28]

In our study, we aim to determine and compare the potential of lyotropic liquid crystalline nanoparticles towards neuronal survival by encapsulating natural lipid and bioactive compounds with and without BDNF loading. To do so, we characterize the loading of human BDNF protein and its co-encapsulation with curcumin by the non-lamellar liquid crystalline nanoparticles from the binary lipid mixture consisting of monoolein (MO) and fish oil (FO), a rich source of ω-3 polyunsaturated fatty acid (Fig. 1). And we elaborate a cellular model to evaluate their neuroprotective potential effect in cell damaged by neurotoxin (Fig. 2).

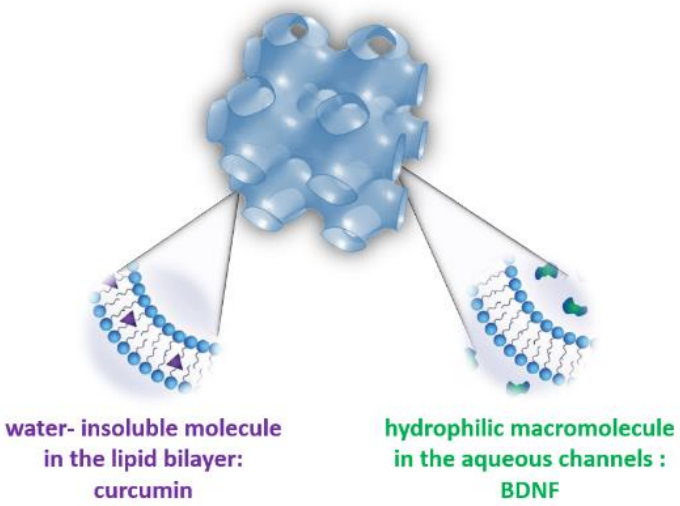

Figure 1. Three-dimensional organizations of primitive cubic liquid crystalline phases (also referred to as *Im3m*/Q^{IIP}), enabling the loading and protection of both hydrophilic and hydrophobic unstable molecules of therapeutic significance: curcumin and brain derived neurotrophic factor (BDNF).

The choice of the cellular model presented in figure 2, created with differentiated SH-SY5Y cells, is based on the following considerations.

Protein misfolding and aggregation are known to be associated with Alzheimer's, Parkinson's, and Huntington's diseases.[29-31] N-linked glycosylation is a key step early in the folding of most proteins that takes place within the endoplasmic reticulum (ER). The inhibition of this process provokes the accumulation of misfolded proteins in the ER, the main hallmark of ER stress. The accumulation of unfolded or misfolded proteins in the ER lumen causes ER stress and activates a compensatory mechanism, called the unfolded protein response (UPR).[30-36] However, when sustained or severe ER stress surpasses the capacity of UPR, apoptotic cell death occurs.[33-38] ER stress has been shown to play an important role in the pathogenesis of various neurological diseases[39-41] and have been implicated in neurodegenerative processes in brain ischemia[42,43], Alzheimer's disease (AD)[44], Parkinson's disease (PD),[45-47] Huntington's disease (HD)[48] and amyotrophic lateral sclerosis (ALS).[49]

Tunicamycin is an N-linked glycosylation inhibitor and is commonly used to induce ER stress experimentally.[50-52] Tunicamycin reduces also the neurotrophin TrkB receptor expression because of the induced ER stress upon which the neurotrophin receptor synthesis is hampered (the cytosolic face of the rough endoplasmic reticulum are the sites of protein synthesis). Tunicamycin treatment provoke ER stress-induced cell death in neuroblastoma cells, SK-N-SH and its neuroblast-type subclone SH-SY5Y cells.[52]

In this study, we expect that tunicamycin cytotoxicity leads to neuronal cell death and induces ER stress in human neuroblastoma SH-SY5Y cells differentiated by the retinoic acid and deprived of fetal bovine serum (FBS). Serum starvation could provoke oxidative stress and cell apoptosis effects. And we expect that the single or the multidrug-loaded LCNPs (fish oil, curcumin, BDNF) protect from the cell damage and promote neuronal survival.

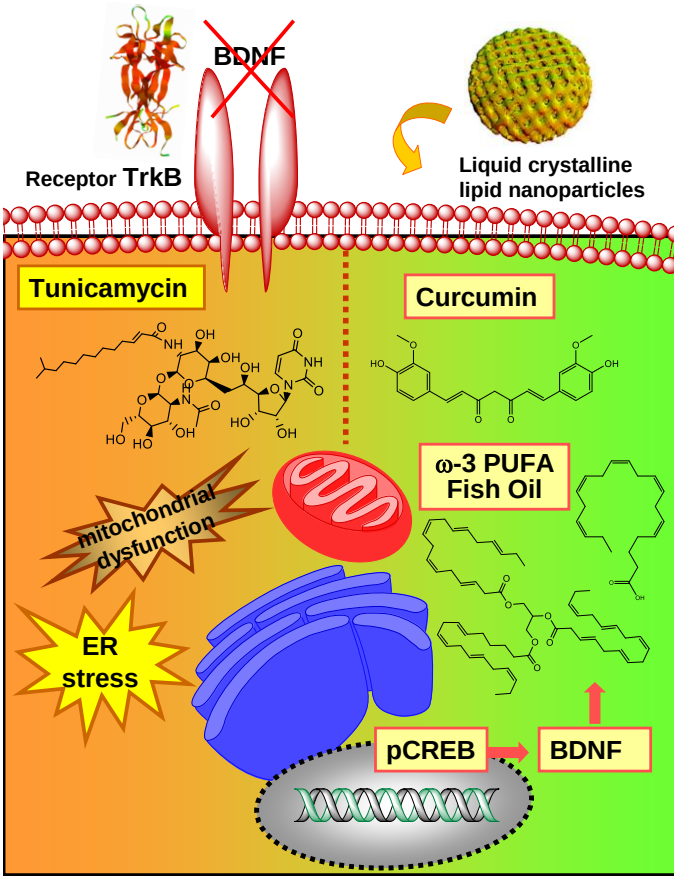

Figure 2. Schematic presentation of the cellular model, created with differentiated SH-SY5Y cells, for investigation of induced endoplasmic reticulum (ER) stress-mediated neurodegeneration. Neuronal damage via ER stress caused by the neurotoxin tunicamycin is accompanied by hampered neurotrophin BDNF/TrkB signaling due to neurotrophin deficiency and oxidative stress mitochondrial damage upon starvation. The regenerative capacity of liquid crystalline lipid nanoparticles loaded by the multiple active ingredients (phytochemical antioxidant curcumin, ω -3 PUFA rich fish oil, and/or BDNF) is studied towards development of emergent combination therapies exploiting natural plant-derived and marine-derived bioactive compounds.

2) Materials and methods

a. Materials

Monoolein (MO) with purity > 99% was obtained from Hampton research. The pegylated amphihile, D-α-tocopherol polyethylene glycol-1000 succinate (denoted as TPGS-PEG1000) was purchased from Sigma Aldrich. Fish oil (FO) and curcumin (CU) with purity > 66% were purchased from Sigma Aldrich. The water used was of MilliQ quality (Millipore Corp., Molsheim, France). Human BDNF was obtained from Sigma (for cell culture experiments) and R&D Systems (BioTechne Ltd, UK) for structural experiments. For cell culture experiments, Dulbecco's modified Eagle's Medium (DMEM), streptomycin-penicillin, phosphate buffered saline (PBS), trypsin, ethylenediaminetetraacetic acid EDTA, retinoic acid (RA) and 3-(4,5-Dimethylthiazol-2-yl)-2,5-diphenyl tetrazolium bromide (MTT) were supplied by Sigma-Aldrich. Foetal bovine serum (FBS) was provided by Thermo Fischer Scientific (Illkirch, France).

b. Preparation of the BDNF-loaded LCNPs

The lipid monoolein (MO), the amphiphilic stabilizer TPGS-PEG_{1000}, fish oil (FO), and curcumin (CU) were weighed and dissolved in chloroform. The samples were prepared at room temperature to obtain four NPs with different compositions (Table 1). The solvent was evaporated under a stream of a nitrogen gas for 1 h at room temperature to create a thin film lipid sample. The samples were lyophilized overnight under cooling to remove the excess solvent. This step was followed by the hydration of the thin film samples by a solution of Milli-Q water at 90 wt% of concentration of aqueous phase with regard to the lipid phase. Finally, the samples were vortexed vigorously at room temperature in cycles during 15 min.

The assemblage of the NPs and the BDNF was obtained from the stock solution of 56 mM of NPs and 500 µg/ml of BDNF. A volume of 4 µL of NPs and 1 µL and BDNF stock solution was mixed to obtain a BDNF-loaded NPs and then stored at 4°C.

Table 1. Compositions of bulk liquid crystalline phases presented as mass proportions of MO, TPGS-PEG_{1000}, FO, CU.

molar ratio (mol/mol)	weight ratio (wt/wt)	MO (g)	TPGS-PEG_{1000} (g)	FO (g)	CU (g)
0/100 FO:MO	0/100 FO:MO	0.01	0.0027		
17/83 FO:MO	30/70 FO:MO	0.01	0.0027	0.00544	
17/83 FO:MO	32/68 FO:MO	0.01	0.0027	0.00544	0.00074
0/100 FO:MO	0/100 FO:MO	0.01	0.0027		0.00074

c. Cryogenic transmission electron microscopy (cryo-TEM)

For cryo-TEM investigation, a sample droplet of 2µL was placed on a lacey carbon film covered copper grid (Science Services, Munich, Germany), which was hydrophilized by glow discharge (Solarus, Gatan, Munich, Germany) for 30 s. Most of the liquid was then removed with blotting paper, leaving a thin film stretched over the lace holes. The specimen was instantly shock frozen by rapid immersion into liquid ethane and cooled to approximately 90 K by liquid nitrogen in a temperature and humidity controlled freezing unit (Leica EMGP, Wetzlar, Germany). The temperature and humidity were monitored and kept constant in the chamber during all sample preparation steps. The specimen was inserted into a cryo-transfer holder (CT3500, Gatan, Munich, Germany) and transferred to a Zeiss EM922 Omega energy-filtered TEM (EFTEM) instrument (Carl Zeiss Microscopy, Jena, Germany). Examinations were carried out at temperatures around 90 K. The TEM instrument was operated at an acceleration voltage of 200 kV. Zero-loss-filtered images (DE = 0 eV) were taken under reduced dose conditions (100-1000 e/nm^2). The images were recorded digitally by a bottom-mounted charge-coupled device (CCD) camera system (Ultra Scan 1000, Gatan, Munich, Germany) and combined and processed with a digital imaging processing system (Digital Micrograph GMS 1.9, Gatan, Munich, Germany). The sizes of the investigated nanoparticles were in the range or below the film thickness and no deformations were observed. The images were taken very close to focus or slightly under the focus (some nanometers) due to the contrast enhancing

capabilities of the in-column filter of the employed Zeiss EM922 Omega. In EFTEMs, the deep underfocused images can be totally avoided.

d. Cell viability studies: MTT Assay

The cell viability after retinoic acid (RA) without fetal bovine serum (FBS) or tunicamycin (TUN) and nanoparticles treatment was determined by the tetrazolium salt test (3-(4,5-dimethylthiazol-2-yl) -2,5-diphenyl tetrazolium bromide, MTT). The solution of MTT was prepared in PBS and was filtered prior to use. This reagent is reduced to formazan by the mitochondrial succinate dehydrogenase enzyme in living cells. The MTT compound forms a purple precipitate, the quantity of which is proportional to the metabolic activity of the living cells. The cells were seeded at a density of 20×10^4 cells/well in 96-well plates. After 5 days of treatment with 10 µM retinoic acid, the RA-differentiated cells were stressed during 24h with by depriving them of FBS or by Tun 1µM incubation. Then non-loaded or BDNF- loaded nanoparticles were incubated with the cells at 37 °C for 24 h at lipid concentrations of 2.5 µM and 5ng/ml of BDNF. Untreated cells maintained in DMEM medium were used as controls. MTT was added at a concentration of 5 mg/mL at 37 °C. After 1 h of incubation of the cells with MTT, the medium was removed, and the cells were dissolved in 100% DMSO to solubilize the formazan precipitate. The optical density of the samples was measured at 570 nm using a multiwell-scanning spectrophotometer (LT-5000 MS, Labtech). The quantification was done using measurements of a minimum of six wells.

e. Cytotoxicity studies: LDH Assay

The cell death and the lived-cells number following retinoic acid (RA) without fetal bovine serum (FBS) or tunicamycin (TUN) and nanoparticles treatment were measured by the CytoTox 96® Non-Radioactive Cytotoxicity Assay. This kit assay quantitatively measures lactate dehydrogenase (LDH), a stable cytosolic enzyme that is released upon cell lysis. Released LDH in culture supernatants is measured with a 30-minute coupled enzymatic assay, which results in the conversion of a tetrazolium salt (iodonitrotetrazolium violet; INT) into a

red formazan product. The amount of color formed is proportional to the number of lysed cells. Visible wavelength absorbance data are collected using a standard 96-well plate reader.

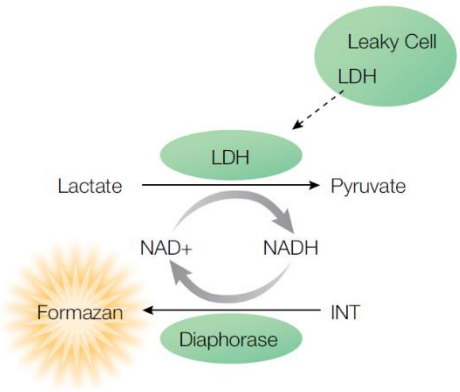

Figure 3. Release of LDH from damaged cells is measured by supplying lactate, NAD+ and INT as substrates in the presence of diaphorase. Generation of a red formazan product is proportional to the amount of LDH released and therefore the number of lysed cells.

To measure cell death following cell starvation and BDNF (5ng/ml)-loaded NPs (48h), cells were seeded at a density of 20 × 10^4 cells/well in 96-well plates. 50 µl aliquots from all test and control wells were transferred to a fresh 96-well flat clear bottom plate and added 50 µl of the CytoTox 96® Reagent, protected from light for 30 minutes at room temperature. Then 50 µl of Stop Solution were added before the recording of the absorbance at 490nm or 492nm within 1 hour.

$$\text{Percent cytotoxicity} = \frac{\text{Experimental LDH Release } (OD_{490})}{\text{Maximum LDH Release } (OD_{490})} \times 100$$

The CytoTox 96® Assay indirectly measures lactate dehydrogenase activity present in the cytoplasm of intact cells. Cell quantitation, therefore, can occur only if the cells are lysed to release the LDH present in the cell. To measure the lived-cells numbers following the different treatments, the medium in the plate with seeded cells were removed after aliquot for cytotoxicity assay. Cell samples of interest are lysed by adding 15µl of Lysis 10X Solution [9% (v/v) TritonR X-100 in water] per 100µl of culture medium, followed by incubation at 37°C for 45–60 minutes. CytoTox 96® Reagent (50µl) is added to each supernatant sample, and the

enzymatic reaction is allowed to proceed for 30 minutes at room temperature, protected from light. The enzymatic assay is then stopped by adding 50µl/well of Stop Solution. Absorbance can be read at 490nm using a plate reader.

f. Microscopy imaging

The cells were seeded at a density of 40 × 10^4 cells/well in 6-well plates and treated with tunicamycin and BDNF-loaded LCNPs. Fluorescent images of live cells were taken under a 63x objective with a Carl ZEISS microscope, Cool SNAP camera and saved using ZEISS ZEN microscope software (Version 3.1, Germany). Fluorescent images were converted to 8-bit before being quantified by mean grey value analysis on ImageJ. A polygon with the same area was selected for each image to normalize the fluorescent data per cell. The excitation and emission settings were: Thioflavin T (ThT) (Ex. 458 nm, Em. 480–520 nm), ER-Tracker™ Blue White DPX dye (Ex. 374, Em. 430–640 nm) and MitoView™ Green (Ex. 490, Em. 523 nm). Each fluorescent channel was imaged sequentially, as opposed to simultaneously, to avoid channel overlap.

g. Human free BDNF quantification

The human free Brain-Derived Neurotrophic Factor (BDNF) concentrations in cell culture supernates were determined using Quantikine® ELISA Human Free BDNF Immunoassay kit (Europe, Middle East, Africa Bio-Techne Ltd, UK) following the manufacturer's instructions.

Briefly, 96 well plates were pre coated with a monoclonal antibody specific for human free BDNF. BDNF standards and samples are pipetted and incubated into the wells for 2 h and any free BDNF present is bound by the immobilized antibody. An enzyme-linked monoclonal antibody specific for human free BDNF is added to the wells for 1 h. All of the incubation stages were conducted at room temperature. Then a procedure of a total of 3 washes with washing buffer was performed to remove any unbound antibody-enzyme reagent. A substrate solution is added to the wells for 30 min and color develops in proportion to the

amount of free BDNF bound in the initial step. The color development is stopped with a stop solution and the intensity of the color is measured. The absorbance at 450 nm was measured within 30 min after stopping the reaction.

Total protein concentration was measured by Bradford Protein Assay (BSA). The stock solution of BSA is at 2mg/ml concentration in PBS from which a calibration range was prepared. 50 µL of BSA standard or samples of cell lysates + 150 µl Bradford reagent. The optical density of each well was measured by using a microplate reader set to 595 nm.

h. Statistical analysis

The data are expressed as mean ± standard deviation (SD) of three independent experiments. The results were analyzed by the Tukey test after one-way analysis of variance. The probability values $p < 0.05$ were considered statistically significant across the treatment groups.

3) Results and discussion

a. Morphological characterization of dispersed liquid crystalline lipid nanoparticles by Cryo-TEM Imaging

The dispersed liquid crystalline lipid nanoparticles with encapsulated ω-3 PUFA rich fish oil and curcumin [MO-FO-CU] stabilized by (TPGS-PEG_{1000}) were visualized by cryo-TEM imaging. The images are shown in Figure 4 and revealed the topology of cubosome and spongosome type lipid nanoparticles loaded by bioactive ingredients. The domain organization show encapsulation of inner oil-rich domains (Fig. 4A, B), or domains rich in phytochemical constituent in the core of the liquid crystalline lipid nanoparticles (Fig. 4C, D). Lipid-based cubosomes and spongosomes involve multiple internal compartments, which represent a structural advantage enabling the encapsulation efficacy and serve as mesoporous reservoirs for co-encapsulation of ω-3 PUFA with water-insoluble drugs and hydrophilic macromolecules toward development of combination treatment. [53]

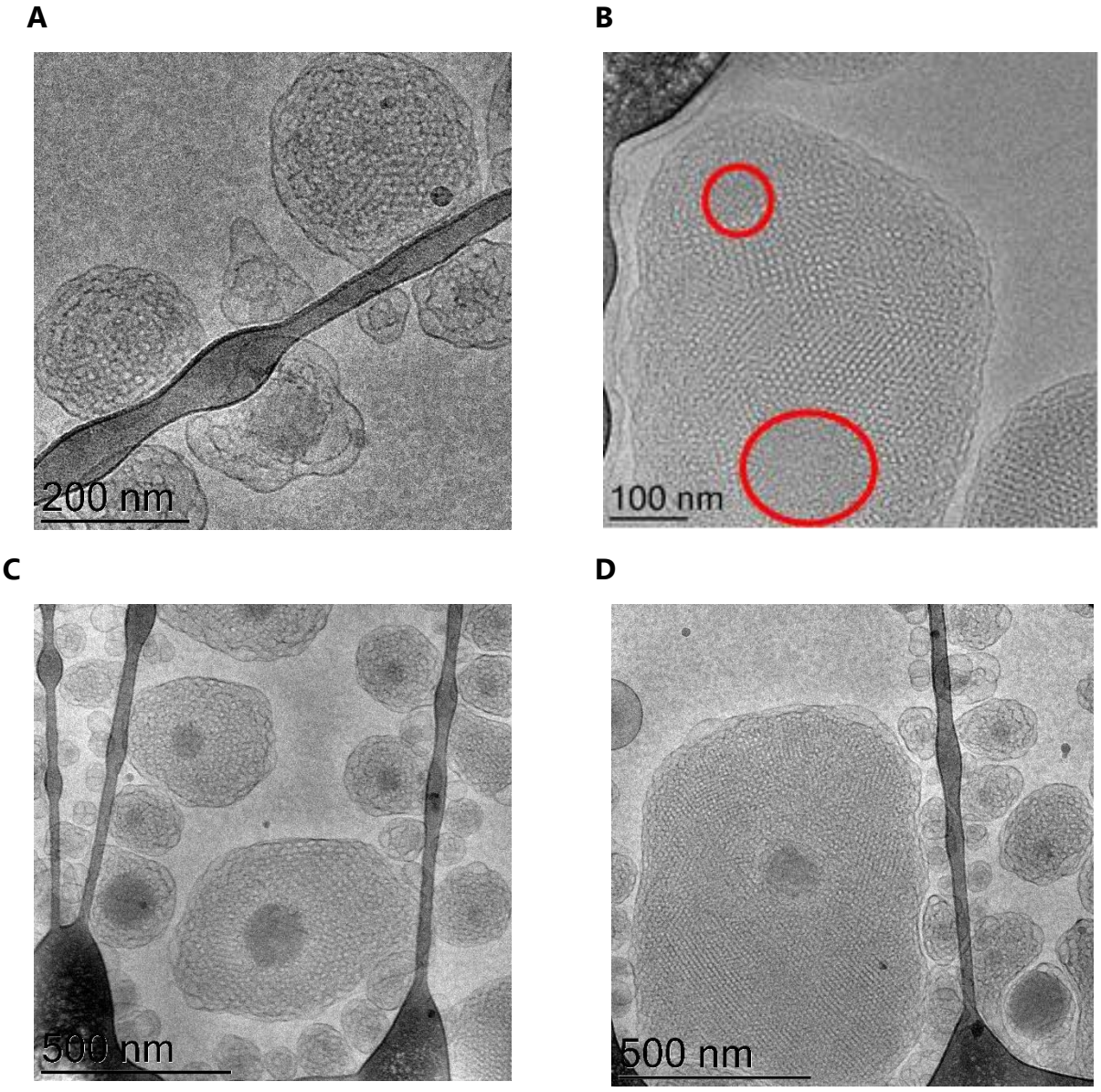

Figure 4. Cryo-TEM images of dispersed liquid crystalline lipid nanoparticles with encapsulated ω-3 PUFA rich fish oil and phytochemical antioxidant. The multicomponent assemblies [MO:FO:CU:TPGS-PEG$_{1000}$] are stabilized by PEGylated amphiphilic stabilizer D-α-tocopheryl-poly(ethylene glycol)1000 (TPGS-PEG$_{1000}$). The incorporated guest molecules lead to distortion of the long-range order of the bicontinuous lipid membrane and lead to formation of cubosomal intermediates and sponge type nanoparticles (**A**), cubosomes with inner oil-rich domains (highlighted in red colour in (**B**)) or inner domains rich in phytochemical constituent (darker domains in the core of the liquid crystalline lipid nanoparticles in (**C**) and (**D**)).

b. Cytotoxicity of the blank and loaded LCNPs

The human neuroblastoma SH-SY5Y cells were seeded and treated with RA (10 µM) for 5 days to obtain the typical neuronal cell phenotype. Then, the cells were starved with FBS-free DMEM for 24 h, the condition for cell treatment with the nanoparticles. Then, they were exposed to the liquid crystalline nanoparticles for 24 or 48 hours. The LCNPs were loaded or not by BDNF (5ng/ml). Unexposed cells to nanoparticles were used as viability controls.

i. *MTT assay with the LCNPs with and without BDNF loading*

The obtained MTT data (Figure 5A, B) demonstrate that the cellular viability decreases from 100 ± 3.2% to 71 ± 4.0% for starved differentiated SH-SY5Y cells (RA(-)FBS), compared to the RA-differentiated SH-SY5Y cells control (RA(+)FBS). FBS deprivation influences significantly (**$p < 0.01$) the cell viability. This result indicated an essential stress condition induced by the starvation.

First cells were exposed to the blank or dual-loaded liquid crystalline (FO-CU) nanoparticles at different concentrations for 24 hours (Fig. 5A). At all concentration, the blank nanoparticles didn't influence the cell viability compared to the starved differentiated SH-SY5Y cells (RA(-)FBS, at 0 µM of NPs)) and presented around 60 % of cell viability. However, the FO-CU-loaded nanoparticles at between 0,5 to 10 µM concentrations, enhanced the cell viability with values from 77 to 87 ± 5.0%. From 10 µM of nanoparticles, there was no significant difference compared to the starved cells. These results show that the nanoparticles are safe. The (FO-CU)-loaded NPs increase cell viability at low concentrations and protect from starvation-induced stress and cell death. This could be explained by the antioxidant effect of curcumin[54] but also its protection of fish oil. A recent study of Shehzad, Q. *et al.*[55] demonstrated the improvement of the stability of fish oil nanoemulsions by co-encapsulation with curcumin and other antioxidant.

Then cells were exposed to the multidrug-loaded liquid crystalline (FO-CU-BDNF) nanoparticles at lipid concentration of 2.5 μM and at BDNF concentration of 5ng/ml for 24 hours (Fig. 5B). The MTT test indicated a cell viability between 82 ± 4.7% to 95 ± 2.1% with the single or multiple drug-loaded nanoparticles with BDNF treatment. The data obtained did not show a significant viability difference as compared to the RA(+)FBS cells control. The significant viability decrease (66 ± 4.7%, $^{**}p < 0.01$) was obtained with the blank nanoparticle (MO). These results evidenced not only the safety of the single or multiple drug-loaded nanoparticles but also the BDNF – loaded NPs effect on cell survival after starvation of RA-differentiated SH-SY5Y cells.

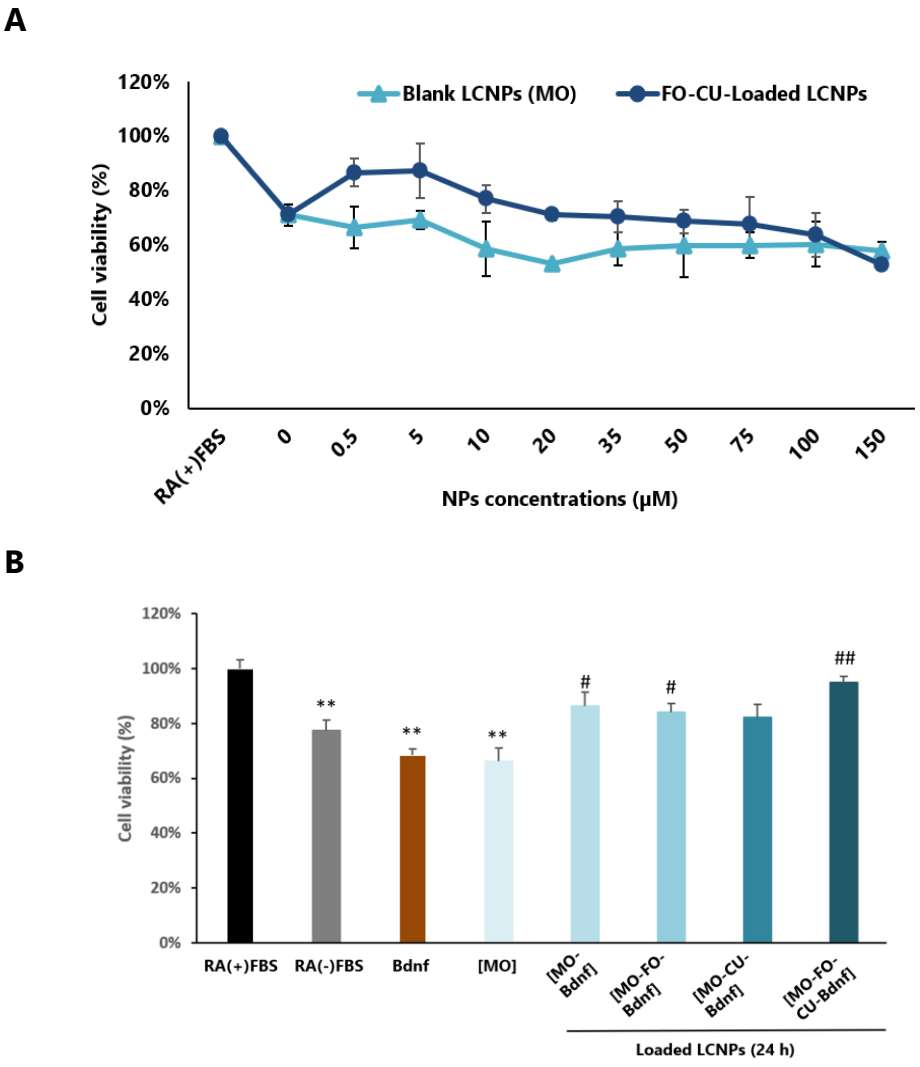

Figure 5. Cellular viability by MTT assay of the retinoic acid (RA)-differentiated SH-SY5Y cells after 24 hours exposure to blank or loaded liquid crystalline nanoparticles: **A)** at

different concentrations **B)** at a lipid concentration of 2.5 µM, significant differences were observed with **p < 0.01 vs RA (+) FBS; #p < 0.05 and ##p < 0.01 vs Bdnf alone.

On the other hand, the percent of cell survival has significantly (#p < 0.05 and ##p < 0.01) increased in the presence of BDNF-loaded LCNPs than with free BDNF treatment alone (Fig. 5B). This result confirms the advantage of using the liquid crystalline nanoparticle to protect and enhance the effect of the neurotrophin. It emphasizes Géral, C. *et al.*[23] and Angelova *et al.* [53] works about the potentiation effect of multicompartment lipid carriers containing omega-3 polyunsaturated fatty acid on the BDNF activity in *in vitro* neuroprotective experiments with SH-SY5Y cell line.

Besides, viability with the multidrug [FO-CU-BDNF]-loaded LCNPs is significantly higher, which could indicate a synergistic effect with the drugs co-encapsulation in the lipid-based nanocarrier (Fig. 5B). Curcumin could mediate the BDNF signal-modulating cascades, which are involved in the neuroprotective effects.[56,57] Zhang *et al.*[58] found that chronic curcumin treatments activate ERK or N-methyl-D-aspartate-CREB signaling, accelerate the expression of BDNF, and enhance pathological, biochemical, and behavioral changes in an Alzheimer's disease rat model induced by ventricular inoculation of $A\beta_{1-42}$. Other study also hypothesized the neuroprotection of curcumin might be mediated via BDNF/TrkB-MAPK/PI-3K-CREB signaling pathway.[59]

ii. LDH assay with BDNF-loaded LCNPs

The dead cells were quantified by lactate dehydrogenase (LDH) released in culture supernatants upon cell lysis due to serum starvation and BDNF (5ng/ml)-loaded NPs for 48 h. The live cells were quantified indirectly by LDH activity present in the cytoplasm of intact cells which were lysed to release the LDH.

The obtained LDH assay data (Figure 6) demonstrated that there was no significant difference (**p < 0.01) between dead cells upon treatment with blank nanoparticles

(MO]NPs and dead cells control (RA(-)FBS or starved cells). However, there was a significant decrease of dead cells upon treatment with all BDNF-loaded NPs compared to the dead cell control. And a significant increase (##p < 0.01) of live cells upon treatment with FO and BDNF-loaded NPs was observed compared to the live cell control (RA(-)FBS or starved cells). The polyunsaturated fatty acid has shown a real effect of potentiation of the neurotrophic factor BDNF in a combination with liquid crystalline monoolein (MO)-based multicompartment nano-assembles.[27,53] A trend of increased live cell was observed with CU, FO, and BDNF-loaded NPs.

These results show that BDNF-loaded LCNPs are safe, influence protection against cell death-induced serum starvation and cellular survival. In fact, serum provides optimal conditions for cell growth and the deprivation induce cell apoptosis. We can considerate a regenerative potential of the BDNF-loaded LCNPs towards neurotrophin deficiency-induced cell apoptosis.

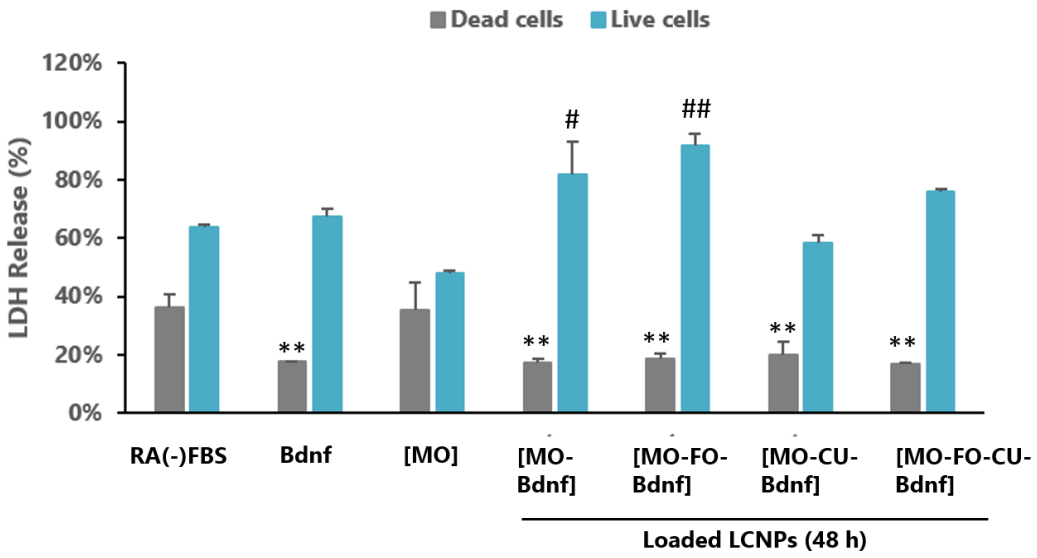

Figure 6. Cytotoxicity by LDH assay of the blank or loaded liquid crystalline nanoparticles in the retinoic acid (RA)-differentiated SH-SY5Y cells after 48 hours exposure to nanoparticles, significant differences were observed with **p < 0.01 vs dead RA(-)FBS cells control; #p < 0.05 and ##p < 0.01 vs live RA(-)FBS cells control.

In conclusion, both MTT and LDH cytotoxicity studies evidenced that the single or multidrug-loaded liquid crystalline nanoparticles with BDNF are safe, protect from cell death and can enhance cellular repair.

c. Cytotoxicity of tunicamycin

The human neuroblastoma SH-SY5Y cells were seeded and treated with RA (10 μM) for 5 days and deprived of FBS for 24h. To establish the optimal concentration of tunicamycin (Tun) that produces a measurable amount of retinoic acid – differentiated SH-SY5Y cell death, the cells were treated with different concentrations of this drug for 24 h (Fig. 7).
Micrographs recorded following the exposition of the RA-differentiated SH-SY5Y cells to tunicamycin are shown in Figure 7A. The microscopy examination showed the attached cells with the elongated neurites to the plates in the control cell with no tunicamycin treatment (0 μM). Some elongated cells tend to evolve into more rounded shapes because of the absence of FBS. Half of the cell became more and more rounded with neurites decrease or detached from the plate prior to tun (1 μM) exposure. This was indicative of an apoptotic and/or cell death process. The exposition to 10 μM Tun which mimics an acute stress condition, revealed massive cell death with a cell confluence < 5%.

The toxicity of tunicamycin to RA-differentiated SH-SY5Y cells was determined by MTT assay at increasing concentrations from 0 to 50 μM (Fig. .7B). We observed a dose-dependent decrease in cell viability. A decrease at 50% of the cell viability is reached at concentrations between 0.5 and 1 μM tunicamycin. Higher concentrations of tunicamycin (10 - 50 μM) caused massive cell death in the cultures. The similar results were observed in Zamarbide M. *et al.* studies in which human neuroblastoma SH-SY5H cells death were measured by the LDH activity released to the culture medium.[51] They observed the dose-dependent increase in cell death that reached a plateau at concentrations of 0.5 and 1 μM tunicamycin. Therefore, the concentration of 1 μM Tun was chosen for the subsequent experiments with 4 h exposure.

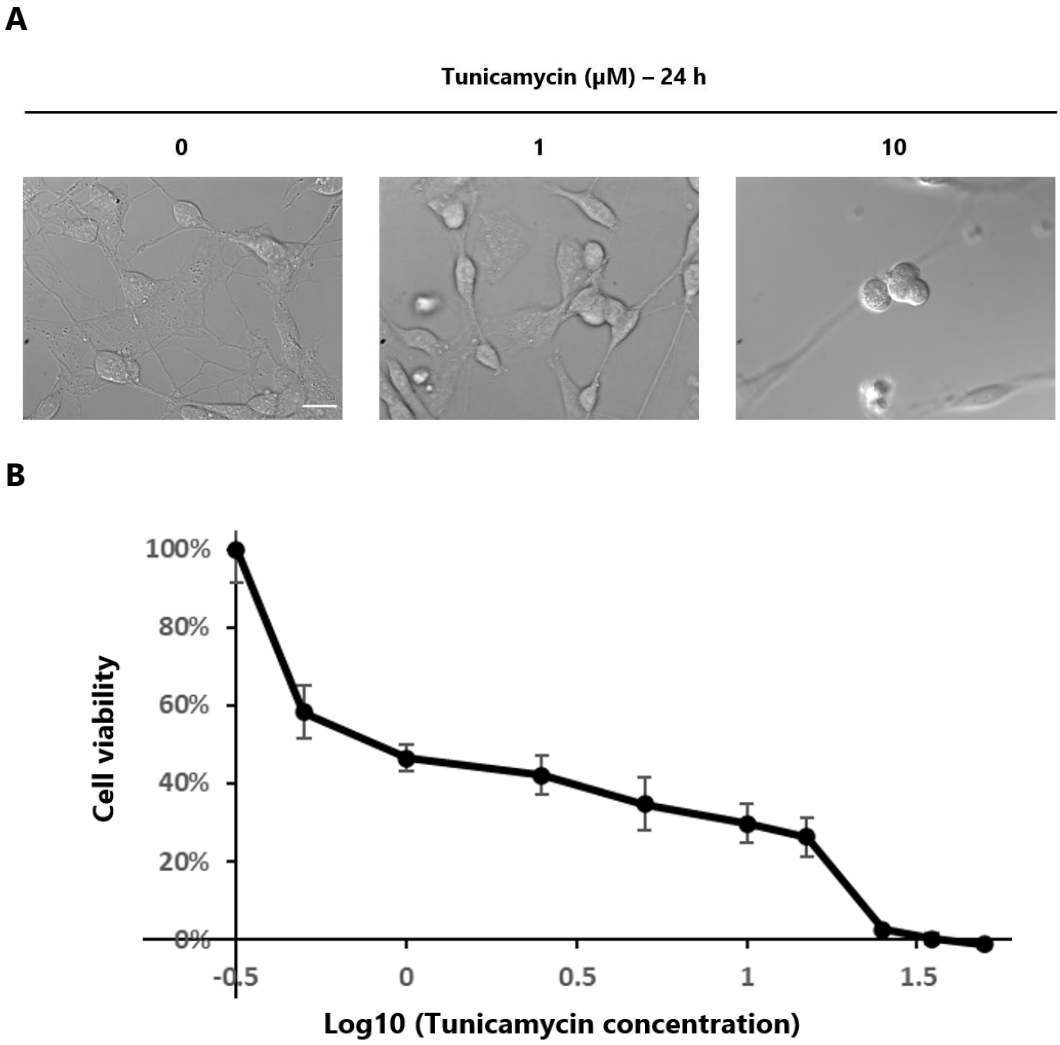

Figure 7. RA-differentiated SH-SY5Y deprived of FBS and treated with different concentration of tunicamycin for 24h. **A)** Micrographs images by Zeiss microscope, objective ×63, scale bar = 15µM. **B)** Cell viability by MTT assay following 0 – 50 µM tunicamycin exposure.

d. Cell viability with multidrug-loaded LCNPs treatment in tunicamycin - induced cell death

To assess the effects of single or multiple-loaded LCNPs in RA-differentiated SH-SY5Y cells damaged by tunicamycin, cells images were captured by confocal microscopy (Fig. 8).

DIC micrograph in figure 8A show the morphology of control cells (RA(-)FBS - SH-SY5Y). Lots of cells were still attached to the plate and a few cells were in an apoptotic state (Fig. 8A). The cellular organelles: endoplasmic reticulum and mitochondria were stained by ER-Tracker™ Blue and MitoView™ Green (Fig. 8A).

DIC micrograph in figure 8B show the morphology of the cell exposed to tunicamycin 1µM for 4 h. We observed live cells with neurites still attached to the plate and many others in a necrotic state. Images of the stained ER and mitochondria showed changes in the cellular organelles network, their morphologies and presumably in their metabolisms (Fig. 8B).

DIC micrograph in figure 8C show the morphology of the cell treated by (FO-CU-BDNF) LCNPs for 24 h after tunicamycin exposure. We observed the cell survival with neurites extension. Images of the stained ER and mitochondria showed the similar network and morphologies as those of live cells control (Fig. 8C). A recent study of Kandezi *et al.*[60] reported the function of PI3/Akt/GSK3 and PI3/Akt/CREB/BDNF signaling pathways in the neuroprotective properties of curcumin and the association of these two main pathways with antioxidant, anti-inflammatory, anti-apoptosis, and biogenesis effects of mitochondria.

In brief, these observations suggest a cellular protection or repair of the damaged cell by tunicamycin by the (FO-CU-BDNF) LCNPs.

Then, cell viabilities were quantified by MTT assay after cell exposure to the neurotoxin tunicamycin for 4 h and cell treatment with the different nanoparticles for 24 h. The LCNPs at a lipid concentration of 2.5 µM were loaded by BDNF (5ng/ml).

The results in figure 9 show a significant decrease (*$p < 0.05$) of cell viability with tunicamycin (43 ± 3.1%) compared to cell viability with starved cell (RA(-)FBS, 74 ± 3.7%).

In comparison to the damaged cell by the neurotoxin, a significant decrease (#$p < 0.05$) of cell viability was observed with free-BDNF and non-loaded NPs (MO). A trend of cell viability increase was observed with both single (BDNF)-loaded NPs and (FO-CU-BDNF)-loaded NPs. A significant increase (#$p < 0.05$) of cell viability was observed with (FO-BDNF)-loaded NPs (57 ± 7.0%) (Fig. 9).

From these results, we can suggest that the BDNF-loaded LCNPs enhance cellular survival upon tunicamycin-induced cell death.

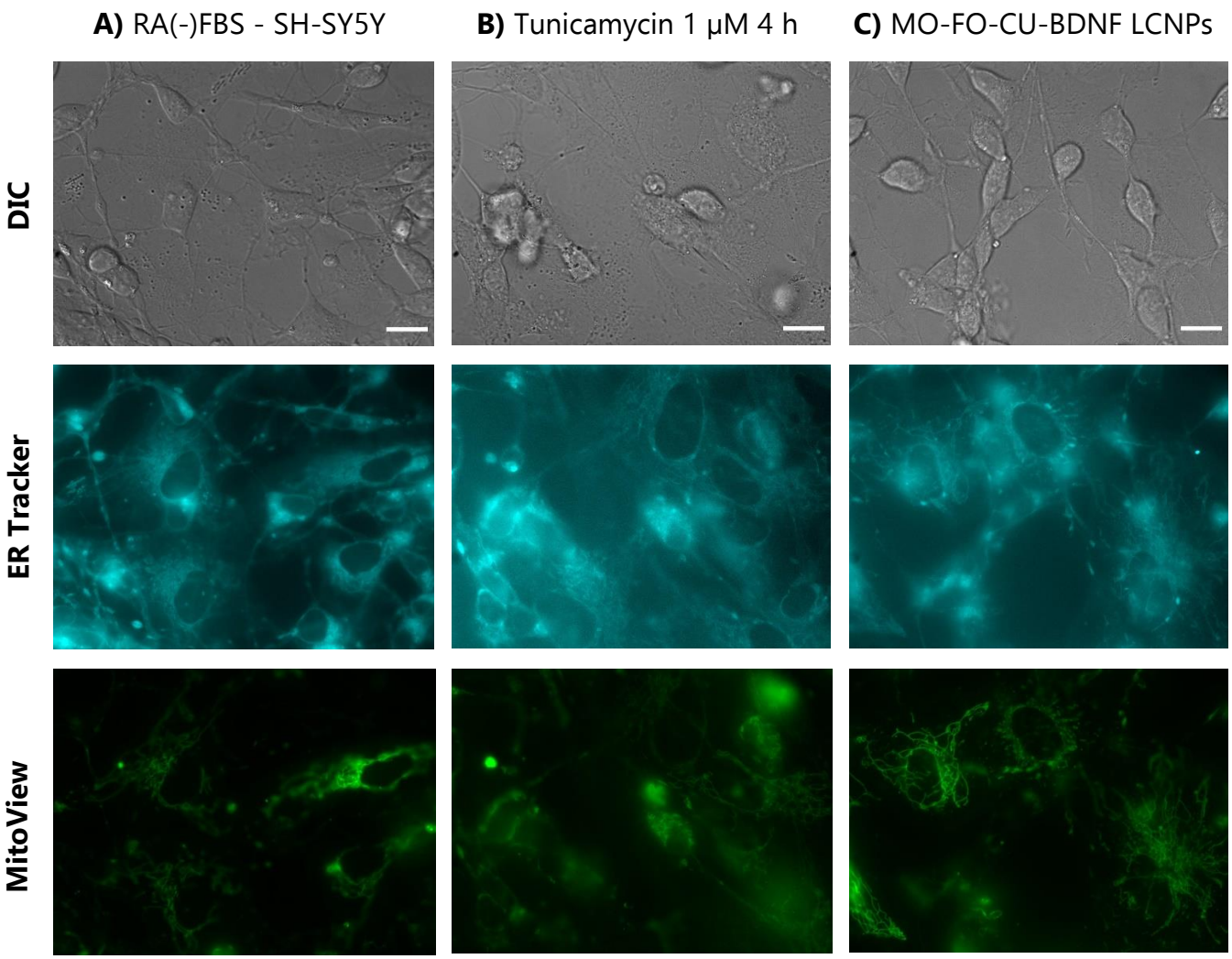

Figure 8. Confocal microscopy images show the SH-SY5Y cellular morphology, the endoplasmic reticulum visualization by ER-Tracker™ Blue White DPX dye staining (Ex. 374, Em. 430–640 nm) and mitochondria visualization by MitoView™ Green (Ex. 490, Em. 523 nm) staining: **(A)** after 5 days of incubation with 10 µM RA and FBS-free serum for 24 h; **(B)** after 1 µM Tunicamycin for 4 h; **(C)** after 1 µM Tunicamycin for 4 h and curcumin, fish oil-BDNF-loaded nanoparticles (MO-FO-CU-BDNF) LCNPs. Scale bar = 15 µm.

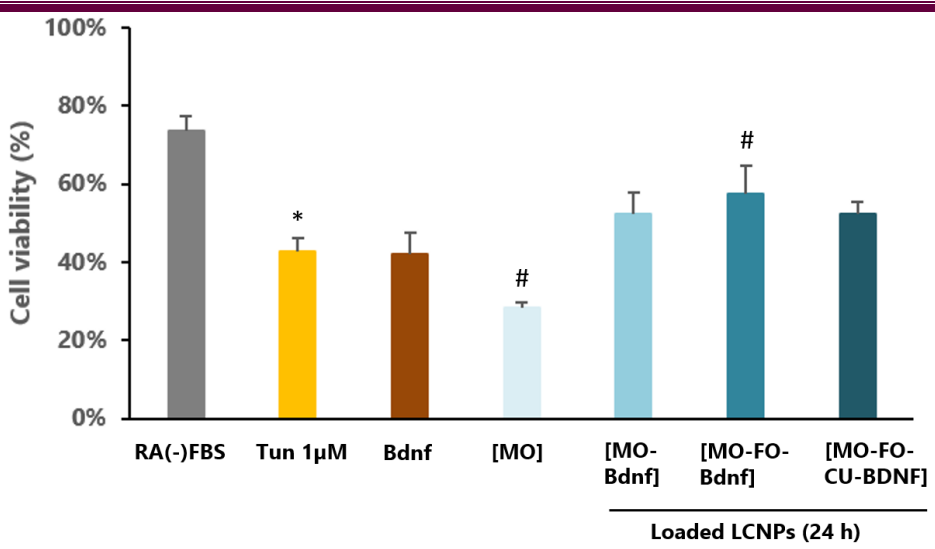

Figure 9. Cell viability by MTT assay of the RA-SH-SY5Y damaged by tunicamycin and treated by blank or loaded liquid crystalline nanoparticles (LCNPs), significant differences were observed with *p < 0.05 vs RA(-)FBS, #p < 0.05 vs tunicamycin.

e. BDNF - loaded LCNPs effects in tunicamycin - induced ER stress

In order to validate our model of ER stress in retinoic acid (RA)-differentiated human neuroblastoma SH-SY5Y cells, Thioflavin T (Tht) (5 µM) were added to the cultures (Fig. 10) in the presence of the ER stress-inducing agent, tunicamycin.[51] Tht is a small molecule with fluorescence properties that has been shown to bind selectively to protein aggregates, particularly β-sheets.[61–63] Beriault D.R. and Werstuck G.H. have shown that Tht is effective as a tool to detect protein aggregates as a measure of ER stress levels in living cells.[64] Enhanced Tht-fluorescence correlates directly with established indicators of unfolded protein response activation.[64,65]

First, we determined the subcellular localization of the Tht staining in RA-differentiated SH-SY5Y cells (Fig. 10A). Cells were treated with 1 µM tunicamycin for 5 h. The microscope images in figure 10A show ER tracker-fluorescence which was visualized in the perinuclear region of tunicamycin treated cells. Tht-fluorescence colocalized to the ER tracker staining in tunicamycin treated cells.

This result is consistent with Tht interacting directly with misfolded proteins in the ER.

Then, we quantified the level Tht-fluorescence in the retinoic acid (RA)-differentiated human neuroblastoma SH-SY5Y cells which were cultured in the absence (controls) or the presence of 1 or 5 µM tunicamycin for 5 h. After tunicamycin exposure, the cells were treated with curcumin, fish oil and BDNF – loaded liquid crystalline nanoparticles [CU-FO-BDNF-LNCPs] 5 µM for 24h (Fig. 10B and C).

The microscope images in figure 10B show a low level of Tht-fluorescence that was detected in the absence of Tunicamycin. And Tht-fluorescence was enhanced in cells exposed to the neurotoxin tunicamycin. Then, it was diminished in cell treated by the nanoparticles.

The quantification results in figure 10C show that Tht-fluorescence was significantly enhanced in tunicamycin treated cells related to controls. A differential in fluorescence was observed in the presence of 1 µM Tunicamycin (6-fold, $^{**}p < 0.01$ compared to RA with FBS and 2-fold, $\#p < 0.05$ compared to RA without FBS). And a significant increase ($p < 0.01$) was seen by increasing tunicamycin concentration at 5 µM compared to the unstressed cells (RA with or without FBS).

No significant difference was seen with cells treated by [CU-FO-BDNF-LNCPs] compared to the unstressed cells (RA with or without FBS) (Fig. 10C). But a significant decrease in Tht-fluorescence was observed with [CU-FO-BDNF-LNCPs] compared with cells exposed to the neurotoxin alone. This result shows the NPs effect on the diminution of tunicamycin-induced ER stress induced in RA-differentiated human neuroblastoma SH-SY5Y cells.

In brief, we can confirm our model of ER stress induced by tunicamycin in RA-differentiated SH-SY5Y cells. And the combined drugs (curcumin, fish oil and BDNF)-loaded by LCNPs is a promising treatment for ER stress in which the neurodegeneration process takes place.

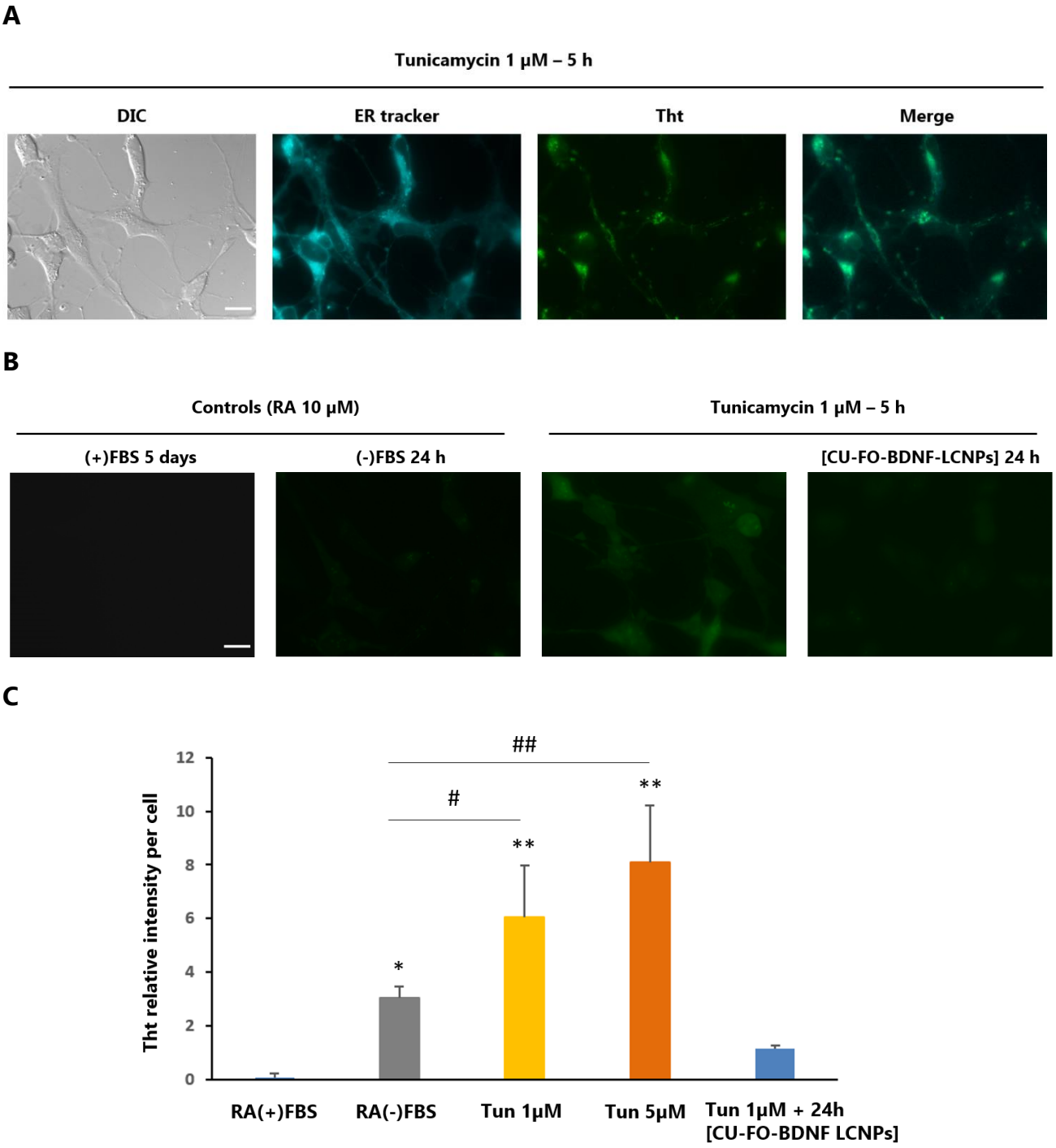

Figure 10. Increased Tht fluorescence in the presence of tunicamycin (Tun). Retinoic acid (RA)-differentiated human neuroblastoma SH-SY5Y cells were treated with 1 or 5 µM tunicamycin (Tun) for 5 h. **A)** Co-localization of Thioflavine T (Tht) and ER tracker in RA-differentiated SH-SY5Y cells treated with Tunicamycin. Cells were stained with 5 µM Tht and ER tracker before visualization. Images were captured using Zeiss microscope. n = 2, Scale bar = 15 µm. **B)** Live cell images were captured with curcumin- and BDNF – loaded

nanoparticles, Scale bar = 15 µm and **B)** fluorescence intensity was determined and quantified. A significant increase in fluorescence was observed with Tun: *p < 0.05 and **p < 0.01 vs RA (+) FBS; #p < 0.05 and ##p < 0.01 vs RA (-) FBS. A significant decrease in fluorescence was observed with [CU-FO-BDNF-LNCPs] compared with Tun. Scale bar = 15 µm.

Chen G. *et al.*[66] reported in their study a molecular mechanism of BDNF-mediated neuroprotection during ER stress responses by the suppression of CHOP. They showed that the pro-apoptotic protein CHOP partially mediated ER stress-induced neuronal death. BDNF suppressed ER stress-induced upregulation/nuclear translocation of CHOP. The transcription of CHOP is regulated by ATF4, ATF6, and XBP1; and BDNF selectively blocked the ATF6/CHOP pathway. Furthermore, BDNF inhibited the induction of death receptor 5 (DR5), a transcriptional target of CHOP.[65] Moreover, tunicamycin was used to measure the activation of components of the unfolded protein response (UPR). When the expression of selected UPR mediators was measured by RT-PCR, exposure to tunicamycin increased the mRNA expression of all of them including CHOP.[60] In addition, it has been shown many mechanisms and pathways involving curcumin and its analogues in the protection from endoplasmic reticulum stress and the promotion of the neuronal survival and repair processes through enhanced BDNF secretion and increased phosphorylation of CREB as compared to untreated degenerating cells.[56-60,67-69]

We can suggest that our system [MO-CU-FO-BDNF] liquid crystalline nanoparticles have a neuroprotection effect against tunicamycin - induced endoplasmic reticulum and show a potential application in neurodegenerative disorders by cell regeneration.

f. Human free BDNF quantification in RA-differentiated SH-SY5Y cells

We quantified the free Brain-Derived Neurotrophic Factor (BDNF) concentrations in SH-SY5Y cell supernates by Quantikine® ELISA Human Free BDNF Immunoassay kit in order to determine the capacity of the NPs to transport the molecule into the cell.

The results in figure 11 show very low BDNF quantities in RA(-)FBS-differentiated SH-SY6Y control cells, in cell exposed to tunicamycin and in cells treated with BDNF non-loaded NPs. But we observed an increase trend of BDNF quantities in cells treated with free-BDNF or BDNF-loaded NPs. And the trend was higher with the single and dual (FO-BDNF)-loaded NPs related to BDNF alone. This suggests the capacity of the NPs to transport the BDNF across the cell membrane. The multiple (FO-CU-BDNF)-loaded NPs may present a competition for the BDNF loading.

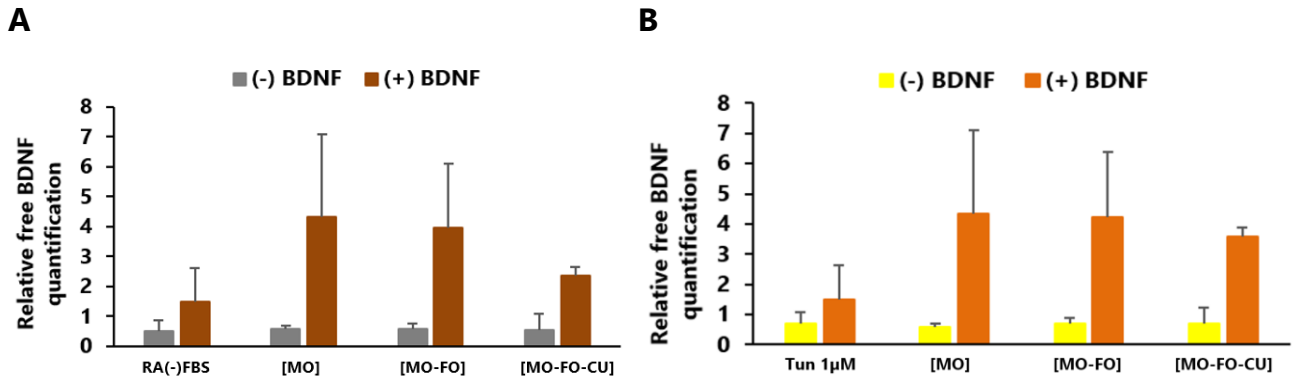

Figure 11. Human free BDNF concentrations normalized with total protein concentration in AR-SH-SY5Y cells supernates: **A)** after NPs 5µM for 48 h treatment **B)** after Tun 1µM 5h and NPs 5µM 48 h treatment. (n=2)

4) Conclusion

In conclusion, single, dual, or multidrug-loaded nanocarriers of the cubosome or spongosome type were obtained. The monoolein MO-based nanoparticles were not toxic and capable to deliver the neurotrophic factor BDNF inside the neuronally derived SH-SY5Y cells as shown by the quantity of free-BDNF in cell. The fish oil promotes the potentiation of BDNF in a combination with the liquid crystalline (MO)-based nano-assembles. The cubosomal nanoarchitectures preserved the antioxidant and the biomolecule in a functional state, ensuring the cell's defense against reticulum endoplasmic stress. But further studies are needed in order to determine an eventual synergistic effect in halting cell death, of curcumin and BDNF upon dual delivery by liquid crystalline nanocarriers.

5) References

(1) Alzheimers'Association. Alzheimer's disease facts and figures. *Alzheimers Dement*. **2016**, 12, 459-509.

(2) Capriotti, T.; Terzakis, K.; Parkinson Disease. *Home Healthc Now*. **2016**, 34(6), 300-307.

(3) Scheltens; P.; Blennow, K.; Breteler, M.M.; de Strooper, B.; Frisoni, G.B.; Salloway, S.; Van der Flier, W.M. Alzheimer's disease. *Lancet* **2016**, 388, 505-17.

(4) Cummings, J.L.; Morstorf, T.; Zhong, K.; Alzheimer's disease drug-development pipeline: few candidates, frequent failures. *Alzheimer's Research & Therapy* **2014**, 6, 37

(5) Aron, L.; Klein, R. Repairing the parkinsonian brain with neurotrophic factors. *Trends in Neurosciences* **2011**, 34(2), 88-100.

(6) Zuccato, C.; Marullo, M.; Vitali, B.; Tarditi, A.; Mariotti, C.; Valenza, M.; Lahiri, N.; Wild, E.J.; Sassone, J.; Ciammola, A. Brain-derived neurotrophic factor in patients with Huntington's disease. *PLoS ONE* **2011**, 6, e22966.

(7) Levi-Montalcini, R. Growth control of nerve cells by a protein factor and its antiserum: discovery of this factor may provide new leads to understanding of some neurogenetic processes. *Science* **1964**, 143(3602),105–110.

(8) Choi, S.H.; Bylykbashi, E.; Chatila, Z.K.; Lee, S.W.; Pulli, B.; Clemenson, G.D.; Kim, E.; Rompala, A.; Oram, M.K.; Asselin, C.; Aronson, J.; Zhang, C.; Miller, S.J.; Lesinski, A.; Chen, J.W.; Kim, D.Y.; van Praag, H.; Spiegelman, B.M.; Gage, F.H.; Tanzi, R.E. Combined adult neurogenesis and BDNF mimic exercise effects on cognition in an Alzheimer's mouse model. *Science* **2018**, 361, eaan8821.

(9) Mitre, M.; Mariga, A.; Chao, M.V. Neurotrophin signalling: novel insights into mechanisms and pathophysiology Clin. *Sci (Lond).* **2017**, 131, 13-23.

(10) Akyol, O.; Sherchan, P.; Yilmaz, G.; Reis, C.; Ho, W.M.; Wang, Y.; Huang, L.; Solaroglu, I.; Zhang, J.H. Neurotrophin-3 provides neuroprotection via TrkC receptor dependent pErk5 activation in a rat surgical brain injury model. Exp. *Neurol.* **2018**, 307, 82–89.

(11) Madduri, S.; Gander, B. Growth factor delivery systems and repair strategies for damaged peripheral nerves. J. *Control Release* **2012**, 161(2), 274-282.

(12) Ferenz, K.B.; Gast, R.E.; Rose, K.; Finger, I.E.; Hasche, A.; Krieglstein, J. Nerve growth factor and brain-derived neurotrophic factor but not granulocyte colony-stimulating factor, nimodipine and dizocilpine, require ATP for neuroprotective activity after oxygen–glucose deprivation of primary neurons. *Brain research* **2012**, 1448, 20-26.

(13) Kowianski, P.; Lietzau, G.; Czuba, E.; Waskow, M.; Steliga, A.; Morys, J. BDNF: A Key Factor with Multipotent Impact on Brain Signaling and Synaptic Plasticity. *Cell. Mol. Neurobiol.* **2018**, 38, 579–593.

(14) Zigova, T.; Pencea, V.; Wiegand, S.J.; Luskin, M.B. Intraventricular administration of BDNF increases the number of newly generated neurons in the adult olfactory bulb. Mol. Cell. *Neurosci.* ***1998***, 11, 234–245.

(15) Pencea, V.; Bingaman, K.D.; Wiegand, S.J.; Luskin, M.B. Infusion of brain-derived neurotrophic factor into the lateral ventricle of the adult rat leads to new neurons in the parenchyma of the striatum, septum, thalamus, and hypothalamus. *J. Neurosci.* **2001**, 21, 6706–6717.

(16) Scharfman, H.; Goodman, J.; Macleod, A.; Phani, S.; Antonelli, C.; Croll, S. Increased neurogenesis and the ectopic granule cells after intrahippocampal BDNF infusion in adult rats. *Exp. Neurol.* **2005,** 192(2), 348-56.

(17) Lee, J.; Duan, W.; Mattson, M.P. Evidence that brain-derived neurotrophic factor is required for basal neurogenesis and mediates, in part, the enhancement of neurogenesis by dietary restriction in the hippocampus of adult mice. *J. Neurochem.* **2002**, 82, 1367–1375.

(18) Palasz, E.; Wysocka, A.; Gasiorowska, A.; Chalimoniuk, M.; Niewiadomski, W.; Niewiadomska, G. BDNF as a Promising Therapeutic Agent in Parkinson's Disease. *Int. J. Mol. Sci.* **2020**, 21, 1170.

(19) Numakawa, T.; Odaka, H.; Adachi, N. Actions of Brain-Derived Neurotrophin Factor in the Neurogenesis and Neuronal Function, and Its Involvement in the Pathophysiology of Brain Diseases. *Int. J. Mol. Sci.* **2018**, 19, 3650.

(20) Price, R.D.; Milne, S.A.; Sharkey, J.; Matsuoka, N. Advances in small molecules promoting neurotrophic function. *Pharmacol. Ther.* **2007**, 115:292-306.

(21) Schmidt, N.; Schulze, J.; Warwas, D.P. Long-term delivery of brain-derived neurotrophic factor (BDNF) from nanoporous silica nanoparticles improves the survival of spiral ganglion neurons in vitro. *PLoS One* **2018**, 13(3), 0194778.

(22) Harris, NM.; Ritzel, R.; Mancini, NS. Nano-particle delivery of brain derived neurotrophic factor after focal cerebral ischemia reduces tissue injury and enhances behavioral recovery. *Pharmacol. Biochem. Behav.* **2016**, 150-151, 48-56.

(23) Xu, J.; Chau, Y. Polymeric nanoparticles decorated with BDNF-derived peptide for neuron-targeted delivery of PTEN inhibitor. *Eur. J. Pharm. Sci.* **2018**, 124, 37-45.

(24) Xing, Y.; Wen, C.Y.; Li, S.T.; Xia, Z.X. Non-viral liposome-mediated transfer of brain-derived neurotrophic factor across the blood-brain barrier. *Neural Regen Res*. **2016**, 11(4):617-22.

(25) Lopes, C.D.F.; Goncalves, N.P.; Gomes, C.P. BDNF gene delivery mediated by neuron-targeted nanoparticles is neuroprotective in peripheral nerve injury. *Biomaterials* **2017**, 121, 83-96.

(26) Jiang, Y.; Fay, J.M.; Poon, C.D. Nanoformulation of Brain-Derived Neurotrophic Factor with Target Receptor-Triggered-Release in the Central Nervous System. *Adv. Funct. Mater.* **2018**, 28(6).

(27) Géral, C.; Angelova, A.; Angelov, B.; Nicolas, V.; Lesieur, S. Multicompartment lipid nanocarriers for targeting of cells expressing brain receptors. In Self-Assembled Supramolecular Architectures: Lyotropic Liquid Crystals; Garti, N., Mezzenga, R., Somasundaran, P., Eds.; John Wiley & Sons, Inc., *New Jersey, NJ*, USA, **2012**, 319–355.

(28) Angelova, A.; Angelov, B. Dual and multi-drug delivery nanoparticles towards neuronal survival and synaptic repair. *Neural Regeneration Research,* **2017**, 12, 886-889.

(29) Glabe, C.G.; Kayed, R. Common structure and toxic function of amyloid oligomers implies a common mechanism of pathogenesis. *Neurology* **2006**, 66: S74–8.

(30) Shacham, T.; Sharma, N.; Lederkremer, G.Z. Protein Misfolding and ER Stress in Huntington's Disease*. Frontiers in Molecular Biosciences* ***2019,*** *6, 20.*

(31) Navit, OS.; Tamuz, BD.; Gerardo, Z. Protein aggregation and ER stress. *Brain Research* **2016**, 658–666

(32) Hetz, C.; Chevet, E.; Harding, H.P. Targeting the unfolded protein response in disease. Nat. Rev. *Drug Discov* **2013**, 12, 703–719.

(33) Cornejo, V.H.; Hetz, C. The unfolded protein response in Alzheimer's disease. Semin. *Immunopathol* **2013***,* 35, 277–292.

(34) Yann, S.; Kyle, R.B. Confounding Roles of ER Stress and the Unfolded Protein Response in Skeletal Muscle Atrophy. Int. J. Mol. Sci. **2021**, 22, 2567

(35) Wang, S.; Kaufman, R.J. The impact of the unfolded protein response on human disease. *J. Cell Biol* **2012**. 197, 857–867.

(36) Hetz, C.; Feroz R. Papa. The Unfolded Protein Response and Cell Fate Control. *Molecular Cell 69* January 18, **2018.** 69, 169-181.

(37) Logue, S.E.; Cleary, P.; Saveljeva, S.; Samali, A. New directions in ER stress-induced cell death. *Apoptosis* 18 **2013**, 537–546.

(38) Chang, T.K.; David, A.L.; Min, L.; Sandoval, W.; Scott, E.; Martin, A.A. Coordination between Two Branches of the Unfolded Protein Response Determines Apoptotic Cell Fate., *Molecular Cell* **2018**. 71, 629–636.

(39) DeGracia, D.J.; Montie, H.L., 2004. Cerebral ischemia and the unfolded protein response. J. Neurochem. 91, 1–8.; Endres, K., Reinhardt, S. ER-stress in Alzheimer's disease: turning the scale? Am. J. Neurodegener. *Dis.* **2013**. 2, 247–265.

(40) Scheper, W.; Hoozemans, J.J. Endoplasmic reticulum protein quality control in neurodegenerative disease: the good, the bad and the therapy. *Curr. Med. Chem*. **2009** 16, 615–626.

(41) Vidal, R.; Caballero, B.; Couve, A.; Hetz, C. Converging pathways in the occurrence of endoplasmic reticulum (ER) stress in Huntington's disease. *Curr. Mol. Med*. **2011**. 11, 1–12.

(42) Xu, K.; Zhu, X.P. Endoplasmic reticulum stress and prion diseases. *Rev. Neurosci.* **2012** 23, 79–84.).

(43) Tajiri, S.; Oyadomari, S.; Yano, S.; Morioka, M.; Gotoh, T.; Hamada, J.I.; Ushio, Y.; Mori, M. Ischemia-induced neuronal cell death is mediated by the endoplasmic reticulum stress pathway involving CHOP. *Cell Death Differ*. **2004**. 11, 403–415.

(44) Katayama, T.; Imaizumi, K.; Manabe, T.; Hitomi, J.; Kudo, T.; Tohyama, M. Induction of neuronal death by ER stress in Alzheimer's disease. *J. Chem. Neuroanat*. **2004**. 28, 67–78.

(45) Chen, G.; Bower, K.A.; Ma, C.; Fang, S.; Thiele, C.J.; Luo, J. Glycogen synthase kinase 3beta (GSK3beta)mediates 6-hydroxydopamine-induced neuronal death. *FASEB J.* **2004**. 18, 1162–1164.

(46) Silva, R.M.; Ries, V.; Oo, T.F.; Yarygina, O.; Jackson-Lewis, V.; Ryu, E.J.; Lu, P.D.; Marciniak, S.J.; Ron, D.; Przedborski, S.; Kholodilov, N.; Greene, L.A.; Burke, R.E. CHOP/GADD153 is a mediator of apoptotic death in substantia nigra dopamine neurons in an in vivo neurotoxin model of parkinsonism. *J. Neurochem*. **2005**. 95, 974–986.

(47) Smith,W.W.; Jiang, H.; Pei, Z.; Tanaka, Y.; Morita, H.; Sawa, A.; Dawson, V.L.; Dawson, T.M.; Ross, C.A. Endoplasmic reticulum stress and mitochondrial cell death pathways mediate A53T mutant alpha-synuclein-induced toxicity. *Hum. Mol. Genet*. **2005**.14, 3801–3811.

(48) Hirabayashi, M.; Inoue, K.; Tanaka, K.; Nakadate, K.; Ohsawa, Y.; Kamei, Y.; Popiel, A.H.; Sinohara, A.; Iwamatsu, A.; Kimura, Y.; Uchiyama, Y.; Hori, S.; Kakizuka, A. VCP/p97 in abnormal protein aggregates, cytoplasmic vacuoles, and cell death, phenotypes relevant to neurodegeneration. *Cell Death Differ*. **2001**. 8, 977–984.

(49) Turner, B.J.; Atkin, J.D. ER stress and UPR in familial amyotrophic lateral sclerosis. *Curr. Mol. Med.* **2006**. 6, 79–86.

(50) Wang, H.; Wang, X.; Ke, Z.; Comer, A.L.; Xua, M.; Frank, J.A.; Zhang, Z.; Shi, X.J.L. Tunicamycin-induced unfolded protein response in the developing mouse brain. *Toxicology and Applied Pharmacology* **2015.** 283(3)157–167.

(51) Zamarbide, M.; Martinez-Pinilla, E.; Ricobaraza, A.; Aragón, T.; Franco, R.; Pérez, M. Phenyl Acyl Acids Attenuate the Unfolded Protein Response in Tunicamycin-Treated Neuroblastoma Cells. *PLoS ONE* **2013**. 8(8): e71082.

(52) Oda, T.; Kosuge, Y.; Arakawa, M.; Ishige, K.; Ito, Y. Distinct mechanism of cell death is responsible for tunicamycin-induced ER stress in SK-N-SH and SH-SY5Y cells. *Neurosci Res.* **2008**, 60, 29-39. doi: 10.1016/j.neures.2007.09.005.

(53) Angelova, A.; Drechsler, M.; Garamus, V.M.; Angelov, B. Liquid crystalline nanostructures as PEGylated reservoirs of omega-3 polyunsaturated fatty acids: Structural insights toward delivery formulations against neurodegenerative disorders. *ACS Omega,* **2018**, 3, 3235–3247.

(54) Salehi, B.; Calina, D.; Docea, A.O.; Koirala, N.; Aryal, S.; Lombardo, D.; Pasqua, L.; Taheri, Y.; Marina Salgado Castillo, C.; Martorell, M.; Martins, N.; Iriti, M.; Suleria, H.A.R.; Sharifi-Rad, J. Curcumin's Nanomedicine Formulations for Therapeutic Application in Neurological Diseases. *J. Clin. Med.* **2020**, 9, 430.

(55) Shehzad, Q.; Rehman, A.; Mahdi, S.; Zuo, M.; Khan, M.A.; Ali, A.; Khan, S.; Karim, A.; Usman, M.; Hussain, A.; Wenshui, X. Improving the oxidative stability of fish oil nanoemulsions by co-encapsulation with curcumin and resveratrol. *Colloids and Surfaces B: Biointerfaces* **2021**, 199, 111481.

(56) Uddin, M.S.; Mamun, A.L.; Rahman, M.; Jeandet, P.; Alexiou, A.; Behl, T.; Sarwar, S.; Sánchez, E.S.; Ashraf, G.M.; Amany, A.; Ghadeer, M.; Peluso, A.I.; Mohamed, M.A. Natural Products for Neurodegeneration: Regulating Neurotrophic Signals. *Oxidative Medicine and Cellular Longevity,* **2021**, 8820406.

(57) Bawari; S.; Tewari, D.; Argüelles, S.; Sah, A.N.; Nabavi, S.F.; Xu, S.; Vacca, R.A.; Nabavi, S.M.; Shirooie, S. Targeting BDNF signaling by natural products: Novel synaptic repair therapeutics for neurodegeneration and behavior disorders. *Pharmacological Research*, **2019**, 148, 104458.

(58) Zhang, L.; Fang, Xu, Y. Curcumin improves amyloid β-peptide (1-42) induced spatial memory deficits through BDNF-ERK signaling pathway. *PLoS One* **2015**. 10, 6, e0131525.

(59) Wang R, Li YH, Xu Y, Li YB, Wu HL, Guo H, Zhang JZ, Zhang JJ, Pan XY, Li XJ. Curcumin produces neuroprotective effects via activating brain-derived neurotrophic factor/TrkB-dependent MAPK and PI-3K cascades in rodent cortical neurons. *Prog Neuropsychopharmacol Biol Psychiatry.* **2010**, 34, 147-53.

(60) Kandezi, N.; Mohammadi, M.; Ghaffari, M.; Gholami, M.; Motaghinejad, M.; Safari, S. Novel Insight to Neuroprotective Potential of Curcumin: A Mechanistic Review of Possible Involvement of Mitochondrial Biogenesis and PI3/Akt/ GSK3 or PI3/Akt/CREB/BDNF Signaling Pathways. *Int J Mol Cell Med.* **2020**, 9, 1-32.

(61) Naiki, K.; Higuchi, M.; Hosokawa, T.T. Fluorometric determination of amyloid fibrils in vitro using the fluorescent dye, thioflavin T1, *Anal. Biochem*.**1989**. 177(2),244–249.

(62) Lindgren, E.M.; Sorgjerd, K.; Hammarstrom, P. Detection and characterization of aggregates, prefibrillar amyloidogenic oligomers, and protofibrils using fluorescence spectroscopy, *Biophys*. J. **2005**. 88(6),4200.

(63) Sigurdsson, E.M. Histological staining of amyloid-beta in mouse brains, *Methods Mol.* Biol. **2005**. 299, 299–308.

(64) Beriault, R.D; Geoff, H.; Werstuck. Detection and quantification of endoplasmic reticulum stress in living cells using the fluorescent compound, Thioflavin T. *Biochimica et Biophysica Acta* **2013.** 1833, 2293–2301.

(65) Verwilst, P.; Kim, K.; Sunwoo,K.; Kim, H.R.; Kang, C.; Kim, J.S. Revealing Protein Aggregates under Thapsigargin-Induced ER Stress Using an ER-Targeted Thioflavin. *ACS Sens*. **2019**, 4, 2858−2863.

(66) Chen, G.; Fan, Z.; Wang, X.; Ma, C.; Kimberly, A.; Bower; Shi, X.; Ke, Z.J.; Luo, J. Brain-Derived Neurotrophic Factor Suppresses Tunicamycin-Induced Upregulation of CHOP in Neurons. *J Neurosci Res*. **2007**. 85(8): 1674–1684.

(67) Shakeri, A.; Zirak, M.R.; Hayes, A.W.; Reiter, R.; Karimi, G. Curcumin and its analogues protect from endoplasmic reticulum stress: Mechanisms and pathways. *Pharmacol Res.* **2019**, 146:104335.

(68) Angelov, B.; Angelova, A., Nanoscale clustering of the neurotrophin receptor TrkB revealed by super-resolution STED microscopy. *Nanoscale*, **2017**, 9, 9797–9804.

(69) Guerzoni, L.P.B.; Nicolas, V.; Angelova, A. In vitro modulation of TrkB receptor signaling upon sequential delivery of curcumin-DHA loaded carriers towards promoting neuronal survival, *Pharmaceutical Research*, **2017**, 34, 492-505.

General conclusion and perspectives

Neurodegenerative disorders (NDs) are characterized by progressive damage of the neuronal cells due to many factors risks: oxidative stress, neurotrophic factors deficiency, reticulum endoplasmic and mitochondrial stress. We designed a novel combination therapy approach by natural active compounds and biomolecules delivered by lipid-based nanoparticles. Our study has brought many useful findings for future research, future therapeutical, food or environmental applications.

First, we **deeply characterized the structural and physico-chemical properties of the monoolein-TPGS-PEG$_{1000}$/fish oil/curcumin assemblies:**

- ✓ We investigated the hydration Level and the FO/MO weight ratio which were necessary for the preparation of stable MO/TPGS-PEG$_{1000}$/FO/CU nanoparticles by self-assembly,
- ✓ We established the phase diagram of the amphiphilic self-assembled systems at 22°C,
- ✓ We highlighted the formation of cubosome and spongosome nanoparticles,
- ✓ We showed the higher entrapment efficiency (and the loading capacity of the nanocarriers for CU compared to other types of NPs.
- ✓ We unveiled the capacity of the liquid crystalline nano-object type to load, to protect and deliver biomolecules as catalase, brain-derived neurotrophic factor (BDNF) into cell.

Then, we **assessed the *in vitro* effect of the drug-loaded cubosome and spongosome nanoparticles in different cellular models of neurodegeneration:**

- ✓ We checked the safety of the nanoparticles in retinoic acid-differentiated SH-SY5Y cells
- ✓ We established serum starvation-induced cell death, H_2O_2-induced oxidative stress, tunicamycin-induced endoplasmic reticulum stress as cellular models
- ✓ We determined the cell protection against cell death and the promotion of cellular survival and repair by the single, dual or multidrug-loaded liquid crystalline nanoparticles.

The nanodispersed self-assembled lipid systems are very attractive for the administration of neuroprotective water-insoluble molecules and proteins to treat neuronal damage linked to the neurodegenerative disorders. The designed [FO-CU-BDNF] liquid crystalline nanoparticles have shown neuroprotection potential and present a promising application in cell repair or neurogenesis.

Further studies are needed to determine an eventual synergistic effect in cell regeneration of curcumin and BDNF upon dual delivery by the liquid crystalline nanocarriers. An understanding of the mechanism of action *in vitro* could be done by determining the implicated signaling pathways.

The development of nanoformulations that consider different routes of administration are perspectives for future applications *in vivo*. A study of the delivery to the brain upon intranasal administration can be realized as regarding the comfort of future patients. Nanoparticles covered by a surfactant may allow delivery of molecules through the blood-brain barrier by receptor-mediated transcytosis. The long-term goal is to achieve neurogenesis and neuroregeneration through synergistic action of innovative neuro-nanodrugs.

List of publications

PUBLICATIONS

- Rakotoarisoa, M.; Angelov, B.; Espinoza, S.; Khakurel, K.; Bizien, T.; Drechsle, M.; Angelova, A. Composition-Switchable Liquid Crystalline Nanostructures as Green Formulations of Curcumin and Fish-Oil. *ACS Sustainable Chemistry & Engineering* **2021,** 9(44).
- Rakotoarisoa M., Angelova A. Chapter 33: Amphiphilic Nanocarrier Systems for Curcumin Delivery in Neurodegenerative Disorders. *In book: The Road from Nanomedicine to Precision Medicine, Part B. Edited By Mousa, SA.; Bawa, R.; Taylor GFT.; Group F. 1st edition* **2020.**
- Rakotoarisoa, M.; Angelov, B.; Espinoza, S.; Khakurel, K.; Bizien, T.; Angelova A. Cubic Liquid Crystalline Nanostructures Involving Catalase and Curcumin: BioSAXS Study and Catalase Peroxidatic Function after Cubosomal Nanoparticle Treatment of Differentiated SH-SY5Y Cells. *Molecules* **2019**, 24(17):3058.
- Rakotoarisoa, M.; Angelov, B.; Garamus, V.M.; Angelova, A. Curcumin- and fish oil-loaded spongosome and cubosome nanoparticles with neuroprotective potential against H_2O_2-induced oxidative stress in differentiated human SH-SY5Y cells. *ACS Omega* **2019**, 4, 3061−3073.
- Rakotoarisoa, M.; Angelova, A. Amphiphilic nanocarrier systems for curcumin delivery in neurodegenerative disorders. *Medicines* **2018***,* 5(4), 126.

ORAL COMMUNICATIONS

"Structural transitions of cubic membrane mimetics and lyotropic liquid crystalline phases upon loading of fish oil and curcumin "

- 1st Annual Meeting of GDR 2088 BIOMIM "Biomimétisme et Bioinspiration", Nice, France, 2020. oral presentation

"Combined loading of curcumin and catalase by cubosome liquid crystalline nanocarriers

and their antioxidant activity in SH-SY5Y neuronal cells"

- ULLA Summer school, Helsinki, Finlande, 2019, Poster
- Workshop Nanosaclay, Orsay, France, 2019, Poster
- Journée des doctorants et post doctorants de l'Institut Galien Paris Sud, Orsay, France, *2019,* présentation orale

"Lipid nanocarriers for curcumin delivery and their neuroprotective potential against H_2O_2-induced oxidative stress in human SH-SY5Y cells"

- Journée de la recherche, Châtenay-Malabry, France, 2018, Poster

"Structural characterization of antioxidant-loaded liquid crystalline nanocarriers and in vitro study in human neuronal SH-SY5Y cells"

- Journée des doctorants et post doctorants de l'Institut Galien Paris Sud, Orsay, France, 2018, Poster
- Journée de l'école doctorale « Innovation thérapeutique : du fondamental à l'appliquée », Châtenay-Malabry, France, 2018, Poster

"Combined loading of fish oil and curcumin in spongosome and cubosome carriers towards protection of human neuronal SH-SY5Y cells against oxidative stress"

- 1er Symposium international de système de délivrance des médicaments et de nouvelles thérapies, Orsay, France, 2018, Poster

" Differentiation of SH-SY5Y cells by retinoic acid and treatment with tunicamycin for the induction of an in vitro model of neurodegeneration"

- Journée de la recherche, Châtenay-Malabry, France, 2017, Poster
- 7ème Symposium annuel du LabEx LERMIT, Orsay, France, 2017, Poster

Titre : Nanovecteurs lipidiques de molécules neuroprotectrices impliquées dans plusieurs mécanismes de régénération

Mots clés : nanoparticules lipidiques, curcumine, BDNF, maladies neurodégénératives, cellules SH-SY5Y

Résumé : Les systèmes nanoparticulaires de délivrance de médicaments à base de lipides présentent plusieurs avantages y compris la co-encapsulation de composés actifs pour le traitement ou la prévention de maladies multifactorielles telles que les maladies neurodégénératives.
Le principal objectif de ce travail de thèse est la formulation et la caractérisation physico-chimique des nanoparticules lipidiques à cristal liquide (cubosomes et spongosomes) pour le transport et la protection de plusieurs principes actifs neuroprotecteurs (curcumine, huile de poisson, catalase, facteur neurotrophique dérivé du cerveau), dont la plupart se comporte comme des molécules instables. La méthode d'autoassemblage a été exploitée pour la préparation des nanoparticules, offrant des avantages de biocompatibilité et l'association de différents composants actifs hydrophiles et lipophiles et matriciels dans chaque type de nano-objet à cristal liquide. L'organisation cristalline liquide interne des vecteurs lipidiques a été caractérisée par la diffusion des rayons X à petit angle (SAXS).
Le deuxième objectif de ce travail est l'évaluation in-vitro des effets neuroprotecteur et régénérateur des nanoparticules lipidiques chargées en une ou plusieurs molécules actives. Les modèles cellulaires de troubles neurodégénératifs étudiés ont été obtenus par traitement des cellules SH-SY5Y du neuroblastome humain avec l'acide rétinoïque et la neurotoxine tunicamycine. Les effets protecteurs des nanoparticules contre le stress oxydatif, l'apoptose cellulaire, le stress du réticulum endoplasmique et d'autres facteurs destructifs provoqués par les neurotoxines ont été examinés.
Les systèmes lipidiques auto-assemblés nano-dispersés de type cubosome et spongosome sont des vecteurs potentiels pour l'administration de molécules insolubles et de protéines neuroprotectrices fragiles pour diminuer les dommages neuronaux liés aux troubles neurodégénératifs.

Title : Lyotropic liquid crystalline nanoparticles for multidrug loading involved in neuroprotection and regeneration mechanisms

Keywords : Lipid nanoparticles, curcumin, BDNF, neurodegenerative disease, cellular model SH-SY5Y

Abstract : Drug delivery systems using lipid nanoparticles have several advantages as the co-encapsulation of multiple active compounds for the treatment or the prevention of multifactorial diseases like neurodegenerative disorders.
The main objective of the PhD work is the formulation and the physico-chemical characterization of lipid-based liquid crystalline nanoparticles (cubosomes and spongosomes) for the loading and protection of multiple neuroprotective active ingredients (curcumin, fish oil, catalase, brain-derived neurotrophic factor), most of which behave as unstable molecules. The self-assembly method was exploited for the preparation of these nanoparticles, which offer advantages of biocompatibility and association of different hydrophilic and lipophilic active and matrix components in every liquid crystalline nano-object type. The inner liquid crystalline organization of the lipid carriers was characterized by small angle x-ray scattering (SAXS).
The second objective of the PhD work is the in-vitro evaluation of the neuroprotective and regenerative effects of single or multidrug-loaded lipid nanoparticles. The studied cellular models of neurodegenerative disorders were obtained by treatment of human neuroblastoma SH-SY5Y cells by retinoic acid and the neurotoxin tunicamycin. The protective nanoparticle effects against the oxidative stress, cell apoptosis, endoplasmic reticulum stress and other destructive factors, provoked by the neurotoxins, were examined.
The obtained nanodispersed self-assembled lipid systems of cubosome and spongosome type appear to be very attractive for the administration of neuroprotective water-insoluble molecules and fragile soluble proteins towards diminished neuronal damage in neurodegenerative disorders.